TECHNISCHE UNIVERSITÄT MÜNCHEN

Fakultät für Elektrotechnik und Informationstechnik

Lehrstuhl für Nanoelektronik

Flexible biosensors using solution processable devices

Saumya Joshi

Vollständiger Abdruck der von der Fakultät für Elektrotechnik und Informationstechnik der Technischen Universität München zur Erlangung des akademischen Grades eines

Doktor-Ingenieurs (Dr.-Ing.)

genehmigten Dissertation.

Vorsitzende(r): Prof. Dr.-Ing. Ulrich Wagner

Prüfer der Dissertation:

1. Prof. Paolo Lugli, Ph.D.
2. Prof. Dr. Oliver Hayden

Die Dissertation wurde am 21.01.2019 bei der Technischen Universität München eingereicht und durch die Fakultät für Elektrotechnik und Informationstechnik am 07.10.2019 angenommen.

To my parents for teaching me to dream big,
To my husband for teaching me how to make dreams real

Abstract

Advancements in the field of organic and flexible electronics have paved path for low cost electronic devices. Sensor technology is another field which has seen tremendous progress over the past few years. Combining these two growing technologies, has led to the development of low cost sensors which are highly sensitive, robust against mechanical deformation and are bio compatible.

In the present thesis, significant contributions are made to this growing field of flexible electronic biosensors. The major transducing element in the current work is an electrolye gated field effect transistor. Two semiconductors, carbon nanotube and indium gallium zinc oxide are used which can be deposited by low cost solution processable techniques like spray deposition. Several different sensing systems like enzyme-based, non enzymatic and immunosensing are demonstrated along with the factors that can potentially affect the sensor response. We have also investigated the use of ion-selective membranes in transistors for sensing ions like H+ and NH_4+. In this thesis, we have also discussed the impact on the transistor device characteristics when an ion-selective membrane is replaced by a lipophilic membrane. Significant changes in the transistor performance are observed as the composition of lipophilic membrane is varied. This also led to a novel n-type water- and air- stable carbon nanotube field effect transistor. We also demonstrated use of logic circuits like inverters in sensing of molecules like H+ ions. Different inverter circuits are explored to find the best sensor in terms of high gain and high noise margin. Various studies are performed which prove that the electrolyte gated systems with transistors and inverters developed in this work are mechanically robust and reusable, and have high potential in making the dream of point-of-care diagnostics a reality.

Zusammenfassung

Die Fortschritte auf dem Gebiet der organischen und flexiblen Elektronik haben den Weg für kostengünstige elektronische Geräte geebnet. Die Sensorik ist ein weiterer Bereich, der in den letzten Jahren enorme Fortschritte erzielt hat. Die Kombination dieser beiden wachsenden Technologien hat zur Entwicklung von kostengünstigen Sensoren geführt, die hochempfindlich, robust gegen mechanische Verformung und biokompatibel sind.

In der vorliegenden Arbeit werden wichtige Beiträge zu diesem wachsenden Bereich der flexiblen elektronischen Biosensoren geleistet. Das wichtigste Wandlerelement in der aktuellen Arbeit ist ein elektrolyt-gesteuerter Feldeffekttransistor. Es werden zwei Halbleiter, Kohlenstoff-Nanoröhrchen und Indium-Gallium-Zinkoxid verwendet, die mit kostengünstigen, lösungsverarbeitbaren Verfahren wie das Sprühverfahren aufgebracht werden können. Mehrere verschiedene Sensorsysteme wie enzymatische, nicht-enzymatische und immunosensorische Detektionserfahren werden zusammen mit den Faktoren, die die Sensorantwort potenziell beeinflussen können, gezeigt. Wir haben auch den Einsatz von ionenselektiven Membranen in Transistoren zur Messung von Ionen wie H+ und NH4+ untersucht. Verschiedene Inverterschaltungen werden untersucht, um den besten Sensor in Bezug auf hohe Verstärkung und hohe Rauschgrenze zu finden. Es werden verschiedene Studien durchgeführt, die belegen, dass die in dieser Arbeit entwickelten elektrolytgesteuerten Systeme mit Transistoren und Invertern mechanisch robust und wiederverwendbar sind und ein hohes Potenzial haben, den Traum von der Point-of-Care-Diagnose zu verwirklichen.

Contents

List of Figures

List of Tables

Chapter 1

Introduction

1.1 Introduction

The word "sensor" originates from the Latin word "sentire" meaning 'to identify'. As described by the Nature journal, "biosensors are devices that are used to detect the presence or concentration of a biological analyte, such as a bio-molecule, a biological structure or a microorganism". Biosensors consist of three main parts: a component that recognizes the analyte and produces a signal, a signal transducer, and a reader device [24]. Biosensors find their use in the fields of environment, biomedical and food industries for detection of contaminants. For example, they can be used for monitoring glucose levels in body, unwanted microbes in food, heavy metal contamination in soil, pesticides in water and other harmful chemicals. Figure 1.1 shows some of these potential applications of biosensors.

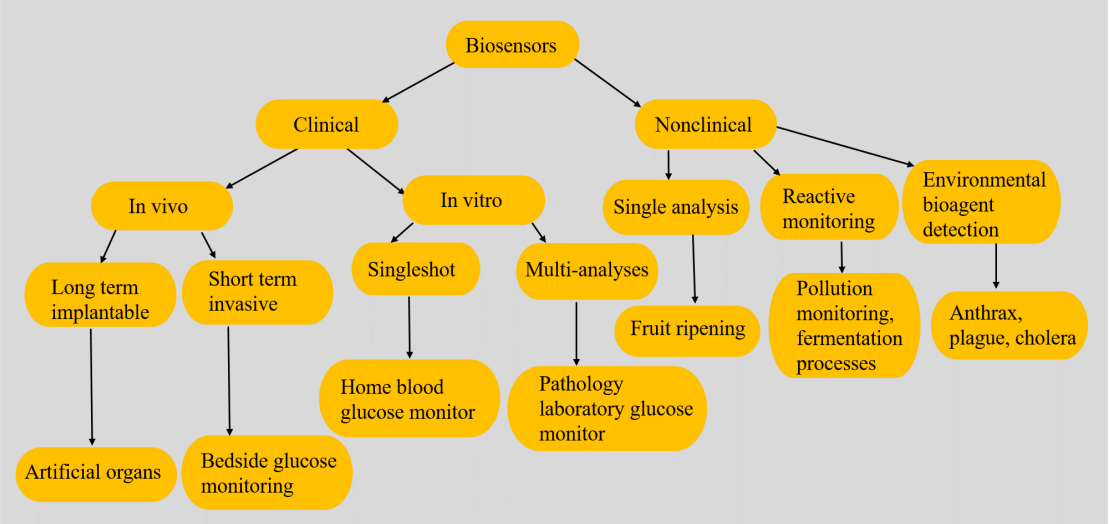

FIGURE 1.1: Potential applications of biosensors [1].

Commonly demonstrated sensors are electrochemical, optical, surface plasmon resonance, enzymatic and bacterial sensors. Among these, electrochemical sensors have gathered the most attention as they provide a simple, inexpensive, yet accurate and sensitive platform for diagnosis [25]. Electrochemical biosensors have an electrical transducer which converts the biological recognition into a useful electrical signal. Amperometric and potentiometric biosensors are the most common biosensors in this category. Potentiometric biosensors convert the biological recognition into a potential signal/change whereas amperometric biosensors work on the conversion into a current response.

In the field of diagnostics, existing laboratory based analytical instrumentation and tests are not sensitive enough for the detection of several bio-molecules In addition, such tests are time-consuming and expensive. Hence, there is clear need for smaller, faster and cheaper sensors which have the capability to produce analytical results available at patient bedside in a time frame of minutes and thus can significantly improve the quality of care and treatment provided. Novel fabrication methods have been demonstrated, where robust sensors are implemented for highly-sensitive chemical analysis without use of heavy equipments [26]. Such sensors can be integrated into flexible substrates like polyethylene terephthalate, polyimide, textile etc. Owing to their intrinsic flexibility, sensors on such substrates can withstand electrical and mechanical strain and deformation that is expected to be encountered during the usage of the sensor [27]. Figure 1.2 shows such sensors where the sensing and transducing element is made on the flexible polyimide substrate.

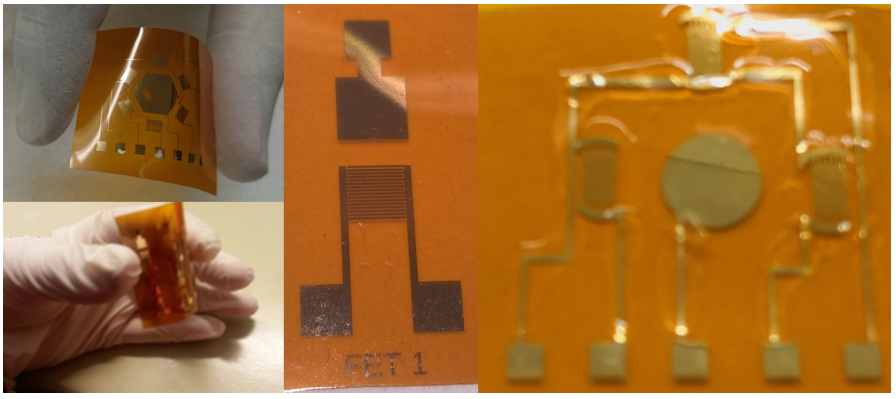

FIGURE 1.2: Sensors made on a flexible substrate polyimide during this thesis work.

In this thesis flexible electrochemical biosensors are fabricated using solution processable techniques. Solution processable techniques are believed to be low cost alternative to traditional silicon-based technologies that can enable the ubiquitous flexible electronics [28]. Towards this, extensive research has been done on solution-processable, functionally capable semiconductors [29]. These semiconductors demonstrate the ability for efficient charge carrier transport and stability such that they can be processed in ambient conditions without need for an expensive environmental setup [30]. In this work, two such semiconductors are discussed, carbon nanotubes and indium gallium zinc oxide. These

semiconductors are used to make field effect transistors and inverters which are then used as the main transducing element of the biosensors. A major difference in these electronic devices from their traditional MOS (metal oxide semiconductor) counterparts is in the nature of gate dielectric. Electronic biosensors have an electrolyte as the gate dielectric which also brings the analyte or bio-molecule of interest to the sensor surface. Below section describes how this work is organized in the present thesis.

1.2 Organization of thesis

Chapter 2 presents three major types of biosensors and their transduction technologies, potentiometric, amperometric and optical. As this thesis is focused on electrochemical sensors, some important electrochemical concepts like nernst potential, debye length and double layer capacitance are explained in detail. This chapter also introduces different sensing parameters relevant to a biosensor like sensitivity, dynamic range and selectivity.

Chapter 3 discusses in detail carbon nanotube (CNT) as an electronic material. This chapter presents different methods for the production of CNTs and their chemical, mechanical and electronic properties. This chapter also includes details on using CNTs as a semiconductor in field effect transistor and possible device topologies. Finally, fabrication methods for carbon nanotube field effect transistors (CNTFETs) are presented including the ones used in this thesis.

Chapter 4 presents different types of biosensors developed using CNTFETs. These sensors are based on different sensing principles like enzyme based, non-enzymatic and immunosensing. This chapter also includes a study on the dependence of the sensor geometry and electrolyte on the performance of a biosensor.

Chapter 5 presents how membranes can play a major role in electrolyte gated field effect transistors and sensors developed using them. Ion-selective membranes are used to develop pH-sensitive and ammonium ion (NH_4+) selective sensors. Lipophilic membranes on the other hand improve or convert the characteristics of the CNTFETs. Theory of logic inverter is also described in this chapter. Finally, pMOS and CMOS logic inverters using only CNTFETs are demonstrated.

Chapter 6 presents work on a novel solution processable semiconductor, indium gallium zinc oxide (IGZO). In the first half of this chapter, fabrication and characterization of IGZO based FETs is described. To have a better understanding of these devices, modeling and parameter extraction is performed along with statistical data analysis. These transistors are later used in developing sensors and inverters with or without CNTFETs for CMOS or nMOS-only logic respectively.

Chapter 7 provides a future outlook on sensing using complex multi transistor circuits fabricated from solution processable technologies.

Chapter 2

Biosensors

2.1 Working Principle

A biosensor is an analytical device that contains an immobilized biological material capable for interacting with a target analyte (compund of interest) specifically and in return producing physical, chemical or electrical signals that can be measured. Biosensors generally perform a quantitative analysis of the analytes by converting their biological response into a measurable signal. The performance of the biosensor is highly dependent on the specificity and selectivity of the immobilized biological material.

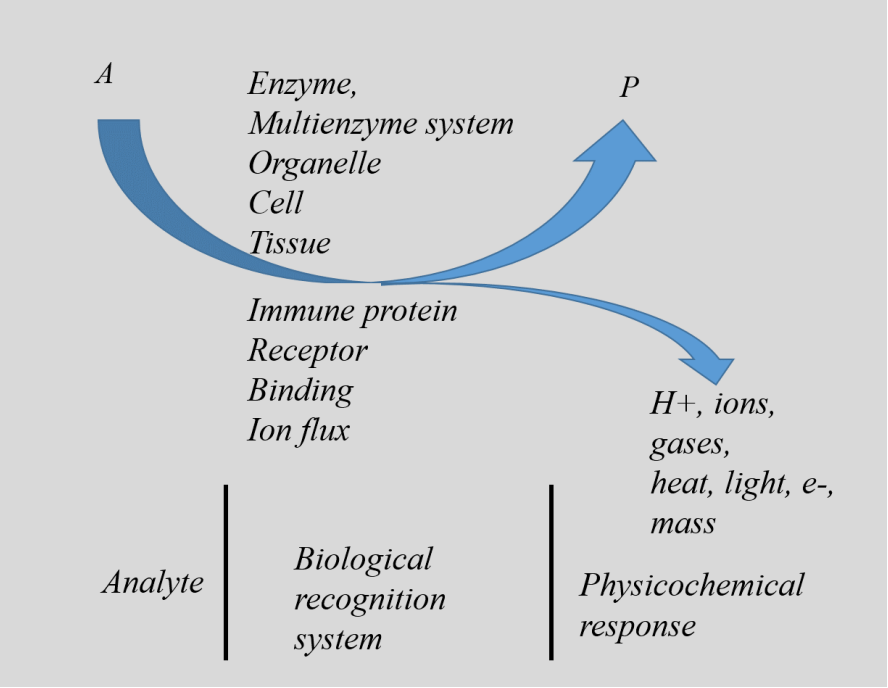

FIGURE 2.1: A biological recognition-response system [2]

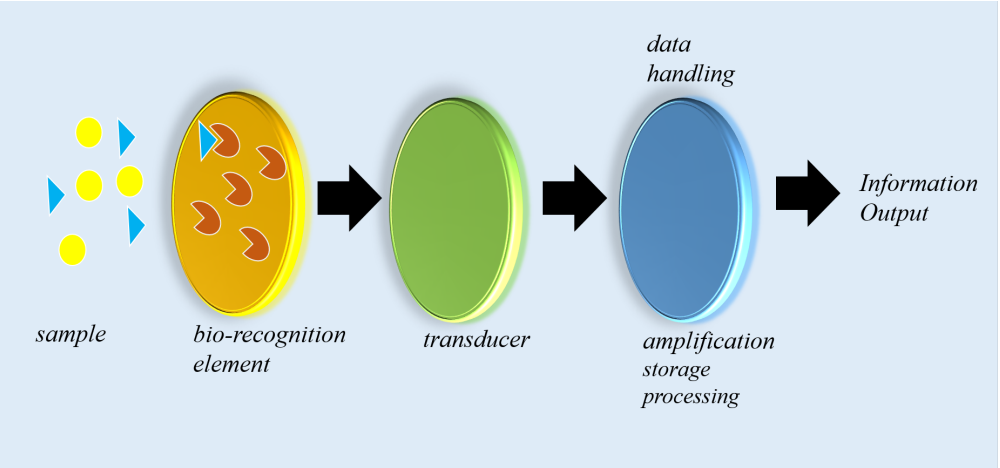

FIGURE 2.2: Schematic of a biosensor showing transducer principle. [2]

Figure 2.1 shows the generalized biological recognition-response system [2]. For better understanding of the working principle of biosensors one can assume an example where a biological interaction may produce change in the ionic concentration like (H+, NH_4+) or release or uptake of gases (CO_2, O_2,NH_3) or in an optical parameter of the system, such that it may be converted into an electrical signal. Figure 2.2 emphasizes on the need of close proximity between the biological recognition response system and the transducer which converts the biological signal into an electrical response. To achieve this proximity the biological recognition element is normally immobilized on the transducer device surface. With an appropriate immobilization scheme, it is possible to construct specific and selective biosensors for the qualification of several potential analytes in such a way that the fabricated biosensors can be repeatedly used several times (may be around 10,000 times) for a long period (many months).

2.2 Transduction Technologies

Table 2.1 mentions four major classes of transducers and their well known and used examples in the field of bio-sensing research. These are : potentiometric, amperometric, optical and other devices.

2.2.1 Potentiometric Sensors

As their name suggests, "potentiometric" sensors measure the electric potential of an electrode when no voltage is present. A common configuration of potentiometric sensors is to measure the potential difference between working electrode and reference electrode. In this configuration the potential of the working electrode depends on the concentration(or activity) of the analyte in the gas or solution phase. The Nernst Equation 2.1 [31] is commonly used to describe the ideal response of such a cell.

class	examples
potentiometric	ion-selective electrodes (ISE) ion-selective electrodes field effect transistor (ISFET) gas selective electrode
amperometric	metal electrodes mediated systems conducting organic salts
optical	ellipsometry planar waveguide fiber optic surface plasmon resonance
other	thermistor surface conductance piezoelectric/surface acoustic wave (SAW)

TABLE 2.1: Classification of Transducers [2].

$$EMF = K + \frac{RT}{zF} ln(a_I) \tag{2.1}$$

where EMF is the electromotive force (the observed potential at zero current), K is a constant potential contribution that often includes the liquid-junction potential at the reference electrode, a_I is the sample activity for the ion I with charge z, and R, T, and F are the gas constant, absolute temperature, and Faraday constant, respectively [31]. It is important to note that the ion activity a_I is the uncomplexed concentration of the analyte, which means that if a complexing agent is present in the sample a_I may be few orders of magnitude smaller than the total analyte concentration.

Ion-elective electrodes (ISEs) represent the largest group among potentiometric sensors. The first and still most used ISE being a pH-sensitive glass electrode. Since that there has been a lot of research done in this area and there are now different types of ISEs that can determine concentration of different ions in liquid sample. A stable reference electrode contacting the sample solution through a liquid junction is used to make measurements with ISEs where charge separation causes signal generation at the interface between ion-selective membrane and the solution [32].

Figure 2.3 shows arrangement for a classical ISEs which is symmetrical as a membrane separates two solutions, the test solution and the inner solution with constant concentration of ionic species. This ISE is connected to a reference electrode (usually Ag/AgCl) in contact with the internal solution that contains chloride ions at constant concentration. The measured ISE potential is the sum of the two reference electrode potentials, the membrane potential constituted by boundary potentials at each membrane/solution interface, and a possible diffusion potential which may be caused by an ion concentration gradient within the ion-selective membrane phase [32].

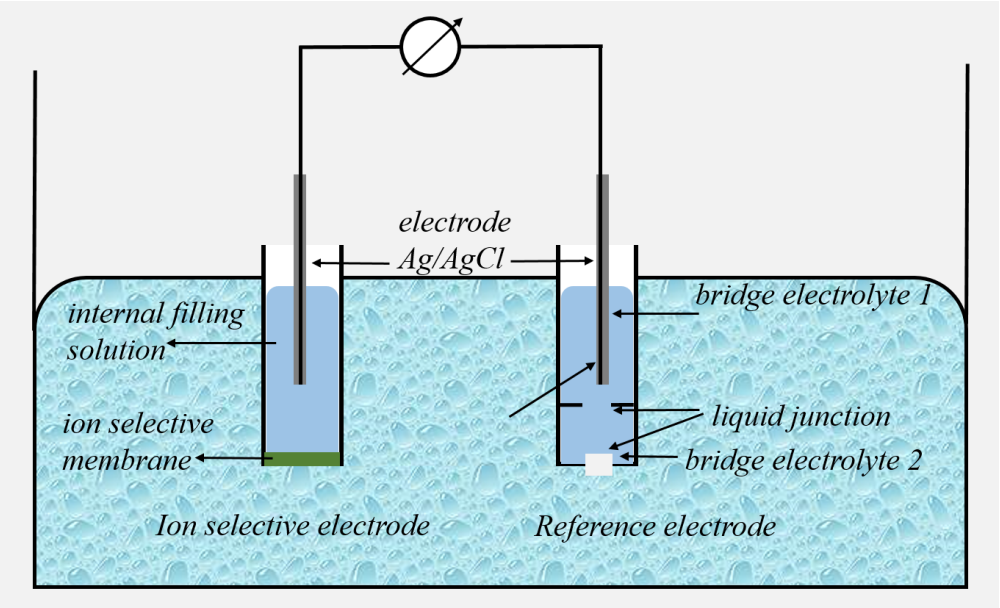

FIGURE 2.3: Potentiometric cell assembly with a liquid inner contact ion-selective membrane electrode and a double junction reference electrode.

Potentiometric ion and chemical sensors based on field-effect devices which can be fabricated and miniaturized, form another group of transducers. Out of these, ion-selective field-effect transistors (ISFETs) [33] are most researched. ISFETs also often called as ChemFETs ("Chemically Sensitive field effect transistors") use different ion-selective membranes which contain some ionophore to obtain sensitivity towards a particular ion. Figure 2.4 shows the schematic and profile of charge, electric field and potential at different interfaces of ISFET. In addition, the combination of ion-selective devices with enzymes and immunological recognition-response systems has extended the range of potentiometric devices to enzymes substrates and antigens. A detail description of such FETs is provided in chapter 4.

2.2.2 Amperometric Sensors

Amperometric sensors work on the current–concentration relationship. The schematic of such an amperometric sensor is shown in Figure 2.5. The working electrode behaves as a cathode or an anode depending on whether the electrons are added to or withdrawn from the sample. As in the case of potentiometric sensors the general condition of the closed circuit must be satisfied, however the requirements on the stability of the reference electrode are relaxed in case of amperometric sensors [3].

The flow of current leads to a measurable change in bulk concentration and this chemical transformation is described well by the Faraday's law given in equation 2.2 [3] where C is the molar concentration and V_{cell} is the volume of the cell.

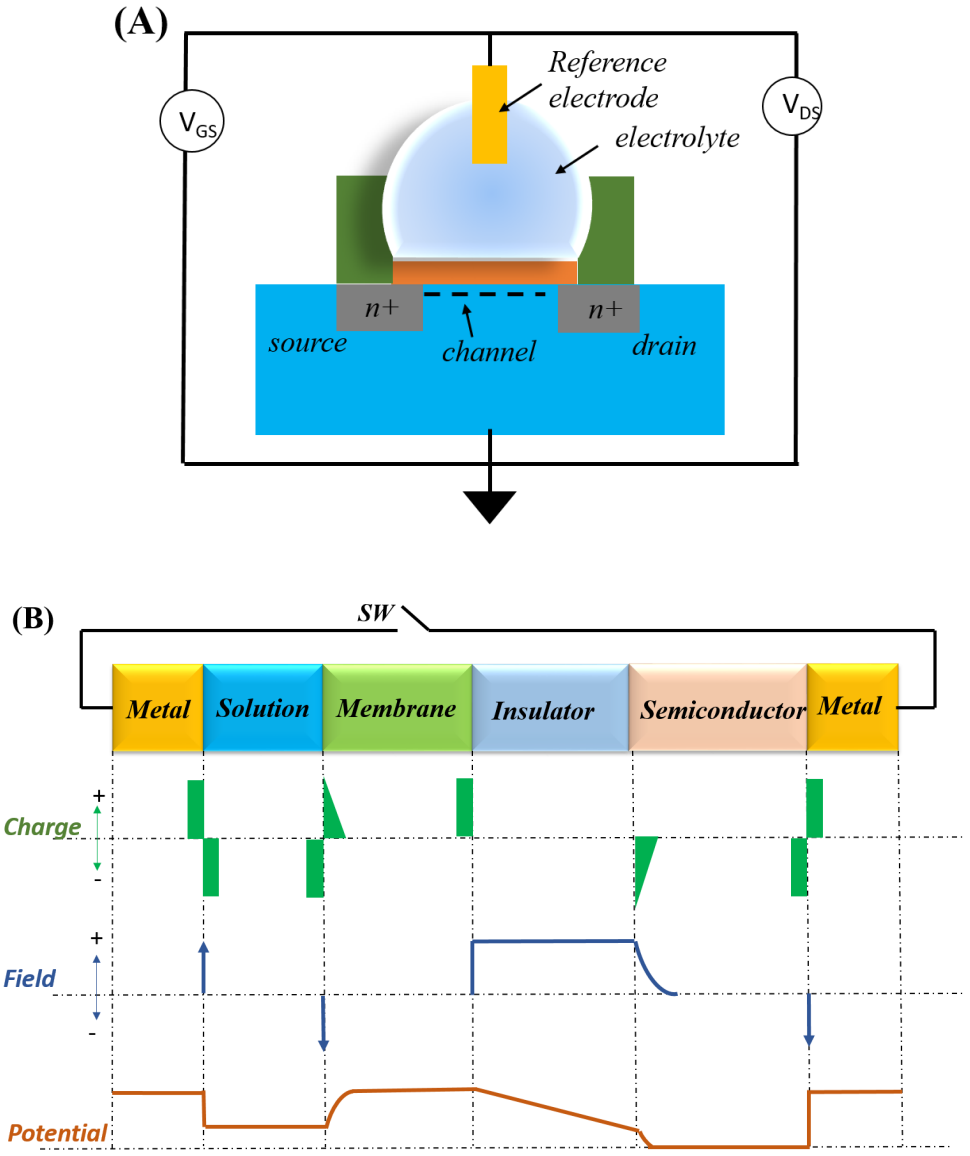

FIGURE 2.4: (A) Schematic of an ion selective field-effect transistor (ISFET). (B) Profiles of charge, electric field, and potential distribution through the gate of an ISFET [3]

$$C = \frac{Q}{nFV_{cell}} \tag{2.2}$$

The equation that describes the current density j as a function of applied voltage E is given in equation 2.3 [3]

$$j = nFk_0\{C_0(0,t)e^{-\alpha f(E-E_0)} - C_R(0,t)e^{(1-\alpha)f(E-E_0)}\} \tag{2.3}$$

where $C_0(0,t)$ and $C_R(0,t)$ are the concentrations of the oxidized and of the reduced

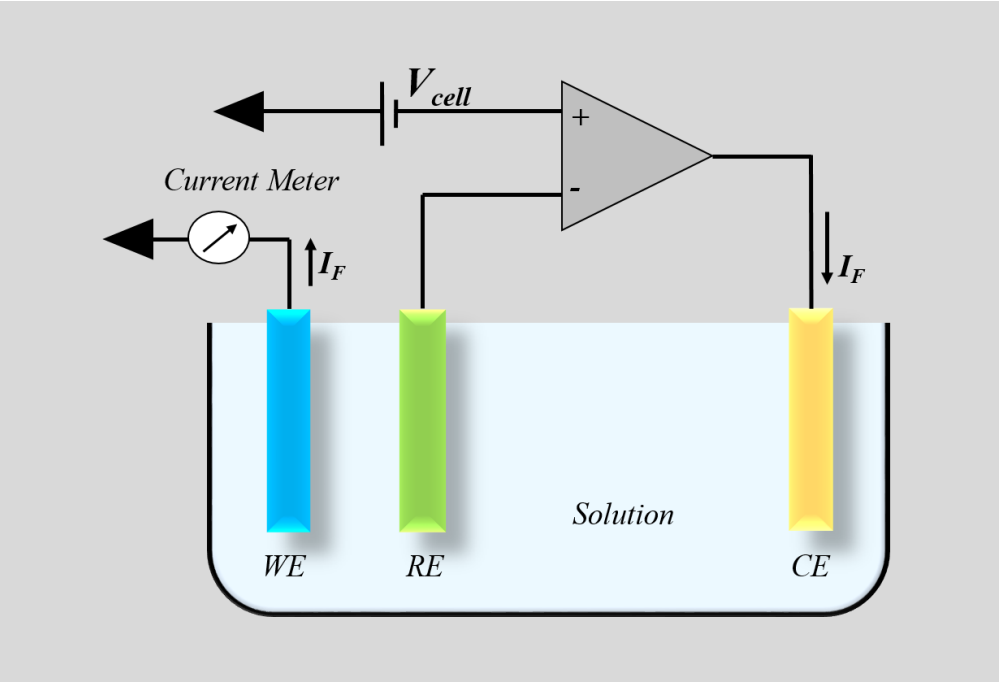

FIGURE 2.5: Schematic of a three-electrode amperometric electrochemical sensor and a potentiostat [4]. WE, RE and CE are indicative of working, reference and counter electrodes.

forms of the redox couple at the surface and at time t, k_0 is the heterogeneous rate constant and E_0 is the standard potential. f represents the multiplier given as equation 2.4 where n is the number of electrons, R is the gas constant, T is the absolute temperature and F is the Faraday constant.

$$f = \frac{nF}{RT} \tag{2.4}$$

From equation 2.3, one can see that as the difference between the standard and the applied potential is increased, it is possible to speed up a slow electrochemical reaction and hence the charge-transfer resistance is small compared to the mass transport resistance. A pictorial representation of these two regions is shown in Figure 2.6.

2.2.3 Optical Sensors

Although the work done in this thesis is based on electrochemical sensors but for sake of completion a brief summary on optical biosensors is presented.

In case of optical detection, sensing is based on the interaction of biorecognition element with the optical field. An optical biosensor contains a biorecognition sensing element integrated with an optical transducer system. A general layout is shown in Figure 2.7 [6]. The primary task of an optical biosensor is to generate an optical signal proportional

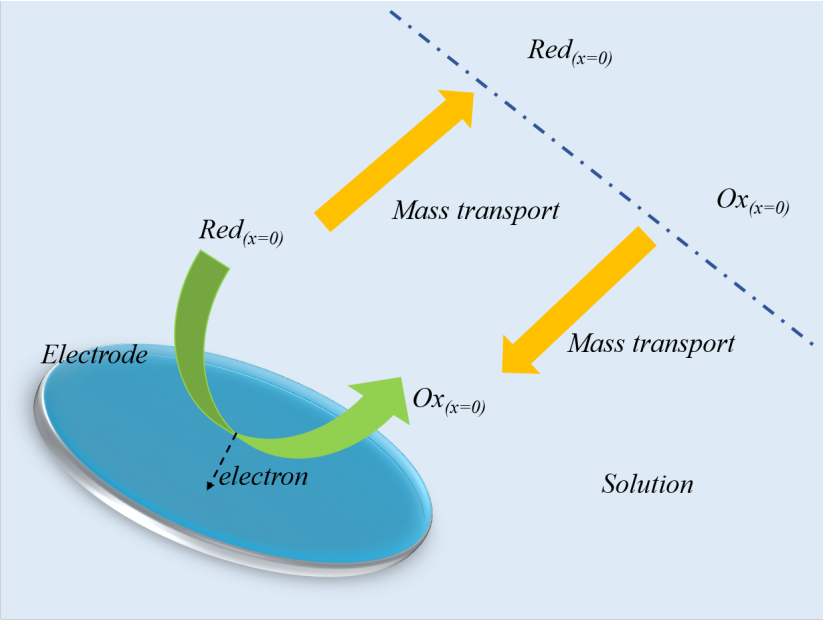

FIGURE 2.6: Schematic of charge transfer and mass transport at the electrode/solution interface [5]. Red and Ox are representative of reduction and oxidation species respectively.

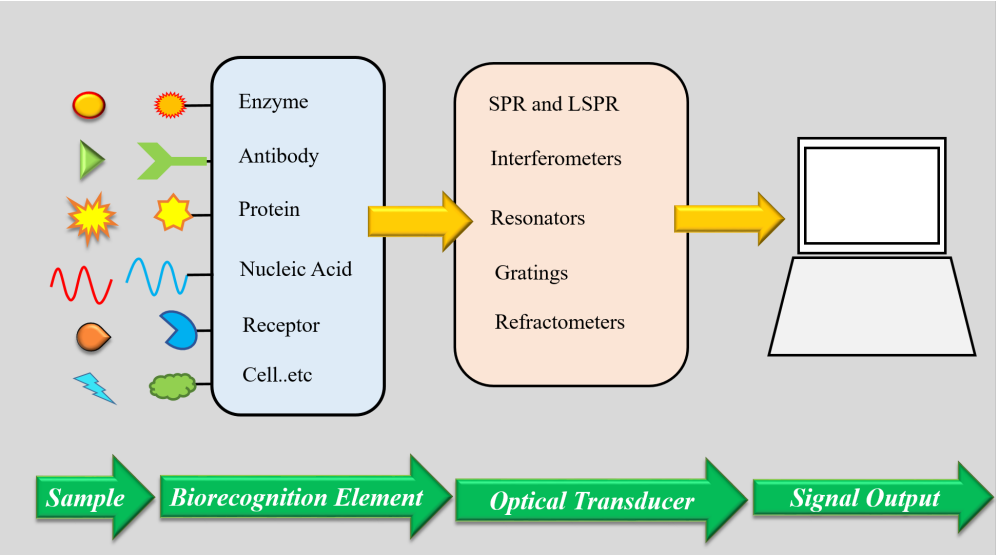

FIGURE 2.7: Principle for Optical Sensors [6].

to the concentration of a measured substance (analyte). The biorecognition element in optical biosensor may include enzymes, antibodies, antigens, receptors, nucleic acids, whole cells and tissues.

Surface plasmon resonance (SPR) is a resonant oscillation of charge-density which exists at the interface of two media with dielectric constants of opposite signs for instance, a metal and a dielectric. This oscillation of charge-density can be associated with an

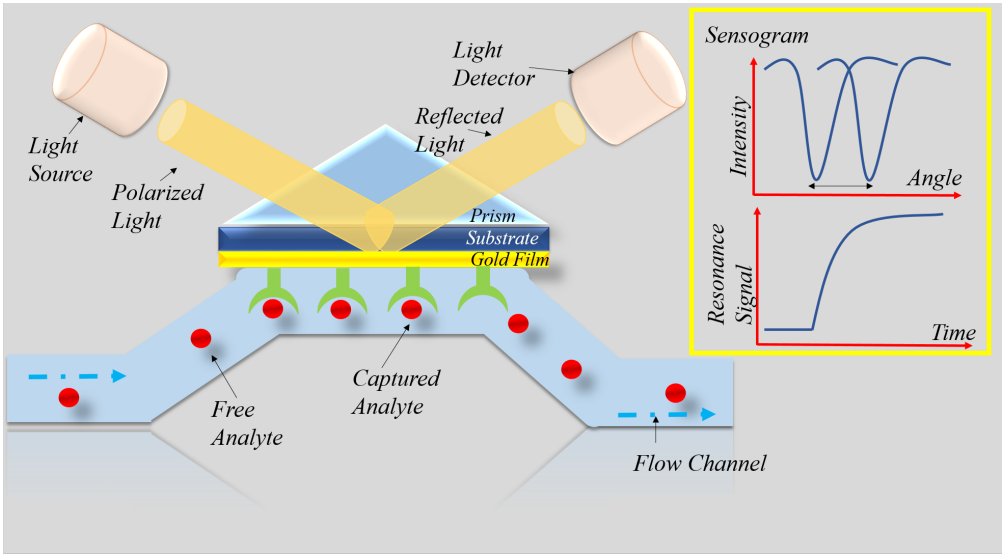

FIGURE 2.8: Typical set-up for an SPR biosensor [7].

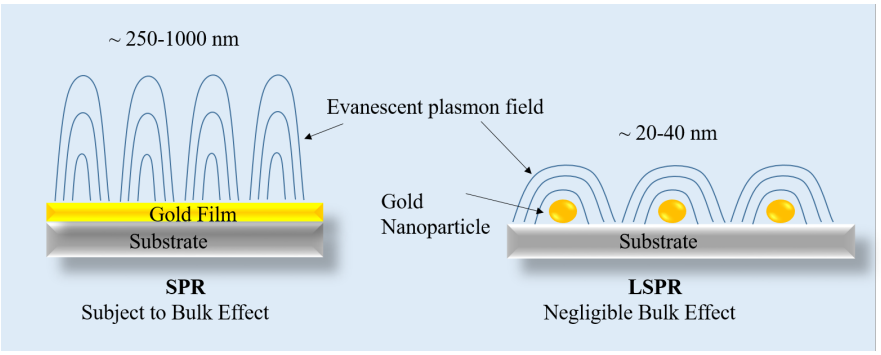

FIGURE 2.9: Schematic comparison of field lines for SPR and LSPR [7].

electromagnetic wave where field vectors reach their maxima at the interface and decay evanescently into both media [34]. If this wave of charge density oscillations is at the boundary of the conductor and the external medium (air, water or vacuum for example), they are extremely sensitive to any change at this boundary, such as the adsorption of molecules to the conducting surface [35] and hence can be used for sensing variations in the surface. Figure 2.8 shows the sensing principle for SPR sensors.

LSPRs or the localized SPR are electron charge oscillations that occur in metallic nanoparticles when light with wavelength larger than these nanoparticles is incident on them. The resonant frequency of these oscillations strongly depends on the composition, size, geometry, dielectric environment and separation distance of nanoparticles. They exhibit enhanced near-field amplitude at the resonance wavelength which is highly localized at the nanoparticle surface and rapidly decays away. The enhancement of the light intensity is one of the most important aspect of LSPRs and localization means the LSPR has very high spatial resolution which is limited only by the size of nanoparticles [36]. Figure 2.9 shows the comparison of the field intensity in SPR and LSPR.

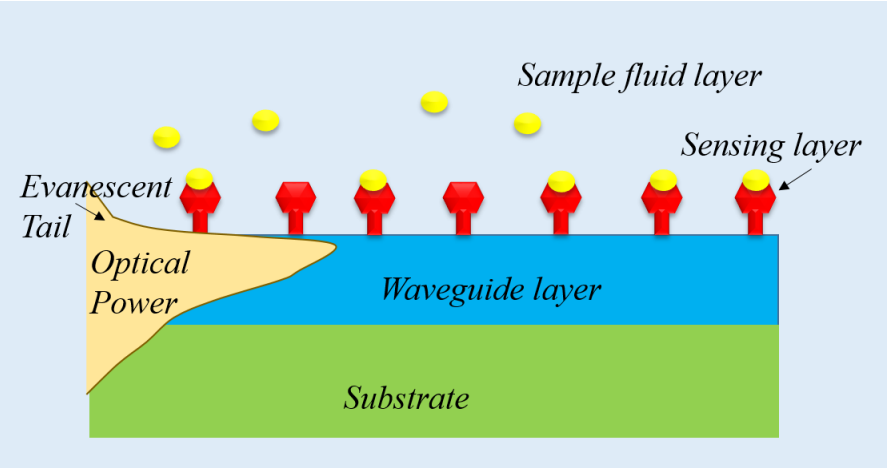

FIGURE 2.10: Schematic of Evanescent wave based sensing [8].

Biosensors based on evanescent wave are another type where the biological recognition and the consequent binding event occur within the confines of an evanescent wave. Evanescent wave are generated when light is confined in an optical waveguide or fibers. At the interface of the waveguide/fiber and the surrounding media which has a lower refractive index, total internal reflection takes place and a small component of electromagnetic field called evanescent wave extends out from the interface as shown in Figure 2.10 and decays exponentially with distance from the surface. As evanescent wave are generated on the surface they can be used to generate surface sensitive fluorescence and hence the background signal from the bulk can be minimized [6].

2.3 Electrochemical Concepts

Sensors or chemical sensors can be based on different physical principles or sensing concepts. In this section, some concepts are presented which are the underlying mechanism for the sensors produced during this thesis work.

2.3.1 Nernst Potential

In a chemical or biological membrane separating two solutions with different ionic concentration a potential (or often called as a membrane potential) is generated. But another important pre-requiste is an ion-selective permeable membrane. To understand this better three cases are discussed in the following paragraphs.

In the first case, we consider a situation where the membrane is such that there can be no ion-exchange between the two solutions, for example a lipid bilayer membrane. Because of absence of ion-exchange the membrane potential or the voltage difference between the two solutions is zero and there is complete charge neutrality in each solution. This

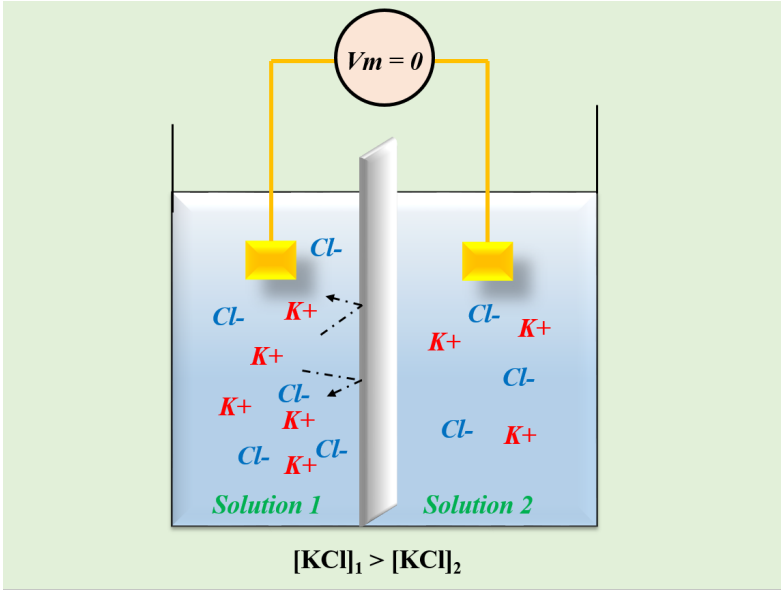

FIGURE 2.11: Two solutions separated by a non permeable membrane [9].

situation is shown in Figure 2.11 where a non-permeable membrane is separating two KCl solutions. Even though there is a difference in KCl concentration of the two solutions, there can be no diffusion of K+ and Cl- ions between them. Hence the membrane potential $V_m = 0$.

In the second case, the non-permeable membrane separating two solutions is replaced by a permeable membrane which is non-selective to a specific ion. This can be visualized as a membrane containing holes large enough to exchange almost all ionic species or solutes present in both solution. Considering again a case where the two solutions on either side of membrane are KCl solutions, both K+ and Cl- ions are allowed to diffuse through the membrane with respect to the concentration gradient of each ion. To maintain electroneutrality same number of the K+ and Cl- ions are diffused from one solution to the other and this diffusion continues until equilibrium is established. At equilibrium condition, the concentration of KCl in both solutions is same and equal to the algebraic average of the initial concentration in both solutions. There is again electroneutrality in both solutions and there is no charge separation across the membrane, hence the membrane potential V_m is zero as no voltage difference exists across the membrane. This case is shown in Figure 2.12.

In the third case, an ion-selective membrane separates the two solutions and is shown in Figure 2.13. Considering the above two cases, if the membrane is selective to K+ ions only and there is a K+ ion concentration gradient between the two solutions, these ions will flow from a higher ion concentration to lower ion concentration. However, in this case chloride ions (Cl-) cannot follow the potassium (K+) ions as the membrane is selective for K+ and hence does not allow Cl- ion-exchange. Hence, there is charge separation across this membrane when K+ ions are exchanged across it. From Figure 2.13 it can be

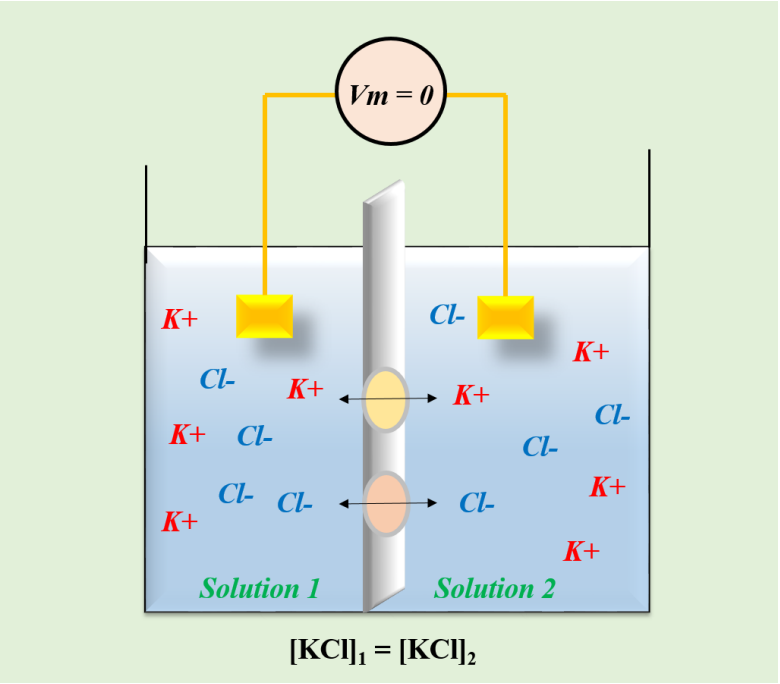

FIGURE 2.12: Two solutions separated by a non-selective membrane [9].

seen that whenever a K+ ion moves from solution 1 to solution 2, it adds a net positive charge to solution 2 and at the same time a net negative charge on solution 1 as it leaves behind a Cl- ion.

This charge separation leads to generation of an electric field and further the membrane potential. The direction of the electrical gradient and chemical gradient is also shown in Figure 2.13. With the continuous K+ ion diffusion, the size of the electrical gradient increases until the concentration gradient from lower to higher concentration balances the electrical gradient in the opposite direction. A point to note is that before any K+ ion-exchange, no potential difference ($V_m = 0\,V$) is developed across the membrane. As soon as the first K+ ion diffuses from solution 1 to solution 2, a small membrane potential is established which increases until the electrical gradient becomes equal to the chemical gradient. At this condition K+ ion is at electrochemical equilibrium and no net ion-exchange takes place. The potential at this electrochemical equilibrium condition is called equilibrium potential or Nernst potential.

Following is a simplified approach to derive equation for Nernst potential [9] using Figure 2.13 [9]. The free energy ($\Delta\,G$) available from the chemical and electrical gradients is given by equations 2.5 and 2.6 :

$$\Delta\,G_{Chemical} = R * T * ln\frac{[K+]_2}{[K+]_1} \tag{2.5}$$

$$\Delta\,G_{Electrical} = z * F * V \tag{2.6}$$

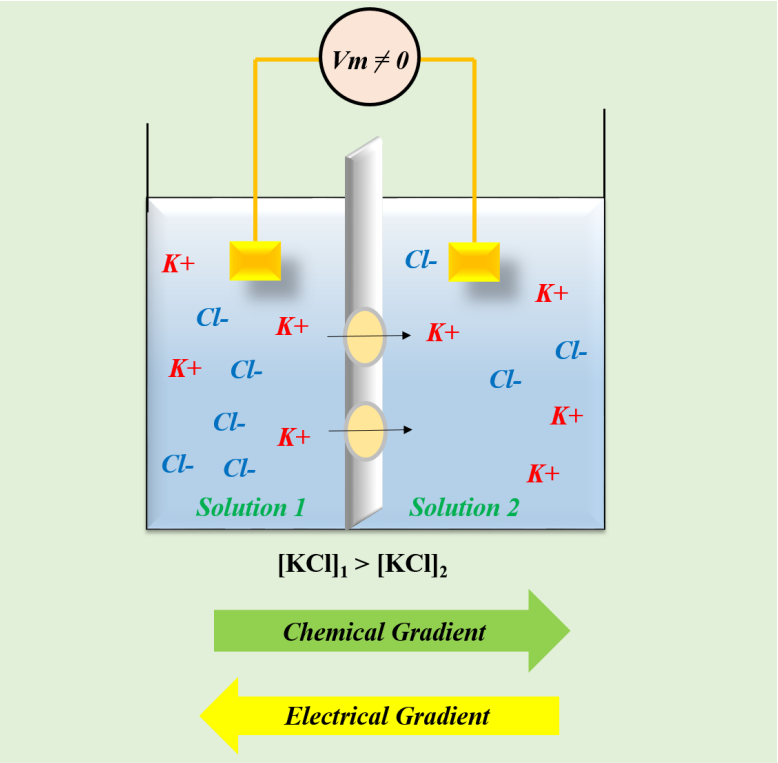

FIGURE 2.13: Two solutions separated by a potassium (K+) selective membrane [9].

where R is the gas constant, T is the absolute temperature, F is the Faraday constant, V is the voltage, and z is the valence of ion. In this case for K+, z = 1. At equilibrium, $\Delta G_{Electrical}$ and $\Delta G_{Chemical}$ are equal and given by equation 2.7 :

$$\Delta G_{Electrical} = \Delta G_{Chemical} \tag{2.7}$$

Equation 2.7 can be written as equation 2.8 :

$$z * F * V = R * T * ln\frac{[K+]_2}{[K+]_1} \tag{2.8}$$

Solving equation 2.8 for voltage V results in equation 2.9 :

$$V = \frac{R * T}{z * F} * ln\frac{[K+]_2}{[K+]_1} \tag{2.9}$$

The above equation is known as the Nernst equation, also introduced in equation 2.1, which gives the potential across the membrane at equilibrium condition.

2.3.2 Debye Length

Electrolytes are ubiquitous in nature and in technology. The properties of concentrated electrolytes are not as well-understood as dilute electrolytes [37]. In case of dilute electrolyte regime Poisson-Boltzmann (mean-field) electrostatics applies and approximations such as in the Debye-Hückel theory are appropriate [38, 39]. Using the classical mean-field theories that explain screening and interactions in dilute electrolytes, the Debye length, λ_D is defined as the scale over which the reach of electrostatic interactions in solution is typically measured. The Debye length can be understood as the distance over which a charge Q is shielded by the ions in a solution [40]. In Figure 2.14, if the charge Q is positive it attracts negatively charged ions in the solution while repelling the positively charged ions. This leads to an excess negative ionic charge around Q. Debye length is the radius of the sphere drawn around Q inside which the excess negative charge is equal to -Q, thus canceling out the field of the primary charge Q at distances further than λ_D.

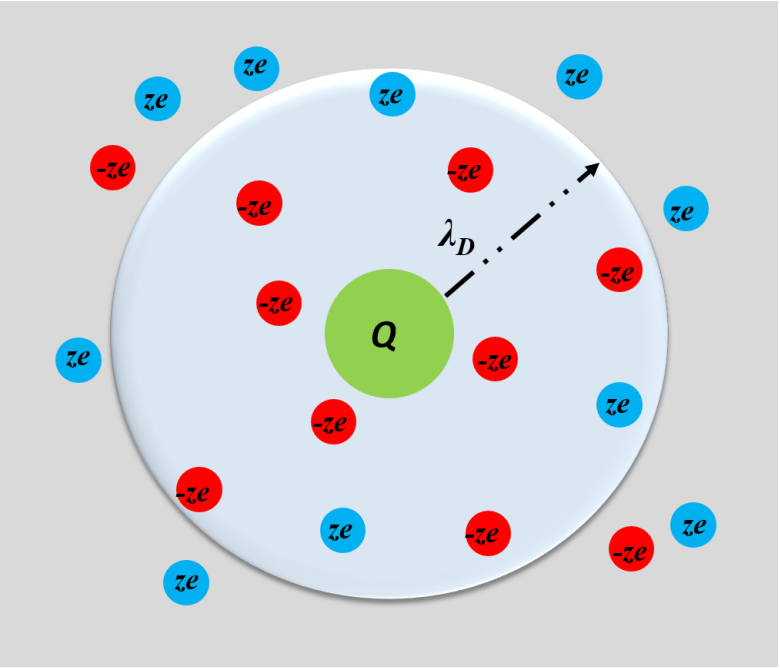

FIGURE 2.14: Debye length for a charge Q in an ionic medium of with positive and negative charge.

The expression of double layer is given as equation 2.10 :

$$\lambda_D = \left(\frac{\kappa * k_B * T}{4 * \pi * Z^2 * e^2 * c_0 * k_c}\right)^{1/2} \tag{2.10}$$

where κ is the relative dielectric constant, k_B is the Boltzmann constant, T is the temperature, Ze is the charge of Q where e is the fundamental charge and Z is an integer

giving the charge state, c_0 is the ambient concentration of ionic charge measured in units of number of ions per cubic meter. Details of the derivation can be found here [40].

2.3.3 Double layer capacitance

When a solid is introduced in an electrolyte, the ionic environment of the electrolyte changes around the solid. In case of electrodes which are under potentiostatic control, there will also be additional influence of the charge held at the electrode [41]. The charge of the electrode must be balanced by a counter charge which occurs in the liquid [42]. This charge is not uniformly distributed throughout the electrolyte but is concentrated near the charged electrode. Thus, there is a small but finite volume of the electrolyte around the charged electrode which is different from the rest of extended electrolyte. This concept is very important in electrochemistry, and reactions within this interfacial boundary that govern external observations of electrochemical reactions. In the following paragraphs three main theoretical explanations for a electrode-electrolyte interface are explained.

Helmholtz Double Layer

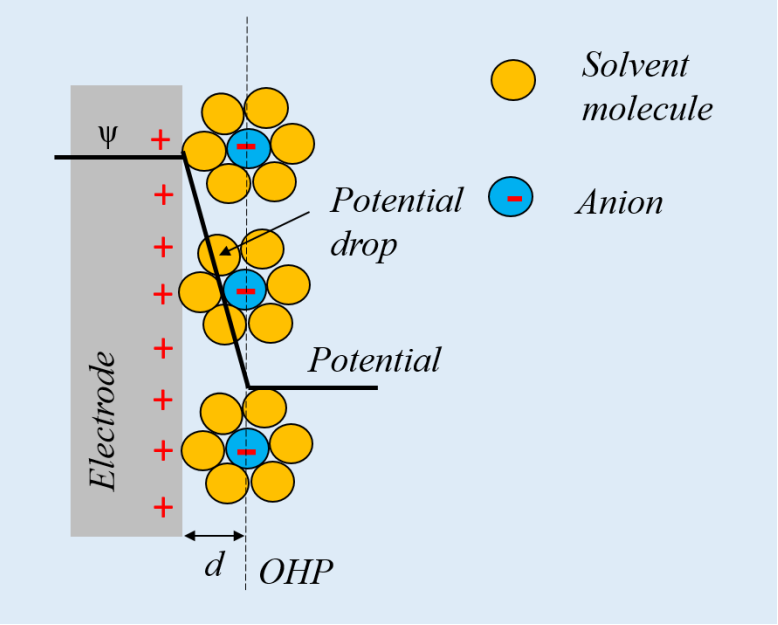

FIGURE 2.15: Schematic representation of electrical double layer structures according to Helmholtz theory.

One of the earliest theories to explain a electrode-electrolyte interface is Helmholtz Double Layer approximation proposed by Helmholtz in 1850's. This theory also introduced the term "electrical double layer". According to this theory, there are no electron transfer reactions occurring at the electrode and the interactions between the ions in the electrolyte and the charged electrode surface are only electrostatic in nature. Hence to achieve charge neutrality there is redistribution of ions in the electrolyte close to the

electrode surface. Figure 2.15 shows the interpretation of electrode-electrolyte interface as per the Helmholtz's theory.

Oppositely charged ions are attracted to the electrode surface and they form a layer balancing the charge of the electrode. The distance of the balancing layer is assumed to be limited by the radius of the ion present in the electrolyte and a single sphere of solvation around each ion. This results in two layers of charge (the double layer) and a potential drop which is confined to only this region (termed the outer Helmholtz Plane, OHP) in solution. This theory resembles an electrical capacitor with two charge plates separated by some distance 'd' with the potential drop occurring in a linear manner between the two plates. However, this simplistic Helmholtz theory cannot adequately explain all the features as it is based on rigid layers of opposite charges which does not occur in nature.

Gouy-Chapman Double Layer

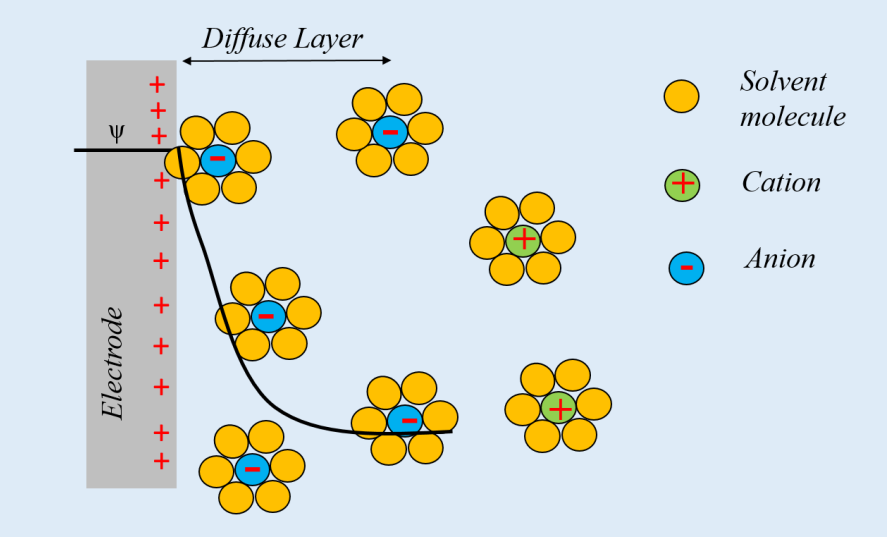

FIGURE 2.16: Schematic representation of diffused double layer according to Gouy-Chapman theory.

To provide a more realistic theory Gouy suggested that the interfacial potential at the charged electrode surface is attributed to the number of ions of a given sign attached to the electrode surface and to equal number of oppositely charged ions in the solution. These counter ions are loosely held and diffuse in the electrolyte solution until the counter potential set up by their diffusion restricts this movement. The thickness of this diffused double layer is decided by the kinetic energy of the counter ions. Gouy and Chapman independently developed this theory about diffused double layer where concentration of counter ions follows the Boltzmann distribution given by equation 2.11 where n_0 is the bulk concentration, z is the charge on the ion, e is the absolute value of the electronic charge, ϕ is the electric potential and k is the Boltzmann constant [43].

$$n = n_0 * exp(-z * e * \phi / k * T) \tag{2.11}$$

The charge density that is charge per unit volume ρ(x) is given by equation 2.12 :

$$\rho(x) = \sum_i n_i * z_i * e \tag{2.12}$$

Rewriting equation 2.12 using equation 2.11 can lead to equation 2.13 :

$$\rho(x) = \sum_i n_i^0 * z_i * e * exp(-z_i * e * \phi / k * T) \tag{2.13}$$

Poisson equation is given as equation 2.14 :

$$\rho(x) = -\epsilon\epsilon_0 \frac{\partial^2 \phi}{\partial x^2} \tag{2.14}$$

Using equations 2.13 and 2.14 leads to 2.15 that is the Poisson-Boltzmann equation :

$$\frac{\partial^2 \phi}{\partial x^2} = -\frac{e}{\epsilon\epsilon_0} \sum_i n_i^0 * z_i * exp(-z_i e\phi / kT) \tag{2.15}$$

When this equation is applied to an electrolyte solution, we obtain equation 2.16 :

$$\frac{\partial \phi}{\partial x} = -(\frac{8kTn_0}{\epsilon\epsilon_0})^{1/2} * sinh(\frac{ze\phi}{2kT}) \tag{2.16}$$

Assuming that ϕ_0 is small, ϕ can be written as equation 2.17 :

$$\phi = \phi_0 * exp(-\kappa x) \tag{2.17}$$

where κ is given as equation 2.18 and has units of 1/distance. κ^{-1} is commonly referred as λ_D, the debye length, given by equation 2.10.

$$\kappa = (\frac{2n^0 z^2 e^2}{\epsilon\epsilon_0 kT})^{1/2} \tag{2.18}$$

This diffused double layer is schematically shown in Figure 2.16.

Stern Modification of the Diffuse double Layer

Although the Gouy-Chapman is a significant improvement in the explanation of the electrical double layer over the Helmholtz theory, it is still limited in terms of quantitative

application. There are certain assumptions made by the Gouy-Chapman theory which might not hold true in real systems. For example, assumptions like behavior of ions as point charges and assuming there is no physical limit for the ions in their approach to the electrode surface are not true [42].

In an attempt to provide a more realistic theory, a modification of the Gouy-Chapman diffuse double layer theory was presented by Stern and he assumed that ions still have a finite size hence they cannot approach the electrode closer than a few nanometers i.e. the radius of ions. Hence in the Stern model the first layer of ions closest to the electrode surface are not exactly on the electrode surface in opposition to the Gouy-Chapman theory but at some distance 'd' away from the surface. This distance 'd' is usually the radius of the ion. Another assumption made by Stern is that some of the ions from the solution will get adsorbed on the surface of the electrode in plane 'd'. This condensed layer is known as 'Stern' layer. The potential drop in this case is first over the condensed molecular layer and then over the diffuse layer. Figure 2.17 shows the diagram for the Stern modified diffused double layer [42].

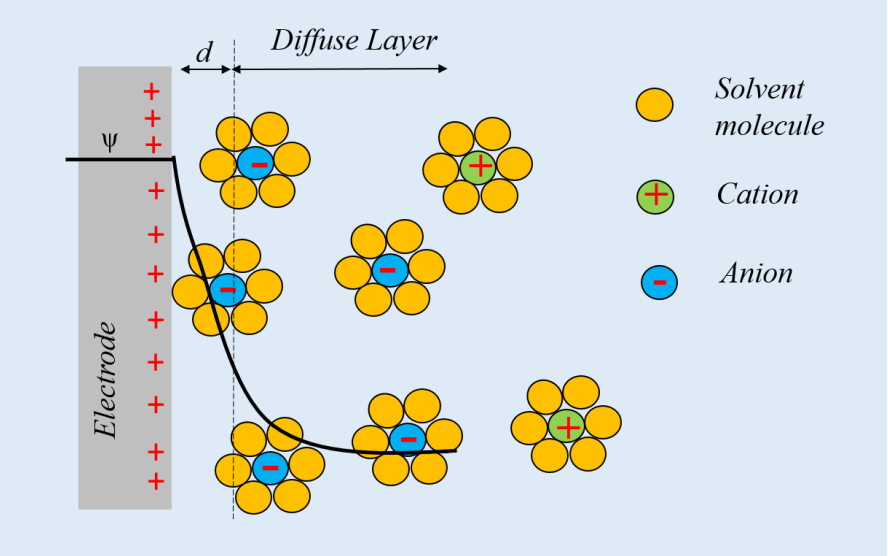

FIGURE 2.17: Schematic representation of Stern modified diffused double layer.

The double layer formed to balance the charge on the electrode creates an electrokinetic potential between the electrode and any point in the electrolyte solution, known as the "surface potential" and is normally in millivolts (mV) range. The strength or magnitude of the surface potential depends on the surface charge and thickness of the double layer. Away from the electrode, surface potential drops almost linearly with distance in the Stern layer and exponentially through the diffuse layer almost approaching zero at the imaginary boundary of the double layer.

2.4 Sensing Parameters

2.4.1 Sensitivity, Dynamic Range and Detection Limit

Sensor response is the measurement of the change in a parameter of the sensor after some chemical stimulation. Although this sensor response is specific to every sensor, a general sensor response containing major features is shown in Figure 2.18 when there is change in concentration of the primary analyte of interest X [3].

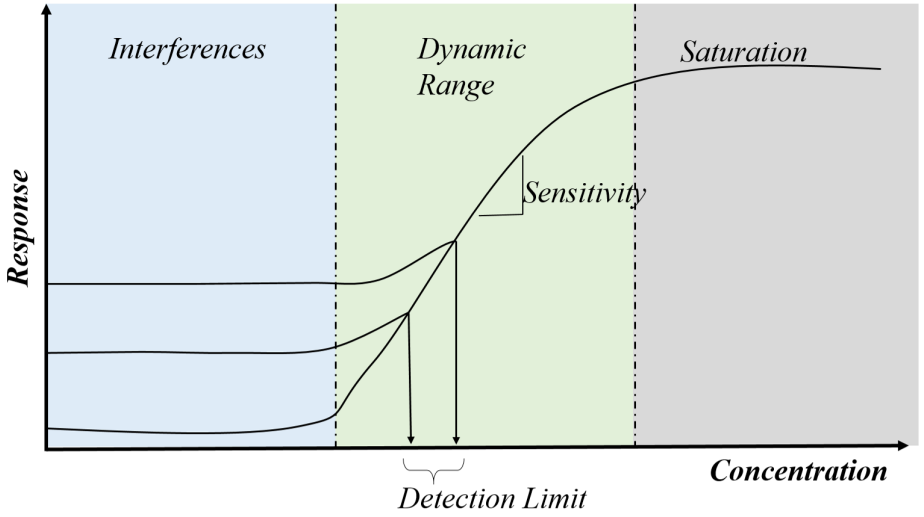

FIGURE 2.18: General response of a sensor indicating dynamic range, sensitivity and detection limit.

In the electrolyte solution, there are several interfering analytes 'i' along with 'X' that compete to bind to the selective bio-recognition element. Assume that sites occupied by interfering analytes are Σa_{Si} and the number of unoccupied sites is a_S and the a_{SX} is the number of sites occupied by X that can result in an output signal. In this case, the total activity of binding sites (a_{ST}) is given as equation 2.19 :

$$a_{ST} = a_{Si} + a_{SX} + a_S \tag{2.19}$$

The activity of total occupied sites (a_0) can be written as equation 2.20 [3] :

$$a_0 = \Sigma a_{Si} + a_{SX} \tag{2.20}$$

The sensor chemical equation can be written as equation 2.21 and the equilibrium constant for this equation is given by equation 2.22 where k_f and k_r are the rate constants for forward and backward reaction respectively [3].

$$X + S \Longleftrightarrow SX \tag{2.21}$$

$$K_X = \frac{a_{SX}}{a_X a_S} = \frac{k_f}{k_r} \tag{2.22}$$

The equilibrium constant for a single interferant (i) can be written as equation 2.23 [3] :

$$K_i = \frac{a_{Si}}{a_i a_S} \tag{2.23}$$

Using the above equations, a_0 can be simplified to equation 2.24 [3] :

$$a_0 = a_{ST} \frac{K_X a_X + \Sigma K_i a_i}{K_X a_X + \Sigma K_i a_i + 1} \tag{2.24}$$

This can be re-written as equation 2.25 where $K_i^{'}$ is the selectivity coefficient for an interfering analyte i :

$$a_0 = a_{ST} \frac{a_X + \Sigma K_i^{'} a_i}{a_X + \Sigma K_i^{'} a_i + 1/K_X} \tag{2.25}$$

There are some conclusions that can be drawn from the above reaction. First, when activity of X is higher i.e. $a_X >> \Sigma K_i^{'} a_i + 1/K_X$ or when there is high number of interfering analyte i.e. $\Sigma K_i^{'} >> a_i a_X + 1/K_X$, there is no unoccupied site. In this condition of saturation limit, the sensor does not respond to change in primary analyte X. Another extreme is when the activity of X or its binding constant K_X is low, in this case most binding sites are occupied by the interfering analyte. In this condition of interference region, also the sensor does not respond to change in primary analyte X. In between the regions of interference region and saturation limit there lies the region of dynamic range. In this region there is linear dependence on the number of occupied sites and the activity of X, i.e. $a_0 = a_{ST} K_X a_X$ [3].

The intercept of this dynamic range and of the interference region defines the **detection limit** [3]. The activity of the primary analyte at the detection limit is given by equation 2.26 :

$$(a_X)_{d.l.} = \frac{\Sigma K_i^{'} a_i}{\Sigma K_i^{'} a_i + 1} \tag{2.26}$$

Similar to the detection limit another important quantity of interest is the **dynamic range**, which is the difference between the analyte activities at the saturation limit and at the detection limit. Expression for dynamic range is given in equation 2.27 :

$$DynamicRange = \frac{1}{K_X} - K_i^{'} a_i \tag{2.27}$$

Close inspection of equation 2.27 reveals that as $K_i^{'} a_i$ term increases dynamic range becomes narrower until eventually it is not present and there is no impact of X on the sensor [3].

Sensitivity is the slope of the sensor response in the dynamic range. Detection limit on the other hand is the minimum detectable response, usually above three times the standard deviation [3].

2.4.2 Selectivity

Selectivity is another very important aspect in chemical sensing. Selectivity refers to the ability of the sensor to selectively show response to only the primary analyte and not to other interfering analytes present in the electrolyte solution. The curve of Figure 2.18 shows the sensor response for two different interfering analytes concentration. When the concentration of the interfering analytes, detection limit for primary analyte increases but the dynamic range becomes narrower. However, in a good sensor wide dynamic range and lower limit of detection are the desired characteristics, which means the construction of the selective layer should be such that it has no affinity for interfering analytes at all. But in real world problems this simple requirement is not straightforward because in most sensing problems the interfering analytes are not known beforehand. Nevertheless attempts are made to achieve a highly selective bio-recognition layer, which can either be homogeneous or containing specific binding sites that are embedded in a matrix.

It is also important to note that the final system configuration is driven by the free energy considerations. It means that the final system must have lower free energy change (ΔG) given by equation 2.28. Hence, one can imagine that if the entropy change is higher, the free energy change is more negative, hence the system is more stable.

$$\Delta G = \Delta H - T * \Delta S \tag{2.28}$$

In living organisms the best selectivity is achieved by shape recognition or stereospecificity. However, in this case if the binding leads to a decrease in the randomness and hence a higher entropy change, this binding will occur only if this increased entropy is compensated by a decrease in the enthalphy. There are several approaches to impart selectivity by stereo specificity and few are explained in the following paragraphs.

Antibodies are one of the best biomolecules that have stereo specificity for antigens, haptens and epitopes. In addition, antibodies can be produced cost effectively for antigens, regardless of their shape or chemical nature. Antibodies belong to the group of

serum proteins called immunoglobulins [44]. The valency of a antibody is determined by the number of antigens that can be bound to it. Usually this valency is two but can be as high as ten. They mainly work against foreign immunogens like proteins, nucleic acids, viruses that might be harmful for the organism. A common two valency antibody is shown in Figure 2.19. The most common bonds in the antibody-antigen binding are Coulombic and van der Waals interactions [3].

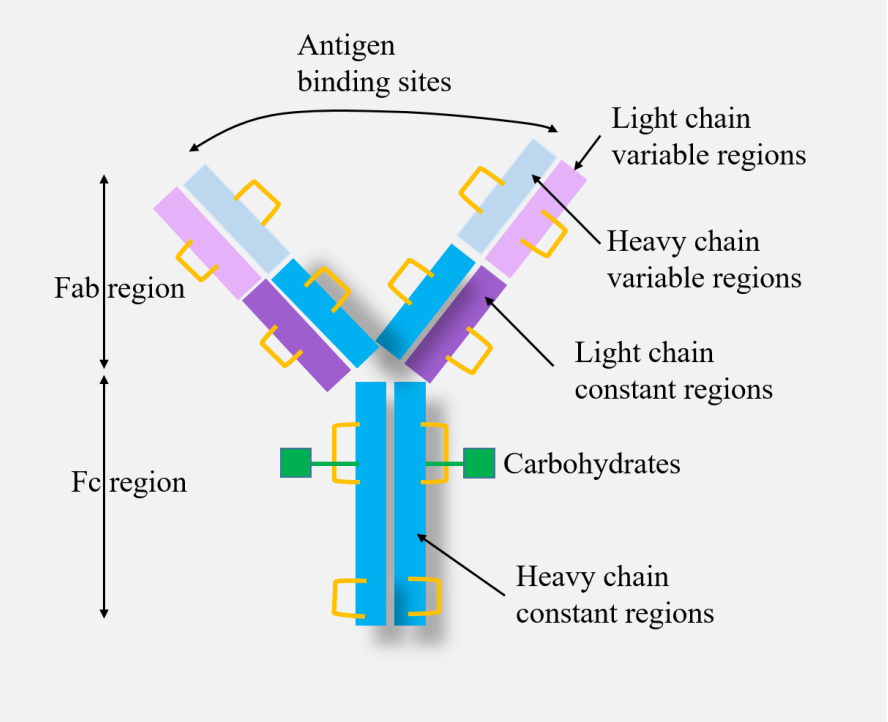

FIGURE 2.19: Schematic of two valency antibody.

Nucleotides including DNA (deoxyribonucleic acid) and RNA (ribonucleic acid) have very high selectivity, and it relies mainly on the high stereo specific hydrogen bonding between base pairs adenine–thymine and cytosine–guanine. This interaction is driven by the increase in enthalphic reasons as ΔH for adenine–thymine binding is almost 20.1 kJ/mol and for cytosine–guanine is 57.5 kJ/mol. As the interaction enthalpies are additive, the overall DNA fragment increases with the number of base pairs, reaching the "reversible" threshold even for a dimer. Figure 2.20 shows the hydrogen bonds in DNA base-pairs.

Aptamers are oligonucleotides that is DNA or RNA molecules either artificial or natural such that they have the biological "lock-and-key" recognition preserved. Aptamers find use mostly in binding small molecules like drugs, small proteins [45]. Aptamers have higher affinity than antibodies due to the the unique folding ability of RNA molecules. Tuerk and Gold in 1990 developed a process called SELEX (Systematic Evolution of Ligands by Exponential Enrichment) for their preparation in vitro [46].

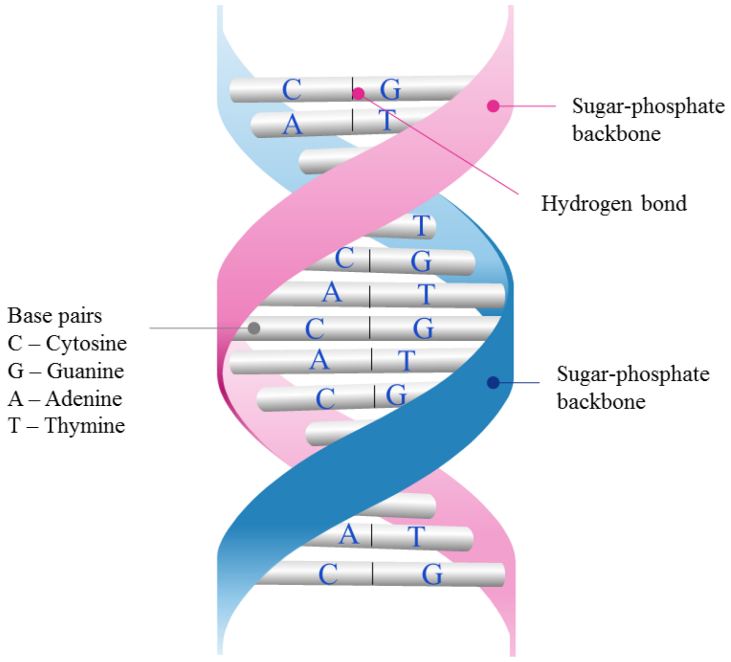

FIGURE 2.20: Schematic of a DNA structure with base pairs, hydrogen bonds and sugar-phosphate backbone.

"Molecular imprinting" is another way to utilize the shape-recognition ability [47, 48]. This process uses a template molecule to create a "footprint" in the polymerizing matrix and when this molecule is removed from the polymerized material this footprint acts as a shape-recognizing binding site for the same template molecule [3]. An example of this process using protein as a template is shown Figure 2.21.

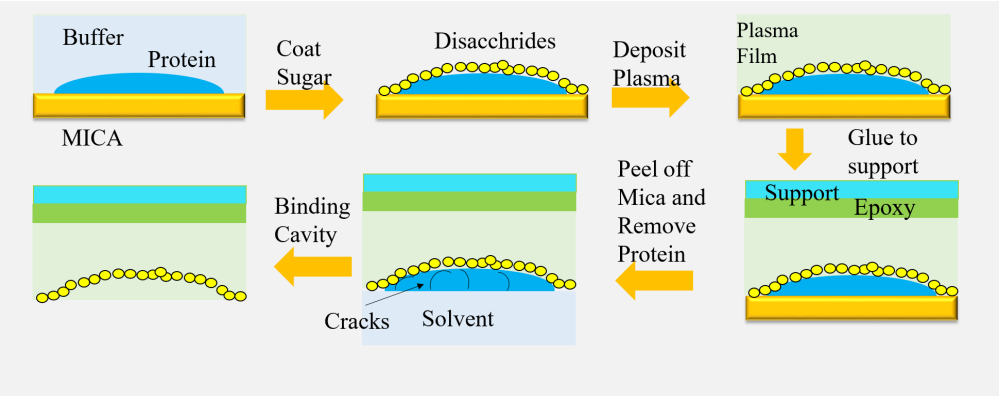

FIGURE 2.21: Schematic of molecular imprinting process.

The selectivity examples given above are for equilibrium-based selectivity but selectivity can also be kinetic which applies mostly to sensors operating in the steady-state regime like amperometric sensors. One of the most widely studied kinetic process is enzymatic. Enzymatic biosensors are the largest group of biosensors where the chemical reaction is catalyzed by proteins called enzymes. Enzymes are interesting due to two remarkable properties, one is that they are highly selective and second that they can highly increase

the speed of a catalytic reaction. A general chemical reaction where conversion of substrate S to product P is catalyzed by an enzyme E, with the formation of an intermediate complex ES is given in equation 2.29 :

$$S + E \underset{\mathrm{k}_{-}1}{\overset{\mathrm{k}_1}{\rightleftarrows}} ES \xrightarrow{k_2} P \tag{2.29}$$

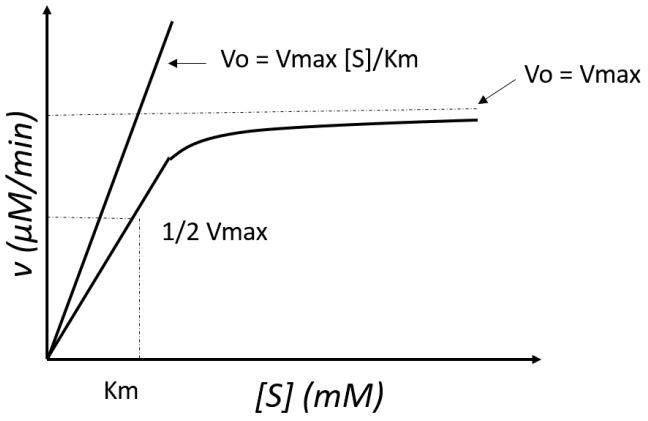

FIGURE 2.22: Michaelis–Menten saturation curve for an enzyme reaction.

The above equation can be described by the Michaelis–Menten mechanism and the reaction velocity for the above equation can be written as the rate of increase of the product concentration, given by equation 2.30 :

$$v = \frac{\partial C_p}{\partial t} = k_2 \, C_{ES} \tag{2.30}$$

When the concentration of substrate is high, reaction velocity saturates at a maximum (v_max). Under these conditions, all the available enzyme E_T is bound in the complex with the substrate and v_max is proportional to total enzyme concentration C_{ET} :

$$v_{max} = k_2 \, C_{ET} \tag{2.31}$$

In steady state condition :

$$\frac{\partial C_{ES}}{\partial t} = k_1 \, C_S \, C_E - (k_{-1} + k_2) \, C_{ES} = 0 \tag{2.32}$$

The Michaelis–Menten constant (K_m) is defined as equation 2.33 :

$$K_m = \frac{k_{-1} + k_2}{k_1} = \frac{C_S\, C_E}{C_{ES}} \tag{2.33}$$

Further simplifications, lead to the final Michaelis–Menten equation :

$$v = \frac{v_{max}\, C_S}{C_S + K_m} \tag{2.34}$$

Michaelis–Menten constant is an important figure of merit for the enzyme activity. Smaller the K_m is, the more strongly the substrate binds to the enzyme. Figure 2.22 shows the michaelis–menten curve.

2.4.3 Labeled and Label-free biosensing

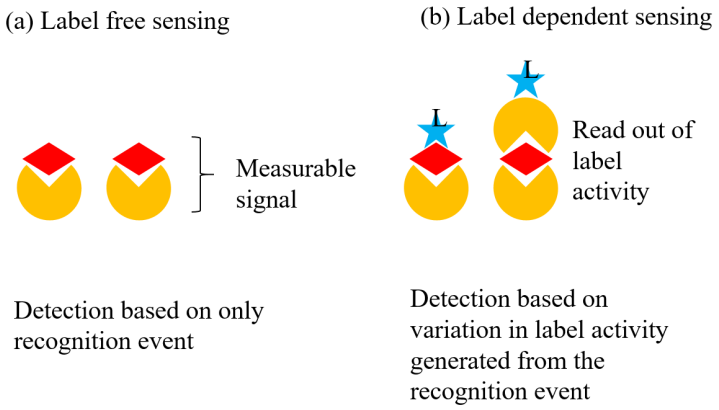

FIGURE 2.23: Schematic Representation of label-free and label dependent sensing.

Label is a foreign molecule chemically or temporarily attached to the analyte for detecting its presence or activity [49]. Labeled detection is widely used in many fields by using labels of various nature like radioactive [50], fluorescent [51], nanoparticle [52] or enzyme based. Sensing is performed by measurement of the activity of the label or the variation in transducer property. To ensure high sensitivity and selectivity, it is important that the the label has easy conjugation and convenient detection. Using a label for sensors, requires an additional immobilization step which is usually low yield, expensive and time consuming. Non-specific adsorptions are also possible, along with the lack of affinity between the labeled receptor and the target analyte. These factors can lead to reduction in the reproducibility, sensitivity or selectivity of the biosensor [53, 54].

In the label-free sensing techniques, one can avoid the laborious labeling steps and the challenging reaction and operation of label. This will lead to cost reduction and time efficient analysis. In such label-free sensing, the bio-recognition element is immobilized

on the transducer surface and the sample solution is placed directly on the functionalized transducer. Analysis is based on the change in electrical or physical properties of the transducer surface which in turn is dependent on the analyte and biorecognition element interaction. Using label-free techniques causes the retention of the high affinity and decreases non-specific adsorptions [55]. Figure 2.23 shows the principal differences between labeled and label-free biosensors.

Chapter 3

Carbon Nanotube : An Electronic material

3.1 Brief History of Carbon nanotubes

Over the years most of the research articles relevant to carbon nanotubes start with an opening statement as "the discovery of carbon nanotubes by Iijima in 1991...". This is because in 1991 Sumio Iijima of NEC Corporation, Japan, published a ground-breaking paper in Nature reporting the discovery of multi-walled carbon nanotubes (MWCNTs) [56]. At the time of writing this thesis, there have been over 45,000 citations of this paper. Undoubtedly, the discovery of Iijima has gathered tremendous attention of researchers which led to CNT becoming one of the most popular material of the current generation science. However, one must also look and not neglect the contributions of various other scientists who worked prior to this citation in the understanding of carbon nanomaterials.

In 1993 two papers where submitted independently in Nature, one by Iijima and Ichihashi [57] in the month of April, and the other by Bethune [58] in the month of May, discussing the formation of single walled carbon nanotubes (SWCNTs). If one wants to be chronologically precise then the claim of formation of SWNCTs go to Ijima and Ichihashi, but one can always argue on the real time taken to conduct research. More important is to realize that the discovery made by both the groups was accidental [59].

Careful and meticulous investigation of the past works lead us to two centuries back, when in 1889 a patent [60] was filed for the use of carbon filaments formed by thermal decomposition of hydrocarbon in gaseous form, in the light bulbs which were recently presented at that time by Edison. Due to lack of sophisticated microscopy techniques such carbon filaments could not be imaged until 1952 when tubular carbon filaments were captured by TEM and published in Journal of Physical Chemistry of Russia [61].

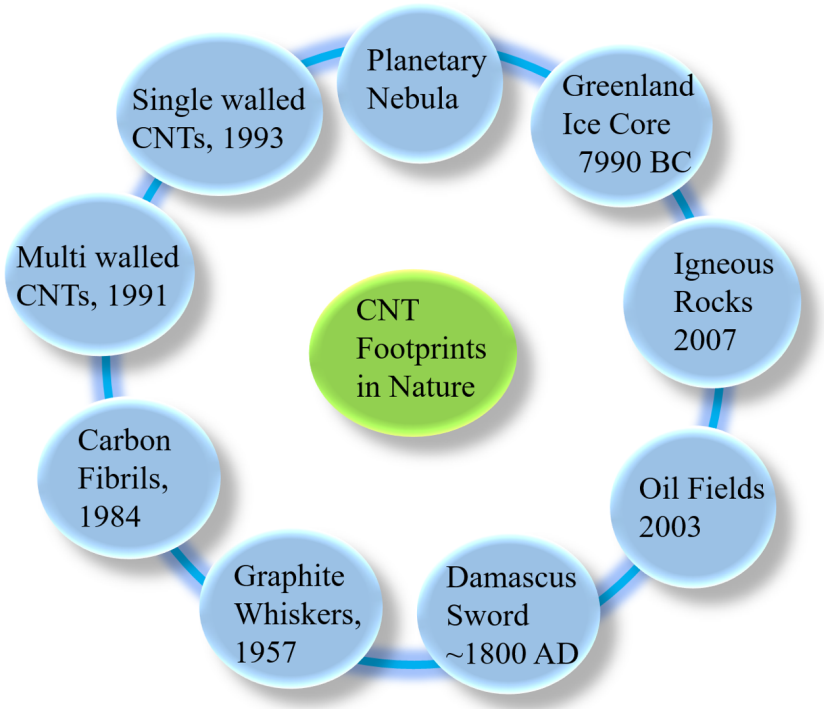

FIGURE 3.1: CNT footprints in nature and their respective year of discovery [10].

This leads to an intriguing question : "why did the scientific community grew interested in CNTs after 1991 when they were around for more than forty years before?" One of the major reasons for this is that major research on carbon filaments and tubes was done by material scientists who wanted to understand the growth of such tubes/filaments in coal and steel processing industry or in the coolant channels of nuclear reactors. Such research and application was not so exciting for the fundamental physicist given the maturity of experimental science during that period. On the other hand, the paper of Iijima in 1991 came at the right time, when the field of nanotechnology was in rising, and thus led to the investigation of applications and properties of CNTs in great detail.

3.2 Growth of Carbon Nanotubes

Before we delve deeper into the properties of carbon nanotubes, we must understand how carbon nanotubes are grown. There are three major methods for the growth of CNTs, namely arc discharge, laser ablation and chemical vapor deposition (CVD). The main principle behind these methods is to provide energy to a carbon source for the generation of CNTs. The energy source used in this process is current in an arc discharge, high-intensity light from a laser in the laser ablation & heat from a furnace in CVD.

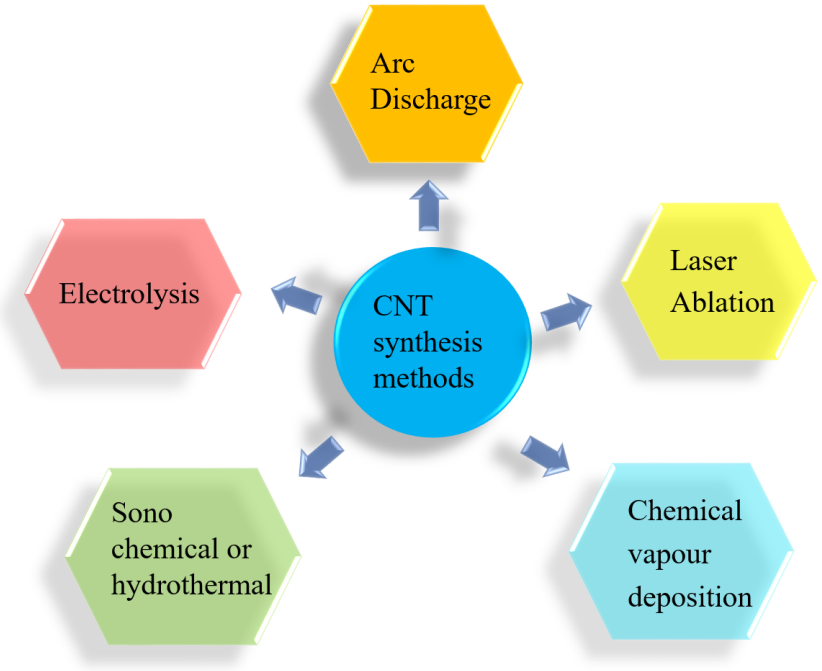

FIGURE 3.2: Most commonly used methods for CNT synthesis.

3.2.1 Arc Discharge

The earliest recognized CNTs were prepared by arc-discharge method. This method uses higher temperatures (above 1700°C) for CNT synthesis and usually results in growth of CNTs with fewer structural defects in comparison with other techniques [62]. It was initially used for the preparation of C_{60} fullerene molecules.

The arc discharge setup consists of a furnace, a stainless steel vacuum chamber, graphite electrodes, a water cooled trap and high voltage power supply. Arc-vaporization of the two carbon rods placed end to end at a separation of approximately 1 mm leads to creation of CNTs. The high temperature arc discharge between the two electrodes is created by a direct current of 50 to 100 A, driven by a potential difference of approximately 20 V [63]. The arc provides high temperature which is needed to vaporize carbon atoms into a plasma (>3000°C). This process is performed in an enclosure that is usually filled with an inert gas at sub-atmospheric pressure (Figure 3.3). The inert gas is mostly helium but some other works in hydrogen or methane atmosphere have been also reported. The final morphology of CNTs is influenced by the atmosphere inside the chamber. The purity and yield of the nanotubes also has direct dependence on the gas pressure in the reaction chamber [64].

The arc discharge deposition of CNTs when done in absence of catalysts leads to production of MWCNTs. On the other hand, the SWNTs are produced when a composition of transition metal catalyst is used in the anode. The commonly used metal catalysts

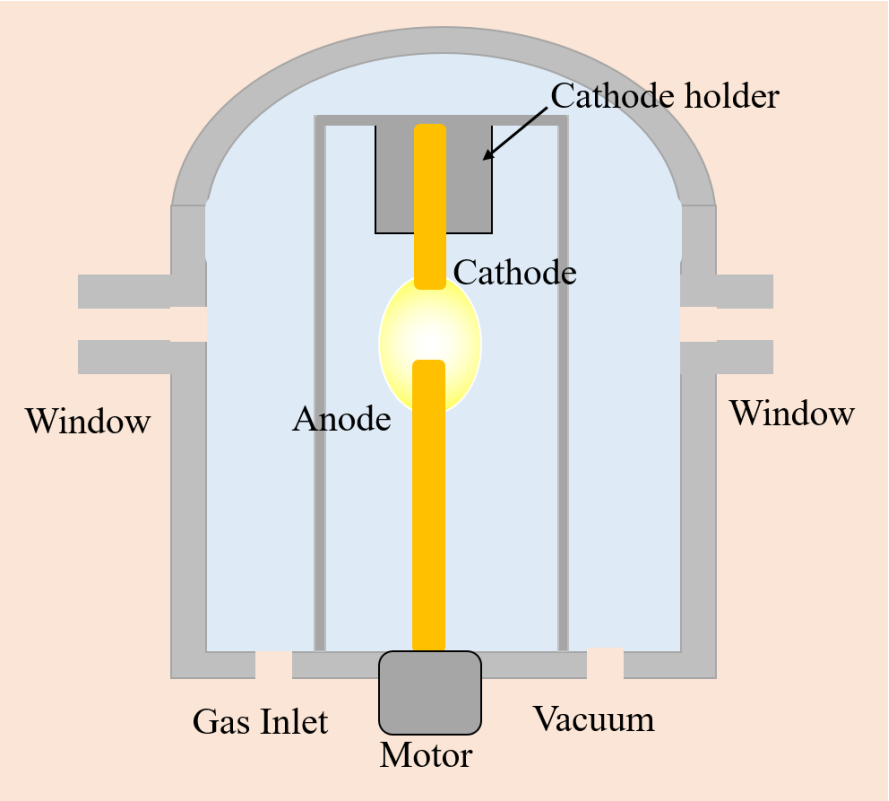

FIGURE 3.3: Arc discharge method for CNT production.

are Nickel (Ni), Iron (Fe), Cobalt (Co), Lead (Pb), Silver (Ag), Platinum (Pt), etc. or mixtures of Co, Fe, Ni with other elements like Co–Ni, Fe–Ni etc.

3.2.2 Laser Ablation

Laser ablation method is another promising technique for production of SW- & MW - CNTs. This method was first reported by Guo et al. in 1995 [65] to synthesize CNTs. A schematic for laser ablation is shown in Figure 3.4. The principle and mechanisms for this method are similar to the arc discharge with the difference that the energy is provided by a laser hitting a graphite pellet containing catalyst materials (usually nickel or cobalt) [66]. Almost all the lasers used for the ablation so far have been Nd:YAG and CO_2.

In principle, a graphite target is vaporized by laser beam under high temperature in an inert atmosphere. The laser produces carbon species, which are swept by the flowing inert gas from the high temperature zone to a conical water- cooled copper collector. The quality and yield of these products depend on the reaction temperature. Additionally, when a small amount of a transition metal such as Ni, Fe or Co is added to the carbon target, SWCNTs are produced. By varying the laser, catalyst composition, growth temperature, nature of gases and gas pressure, the average nanotube diameter and size distribution can be varied. As the vaporized species cool, small carbon molecules

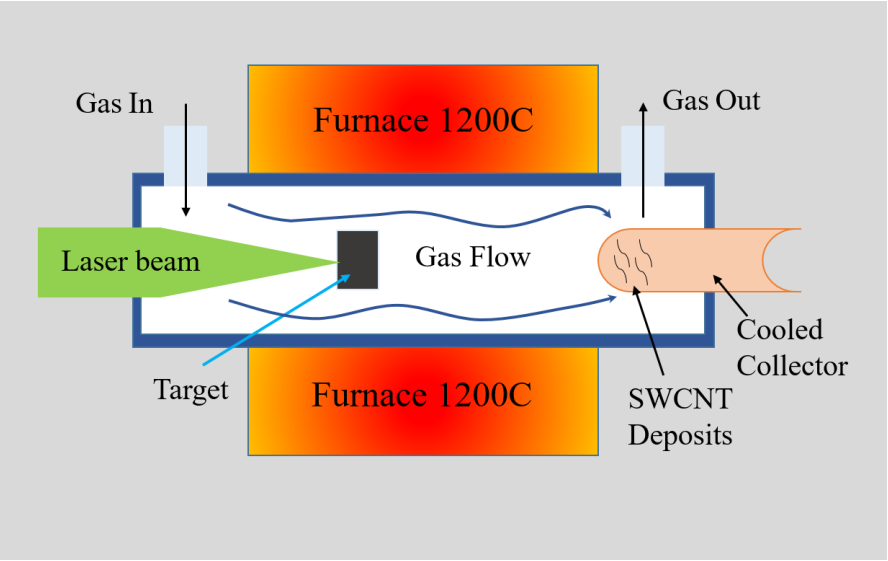

FIGURE 3.4: Laser Ablation method for CNT production.

and atoms quickly condense to form larger clusters, possibly including fullerenes. The catalysts also begin to condense, but more slowly at first, and attach to carbon clusters. From these initial clusters, tubular molecules grow into single-wall carbon nanotubes until the catalyst particles become too large, or until conditions have cooled sufficiently that carbon no longer can diffuse through or over the surface of the catalyst particles. Recent works have also pointed out the role of some laser parameters (such as laser power, repetition rate, pulse duration & laser wavelength) on the synthesis & characteristics of SWCNTs. In this method continuous wave CO_2 laser is used without applying additional heat to the target. The average diameter of SWCNTs increases with increasing CO_2 laser power from 500 to 800 W. Laser ablation, is one of the superior methods to grow SWNTs with high-quality and high-purity.

3.2.3 Chemical Vapor Deposition

Out of all the methods, chemical vapor deposition (CVD) is the most popular method of producing CNTs nowadays. In this process, thermal decomposition of a hydrocarbon vapor takes place in the presence of a metal catalyst. Hence, it is also known as thermal CVD or catalytic CVD (to distinguish it from many other kinds of CVD used for various other purposes). Figure 3.5 shows the experimental set-up used for CNT growth by CVD method. The process involves passing the precursor, hydrocarbon vapor, through a tubular reactor in which a catalyst material is present at sufficiently high temperature, around 600–1200 °C to decompose the hydrocarbon. CNTs grow on the catalyst in the reactor, and are collected upon cooling the system to room temperature.

In case the precursor is liquid hydrocarbon (benzene, alcohol, etc.), the hydrocarbon is heated in a flask and an inert gas is purged through it, which in turn carries the

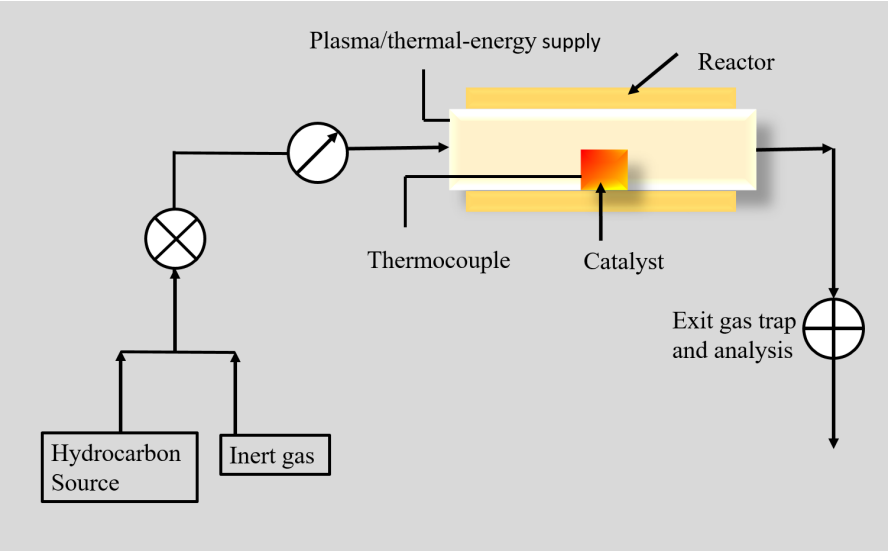

FIGURE 3.5: Chemical vapor deposition method for CNT production.

hydrocarbon vapor into the reaction zone. If the precursor is solid hydrocarbon, then it can be directly kept in a low-temperature zone of the reaction tube. Volatile materials (camphor, naphthalene, ferrocence etc.) directly turn from solid to vapor and CVD process can be performed while passing the vapors over the catalyst kept in the high-temperature zone. It is possible that the process uses catalysts precursors like the precursors of CNT. These precursors can again be in solid, liquid or gas form such that they can be suitably placed inside the reactor or fed from outside [67].

The three main parameters which affect CNT growth in CVD are the hydrocarbon, catalyst and growth temperature. Generally, low-temperature CVD (600-900 °C) yields MWNTs, whereas a higher temperature (900-1200 °C) reaction favors SWNT growth, indicating that SWNTs have a higher energy of formation, probably owing to their small diameters, which results in high curvature and high strain energy. The catalyst particle size has been found to dictate the nanotube diameter. Hence, metal nanoparticles of controlled size can be used to grow CNTs of controlled diameter. Thin films of catalyst coated onto various substrates have also been successful in achieving uniform CNT deposits. In addition, the material, morphology and textural properties of the substrate greatly affect the yield and quality of the resulting CNTs [63].

3.3 Structure & Band Structure of Carbon Nanotubes

As their name illustrates carbon nanotubes are *tubular* structures which have nanometer size diameter and are several micrometers long. The possibility of atomic size diameters and exceptionally large aspect ratio (larger than 10^4) often leads to consideration of CNTs as a prototype one-dimensional system (conduction in only one direction). All the earliest observed structures of carbon nanotubes were of the multiwall morphology

i.e. coaxial cylinders which were arranged in a "Russian doll" configuration. It is interesting to note at this point that coaxial multiple nanotubes are called multi walled carbon nanotubes (MWCNT) only when the outer diameters are less than 15 nm. Above 15 nm diameter the nanostructures are called carbon *nanofibers*. The properties of such nanofibers lie in between that to MWCNTs and carbon fibers [68].

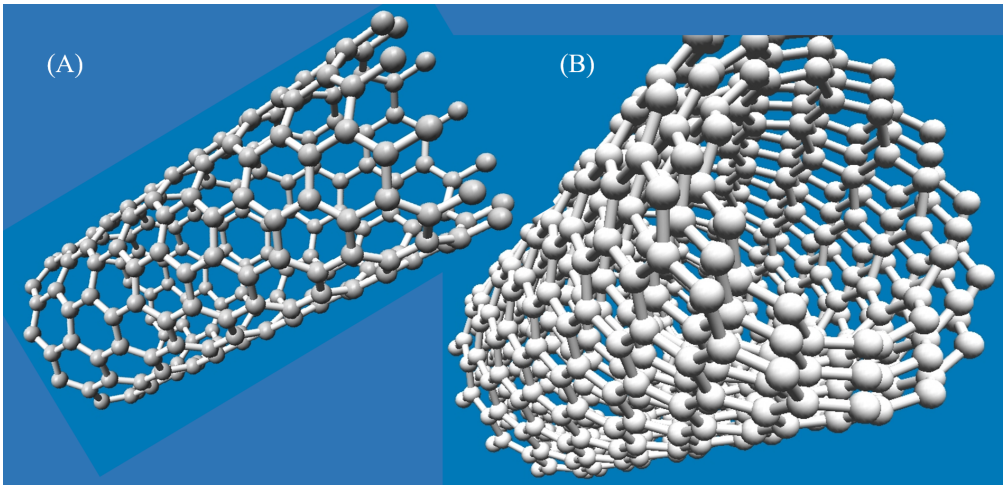

FIGURE 3.6: Structure of (A) SWCNT and (B) MWCNT, drawn using software nanotube modeler [11].

It is no surprise that wide fame of MWCNTs led scientists to explore its basic building block i.e. single walled carbon nanotube (SWCNT) in detail. SWCNTs are a single tube, one atom thick in the radial direction. A SWCNT is often described as a single graphene sheet with number of carbon atoms between ten and forty rolled into a cylinder [69]. Figure 3.6 (A) and (B) shows the structure of SWCNT and MWCNT. A carbon nanotube is specified by the chiral vector C_h defined in equation 3.1, where indices n and m are the number of unit vectors na_1 and ma_2 in the hexagonal honeycomb lattice contained in the vector C_h.

$$C_h = na_1 + ma_2 \tag{3.1}$$

The a_1 direction shown in Figure 3.7 (A) is also called the zigzag direction and the angle θ that the chiral vector C_h makes with this direction is called the chiral angle. When this chiral angle $\theta = 0\,^\circ$ the carbon nanotubes are called zigzag nanotubes and when $\theta = 30\,^\circ$ the carbon nanotubes are called armchair nanotubes. The carbon nanotube cylinder is formed by joining the line AB′ to OB as shown in Figure 3.7 (A). The diameter of the nanotube formed, can be expressed in terms of integers n and m as shown in equation 3.2, where $a_{C\text{-}C}$ is the nearest-neighbor C – C distance (1.421 A° in case of graphite), C_h is the length of the chiral vector C_h, and the chiral angle θ is given by equation 3.3.

$$d_t = C_h/2\pi = \sqrt{3} * a_{C\text{-}C}(m^2 + m * n + n^2)^{1/2}/\pi \tag{3.2}$$

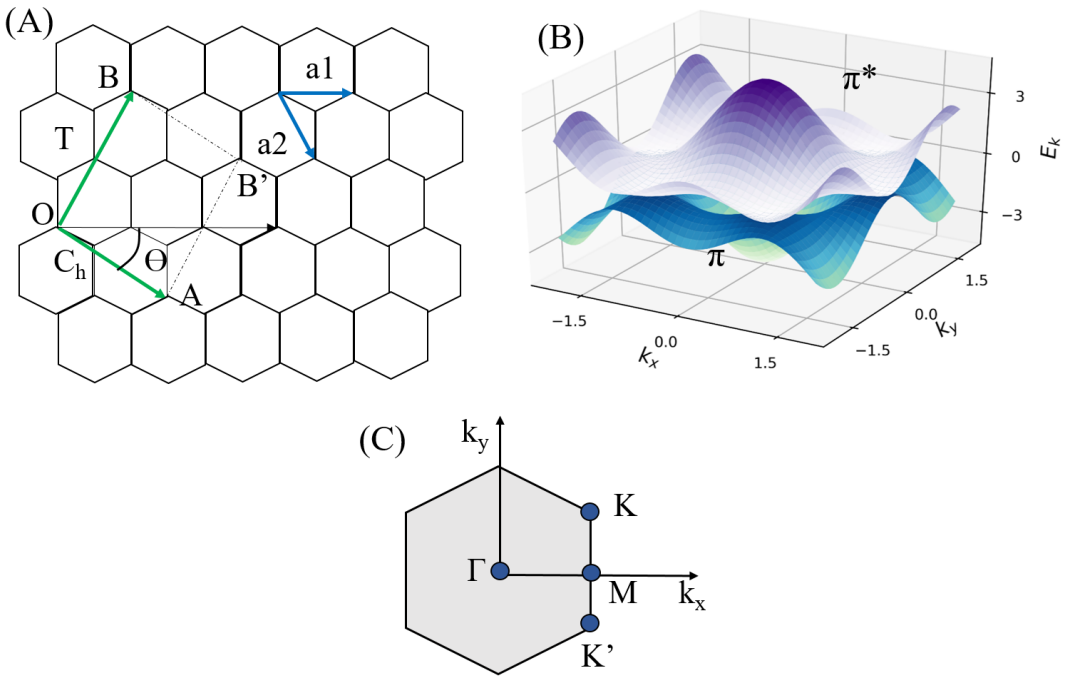

FIGURE 3.7: (A) Structure of a graphene sheet where. (B) The dispersion relation of charge carriers in graphene. (C) The Brillouin zone of graphene.

$$\theta = tan^{-1}[\sqrt{3} * m/(m + 2 * n)] \tag{3.3}$$

Hence, the nanotube can be specified by either indices n and m or by d_t and θ.

Figure 3.7 (B) shows the band structure of graphene. The dispersion relation used to compute the band structure is given in equation 3.4, where k_x and k_y are described further in this section, a is the lattice constant and equals to $\sqrt{3}\, a_{C-C}$.

$$E(k_x, k_y) = \pm\gamma_1 \sqrt{1 + 4\, cos(\frac{\sqrt{3}ak_y}{2})\, cos(\frac{ak_x}{2}) + 4\, cos^2(\frac{ak_x}{2})} \tag{3.4}$$

In the 3D plot we see two bands, one with lower energy and one with higher energy. These are so-called bonding and anti-bonding orbitals. It can also be seen that the two bands, bonding and anti-bonding, touch each other at six points lying at the Fermi energy (Fermi points). In most directions in k-space, as in the Γ-M direction, the electrons encounter a semiconductor-like band gap. In the Γ-K direction and in five other directions that pass through the Fermi points, or K-points, there is no band gap and electrons have free motion. These directions are shown in Figure 3.7 (C) which is the hexagonal shape of the first Brillouin zone. When we deduce the band structure of CNTs from graphene we must take into account that electrons in nanotubes are confined

along the circumference. Because the diameter of SWNT is on the order of 1 nm, the wave vector along the circumference k_y is quantized. Since the length of nanotubes is typically from one mm to hundreds of mm, the wave vector along the tube axis k_x is considered continuous. These directions k_x and k_y are shown in Figure 3.7 (C). Due to the quantization of k_y, not all the points in the graphene bands are accessible to nanotubes. It is shown that (n, m) tubes are metallic when (n-m)/3 is an integer. If (n-m)/3 is not an integer, the tubes are semiconducting. That means 1/3 of nanotubes typically are metallic and 2/3 are semiconducting [70].

In terms of hybridization, the carbon atoms are arranged in a hexagonal lattice. Each carbon atom is covalently bonded to three neighbor carbons via sp^2 bonding. The fourth valence electron, in the p_z orbital, hybridizes with all the other p_z orbitals to form a delocalized π-band. As the unit cell of graphene has two carbon atoms an even number of electrons are contained in the basic nanotube structure, which consequently can be metallic/semiconducting [71].

3.4 Properties of Carbon Nanotubes

3.4.1 Electrical Properties

The intriguing electrical properties of CNTs are due to the peculiar electronic structure of graphene [72]. Graphene has high intrinsic electron mobility [73] due to its lack of lattice defects as compared to most other semiconductor materials and its unique linear dispersion relation. As explained in the above section CNTs can be metallic or semiconducting depending on their chirality.

High quality SWNTs can have mobility larger than 10,000 $cm^2V^{-1}s^{-1}$ and mean free path longer than 1 mm. In addition to extraordinary conductance, when SWCNTs are used in FETs, they can have minimum capacitance coupling with gates, which leads to small RC time constant. Researchers have demonstrated SWNT FETs operating at up to 50 GHz [74]. The unique band structure and one dimensionality also make carbon nanotubes a unique optoelectronic material. The electron density of states in nanotubes has a series of singularities, associated with the onsets of subbands. CNTs can be viewed as semiconductors with multiple bandgaps and can efficiently absorb lights of a wide spectrum [75, 76].

3.4.2 Chemical and Biological Properties

Defect free ideal SWCNTs are chemically inert and hence are chemically stable and biologically compatible. It has been shown that field effect transistors with SWCNT as semicondutor can operate in aqueous solutions [74, 77]. In addition, because of

their molecular-scale size and extreme sensitivity to environments, SWNTs are ideal materials to make detectors that are capable to reach single-molecule level sensitivity [78, 79]. However their applications are not limited to sensors. SWCNTs have very large surface to volume ratio in addition to their chemical stability. This makes them highly interesting as electrode material in electrochemistry research [80].

In the biological applications, SWNTs are shown as drug delivery vehicles to bring chemicals into cells [81]. However there are still open questions about the toxicity of SWNTs, but it is more than likely that these concerns will be resolved as recent studies have shown that injected SWNTs can be excreted out from the bodies of mice within a couple of months [81], and during this time no toxic effects were observed.

3.4.3 Mechanical Properties

One of the remarkable mechanical property of CNTs is their high strength. To use a material as a structural element, knowledge of its Young's modulus (E) is necessary. Young's modulus is directly related to the cohesion of the solid and therefore to the chemical bonding of the constituent atoms [82]. For a thin rod of isotropic material of length l_0 and cross-sectional area A_0, the Young's modulus is

$$E = \frac{stress}{strain} = \frac{F/A_0}{l/l_0} \tag{3.5}$$

A molecular solid has a low modulus (usually less than 10 GPa) since van der Waals bonds are weak (typically 0.1 eV), whereas a covalently bonded solid like graphite, diamond and SiC has a high modulus (higher than 100 GPa). The Young's modulus of CNTs is in the order of $\sim$ 1TPa, which is five times higher than that of steel [83].

CNTs also have extremely high tensile strength (i.e. the maximum tensile stress a material can sustain before failure). The theoretically predicted tensile strength is 130 GPa [84]. For MWCNTs the largest measured tensile strength is 63 GPa [85]. One can compare this value with the tensile strength of steel, which is less than 1 GPa. At the same time, SWCNTs are extremely light. There was even a proposal to build a space elevator using SWCNT ribbons [86].

3.5 Carbon nanotube Field Effect Transistors

3.5.1 Metal Oxide Semiconductor Field Effect transistor

In a field effect transistor (FET) the charge conduction occurs through a semiconductor channel which is connected by two contacts "source" and "drain" on either sides. The

number of charge carriers in the channel is controlled by the third "gate" contact. In the vertical direction, gate metal, oxide and semiconductor, also known as the MOS structure behaves as a rectifying device that controls the mobile charge in the channel by capacitive coupling (field effect).

The channel is primarily the inversion layer at the semiconductor–oxide interface. For an n-channel MOSFET, the substrate is p-type silicon and the inversion charge consists of electrons that form a conducting channel between the n+ doped source and the drain contacts. A schematic view of a MOSFET is shown in Figure 3.8 (A). The inversion charge in the channel is induced by applying a suitable gate voltage and the onset of strong inversion is marked by the threshold voltage V_{th}. Figure 3.8 (B) depicts the three inversion regions of a MOSFET.

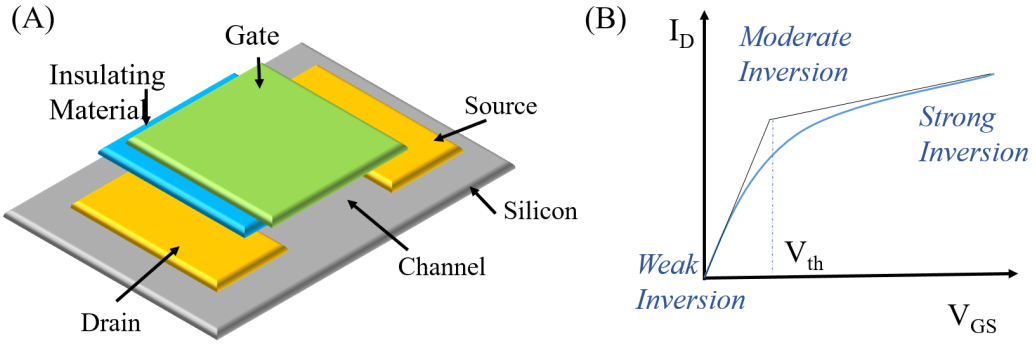

FIGURE 3.8: (A) Schematic of a MOSFET (metal oxide field effect transistor), (B) Different inversion Regions of a MOSFET.

Application of a drain to source bias (V_{DS}) in the above threshold region causes the electrons to move in the channel inversion layer from source to drain. A change in the gate-source voltage V_{GS} alters the electron sheet density in the channel hence modulating the channel conductance and the drain current (I_D).

3.5.2 Need for an alternate semiconductor

Field Effect Transistors are the most common electronic devices. Currently, around 10^{19} FETs are manufactured per year, most of them (∼99 %) on single-crystal silicon wafers. Silicon serves as the substrate as well as the semiconductor in which a channel of charge carriers is accumulated by a transverse electric field from a conducting gate electrode through a gate dielectric. Since the channel is formed close to the semiconductor/dielectric interface, mobility of charge carriers in the channel is usually less compared to that in the bulk [87].

In a silicon FET, a gate dielectric with excellent bulk and interface quality is readily obtained by oxidizing the silicon surface at high temperature in dry oxygen. It is possible

to scale down the thickness of the SiO_2 layer formed after oxidation to a few nanometers. This gate-dielectric scaling is necessary as the channel length of the transistor is scaled so that carrier density in the channel is controlled by the transverse gate field rather than by the lateral drain-source field [88].

This miniaturization of nanoelectronic devices however comes at a cost of increased tunneling current which leads to problems related to off-state current, power consumption, and heat dissipation [89]. To solve this, high-K dielectrics like HfO_2 replace thermally grown SiO_2 as gate dielectric such that the same gate capacitance corresponds to a thicker dielectric (and hence smaller gate leakage). However, the interface quality of such dielectrics is much lower and there is an increase in the number of scattering centers which leads to further reduction in the charge carrier mobilities [90]. These considerations have led to the research on alternative semiconductors that are compatible with silicon technology platforms but are capable to provide higher carrier mobilities than silicon. The fabrication of the first carbon nanotube-based FET in 1998 [91] was an important milestone in this direction.

3.5.3 SWCNT FETs

3.5.3.1 Back gated CNTFET

One of the earliest techniques for fabricating CNTFETs involved pre-patterning parallel strips of metal across a silicon dioxide substrate, and then depositing CNTs [92]. The semiconducting CNTs between two metal strips meet all the requirements necessary for a rudimentary field-effect transistor. One of those metal strip functions as the "source" contact while the other acts as the "drain" contact. The silicon oxide is the gate oxide and the metal contact under the oxide makes the semiconducting CNT gateable, as shown in Figure 3.9(A). Such back gate CNTFETs have high contact resistances (≥ 1 MΩ), which leads to a low transconductance g_m ($= dI/dV_{GS}$) of about $10^{-9} A/V$.

3.5.3.2 Top gated CNTFET

In order to optimize the gate switching, the capacitive coupling of the gate electrode has to be enhanced. In the most optimum case, the gate capacitance C_g should be larger than the quantum capacitance C_q of the nanotube ($C_q = 10^{-16}$ Fμm^{-1}) [93], so that it dominates the switching action [94]. Strong gate coupling can also be implemented by an additional top gate separated from the nanotube by a few nanometers thick layer of a high-k dielectric, such as TiO_2 (k = 80) [95] or HfO_2 (k = 25) [96]. Such a top gated FET is shown in Figure 3.9(B).

In one of the earliest works of fabricating top gated CNTFETs [97], single-walled carbon nanotubes were deposited onto a SiO_2 substrate followed by source/drain contact

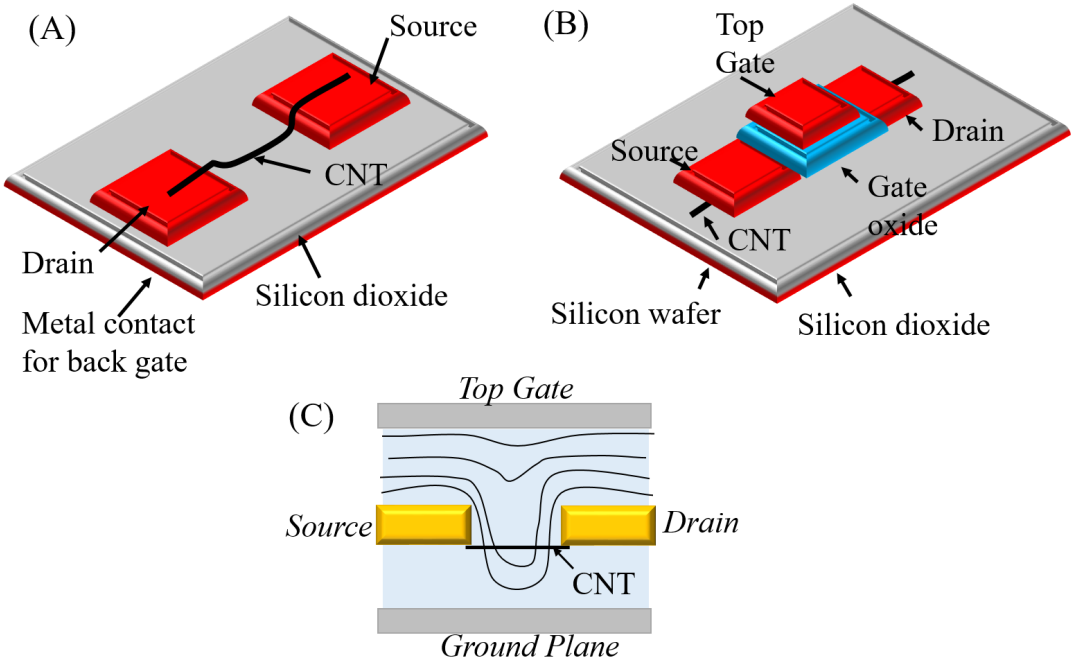

FIGURE 3.9: Different configurations of CNTFETs. (A) Schematic of a back gated single nanotube FET. (A) Schematic of a top gated single nanotube FET. (C) Device geometry for Schottky barrier (SB) FETs, where contour lines show the electrostatic potential (this curve is only representative).

patterning and deposition. A high temperature anneal step was done to reduce the CNT-metal contact resistance. To make the top gate, a thin top-gate dielectric was deposited on top of the nanotube and the top gate contact is deposited over the gate dielectric, completing the process. Due to the thin top gate dielectric, a small value of gate voltage can generate large electric field. This is one of the few advantages that make top gated FETs preferred over back gated ones, despite their more complex fabrication process.

3.5.3.3 CNTFETs as SB-FETs

The exact working mechanism of SWCNT-FETs is not fully understood till now. However, there is a general consensus that these transistors operate as Schottky barrier (SB) FETs in contrast to the conventional bulk transistors. In such SB-CNTFETs, the gate potential modulates the transmission through the Schottky barriers at the contacts in addition to modulating the carrier density Figure 3.9 (C). Thus, in principle the gate is affecting both the contact and channel resistance [98]. One can imagine that by proper choice of contact metal it is possible to minimize the schottky barrier for one carrier type [99].

3.5.4 Challenges in single nanotube CNTFET

One of the major problem in the fabrication of SWCNT-FETs is the lack of synthesis methods that would yield exclusively semiconducting nanotubes. Towards this goal numerous attempts have been made to either separate semiconducting tubes from the as-prepared material or to selectively eliminate the metallic tubes [100]. The basis of separation approach is the noncovalent chemical functionalization by various types of polymers which are capable of selectively wrapping semiconducting SWCNTs, most prominently DNA [101] and polyfluorenes [102]. Self-sorting semiconducting-SWCNTs networks can also be obtained by spin-coating nanotubes from solution onto appropriately surface-functionalized Si/SiO_2 substrates [103]. The method is based on the principle of selective binding of semiconducting tubes by the terminal amino groups of the silane layer on the silica [104]. Efficient chemical methods to eliminate the metallic tubes in nanotube ensembles include the coupling of benzene diazonium salts[105, 106] and methane plasma etching. Preferential destruction of metallic tubes has also been achieved through selective photo-oxidation using laser irradiation of appropriate wavelength [107].

Significant progress has been made in the development of FETs incorporating highly ordered SWCNT arrays produced via oriented CVD growth on quartz substrates[108]. After transferring the arrays onto a polymer substrate and selective electrical breakdown of the metallic tubes, the devices display very good performance.

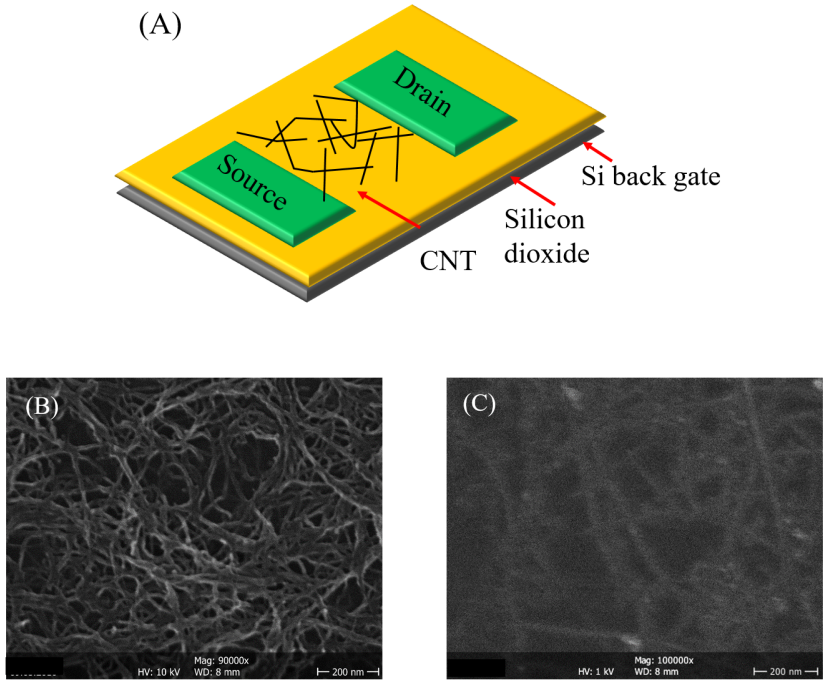

FIGURE 3.10: (A) Schematic drawing of a random network CNTFET. SEM image of (B) multi walled CNT and (C) single walled semiconducting CNT.

3.5.5 CNTFETs from random network of CNTs

One possible way to solve the challenges associated with single nanotube FETs is to use instead thin films consisting of large numbers of SWNTs in the form of random networks. These devices incorporate thousands or tens of thousands of SWNTs. Such an approach might represent a viable route to a technology due to (1) statistics that minimize the device-level effects of electronic heterogeneity in the SWNTs, (2) large active areas and high current outputs provided by the large numbers of SWNTs in each device, and (3) relaxed requirements of precise spatial position or orientation of any individual tube in the film [109].

There are two possible approaches to make such a random network of CNTs. CNTs can be deposited from their solution suspensions onto a solid substrate, utilizing specific interactions between SWNTs and the substrate. In the second approach CNT films are grown directly using chemical vapor deposition (CVD). Schematic of a CNTFET fabricated using random network of CNTFETs is shown in Figure 3.10 (A). In this thesis work, random network of carbon nanotubes is deposited using spray deposition techniques. Figure 3.10 (B) and (C) are random network of MWCNT and SWCNT sprayed on a polyimide substrate.

3.6 Fabrication of CNTFETs

Three major processes involved in semiconductor device fabrication are patterning, thin film metal deposition and semiconductor deposition.

3.6.1 Patterning using Photolithography

"Lithography" word has Greek roots where "lithos" translates to stone and "graphia" to write. So, literally lithography means to write on stones. Pertaining to semiconductor industry, patterns are created (or written) on silicon wafers using a light-sensitive polymer called photoresist. In fabrication of an integrated circuit where there are millions of transistors, lithography processes are performed twenty to thirty times in such a way that every new pattern is aligned with respect to the previous pattern [110]. Lithography is one of the most critical steps in device fabrication as 30 % of the manufacturing costs are associated with lithographic processes. In addition, lithography stands as one of the major technical limiter for further reduction in feature size, hence prohibiting further reduction in transistor speed and silicon area.

Optical lithography is a process where a light sensitive polymer (photoresists) is exposed and developed to form a three-dimensional image on the substrate. In general, this image will be an exact replica of the intended pattern. The final substrate is in

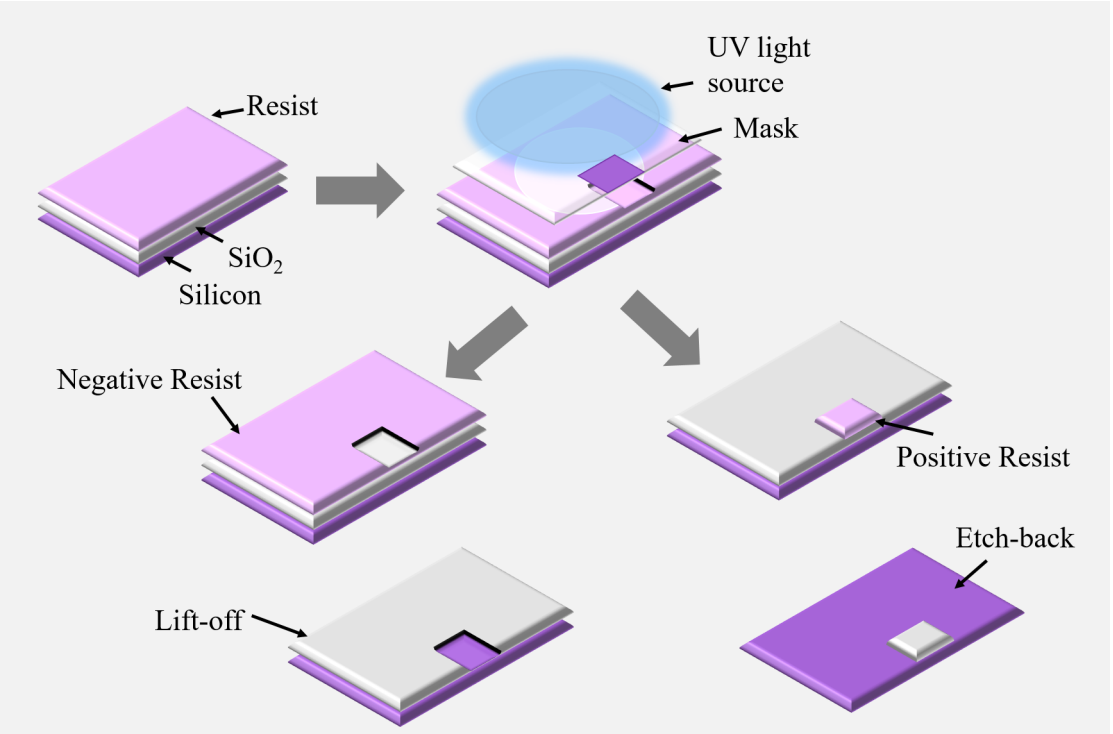

FIGURE 3.11: Schematic drawing of positive and negative photolithography.

parts covered with resist while other parts are completely exposed. In general following sequence of processing steps are part of a typical photolithography process: substrate preparation, photoresist spin coat, prebake, exposure, post-exposure bake, development, and postbake. Stripping of remaining resists after pattern transfer is the final step in the photolithographic process.

These individual processing steps are shown in Figure 3.11. In the following subsections a brief description of each step is presented.

3.6.1.1 Substrate Preparation

As its name suggests substrate preparation step prepares the substrate so that there is optimum photoresist adhesion. To achieve this the substrate is cleaned to remove contaminants [111]. Contaminants can be organic or inorganic molecules which result in poor photoresits adhesion and loss of line-width control. Chemical and mechanical cleaning processes along with chemical, ozone, or plasma stripping are usually employed to remove the contaminants. Water is another contaminant which is removed by a dehydration bake process by baking the substrate at temperatures of around 200°C to 400°C, usually for 30 to 60 minutes and cooling in a dry environment. The final substrate cleaning step is use of adhesion promoters to improve the adhesion of photoresist on the substrate. Adhesion promoters react chemically to replace the surface -OH group with

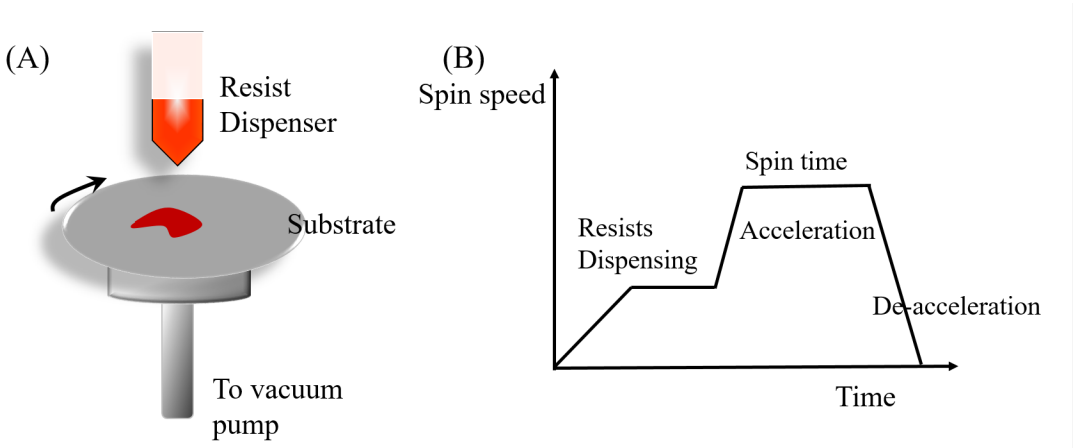

FIGURE 3.12: (A) Schematic of the spin-coating process. (B) Representation of spin speed vs time.

an organic functional group which offers good adhesion to photoresist. One of the most common adhesion promoter is hexamethyl disilizane (HMDS) [112].

3.6.1.2 Spin Coating

Spin coating is the commonly used process to achieve a thin, uniform coating of photoresist present in liquid form. This photoresist is poured onto the wafer substrate which is spun a high speeds to produce a desired film as shown in Figure 3.12(A). During this process several parameters must be controlled to meet the requirements for thickness control and uniformity with low defect density. For example, one can choose between static dispense where the wafer is stationary during the resists dispensing or dynamic dispense where the wafer is spinning during resists dispensing. One also has the choice of spin speeds and times, and accelerations for each of the spin speeds. Also, one can imagine the volume of resists and its viscosity along with the topography of substrate will play an important role in determining the resist thickness uniformity. In addition practical aspects like temperature and humidity control often affect the spin coating process [110]. Figure 3.12(B) presents an example of a photoresist spin coat cycle.

3.6.1.3 Soft Bake

After spin coating, the resists film contains 20 - 40% by weight solvent and during the soft bake process this excess solvent is removed. Before the soft bake process, solvent present in the resists film gradually evaporates hence causing a change in the properties of the film with time. During the soft bake process majority of the solvent is removed hence making the film stable. The major effects that occur during soft bake are reduction in the film thickness, improvement in adhesion and reduction in particulate contamination

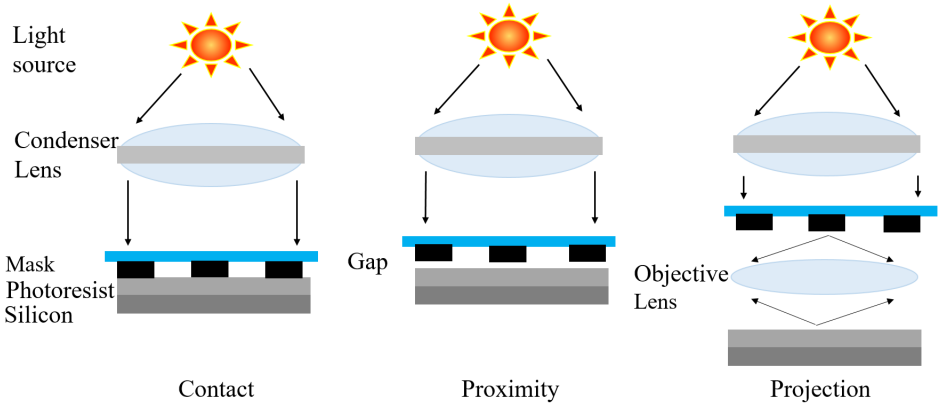

FIGURE 3.13: Three different exposure or alignment systems used in wafer exposure.

susceptibility. Usually after soft bake step there is 3 to 8 % residual solvent left in the resist film, which is sufficiently small and hence the film is stable during further processing. The most commonly used equipment for soft bake is hotplate. The wafer is placed on a high mass metal plate and silicon heats to near the hot plate temperature due to its high thermal conductivity. Usually the wafer is immediately placed on a chill plate so that heating stops immediately [110].

3.6.1.4 Exposure

The basic idea behind photolithography is that on exposure to light there is change in the solubility of resists in developer solution. The simplest methods to expose a photoresists through a photomask are contact and proximity lithography shown in Figure 3.13 (A) and (B). In case of contact lithography, the mask and substrate wafer are in direct contact, hence causing damage to photomask. To protect the mask, proximity lithography maintains a distance (in the orders of μm) between the mask and substrate. However, there is loss of the lowest resolution that can be achieved. The most commonly employed exposure method today is projection lithography shown in Figure 3.13 (C). As its name suggests an image of the pattern is projected onto the wafer using the aid of sophisticated lens systems possessing very few lens aberrations.

An important aspect in lithography is the resolution, which is the smallest feature size that can be produced. Resolution is computed by the Rayleigh criterion given by equation 3.6 where λ is the wavelength of imaging light and NA is the numerical aperture of the lens system.

$$R \propto \lambda / NA \tag{3.6}$$

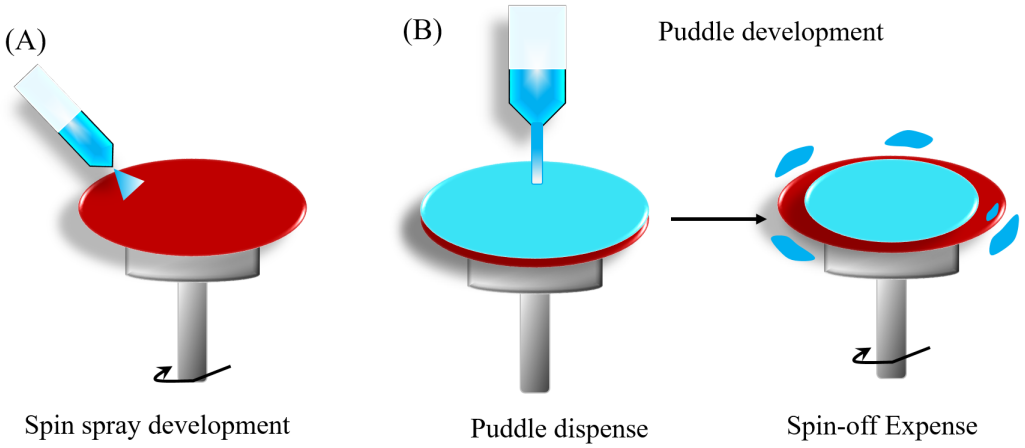

FIGURE 3.14: Schematic of (A) Spin spray development and (B) Puddle development processes.

To achieve lower resolutions the wavelengths used in lithography systems have reduced from blue (436 nm) to UV (365 nm) to deep UV (248 nm) and eventually to ultra deep UV (193 nm). At the same time, numerical apertures have increased to 0.93 NA in order to produce sub 100 nm features [110].

3.6.1.5 Development

After exposure the photoresists is developed in a developer solution (usually aqueous based). In batch processing multiple wafers are developed together at the same time in a large beaker full of developer solution. However recently several inline development processes have emerged, for instance spin development where developer is poured onto a rotating wafer. In such process the rinsing and drying of wafer also takes place while it is still rotating (or spinning). A variation of spin development is spray development where developer is sprayed in the form of fine mist on the wafer through a nozzle. This process uses low developer volume and provides uniform developer coverage. Third inline development process is puddle development where developer is poured on a wafer and is then left in this stationary state for the entire development time. Finally the wafer is rinsed and dried [110]. Figure 3.14 summarizes the various development processes.

3.6.1.6 Hard Bake

Hard bake or also commonly known as postbake is often done to harden the resists image so that it can withstand harsh conditions of subsequent processing steps. This is often done using a high temperature (120 °C - 150 °C) step that crosslinks the resin polymer in the photoresists leading to increase in its stability. Hard bake also does residual solvent,

water and gas removal hence improving the adhesion of the photoresists. Deep UV light can also be used instead of high temperature in hard bake step [110].

3.6.1.7 Pattern Transfer

To transfer the patterns onto the substrate there are three main approaches namely, subtractive transfer (etching), additive transfer (selective deposition), and impurity doping (ion implantation). In "etching" process, a uniform layer of the desired material is deposited on the substrate. In the next step of lithography those areas in this uniform layer are exposed where the desired material is not wanted. A chemical step is then performed where the exposed material is etched away selectively, followed by a resists strip step. In case of "additive" process the first step is lithography to expose the areas where certain material deposition is desired. Deposition methods like electroplating, sputtering are performed to deposit metal in these areas which is followed by a resists stripping step. "Ion implantation" is often done after lithography to selectively dope areas in the substrate which are exposed and other parts of substrate are protected by photoresists [110].

3.6.1.8 Strip

After all the above processes of pattern transfer the residual photoresist must be removed from the substrate. There are mainly two ways to perform photoresists strip: "wet" (chemical) stripping or "dry" (plasma) stripping. For wet stripping organic or inorganic chemicals are used. One of the simple stripper is acetone. However there is problem of scumming with acetone and hence often phenol based strippers are used. A wet stripping is often followed by a plasma step to completely clean the substrate. Plasma stripping, often done in oxygen plasma environment is very good for cases where resists has hardened during processing. However, it only works for organic polymers and often leaves inorganic materials untouched[110].

3.6.2 Alternate Lithography Techniques

3.6.2.1 Ebeam Lithography

The development of electron beam lithography tools started in the late 1960s by modifying the design of scanning electron microscopes. This technique is usually used for small features in sub-10 nm range which are otherwise hard to make using conventional photolithography. In electron beam lithography an accelerated electron beam directly writes on the surface of a substrate which is covered with an electron beam sensitive material. When the electron beam sensitive material is exposed to electron beam its

solubility changes according to the energy of the electron beam. The highly focused electron beam moves over a sample to write out a pattern designed with suitable CAD tools. [113]

3.6.2.2 X-ray Lithography

X-ray lithography was proposed by H. Smith and Spears at MIT. X-ray lithography can be understood as optical lithography but with shorter wavelengths. This type of lithography is often carried out in a projection transmission proximity printing mode instead of the usual reflection mode because of the difference in penetration and reflection of X-rays in matter. A special mask which has areas with difference in local absorptive coefficients is used to define patterns of a substrate covered with resists. If the resist is negative there is crosslinking on the X-ray exposed areas or, bond breaking in the case of positive resists [114]. Steppers are often used in lithography to increase the throughput, that is number of wafer processed/hour.

3.6.2.3 Laser Direct Writing

Lithography processes today are mostly projection printing where a reduced image of the mask is printed onto a photoresist. This is essentially done to provide high throughput, however lithography methods in general lack flexibility. Usually multiple lithography steps are required in production of a semiconducting device and one can assume that a minor change in the design often needs the entire processes to be redone. This causes extreme loss of time and money. In situations where higher flexibility and lower production rates are desired direct writing techniques like electron, ion, or laser scanning can be an optimal choice. Such direct techniques write serially pixel by pixel on a photoresists by modulation of an electron beam [115].

3.6.2.4 Nanoimprinting

Nanoimprint lithography was developed more than twenty years ago with the intention for low cost and high throughput nanoscale fabrication process. Over the years it has developed as an alternative to conventional lithography with applications in many areas of nanoscale device fabrication. A mold is used to define nanoscale deformation of a resist which is later cured by heat or UV application. After curing of resists, this mold is removed and the final structure is generated on the patterned resist. If a relatively rigid mold is used, the process is called hard nanoimprint lithography and results in high resolution features $\sim 5\,\mathrm{nm}$ but higher defect rates. On the other hand, in case of soft lithography, elastomeric molds made of materials like poly(dimethylsiloxanes) (PDMS), polyimides and polyurethanes are used. Soft nanoimprint lithography is also extended

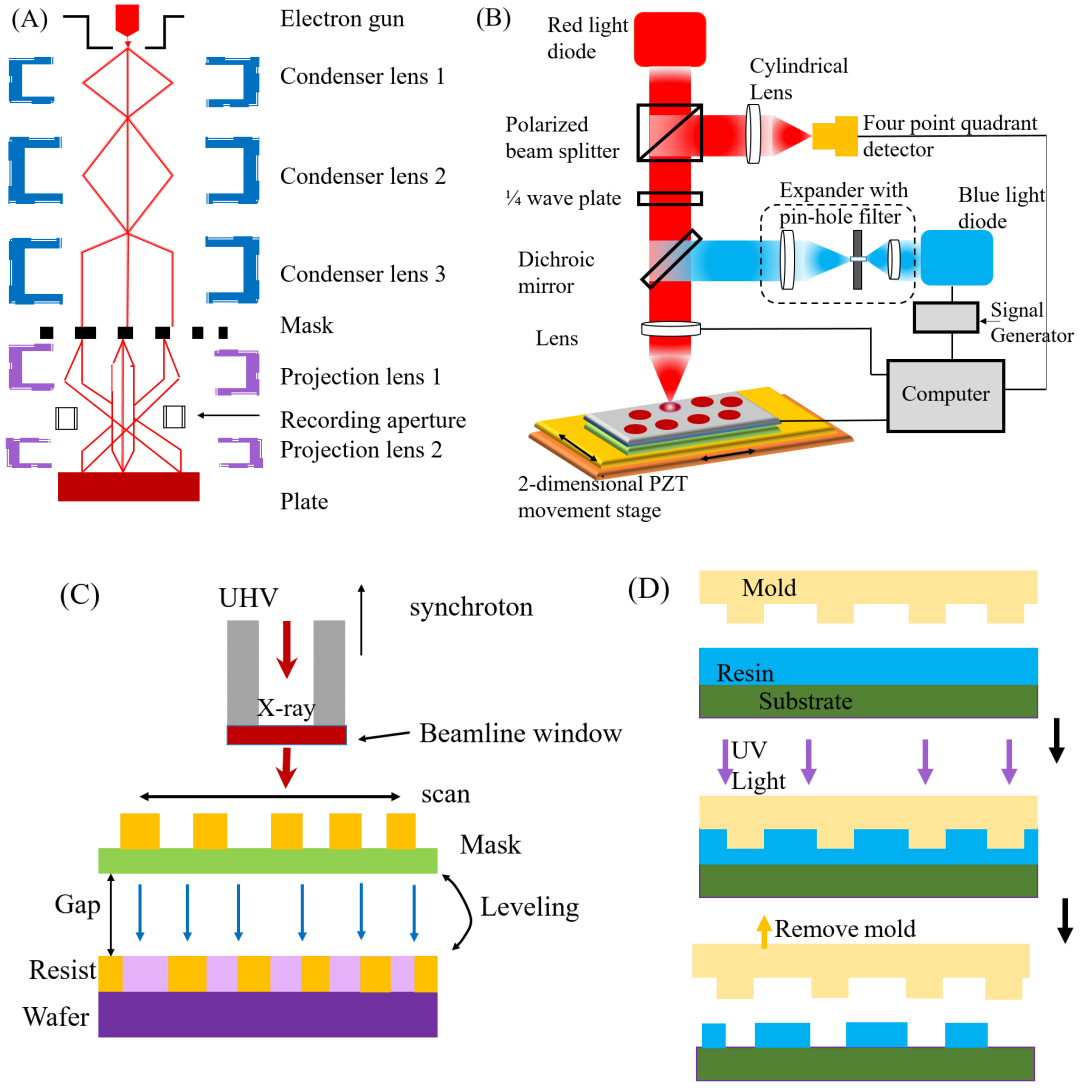

FIGURE 3.15: Schematic of (A) e-beam lithography, (B) direct laser writing system, (C) x-ray lithography and (D) nanoimprinting.

to roll-to-roll lithography for extremely high volume, low cost applications and holds enormous promise in future [116].

Figure 3.15 shows the schematic of the alternate lithography techniques discussed above.

3.6.3 Metal deposition techniques

There are several methods that are used for deposition in microelectronic fabrication. These can be broadly classified into two groups, chemical deposition and physical deposition. Chemical deposition methods are based on creating solid materials directly from chemical reactions. Usually in this process, there are byproducts in the form of gases, liquids and even other solids. In physical deposition on the other hand, the material

is physically deposited on the substrate without any chemical reaction involved [117]. Some the chemical and physical deposition techniques are described below in brief.

3.6.3.1 Chemical Deposition

Chemical Vapor Deposition

Chemical vapor deposition (CVD) was introduced in section 3.2.3 for growth of carbon nanotubes, but CVD is also widely used for metal deposition. This process belongs to a class of vapor-transfer processes where the deposited species are atoms or molecules. In this process deposition of a material takes place by its chemical reaction in the vapor phase with a heated substrate. CVD can be used in conjunction with PVD (physical vapor deposition) which otherwise can also be a competing process [118]. However one of the distinct advantage of CVD over PVD is the possibility of 3D-deposition. CVD can have variants when performed under different pressure conditions, like low pressure CVD (LPCVD) or atmospheric pressure CVD (APCVD). CVD can also be used in conjunction with other processes like plasma enhanced CVD (PECVD) [119].

Atomic Layer Deposition

Atomic layer deposition (ALD) technique has the capability to produce thin films of various different materials from vapor phase. As the scaling in semiconductor industry demands smaller structures, deposition techniques like chemical vapor deposition and physical vapor deposition are not very efficient. However, ALD offers very high conformability even on high aspect-ratio structures and very good thickness control even sub-nm thickness due to its sequential, self-limiting reactions [120].

Electrochemical Deposition

In electrochemical deposition or electrodeposition, as it is also called a thin film of metal, oxide, or salt is deposited on the substrate using electrolysis of a solution containing the desired metal ion or its chemical complex [121]. When using this process to deposit metals for contact on silicon, a seed layer (usually a thin layer of metal) is deposited on the wafer. A seed layer is important as silicon being a semiconductor is not as conductive for electrochemical deposition. The wafer is then immersed in a metal ion solution and is connected to the negative terminal of a voltage controlling system. The positive terminal is connected to a metal block. Under applied voltages, metal dissolves from the block maintaining a uniform concentration of metal in the solution, while there is continuous deposition on the wafer [122].

Molecular Beam Epitaxy

"Epitaxy" word is made up of two Greek words "epi" and "taxis" meaning above or upon and arrangement or order respectively [123]. Hence, the word epitaxy refers to the

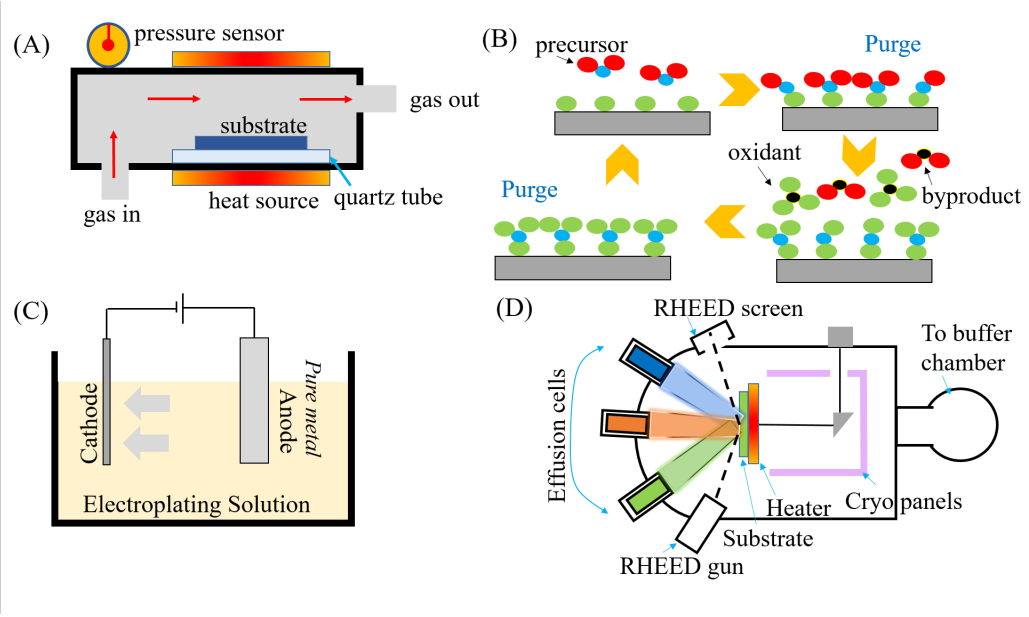

FIGURE 3.16: Schematic of (A) Chemical vapor deposition, (B) Atomic layer deposition, (C) Electroplating and (D) Molecular beam epitaxy, (RHEED stands for reflection high-energy electron diffraction).

process of growing one ordered layer of a crystalline material on top of another layer of same (or related) crystal arrangement. Hence, surface preparation is an important aspect especially for the growth of first few layers. Molecular beam epitaxy (MBE) is an atomic layer by layer epitaxial growth technique by reacting molecular or atomic beams (unidirectional flow of atoms or molecules without collisions) with a heated crystalline substrate in an ultra-high vacuum (UHV) environment. The term "molecular beam epitaxy" was coined in 1971 by Cho et. al. [124].

Figure 3.16 shows the four chemical deposition techniques described in this section.

3.6.3.2 Physical Deposition

Physical Vapor Deposition

There are two main processes in physical vapor deposition (PVD), namely evaporation and sputtering. They are widely used for metal deposition as they are cost-effective and less complex compared to CVD, but a disadvantage is that the quality of films might be poor than deposited by CVD.

Evaporation

In this process metal is melted and transported to the substrate in vacuum conditions. Deposition rate is highly dependent on the conditions of pressure, temperature and atomic mass of species that need deposition. For uniform deposition, substrate is often placed in rotating platform. There are mainly two types of evaporation, thermal

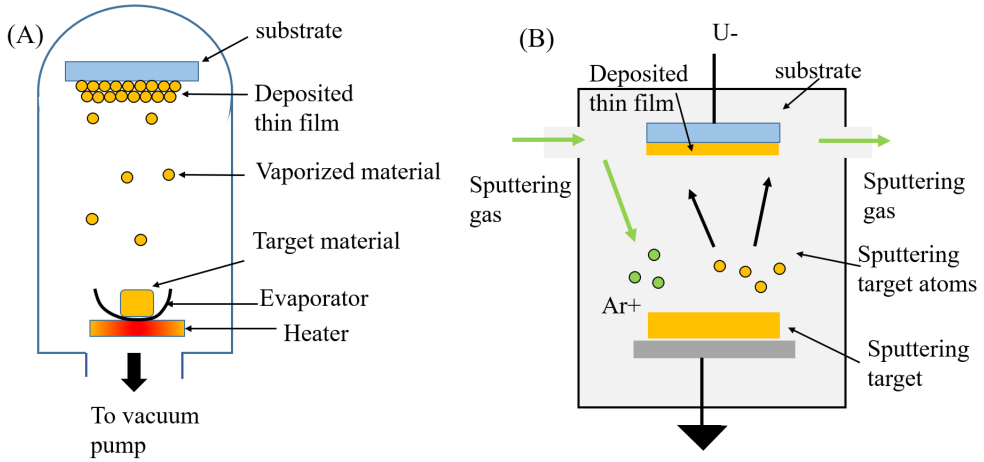

FIGURE 3.17: Schematic of physical vapor deposition methods, (A) Thermal Evaporation and (B) Sputtering.

evaporation or e-beam evaporation. In thermal evaporation the source metal is usually heated by resistive elements or inductive heating. In e-beam evaporation, an electron beam is focused on the source metal causing local heating and evaporation. Choice of evaporation method typically relates to the phase transition properties of that material (for example, aluminum is quite difficult to evaporate using resistive heating) [117].

Sputtering

Sputtering is a process in which atoms on the surface of a solid metal are physically ejected by momentum transfer from an atomic-sized energetic bombarding particle, usually a gaseous ion, accelerated from a plasma. In this case the distance between the substrate and the source metal is smaller than in processes involving vacuum deposition. One of the common approaches in sputtering is to use magnetron source where the positive ions present in the plasma of a magnetically enhanced glow discharge bombard the target. Sputtering can also be done by adding a reactive gas to the plasma for depositing a compound layer, i.e. reactive sputtering [125].

Figure 3.17 shows the schematic of thermal evaporation and sputtering processes.

3.6.4 Solution processable semiconductor deposition

Conventional semiconductor materials such as silicon are grown in the form of large perfect single crystals which are then cut and processed into devices under clean room conditions. This semiconductor technology is highly optimized and efficient but extremely expensive. An alternative to this technology is using semiconductors which can be prepared and processed in solutions. This solution processability not only is cost-effective but also imparts additional possible benefits like flexibility, bio-compatibility. The three widely used solution processable semiconductor deposition techniques are **spin coating**,

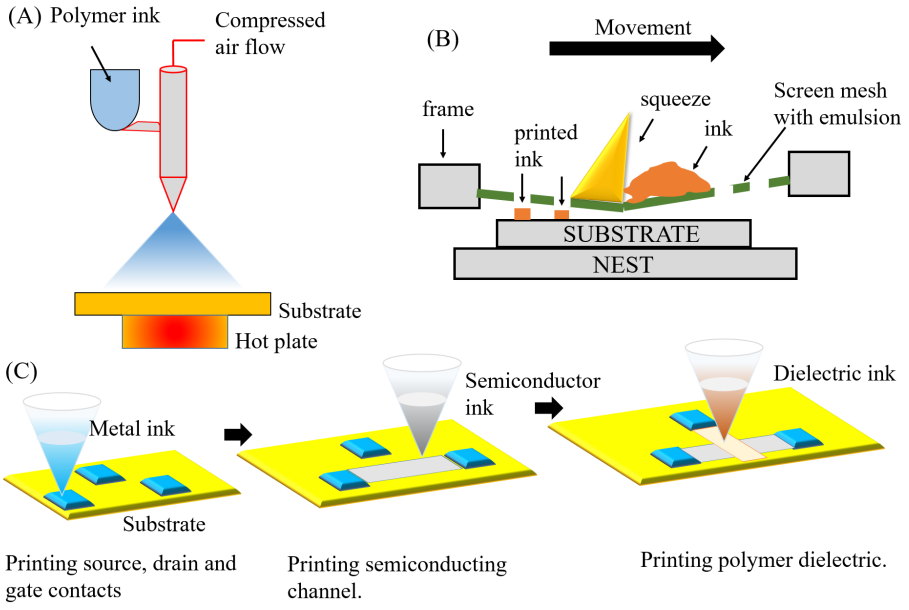

FIGURE 3.18: Schematic of (A) spray deposition, (B) screen printing and (C) ink-jet printing.

spray deposition and **printing**. In section 3.6.1, spin coating is already explained. In the below sections the remaining two techniques are discussed.

3.6.5 Spray Deposition

Spray deposition is a pneumatically driven ejection method which is very well-known in everyday life applications like spray-painting. Using this method in electronic device fabrication is possible due to the capability of polymer semiconductors to be soluble in various solvents [126]. Some of the advantages of this process are that it is highly scalable, use of material is in a far more cost effective way than spin-coating, there is no strict requirement for high-quality substrates and it is possible to make different nature of films like dense, porous and even multi-layered films [127]. A spray deposition set-up shown in Figure 3.18 (A) consist of an air-atomizer, spray nozzle, ink supply/solution holder, substrate heater, and temperature controller. The solution is sprayed through the spray nozzle directed towards the substrate which is placed on a heater. Most of the solvent evaporates during spraying. It is possible to control the homogeneity of the polymer film by controlling the droplet size of the aerosol [128].

3.6.6 Printing

The need for flexible, low cost and large area devices has led to significant progress in developing printing methods for semiconductor device fabrication. Screen printing and

ink-jet printing processes find their use in several applications around us and are now under investigation for thin film deposition [129].

Screen Printing Screen printing was used in the past in electronic industry for printing circuit boards [129]. The process is to squeeze ink of desired material on a substrate through a screen mask as shown in Figure 3.18 (B). There have been demonstrations in the past where all the active layers of a transistor were printed using this technique and device properties comparable to devices made from standard processes were extracted [130]. One of the main limitations of this process is that the lowest feature size printed is around 75 μm hence ultra small devices are not possible.

Ink-jet Printing A complete ink-jet printed thin film transistor can be made by replacing the inks in the cartridges with polymer solutions for metal and semiconductor [131]. Without any processing ink jet printing can print features as small as 25 μm in size, but research is continued for going to further small dimensions. Figure 3.18 (C) shows a schematic for ink-jet printing of thin film transistors.

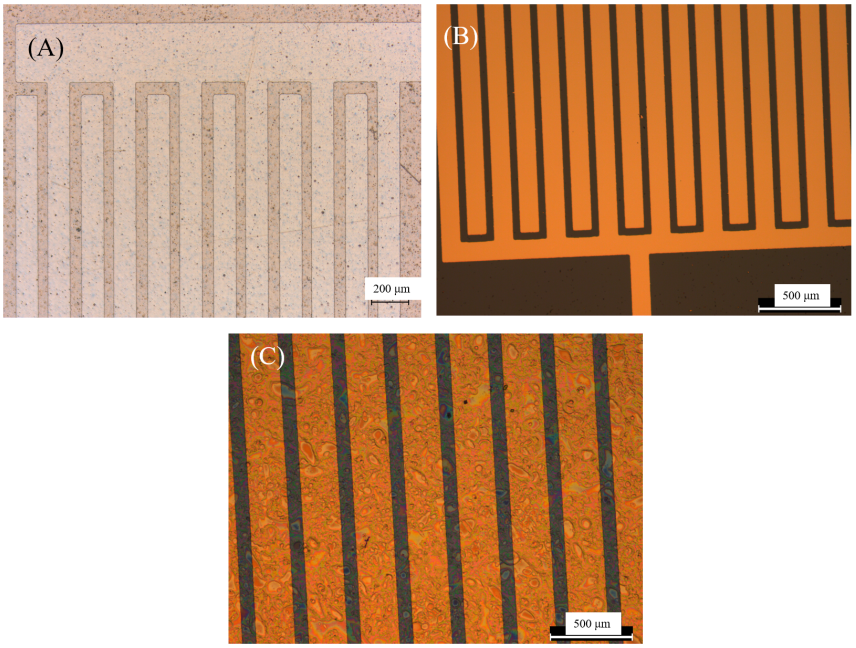

FIGURE 3.19: Optical microscope images of the interdigitated electrode structure (A) after development, (B) after lift-off and (C) after spray of semiconductor CNT solution.

Each of these techniques have their own merits and limitations, hence depending on the desired result one of them has to selected. For example, spin coating offers good uniformity, reproducibility and good control of thickness however the major disadvantages of spin coating is the wastage of material and no large area coverage. Spray deposition on the other hand offers large area coverage and possibility to deposit on many different substrates. The film thickness and morphology can be controlled in spray deposition by several parameters like air pressure, solution viscosity, nozzle-substrate distance among

others. One of the major limitation in spray deposition is resolution, which is also a major issue with screen printing technique. Other than resolution screen printing involves waste of material and use of only viscous materials, however screen printing process is a very simple process [132]. Inkjet printing in contrast offers high resolution but its a relatively slow process.

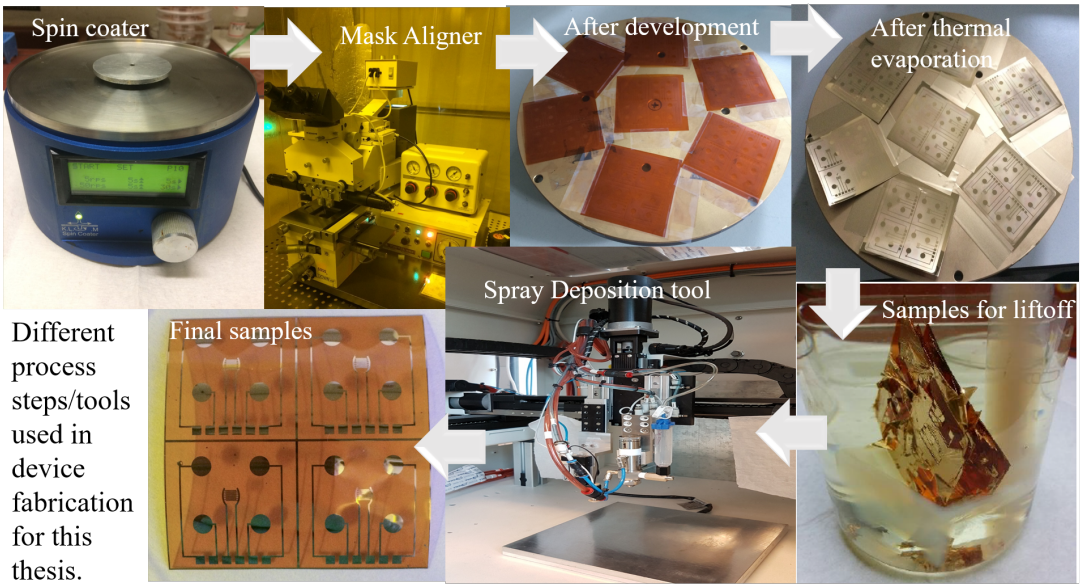

FIGURE 3.20: Different process steps/tools used in the device fabrication for this thesis work.

3.7 Process steps used in this thesis

In this thesis random network of carbon nanotube serve as the semiconductor channel. Negative photolithography with photoresists MAN-1420 is performed to pattern source, drain and gate contacts. Interdigitated electrode structure (IDES) is used for the source and drain contacts. Post exposure, development is done in developer solution MAD-533S by immersing the samples completely in the developer solution. Figure 3.19 (A) shows the IDES after development. The metal deposition is done by thermal evaporation. The contact metal is gold (Au) but the deposition of gold is preceded by deposition of a thin film (5 nm) of Chromium (Cr) for improved adhesion of the metal to the substrate. Liftoff is performed in acetone and the samples are rinsed with iso-propanol (IPA) and dried with dry nitrogen. Figure 3.19 (B) shows the IDES after liftoff. Finally spray deposition is used to spray the aqueous solution of CNTs. This aqueous solution is prepared by dispersing CNTs in a solution of sodium dodecyl sulfate (SDS) with deionized water (DI-water). 1 wt% aqueous solution of SDS is prepared and stirred for 12 hours at room temperature to uniformly disperse the surfactant in water and this stock solution is used for dispersing CNTs. The dispersion is achieved by sonication of the solution in horn sonicator. The solution is later centrifuged and the final solution

is obtained by decanting the top 80% of the supernatant. An automated spray system equipped with an industrial air atomizing spray valve and an overhead motion platform is used for spraying. The samples are immersed in DI-water for 15 minutes at room temperature to remove the remaining surfactant, and the devices are subsequently dried with nitrogen [133]. Figure 3.20 shows different process steps or equipments used in the device fabrication for this thesis work.

Chapter 4

Biomolecule sensing using field effect transistors

4.1 Electrolyte gated FETs

4.1.1 Electrolytes

An electrolyte is mobile ion containing medium which can be either in liquid or solid form. Electrically, electrolyte is neutral but when an electric potential is applied to it, the cations present in the electrolyte are drawn to the electrode that has excess of electrons, while the anions move to the electrode with deficiency of electrons. The movement of anions and cations in opposite directions result in a current. One of the simple example of an electrolyte is a salt solution in water. Water can release ions from the crystal lattice of many solid salts and can hydrate them within liquid water.

Below are briefly described some electrolytes used in this work.

Deionized-Water
Even deionised water (DI water) acts as an electrolyte through 'autoprotolysis' which is the spontaneous separation of water molecules into hydroxide ions (OH-) and hydronium ions (H_3O+) as shown in Figure 4.1 and give by equation below:

$$2\,H_2O \rightleftharpoons H_3O^+ + OH^- \tag{4.1}$$

At room temperature (25° C), the chemical equilibrium for an autoprotolysis is strongly on the non-dissociated side, hence DI water displays a low conductivity with pH value of around 7. On exposure to air, the conductance of DI water increases because carbon dioxide from air dissolves in it resulting in the formation of carbonic acid with pH changing to 5.5. But still, DI water can build an electric double layer with a double layer

capacitance of $3\mu F/cm^2$ at its interface with electric contacts [134]. The electrochemical window for water is 1.2V [135] and hence for most measurements with DI water the maximum bias applied in this work is 0.8 V.

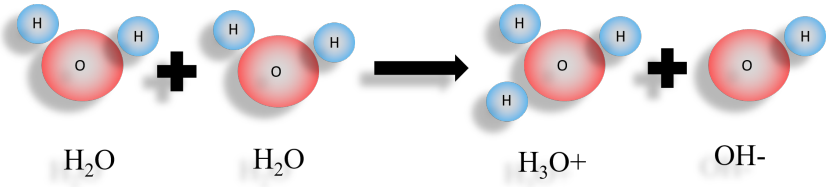

FIGURE 4.1: Autoprotolysis of deionized water.

Buffer Solution

A buffer solution consists of a weak acid (HA) and its conjugate base (A-), as shown in Figure 4.2. The important property of interest is that buffer solution resists changes in pH after adding small quantities of acid or base. In biosensing applications phosphate buffer saline (PBS) is used to maintain pH because it is a biologically realistic aqueous electrolyte, as a simulated fluids of bio-organisms [136].

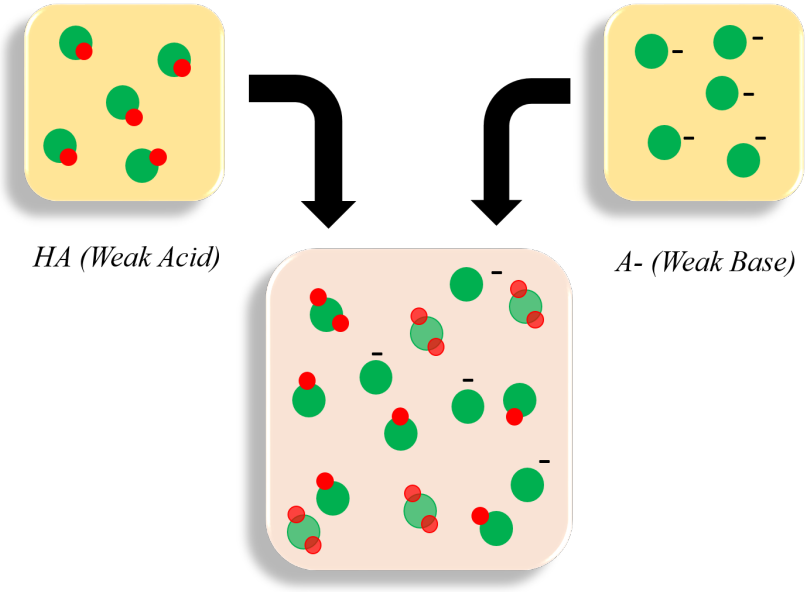

FIGURE 4.2: Buffer solution prepared by adding a weak acid and a weak base.

Ionic Liquid

Ionic liquids are made of organic salts with melting point below room temperature. Ionic liquids are extremely stable chemically, thermally and electrochemically. They have high conductivity due to high ionic concentration [137]. Figure 4.3 shows the chemical structure of 1-Butyl-3-methylimidazolium hexafluorophosphate, ionic liquid used in this thesis.

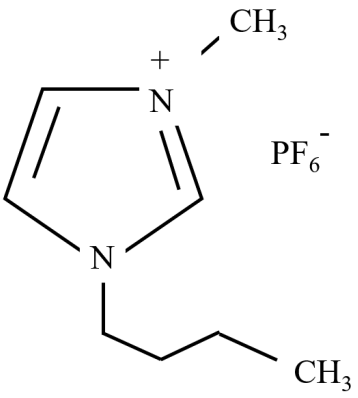

FIGURE 4.3: Chemical Structure of ionic liquid 1-Butyl-3-methylimidazolium hexafluorophosphate.

4.1.2 Structure and operating principle of Electrolyte-Gated FET

Electrolytes can be used as alternative to conventional dielectric insulators as gate media in thin film transistors. In the early 2000s, ionic liquids and solid state electrolytes were introduced as potential gate media materials [138, 139]. Kerogat et.al. showed [140] that even pure water can be used to gate a semiconductor film and result in a transistor, the high double layer capacitance leads to low threshold (around $\sim$0.3 V), within the electrochemical window of water. This work has paved path for water based analysis, where aqueous media is an active part of the transducer. In presence of a recognizing element on the surface of transistor, introduction of target analyte can impact the electrical characteristics of the transistor.

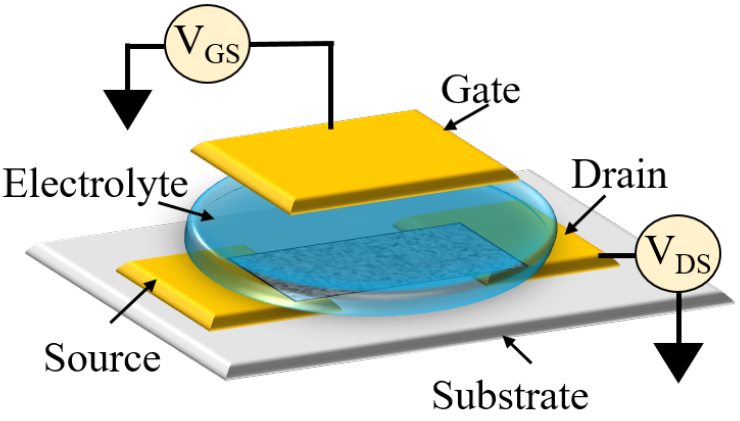

FIGURE 4.4: Schematic of an electrolyte gated field effect transistor.

Figure 4.4 illustrates the schematic of an electrolyte gated field effect transistor (EGFET). There is formation of electrical double layer at the semiconductor and gate interfaces and hence the gate capacitance in electrolyte gated FETs is double layer capacitance. On applying appropriate gate to source (V_{GS}) and drain to source (V_{DS}) voltages electrical

characteristics of an electrolyte gated field effect transistor can be recorded. Figure 4.5 shows the transfer characteristics for the EGFET measured in 0.1 M NaCl aqueous solution as the gate electrolyte and 50 μl of this solution is manually drop-casted over the gate and channel using a Gilson pipette. The applied drain to source voltage is fixed to -0.2 V while the gate to source voltage is swept from +0.8 V to -0.8 V. The channel length of the transistor is 300 μm and the channel width 700 μm . The ON/OFF ratio of this device is around 2.3 orders of magnitude and the transconductance is 3.5 μS.

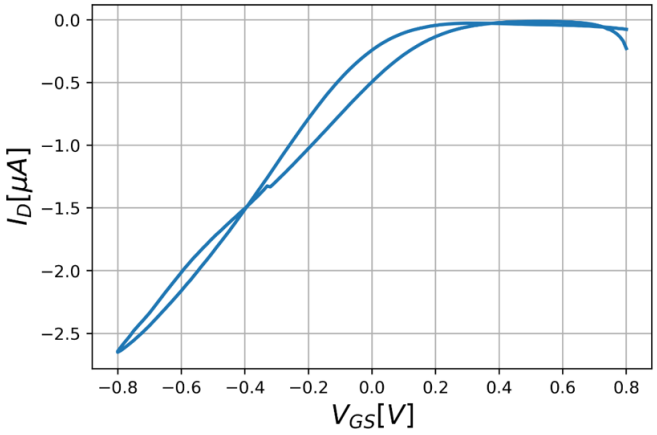

FIGURE 4.5: Transfer curve (I_D versus V_{GS}) for p-type electrolyte gated field effect transistor.

Figure 4.6 shows the output characteristics for the same transistor measured again in 50 μl 0.1 M NaCl solution. The drain–source voltage sweeps from 0 V to -0.6 V with a -10 mV step and the gate–source voltage varies from 0.4 V to -0.4 V with a -0.2 V step. It is important to note that the semiconducting channel for this FET is random network of carbon nanotubes and thus there are variations in the device characteristics from one device to another.

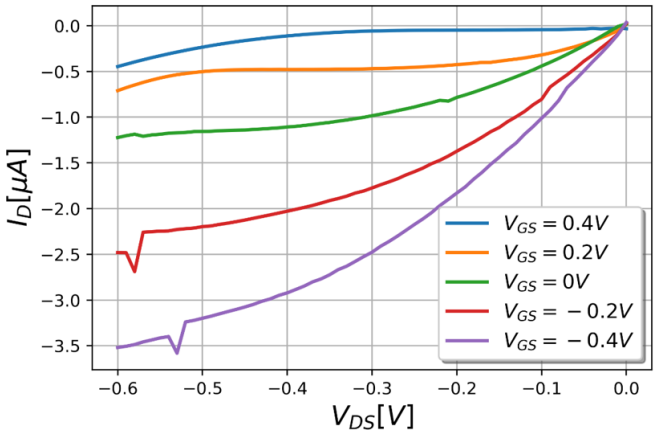

FIGURE 4.6: Output curve (I_D versus V_{DS}) for p-type electrolyte gated field effect transistor.

4.2 Biomoelcule Sensing

One of the most important applications of electrolyte gated field effect transistor is using them for bio-sensing applications. As water is the natural environment for biological receptors and can also act as an electrolyte, aqueous gated field effect transistors are very good candidates for biosensors [141]. In the following sections three different types of biosensing mechanisms are presented namely : enzyme based, non-enzymatic sensing and immunosensing. In all the sensors described below the basic transducing element is an electrolyte gated random network CNTFET.

4.2.1 Glucose & Lactate Sensors : Enzyme based sensing

Around 450 million people worldwide suffer from diabetes and this number is expected to increase much more in the coming years. Diabetes is one of the main reasons of death and disability, such as blindness, nerve degeneration and kidney failure [142]. The diagnosis and management of the disease requires precise monitoring and control of the glucose level in the body. Lactate is another important biomolecule which is primary metabolized in kidney and liver. In the area of human performance monitoring, lactate levels are important parameters for brain blood flow and impact brain activation during exercise-induced fatigue [143]. In this section, enzyme based glucose and lactate sensors are presented. Enzymes glucose oxidase (GOx) and lactate oxidase (LOx) catalyze biomolecules glucose and lactate respectively. Both these chemicals belong to a family of enzymes which produce hydrogen peroxide (H_2O_2) as a by-product of the reaction [144]. The peroxide can influence the electrical conductivity of the semiconducting transistor channel [145]. The sensing mechanism can be described by the following reactions:

$$\beta\text{-D}-\text{glucose} + \text{O}_2 \xrightarrow{\text{GOx}} \text{D}-\text{glucono}-\delta\text{-lactone} + \text{H}_2\text{O}_2 \tag{4.2}$$

$$\text{L}-\text{lactate} + \text{O}_2 \xrightarrow{\text{LOx}} \text{pyruvate} + \text{H}_2\text{O}_2 \tag{4.3}$$

The scheme to immobilize the enzymes is presented in Figure 4.7 (A). Glutaric acid, a dicarboxylic acid is used as the linking molecule between the -NH_2 groups of the kapton surface and the enzyme, hence forming two imide bonds. Both the carboxyl groups are activated using EDC (N-Ethyl-N'-(3-dimethylamino-propyl) carbodiimide hydrochloride) and NHS (N-hydroxysuccinimide) [146]. AFM image of the semiconducting CNT channel before and after functionalization with enzyme GOx is shown in Figure 4.7 (B) and (C).

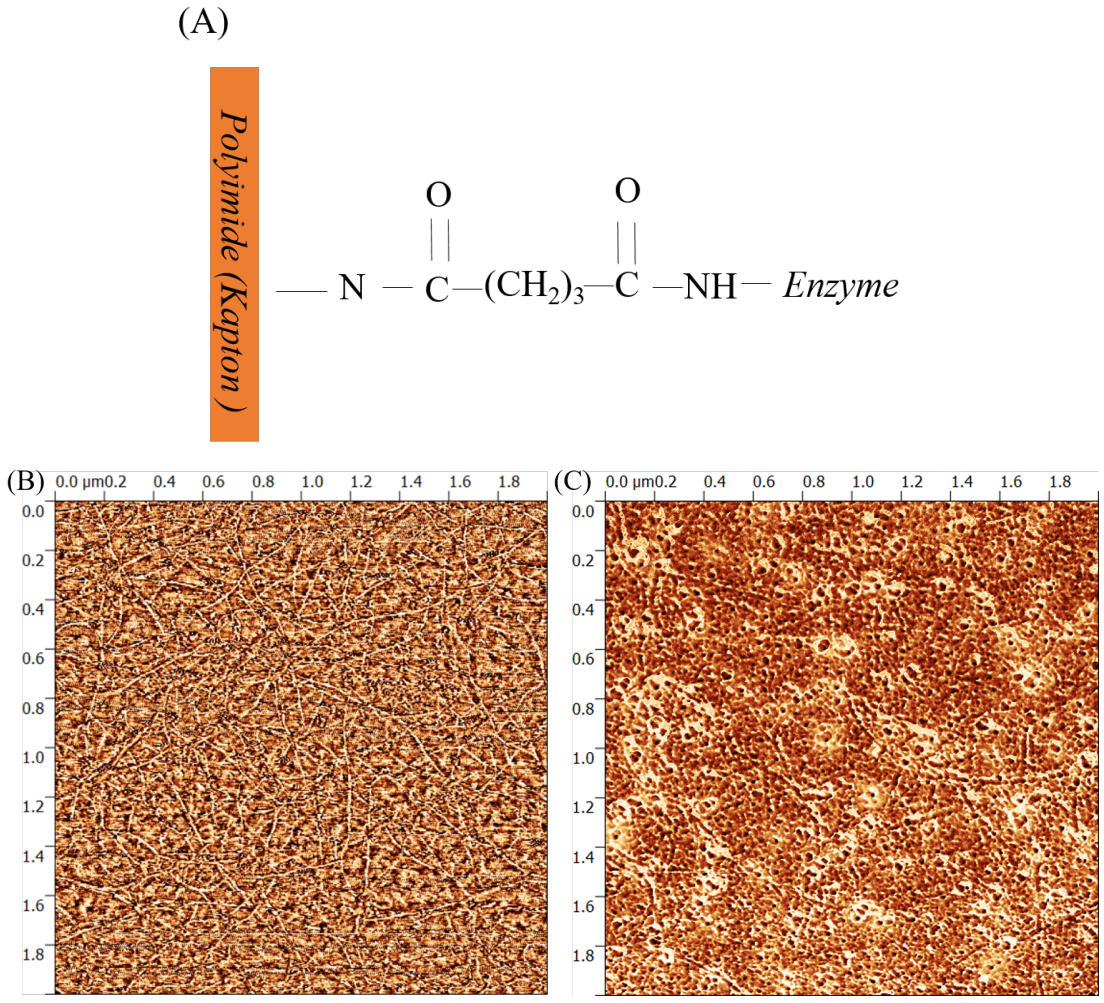

FIGURE 4.7: (A) Enzyme immobilization scheme for glucose oxidase and lactate oxidase. AFM image of the polyimide substrate (B) before and (C) after immobilization of enzyme (GOx).

Figure 4.8 (A) and (B) shows the response of the lactate/glucose sensor to different concentrations of lactate/glucose respectively. The applied V_{DS} used in these measurements is fixed to -0.1 V and V_{GS} is swept from +0.8 V to -0.7 V. Results show that as the concentration of lactate/glucose increases, the drain current (I_D) increases.

The sensitivity of lactate and glucose sensors can be calculated by a linear fit of the current versus concentration curve as shown in Figure 4.9. The slope of the linear fitting line gives the sensitivity of the sensor. The calculated sensitivities for the lactate and glucose sensors are 2.198 μA/decade and 1.767 μA/decade respectively. These values are comparable to recent works on enzymatic sensors developed using MOS_2 based FET [147] and graphene based FET [148]. However in these works, the enzyme immobilization scheme is either complex using multiple layers of polymer and nanoparticles [148] or the enzyme is introduced into the FET surface only during sensing [147]. The functionalization of the substrate (i.e. kapton here) provides additional advantage of minimum device degradation post enzyme immobilization.

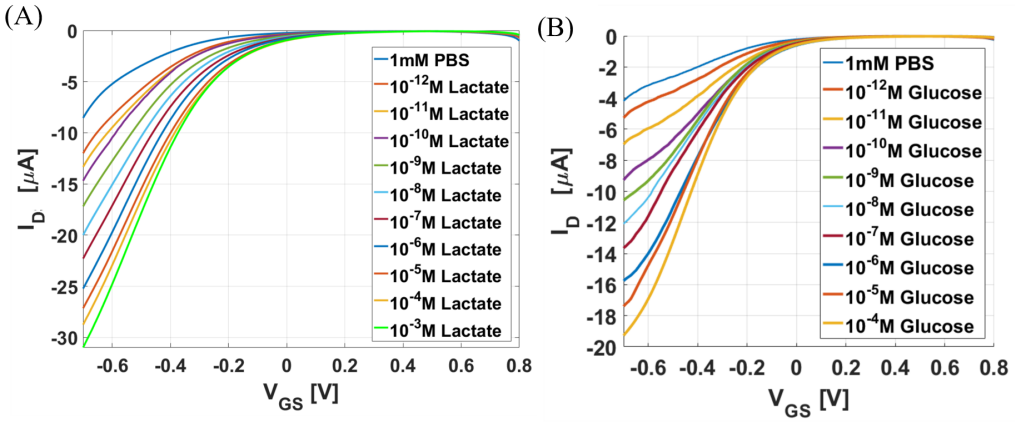

FIGURE 4.8: (A) Response of glucose sensor to varying concentrations of glucose. (B) Response of lactate sensor to varying concentrations of lactate.

To investigate the shelf life of sensors, stability tests are performed. The sensors are re-measured after a period of three to four weeks when they are stored at 4°C and compared to their previous measurement. Figure 4.9 (A) and (B) show that there is small change in the overall sensitivity of the sensors due to decreased enzyme activity over the period of time.

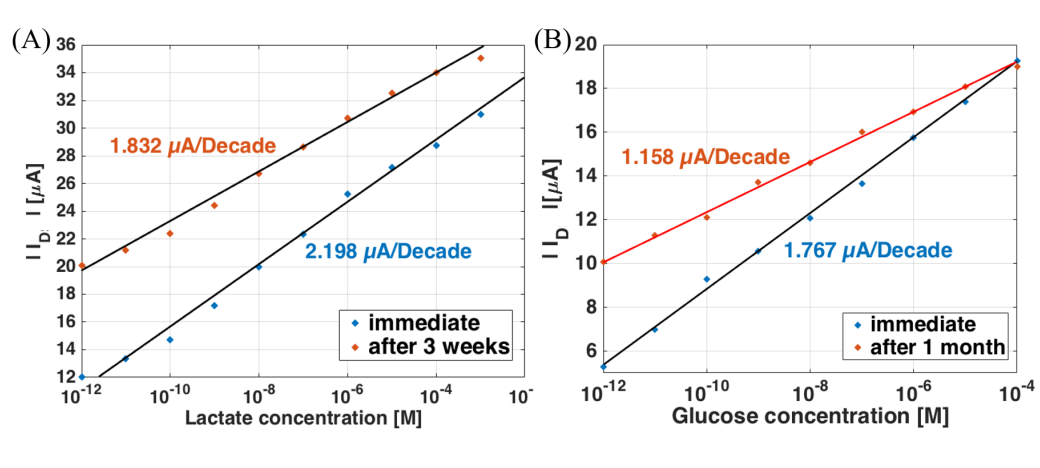

FIGURE 4.9: (A) Current versus concentration curve for lactate sensor measured immediately after sensor production and then re-measured after three weeks. (B) Current versus concentration curve for glucose sensor measured immediately after sensor production and then re-measured after three weeks.

A major advantage of flexible sensors is their potential to be used in wearable or implantable devices where continuous real time monitoring of an analyte is possible, for example using them as an electrochemical tattoo [149] or a contact lens [150]. However, such devices will experience continuous mechanical stress because of bodily movements. Therefore it becomes important to evaluate the endurance of such devices against mechanical deformation. To verify this, the sensors are flexed to a 90 ° angle at the radius

of 0.17 cm with a speed of 50 mm/sec for more than 400 total iterations and the response of the sensor is recorded after every 100 iterations with a concentration of 10 μM analyte (glucose or lactate). As seen in Figure 4.10 (A) and (B) the current response is well maintained after such repeated bending cycles, indicating the robustness of the sensors against mechanical deformations or stress.

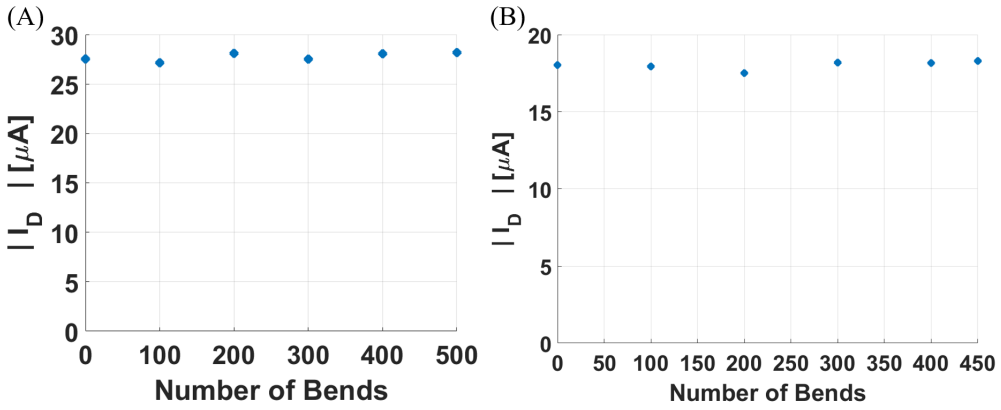

FIGURE 4.10: (A) Flexibility tests for lactate sensor. (B) Flexibility tests for glucose sensor.

4.2.2 Dopamine Sensing : Non-enzymatic sensing

Dopamine is a neurotransmitter belonging to the catecholamine and phenethylamine families. It performs crucial functions in the brain and the central nervous system (CNS) as a local chemical messenger that controls the immune system and digestive system, among others [151, 152]. Abnormality in dopamine level can lead to serious medical and neurological conditions, such as Parkinson's disease, Alzheimer's disease, depression, addiction, and schizophrenia [153, 154]. Various analytical techniques such as chromatography [155], spectrophotometry [156] and electrochemical methods [157] have been developed for measuring dopamine levels. There have also been reports on the use of electrochemical electrodes made of carbon nanotubes [158], carbon [157], organic materials[159], etc. for the detection and recognition of dopamine. In the past few years biosensors based on field-effect transistors (FETs) are also investigated to achieve real-time and rapid dopamine detection [160–162].

In this thesis work, non enzymatic dopamine sensors are prepared by functionalizing kapton substrate. Carboxyphenyl boronic acid (CPBA) is a molecule which can bind to dopamine and form a charged boronate ester which can then modulate the surface charge on the semiconducting channel [163, 164]. EDC and NHS are used for the activation of CPBA. Figure 4.11 (A) shows this functionalization scheme. Attenuated total reflection fourier transform infrared (ATR-FTIR) measurement is performed on the polyimide sample before and after it is functionalized with CPBA. The spectral resolution is set to 2 cm^{-1}, and 24 scans are recorded and averaged per sample. Figure 4.11 (B) shows the

spectra of bare polyimide and the polyimide functionalized with CPBA zoomed-in on the range from 1500 cm^{-1} to 1800 cm^{-1}. The width and height of the C=O peaks around 1700 are modified after functionalization, indicating a change in the environment [165]. Figure 4.11 (C) shows the spectra in the range 1300 cm^{-1} to 1500 cm^{-1}; a slight peak seen just above 1380 cm^{-1} is a signature of the B-O bond of the boronic acid [166], hence confirming successful surface functionalization.

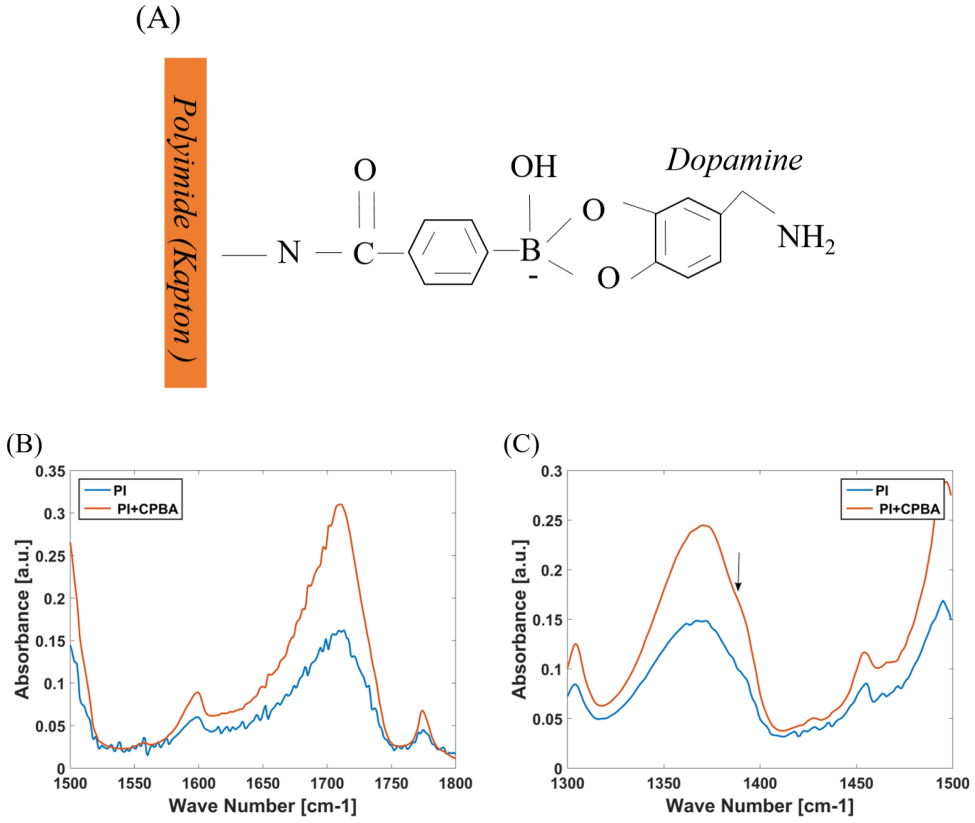

FIGURE 4.11: (A) Functionalization of the polyimide substrate for dopamine sensing. Attenuated total reflection fourier transform infrared (ATR-FTIR) measurement for bare polyimide (PI) and polyimide with CPBA for the range (B) 1500 cm^{-1} to 1800 cm^{-1} and (C) 1300 cm^{-1} to 1500 cm^{-1}.

Figure 4.12 (A) shows the transfer curves for the dopamine sensor recorded with varying concentrations of dopamine in 10 mM PBS buffer solution at pH value chosen at its pKa (i.e., pH = 7). Figure 4.12 (B) is the maximum current versus concentration response for dopamine sensor measured at fixed V_{DS}=-0.1 V and V_{GS}=-0.8 V. To extract the sensitivity of the sensor a linear fit of the current versus concentration curve is done and the calculated sensitivity is 36 μA/decade. With the increase in the concentration of dopamine there is continuous increase in the drain current for the transistor. The boronic acid immobilized on the polyimide surface binds to the dopamine mixed in the buffer solution as shown in Figure 4.11 (A). The formed boronate ester has a negative charge on the boron atom and influences the device characteristics of the CNTFET. With the increase in dopamine concentration in the measuring solution, there is an

increase in the negative charge near the surface of the p-type semiconducting channel. This negative charge attracts more holes (majority carriers) on the surface of CNTs, thus causing an increase in the current for p-type FET.

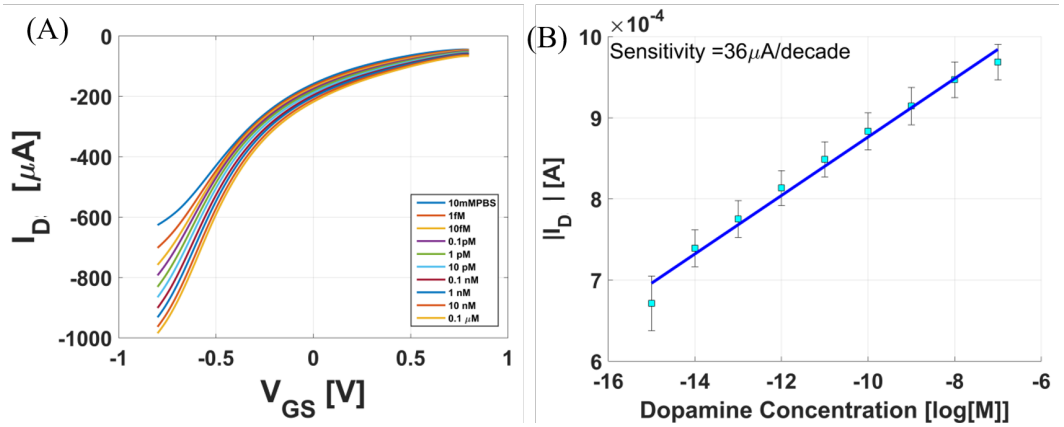

FIGURE 4.12: (A) Transfer curve for a dopamine sensor measured with different dopamine concentrations. (B) Maximum current versus concentration curve to extract sensitivity of the sensor.

The above dopamine sensor has a very wide linear range from 1 fM to 0.1 μM and is highly sensitive even in very low concentrations. Such high sensitivities are not reported even in those sensors where extra elements like metal nano-particles are introduced in the transducer surface to increase their sensitivity [167]. We believe this is because of two reasons which arise due to the functionalization of kapton substrate. First is higher number of recognition sites because there is larger functionalized area and second is that these sites are very close to the semiconductor and hence they can easily affect its charge density.

One crucial difference between enzymatic and non enzymatic sensors is in their selectivity. Enzyme based sensors are highly selective as enzymes have very powerful specificity to target analytes. Non-enzymatic sensors on the other hand do not have this intrinsic selectivity. For example, the dopamine sensor described in Figure 4.11 (A) can be used to sense other molecules with similiar chemical structure. An implication of this is described in section 4.3.2.

Another important aspect in such sensors is their regeneration so that they can be reused. It is observed that for regeneration of biosensors, the solvent environment needs to be altered in such a way that the analyte/receptor binding is weakened. The main reagents used to achieve this are acid/base (pH change), detergents, glycine, and urea [168]. For regeneration of dopamine sensors hydrochloric acid (HCl) solution is used in this work [169]. For very high concentrations of dopamine ($\sim$ 1 mM), the sensor saturates and cannot be turned on, as seen in Figure 4.13 (A). This can be partly because the debye length significantly decreases for very high concentrations of dopamine solution. After the measurement in highly concentrated dopamine solution, the CNTFET is rinsed thoroughly with 0.5 M HCl and then with DI-H_2O. As seen from Figure 4.13 (A), the

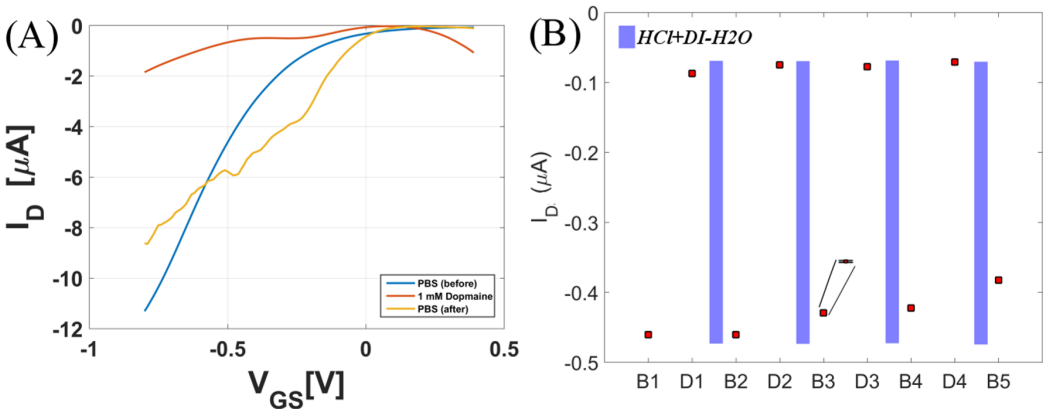

FIGURE 4.13: Regeneration of dopamine sensor: (A) after treatment with 0.5 M HCl; (B) four regeneration cycles where B(1,2,3,4,5) refer to the number of times the sensor was measured in buffer and in between the 1mM dopamine measurements D(1,2,3,4), the blue bar indicates HCl treatment.

dopamine sensor recovers and the CNTFET turns on with a loss of about 20% in the maximum current after it is treated with HCl. In an attempt to recover the device more effectively, a lower concentration of HCl (10 mM) is used after the device is subjected to 1 mM dopamine. Figure 4.13 (B) depicts the drain current of the measurement where first the device is measured in buffer solution (B1), and then with dopamine (D1). After this, the device is exposed to 10 mM HCl for 5 minutes and subsequently thoroughly washed with DI-H_2O. This process of regenerating the sensors with HCl after measuring in buffer B(1,2,3,4,5) and dopamine D(1,2,3,4) is performed four times. It is observed that there is a 19% decrease in the current level after four regeneration cycles with 10 mM HCl. This study proves that such non-enzymatic sensors can be used multiple times with a slight decrease in their sensitivity.

4.2.3 Protein Sensing : Immunosensors

Tumor necrosis factor - alpha (TNF-α) is a pro-inflammatory cell signaling protein (cytokine) and a key biomarker associated with host defense and immunosurveillance [170, 171]. It is shown that TNF-α secreted from immune cells stimulated with lipopolysaccharide (LPS) - an endotoxin causing septic shock due to severely pronounced immune response of the human body – reflects a functioning innate to immune response [172]. This makes immunosensing using TNF-α an area of interest.

Immunosensing using transistors was introduced by Shenck in 1978 [173]. In this thesis, initial work for immunosensing using CNTFET is performed. There is some literature already available on immunosensing using CNTFETs where the functionalization of aptamers or antibody is done directly on the carbon nanotubes[174, 175]. However, the focus of this thesis is in developing such functionalization schemes where the core semiconductor is not chemically modified (for minimum device degradation).

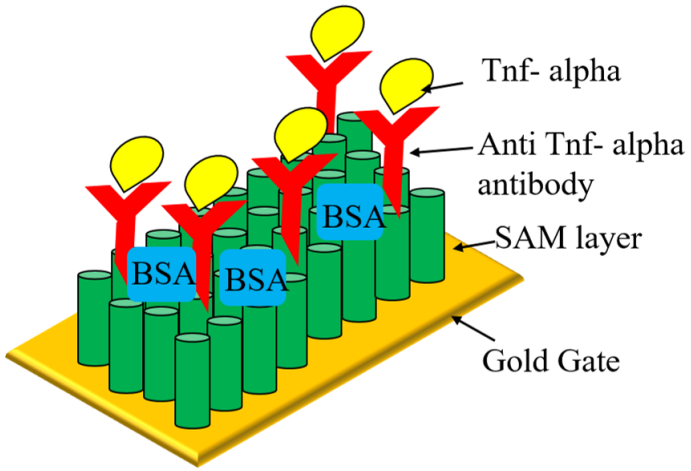

FIGURE 4.14: Immobilization of anti-TNF-α antibody through SAM layer to capture TNF-α.

In this work gold gate electrode is functionalized using self assembled monolayers (SAMs) exploiting a well known thiol-gold chemistry [176]. Further functionalization of the gate electrode's surface is done by immobilizing anti-human TNF-α antibody on top of the SAM layer. It is important, that this immobilization results in controlled coverage and orientation of antibodies, so that there is optimal biological activity and minimal non-specific adsorption. To promote this, bovine serum albumin (BSA) is introduced to cover the open SAM layer. The immobilized antibody binds to its selective antigen, that is TNF-α in this case and causes a variation in the electric double layer capacitance, resulting in the modulation of drain current. This variation in current can be correlated to the analyte concentration. The functionalization scheme is shown in Figure 4.14. After the functionalization an extra layer of the SAM and the antibody is introduced between the gate electrode and the channel. This extra layer would modulate the overall gate capacitance and hence the drain current of the transistor.

Figure 4.15 shows the real time measurement of a TNF-α sensor measured when the gate to source (V_{GS}) and drain to source (V_{DS}) voltages were fixed to -0.8 V. The current increases when 1 nM TNF-α is introduced in the buffer and further when a higher concentration of 10 pM is added. This is because introduction of functionalizaton layers causes a reduction in the overall gate capacitance hence causing a reduction in the drain current of the transistor.

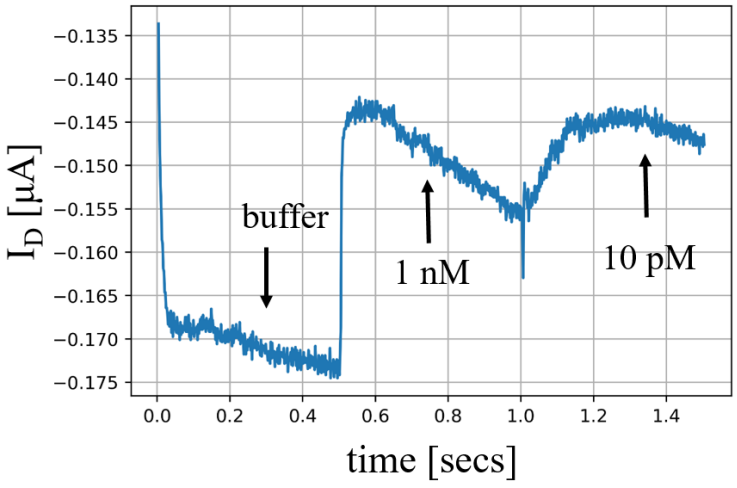

FIGURE 4.15: Drain current measured at fixed biases for 0.5 secs with different concentrations of TNF-α in the electrolyte buffer.

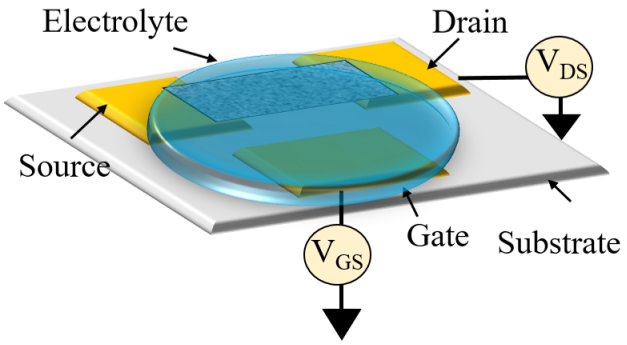

FIGURE 4.16: Schematic of a in-plane gate electrode electrolyte gated field effect transistor.

4.3 Considerations for biosensing using field effect transistors

4.3.1 Geometry of gate electrode

Figure 4.4 shows a schematic of one of the earliest electrolyte gated FET, however recently an in-plane gate design is used where the gate electrode is fabricated in the same lithography step as the source and drain electrodes. Such an EGFET is shown in Figure 4.16.

In this section, impact of the in-plane gate electode's geometry on the transistor device characteristics are discussed. The study is focused on two aspects: (i) the impact of varying gate electrode area and (ii) the impact of varying distance between gate electrode and the channel, on the transistor performance. For the first study, equidistant gate

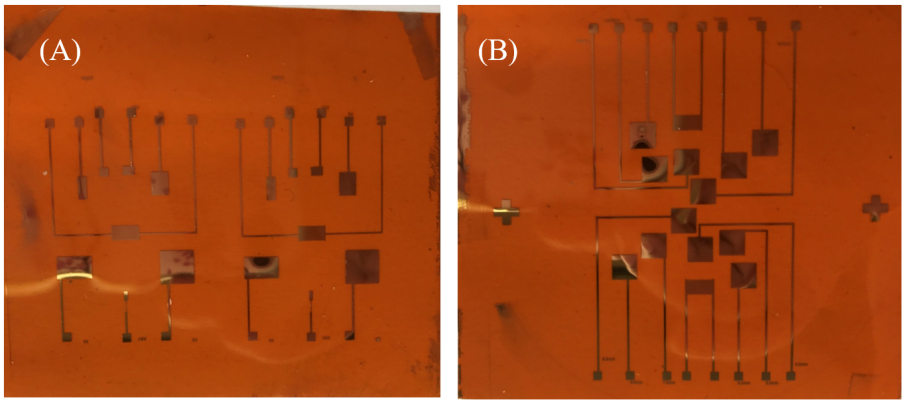

FIGURE 4.17: Image of the devices used for (A) gate electrode area and (B) distance between gate electrode and area study.

electrodes are placed around the channel with gate area to channel area ratios as 0.17:1, 1:1, 2:1, 4:1 and 6:1, where 1 refers to area of 2.5 mm^2. The image of the device is shown in Figure 4.17 (A). Multiple devices are measured and four major transistor characteristics namely maximum drain current, on-off ratio, hysteresis and maximum transconductance are studied.

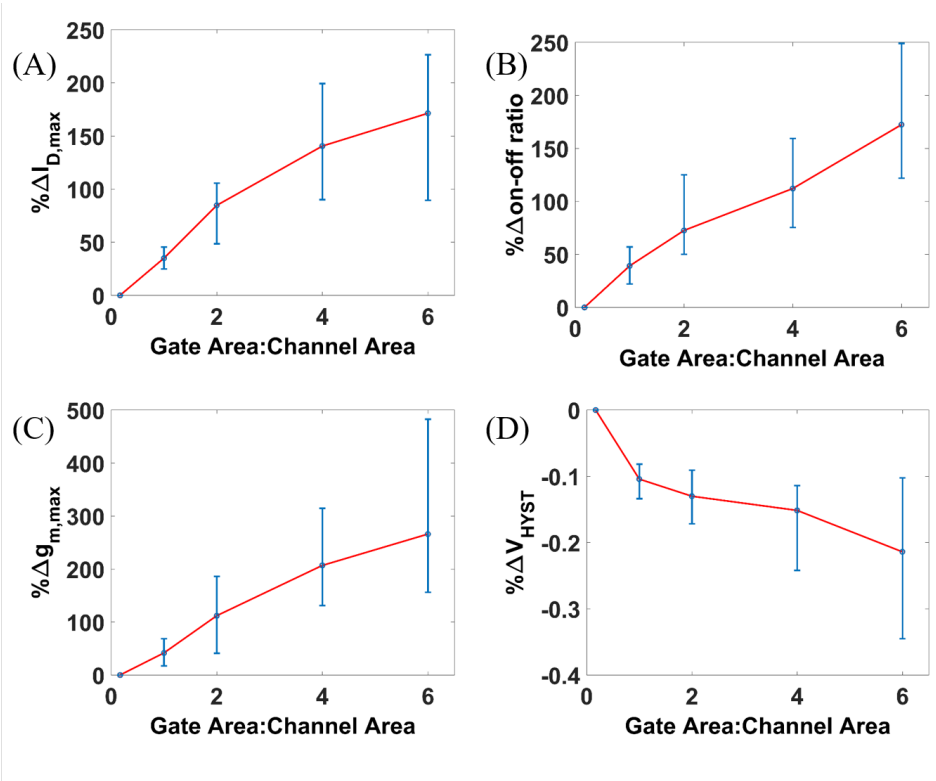

FIGURE 4.18: Variation in transistor properties with gate electrode area. Percentage change in (A) maximum drain current, (B) on-off ratio, (C) maximum transconductance and (D) hysteresis.

Figure 4.18 (A) shows the percentage change in the on-current with the increase in gate

area. The on current increases almost linearly with the increase in the gate electrode area. This is because I_D is proportional to gate capacitance, which in turn is linearly related to the gate electrode area. This dependence is also seen in the relative change of the on/off ratio (Figure 4.18 (B)) and transconductance (Figure 4.18 (C)) with the gate electrode area, as these two properties are directly proportional to I_D. Figure 4.18 (D) shows the variation of hysteresis with the gate electrode area. It is observed that hysteresis decreases continuously with the increase in gate electrode area. Hysteresis, in field effect transistors leads to variation in major device properties like mobility, threshold voltage, on/off ratio and sub-threshold slope between the forward and backward sweeps, hence lowering the reliability of devices. The major reasons for hysteresis are considered to the adsorbed water and oxygen molecules on CNT surface or surface traps that are capable to trap the induced charges due to the field effect [177]. Hysteresis (V_{HYST}) is defined as the difference of the voltages that should be applied to the gate in forward and backward sweep directions to get the drain current equal to the average of maximum and minimum drain current, i.e., $(I_{D,max} + I_{D,min})/2$. Thus improving the gate control in the FET would lead to lowering the hysteresis in the I-V characteristics, and the same is observed in Figure 4.18 (D).

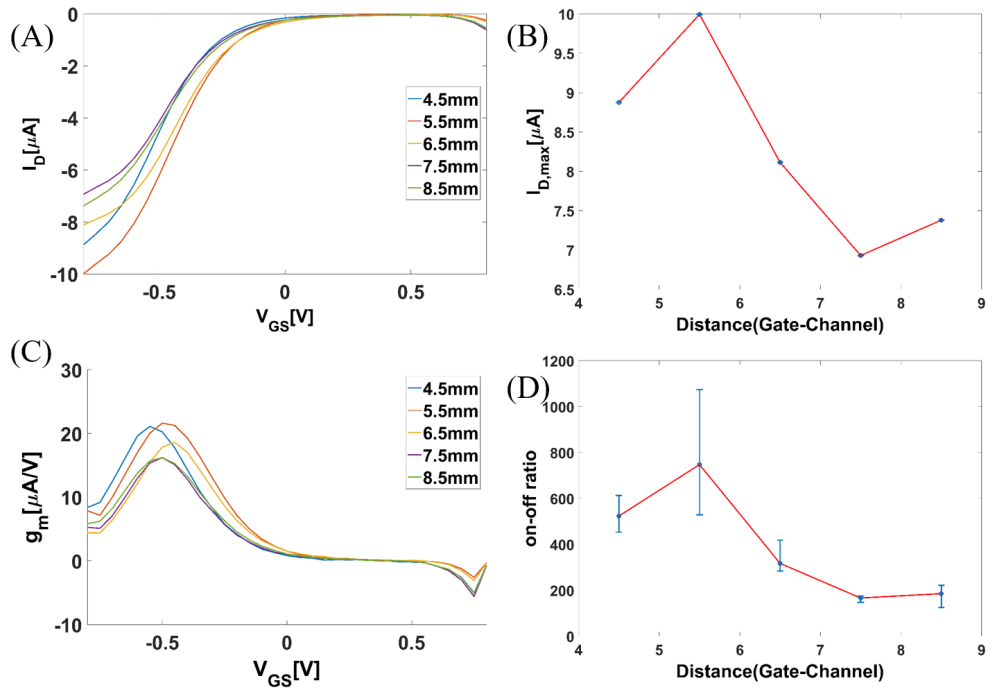

FIGURE 4.19: Characteristics for transistors which share the same channel but their equal area gate electrodes are placed at different distance from it. (A) Transfer curve (B) variation of maximum I_D with the distance between gate and channel, (C) transconductance vs V_{GS}, (D) variation of on-off ratio with distance between gate and channel.

For the second study on the dependence of transistor characteristics on varying distance between the gate electrode and the channel, equal area gate electrodes (2.5 mm^2) are placed at distances 4.5 mm, 5.5 mm, 6.5 mm, 7.5 mm and 8.5 mm away from the channel.

The image of the device is shown in Figure 4.17 (B). To achieve such a pattern the equal area gate electrodes are arranged on imaginary concentric circles around the channel. Figure 4.19 (A) shows the transfer curve for five devices which share the same channel, and the equal area gate electrodes are positioned at different distances from the channel. From 4.19 (B) there seems to be an overall decrease of current when the gate is placed far from the channel. However, the dependence of I_D on varying gate distance is not as clear as the dependence on varying gate electrode area. Double layer capacitance does not have a real dependence on the distance between the two electrodes, namely gate and channel. Hence, for equal area gate electrodes which are not equidistant from the channel, any change in the drain current cannot be attributed to change in double layer capacitance. However, another contribution of the electrolyte solution is the solution resistance (R_s) which scales linearly with the distance between gate electrode and the channel. Linear increase in R_s results in a linear increase in the transient time constant(τ = R_s * gate capacitance), which leads to an exponential decrease in the transient drain current, when the distance between gate electrode and the channel increases. However, experimental factors like the variation in the amount of electrolyte and the orientation of gate electrodes with respect to channel significantly affect the measurements. But, it can still be observed from Figure 4.19 that as the distance between the gate electrode and channel increases there is an overall decrease in the drain current (Figure 4.19 (B)), the transconductance (Figure 4.19 (C)) and the on-off ratio (Figure 4.19 (D)).

4.3.2 Nature of electrolyte

In section 4.2.2 dopamine sensors are measured for varying concentrations of dopamine in PBS buffer solution. The same kind of sensor is measured in dopamine solutions prepared in three different buffers MES (2-(N-morpholino)ethanesulfonic acid), HEPES (4-(2-Hydroxyethyl)piperazine-1-ethanesulfonic acid) and TRIS (tris-(hydroxymethyl)-aminomethane). Figure 4.20 shows the current versus concentration curve for dopamine sensors measured in all these buffer solutions. It is clearly seen that as the concentration of dopamine increases in the electrolyte solution there is an increase in drain current when dopamine solutions were prepared in PBS and MES buffer (Figure 4.20 (A) and (B)). However, when dopamine solutions are prepared in TRIS and HEPES buffer, the current decreases as the concentration of dopamine increases (Figure 4.20 (C) and (D)). This trend is consistent when measured over several devices.

To investigated the "unexpected" response of sensors to varying dopamine concentrations in HEPES and TRIS buffer, chemical structures of dopamine, TRIS, HEPES, and CPBA are shown in Figure 4.21. During dopamine sensing a boronate ester is formed and during the formation of this boronate ester three hydroxyl groups come together and a condensation reaction takes place. Looking at the chemical structure of HEPES and TRIS, it is clear that both the molecules have -OH groups such that an esterification

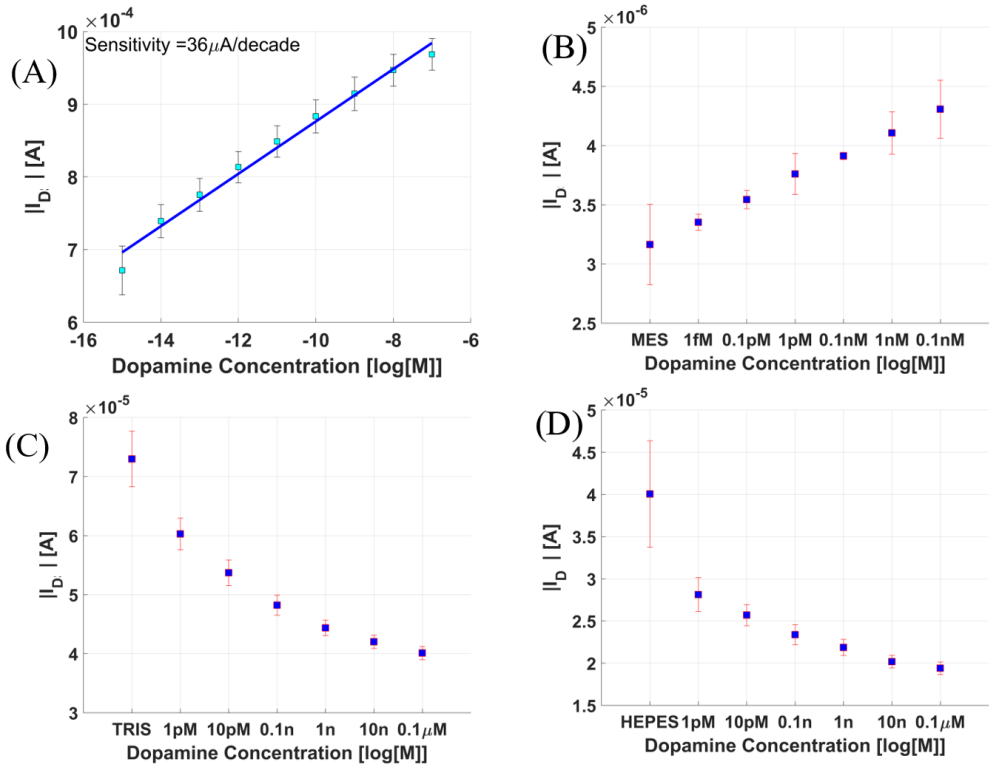

FIGURE 4.20: Current versus concentration curve for dopamine solutions prepare in (A) PBS, (B) MES, (C) TRIS and (D) HEPES buffer.

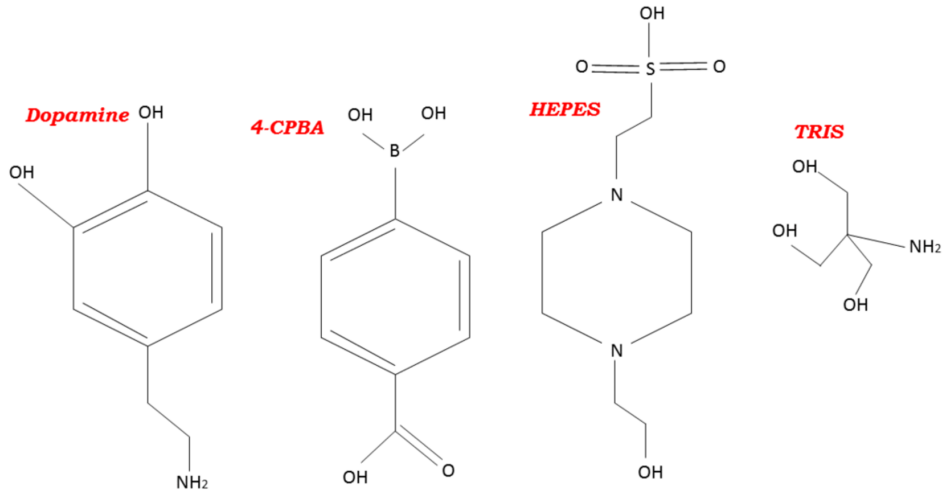

FIGURE 4.21: Chemical structure for dopamine, CPBA, TRIS, and HEPES.

reaction can also take place between these buffer molecules and CPBA, instead of CPBA and dopamine.

To confirm this, response of the dopamine sensor to varying concentrations of TRIS and HEPES in PBS buffer solution is measured as shown in Figure 4.22 (A) and (B) respectively. As the concentration of TRIS and HEPES increases there is an increase in

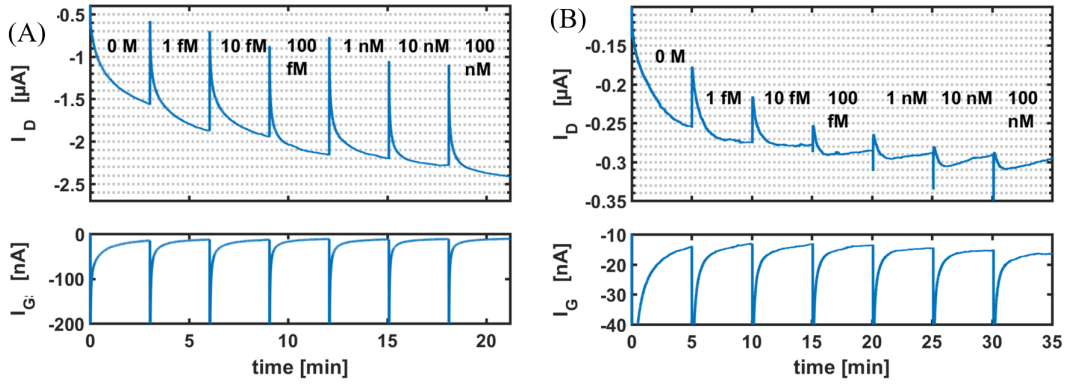

FIGURE 4.22: Real-time response of functionalized dopamine sensor to varying concentrations of (A) TRIS and (B) HEPES in 10 mM PBS with constant applied bias V_{DS}= -0.1 V and V_{GS}= -0.8 V.

the drain current. It is important to see that this is not a faradic current, as no change is seen in the gate current (I_G). These measurements clearly indicate that the HEPES and TRIS molecules interact with the functionalization (CPBA) and hence interfere with the normal operation of the sensor.

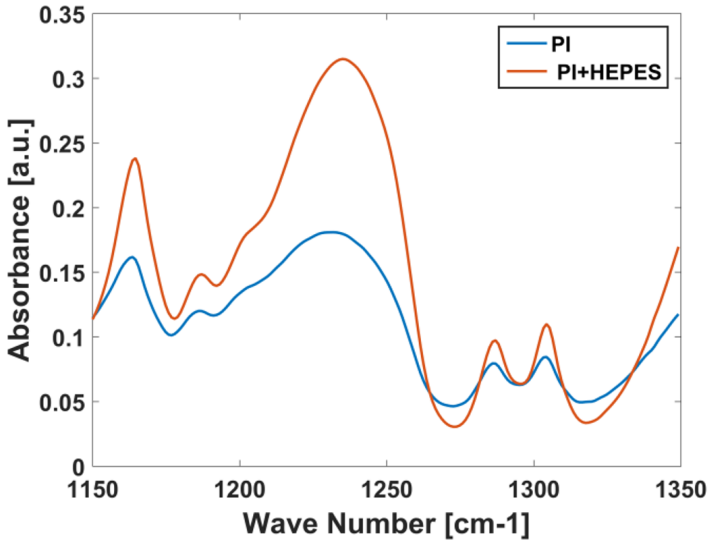

FIGURE 4.23: ATR-FTIR spectra of bare polyimide substrate (PI) and after a dopamine sensor on such a substrate is measured with HEPES solution (PI+HEPES).

The ATR-FTIR spectra of sensors after measuring them in varying concentration of HEPES (measurement shown in Figure 4.22 (B)) is recorded. Figure 4.23 compares such spectra with that of a bare polyimide kapton film (PI). An increase in the band just below 1250 cm^{-1} is seen, which originates mainly from the O=S=O vibration [178] and hence indicates that HEPES molecules have a tendency to bind to the functionalization.

4.4 Conclusion

In this chapter, sensing of biomolecules like glucose, lactate, neurotransmitters (for example, dopamine) and proteins is demonstrated using electrolyte gated field effect transistor. In principle, either of the substrate, gate or channel can be functionalized to impart selectivity to the sensor, however in this work we have focused on schemes where the semiconductor (channel) is untouched. It is also important to consider the negative impact of other device elements on the sensor response. We have found that such study is highly overlooked in the field of biosensors. The study on the geometry of in plane gate electrode and nature of electrolyte is a step in this direction.

Chapter 5

Using membrane in electrolyte gated devices

5.1 Ion selective membrane in field effect transistor

The idea of ion selective field effect transistor (ISFET) was proposed independently by Bergveld (1970) [179] and Matsuo et. al. (1971) [180]. In case of ISFETs an ion selective polymer membrane is placed over the gate/semiconductor of a transistor. A Nernst potential is developed similar to that in an ion selective polymer membrane discussed in detail in chapter 2. Figure 5.1 shows the results of real-time measurement of a CNTFET where the channel is covered with an ion-selective membrane selective to ammonium ions (NH_4+). Solutions of varying ammonium concentration are used for this measurement but after they are balanced by 1 M NaCl (sodium chloride) salt solution to have same conductivity. This ensures that the current response is only due to difference in ionic concentration and not due to difference in conductivity. These measurements are done after conditioning the device in 0.1M NH_4Cl solution for 24 hours. Conditioning helps to saturate the membrane. The calculated sensitivity of the sensor shown in Figure 5.1 is -0.11μA/decade.

The selectivity of such an ISFET is attributed to the presence of ionophores in the membrane. Ionophores or ion carriers are an important component of ion-selective membranes. They impart selectivity to an ion-selective electrode (ISE) or ISFET for a particular ion as it allows the selective passage of ions through the membrane and suppresses competition from interfering ions [181]. A large variety of ionophores enable selective sensing of various analytes, mostly towards a particular ion but sometimes also neutral species. The ion selectivity of ionophores and their electrometric effects on artificial thick membranes have provided the basis for ion-selective electrodes based on ionophore membranes [182]. Figure 5.2 shows the chemical structure of **Nonactin**, one of the most popular ionophores used in ammonium selective membranes. Apart from

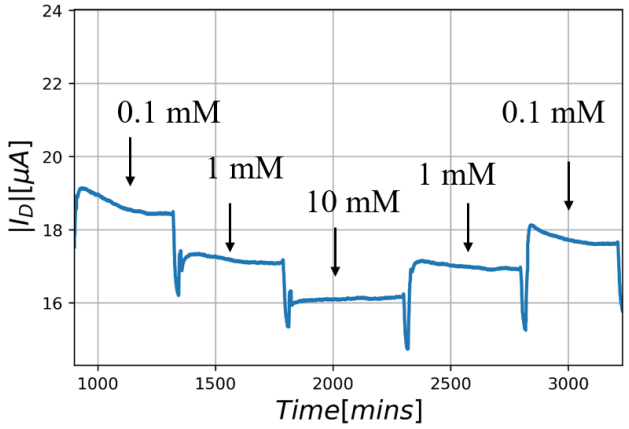

FIGURE 5.1: Real time measurement for NH_4+ selective CNT-ISFET. The gate to source voltage V_{GS} and drain to source voltage V_{DS} are fixed to -0.8 V.

ionophores an ion-selective membrane contains a base which is poly vinyl chloride (PVC) in this work and a plasticizer dioctyl sebacate (DOS). The final membrane suspension is prepared by mixing all the salts in tetra hydrofuran (THF).

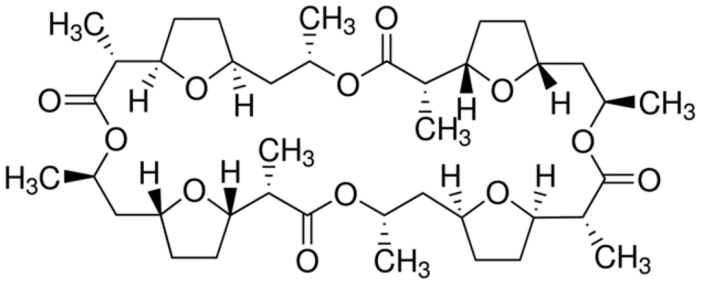

FIGURE 5.2: Chemical structure of ionophore nonactin used in NH_4+ selective membranes [12].

One of the other popular ion selective sensor is pH sensor, which is in fact the first ion sensor developed. An analysis of the pH sensor is inevitable as a preliminary characterization of the sensing platform. There are many biological processes that are triggered by a change in the acidity of their bio-environment or induced by local pH changes. It is therefore necessary to know the pH response of the sensor in order to extract the signals of the biological processes of interest [183]. Figure 5.3 shows the response of the H+-selective membrane placed on the CNTFET. The different pH solutions are prepared using universal buffer, hydrochloric acid (HCl) and sodium hydroxide (NaOH).

The calculated sensitivity of the sensor is -1.89 μA/decade in the increasing pH direction. During the course of this thesis, sensing capabilities of several novel transistor based devices is verified by pH sensing.

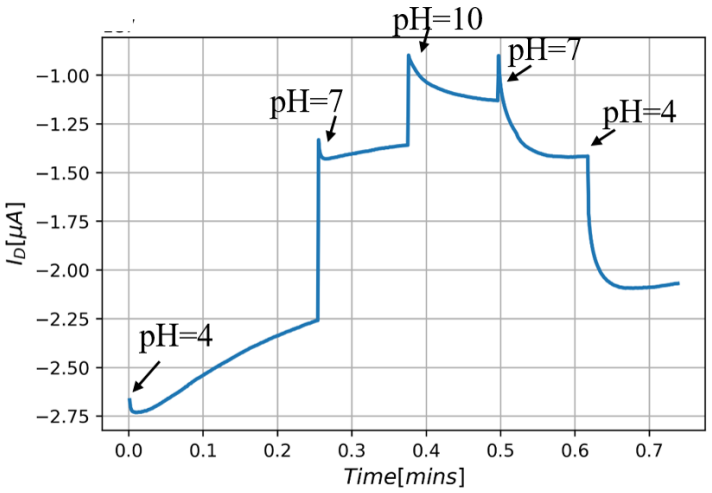

FIGURE 5.3: Real time measurement for H+ selective CNT-ISFET. The gate to source voltage V_{GS} and drain to source voltage V_{DS} are fixed to -0.8 V and -0.2 V respectively.

To explain the ISFET behavior, transistor current voltage relationship is rewritten in equation 5.1, where V_{FB} is the flat band voltage, Q_B is the depletion charge, C_{ox} is the oxide capacitance and ϕ_F is the fermi potential.

$$I_D = \mu * C_{ox} * \frac{W}{L} * (V_{GS} - V_{FB} + \frac{Q_B}{C_{ox}} - 2 * \phi_F - \frac{1}{2}V_{DS}) * V_{DS} \tag{5.1}$$

The flatband voltage (applied gate to source voltage that yields a flat energy band in the semiconductor) of an ISFET is given by equation 5.2 [33] where E_{ref} is the reference potential relative to vacuum, ψ_0 is the surface potential, χ_{sol} is the surface dipole potential of the solution, ϕ_S is the semiconductor work function, Q_{ss} is the surface state density at semiconductor surface and Q_{ox} is the fixed oxide charge.

$$V_{FB} = E_{ref} - \psi_0 + \chi_{sol} - \frac{\phi_S}{q} - \frac{Q_{ss} + Q_{ox}}{C_{ox}} \tag{5.2}$$

In the above equation all the terms except ψ_0 are constant and it is this term which makes the ISFET sensitive to ionic concentration. The dependence of ψ_0 on the concentration of ammonium ion (a_{NH4+}) is given by equation 5.3 [184] where α is the sensitivity factor, R is the gas constant, F is the farady constant and T is the temperature.

$$\Delta\psi_0 = 2.3\alpha\frac{RT}{F}\Delta log_{10}(a_{NH4+}) \tag{5.3}$$

From equations 5.1 to 5.3 it can be clear that as concentration of NH_4+ ion changes there is change in the surface potential of the ISFET, which in turn affects the flat band voltage. Flat band voltage, V_{FB} is related to the threshold voltage, V_{th} by equation 5.4 :

$$V_{th} = V_{FB} - \frac{Q_B}{C_{ox}} + 2 * \psi_F \tag{5.4}$$

This explains how change in concentration causes a change in the threshold voltage, which in turn leads to change in drain current.

Ion selective membranes are widely studied and have gained large popularity in their use in EGFETs. However, there is another class of membranes called lipophilic membranes which are not quite popular in the field of EGFETs. In the below section we demonstrate different ways in which such lipophilic membranes can be used to alter/enhance the electrolyte gated CNTFETs. The ion-selective and lipophilic membranes used in this work were received from our collaborators in University of Warsaw, Poland.

5.2 Lipophilic membrane in field effect transistor

In terms of their solubility, molecules can be divided into two categories namely hydrophilic and lipophilic. Hydrophilic molecules are those that are dissolved in water but not in lipid medium and lipophilic molecules are those that are dissolved in fats, oils, lipids, and non-polar solvents such as hexane or toluene [185]. In this section, membranes containing lipophilic ions are placed on the CNTFET and the variation in device characteristics are investigated. Variation in the composition of lipophilic membranes impart different unique characteristic to the electrolyte gated CNTFET. The lipophilic salt used in all membranes is Tetradodecylammonium tetrakis(4-chlorophenyl)borate also called ETH500. The chemical structure of this salt is given in Figure 5.4. This is a large molecule with very higher molecular weight cation and anion.

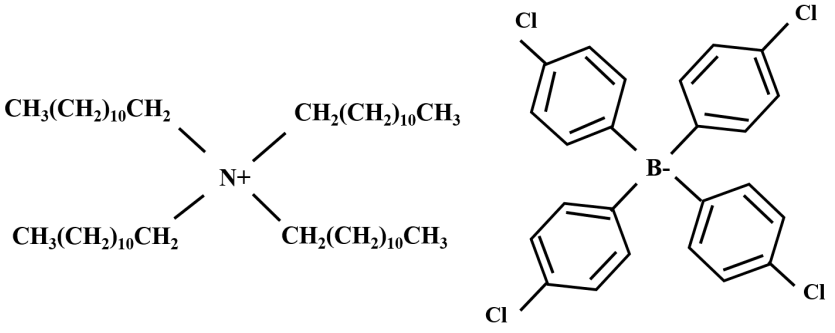

FIGURE 5.4: Chemical structure of lipophilic salt tetradodecylammonium tetrakis(4-chlorophenyl)borate [13].

5.2.1 Enhanced p-type CNTFET (Pure Lipophilic Membrane)

Electrolyte gated CNTFETs made from random network of carbon nanotubes have experienced significant progress, however there are still certain challenges that need to be addressed like high gate leakage current, hysteresis and low on-off ratio [186]. High gate leakage current in such electrolyte gated FETs is because of two main reasons, high parasitic capacitance, also called the overlap capacitance [187], and redox reaction occurring at the gold gate which gives rise to faradic current. Large leakage current degrades the transistor such that its switching speed is lowered and it consumes high power. High Hysteresis makes difficult to have reliable and energy-efficient system [186, 188]. Poor on-off ratio causes slow output transitions or low output swing while a higher on-off ratio is needed for better speed and lower leakage current [189].

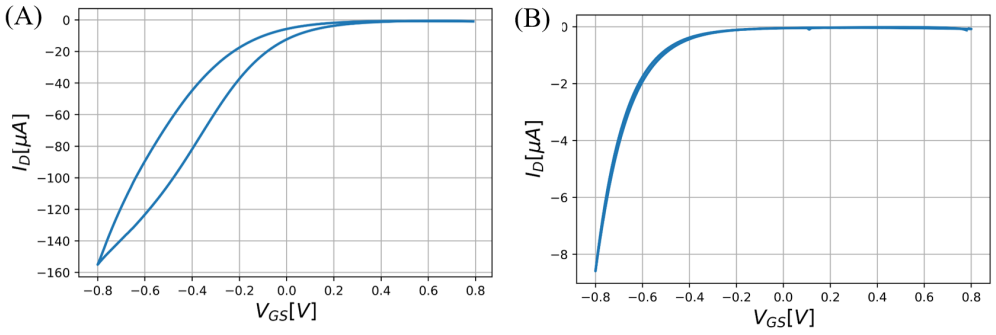

FIGURE 5.5: Transfer curve (A) before and (B) after, a pure lipophilic membrane is placed on the channel [14].

With the aim to improve these device characteristics, a poly-vinylchloride (PVC) membrane containing ETH500 and plasticizer dioctyl sebacate (DOS) in tetrahydrofuran (THF) is prepared and placed on the channel of the CNTFET. Figure 5.5 (A) and (B) show the transfer curve before and after the membrane is placed on the channel respectively. The gate to source voltage (V_{GS}) is swept from +0.8 V to -0.8 V and drain to source bias (V_{DS}) is -0.2 V. Few conclusions can be drawn by comparison of the two curves. After membrane deposition there is ten times reduction in the on-current of the transistor. In addition, there is more than two fold increment in the on-off ratio. The threshold voltage is extracted using ELR (Extrapolation in the linear region) [190] method. The extracted threshold voltage for the transistor before the membrane is placed on the channel is -0.39 V and the threshold voltage after membrane placement is -0.71 V [14].

From Figure 5.5 (A) and (B) one can also realize that there is decrease in the hysteresis after placing the membrane on the CNTFET. This is also confirmed by Figure 5.6 which shows hysteresis comparison of six devices before and after placing the membrane on the channel. Hysteresis also has dependence on the sweep rate. Sweep rate is defined as V_{step}/t_{step} where V_{step} is the magnitude of step in applied bias (V_{GS}) and t_{step} is

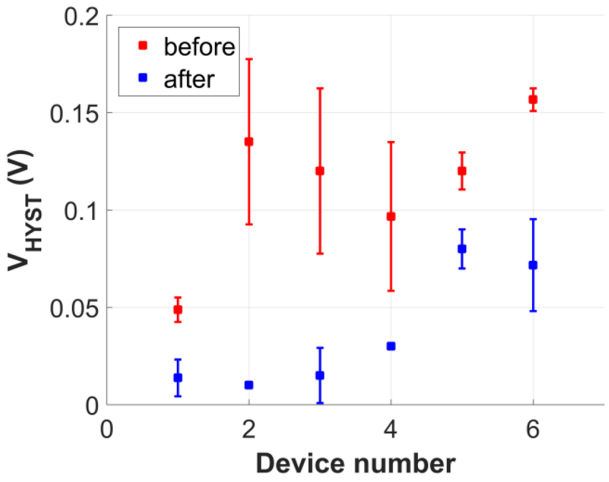

FIGURE 5.6: Statistical hysteresis comparison of six devices before and after membrane.

the time between such steps. Figure 5.7 shows the transfer curves before and after the membrane is placed on the channel for three different sweep rates.

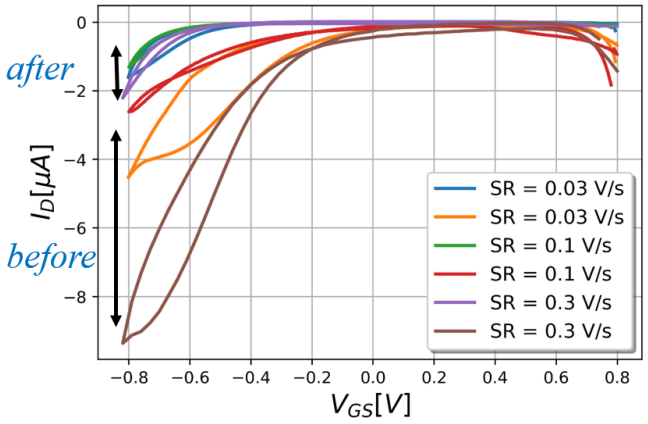

FIGURE 5.7: Transfer curve for a CNTFET before and after membrane is placed on the channel for three different sweep rates.

To study the impact of lipophilic membrane deposition on the gate, gate current versus V_{GS} before and after membrane is placed on the channel are recorded as shown in Figure 5.8. There is reduction of around two orders of magnitude in the gate leakage current after placing membrane on the channel.

A possible reasoning for the change in device characteristics of CNTFET is the property of lipophilic membranes that in contrast to ion-selective membranes they are completely polarizable. A pure lipophilic membrane, such as used here contains large ions that cannot be exchanged between the membrane and the electrolyte phase. Hence there is no faradic reaction at the gate electrode, therefore we see a significant reduction in the gate current.

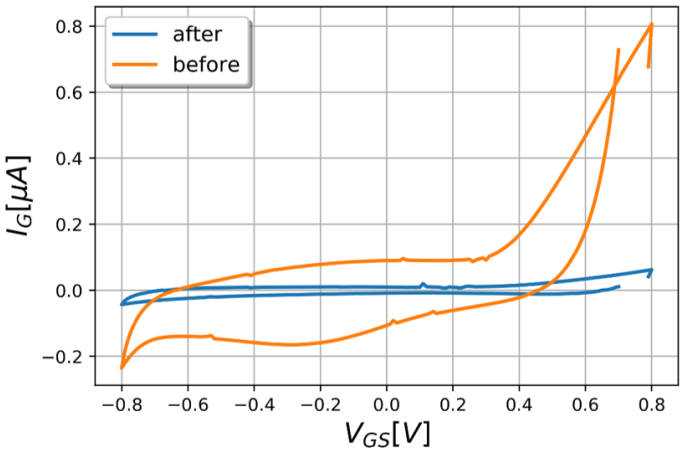

FIGURE 5.8: Gate current versus gate to source voltage (V_{GS}) for before and after membrane is placed on the channel of the transistor.

It is important that the improved p-type CNTFET keep its chemical sensing properties. To verify this, improved CNTFETs are used for pH sensing. Solutions of varying pH are exchanged on the membrane modified CNTFET and drain current is measured continuously. The gate to source voltage is fixed at -0.8 V and drain to source voltage is fixed at -0.2 V. Figure 5.9 (A) and (B) show that when going from higher pH to a lower pH the drain current decreases and can be recovered when going from a lower to higher pH (indicating absence of any degradation of the membrane during measurements). This response is similar to that observed in traditional electrolyte gated CNTFETs [191].

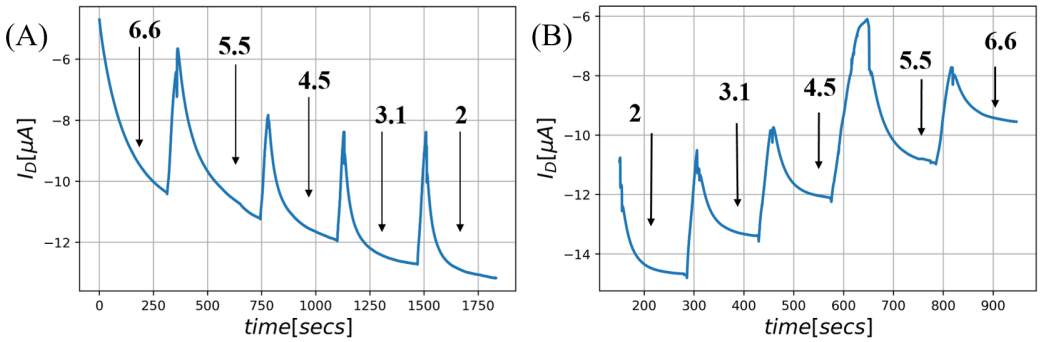

FIGURE 5.9: pH response for a pure lipophilic membrane with (A) decreasing pH from 6.6 to 2.0 and (B) increasing pH from 2 to 6.6. The applied voltages are fixed to V_{GS} = -0.8V and V_{DS} = -0.2V

This study clearly indicates that a pure lipohilic membrane can significantly enhance a CNTFET. There is significant increase in the on-current, decrease in the gate current, reduction in hysteresis and meanwhile the sensing capabilities of the device are preserved.

5.2.2 Ambipolar CNTFET (Lipophilic membrane + Ion-Exchangers)

In the previous section, it was stated that lipophilic membrane in itself cannot exchange ions with the solution and this property reduces the gate leakage current and hence improves the transistor performance. However when the membrane containing lipophilic salt contains additional cationic and anionic ion-exchanging salts, the p-type transistor characteristics change to ambipolar device characteristic. The salt that contains cationic ion-exchanger is potassium tetrakis(4-chlorophenyl)borate (KTChP) and one that contains anionic ion-exchanger is methyltridodecylammonium chloride (MDDA-Cl). Chemical structure of these molecules is shown in Figure 5.10.

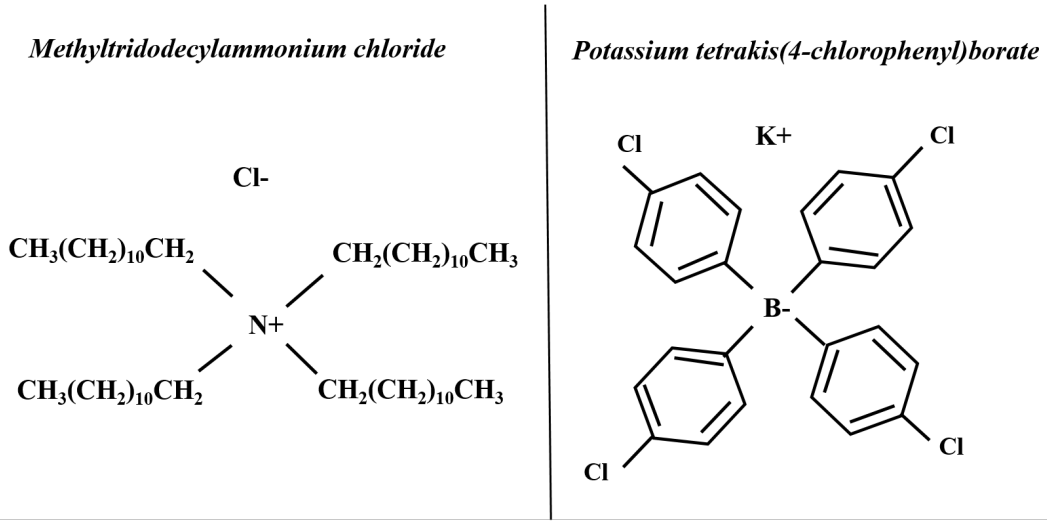

FIGURE 5.10: Chemical structure of methyltridodecylammonium chloride and potassium tetrakis(4-chlorophenyl)borate [15, 16].

These salts are chosen carefully such that KTChP has a smaller cation (K+) which can be exchanged with the solution but the large anion tetrakis(4-chlorophenyl)borate is same as that of ETH500. In the same way MDDA-Cl has a smaller anion (Cl-) but the large cation is methyltridodecylammonium same as ETH500. The difference in the device characteristics of the CNTFET due to the presence of these smaller ions K+ and Cl- at the membrane-solution interface can be understood by Figure 5.11. When such small ion containing membrane is placed on CNTFET, ion-exchange processes occur at membrane/solution and membrane/CNTs interfaces.

To understand better the impact of ion-exchangers in a lipophilic membrane potentiometric measurements are performed. Figure 5.12 shows these measurements for a pure lipophilic and a lipophilic membrane with ion-exchangers placed on a glassy carbon electrode in different concentrations of KCl solution. As already mentioned the theoretical Nernstian response is $\pm 59\,\mathrm{mV}$ / decade for cationic and anionic (ion-selective) membranes. For reference this theoretical Nernstian response is also added in Figure 5.12 (shown as solid lines). It is important to note that measured potentials are relative to $1\,\mu$M KCl solution. Few conclusions that can be made from Figure 5.12 are described in

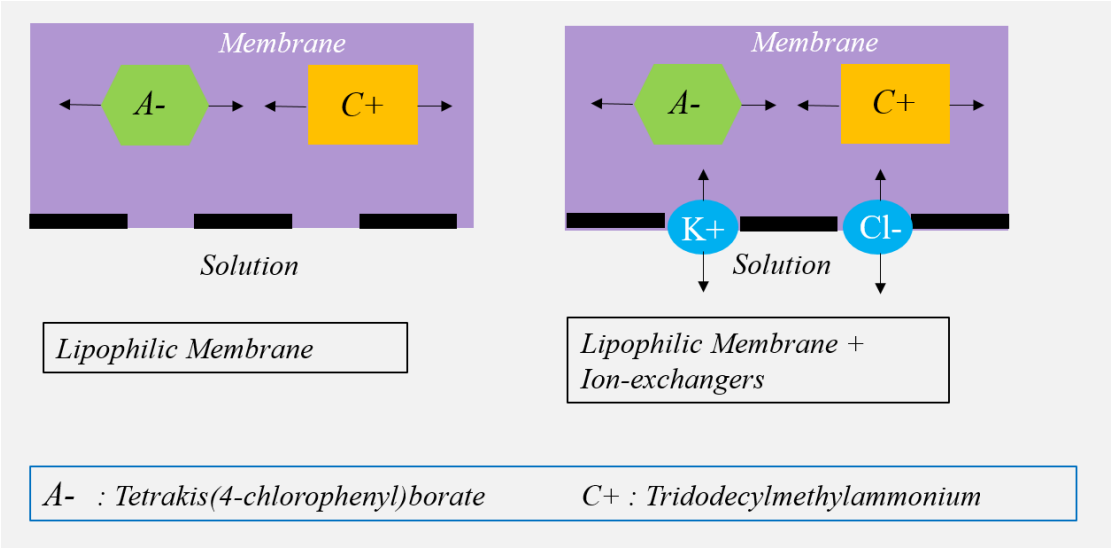

FIGURE 5.11: Ion-exchange processes at the membrane-electrolyte interface in the absence or presence of mobile ions.

following sentences. Both the lipophilic membranes exhibit much lower potentiometric slope than the theoretical Nernstian response. For KCl concentration of around 10 mM, the response of lipophilic membrane with ion-exchangers is higher than that of pure lipophilic membrane and this response is primarily cationic. This is because the exchange of potassium cation is easier than the chloride anion. However at high saturated KCl concentrations even the lipophilic membrane exchanges ions with the solution due to Donnan exclusion failure [192].

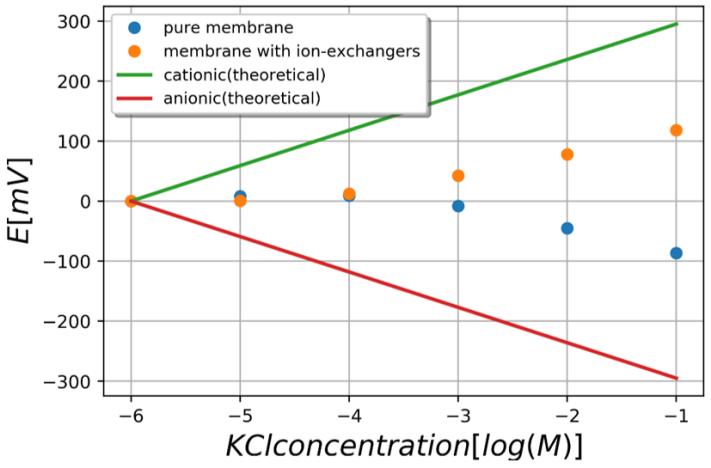

FIGURE 5.12: Potentiometric measurements performed on pure lipohilic and mobile ion containing lipophilic membrane for various KCl solution.

Further, electrochemical measurements are performed on both pure lipophilic and ion-exchanger containing lipophilic membrane. Two glassy carbon electrodes are covered with carbon nanotube and then pure lipohilic and ion-exchanger containing lipophilic

membrane are placed on them separately Electrochemical impedance spectroscopy measurements are carried out in 0.1 M KCl solution at an amplitude of 50 mV at a potential of 0.5 V, within the frequency range from 0.01 Hz to 10^5 Hz. Figure 5.13 shows the complex plane impedance plots obtained for both pure lipophilic and ion-exchanger containing lipophilic membrane.

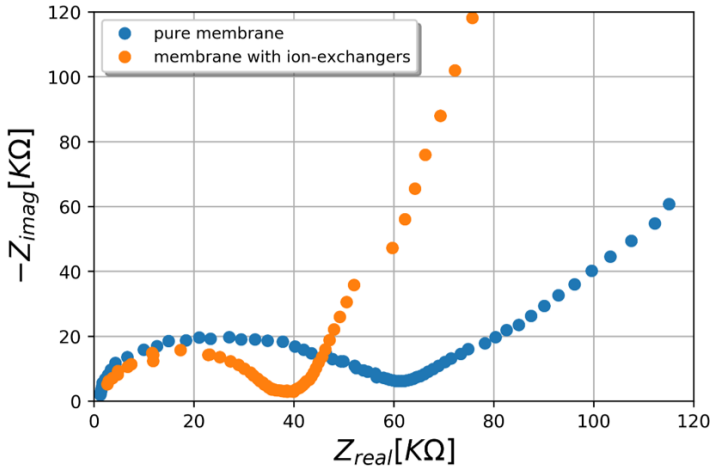

FIGURE 5.13: Impedance spectroscopy results of glassy carbon electrode coated with CNT and different lipophilic membranes measured at voltage 0.5 V.

A simplified Randles circuit shown in Figure 5.14(A) is used to describe the above measurements [17]. This circuit includes a solution resistance (R_S), a constant phase element which in simplified case can be represented as a double layer capacitance (C_{dl}), a charge transfer resistance (R_{ct}) and a diffusional resistance element (Warbung impedance W). The Nyquist plot for such Randles circuit is shown in Figure 5.14(B), which also indicates how the values of various model parameters can be extracted. Using Figure 5.14 as reference, the electrode impedance spectroscopy results shown in Figure 5.13 can be explained. Figure 5.13 indicates that the semi-circle for the pure lipophilic membrane is larger than the ion-exchanger containing lipophilic membrane. This is because in a pure lipophilic membrane, absence of mobile ions does not allow ion-exchange between membrane and solution and hence the charge resistance resistance is high, which is reflected in the Nyquist plot as a larger semicircle. This also gives rise to lower gate leakage current seen in Figure 5.8.

Figure 5.15 shows the transfer curve for a CNTFET before and after ion-exchanger containing lipophilic membrane is placed on the channel of the CNTFET. As with a pure lipophilic membrane there is decrease in the on-current. To understand in detail the effect of the presence of the ion-exchanger, the transfer curve after placing membrane on the channel is added in the inset of Figure 5.15. The membrane modified CNTFET shows an ambipolar response with on-currents being in the same order of magnitude for both positive and negative voltages. However, the value of on-current for the negative

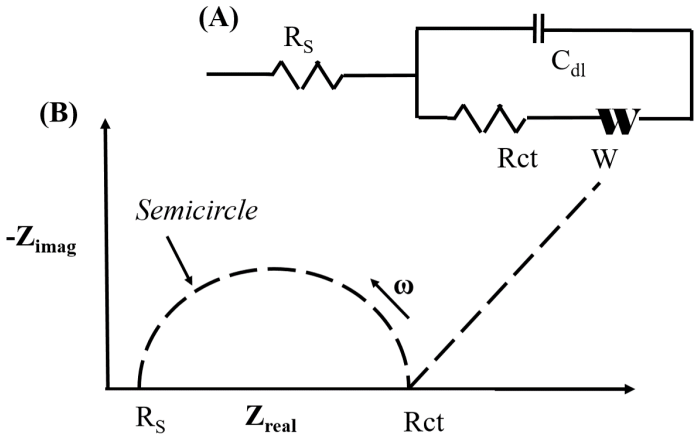

FIGURE 5.14: (A) Randles circuit and (B) real versus imaginary part of impedance plot [17].

voltage is higher than the positive voltage. The on-off ratio in the negative gate voltages show four fold increment and on-off ratio in the positive voltage show two fold increment than the bare unmodified p-type CNTFET.

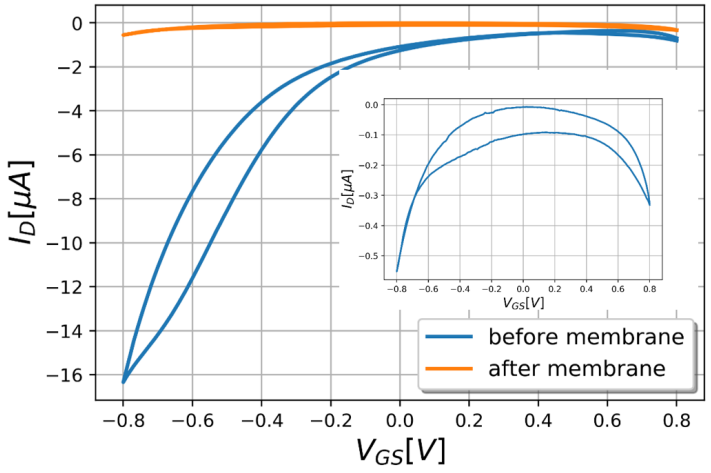

FIGURE 5.15: Transfer curve before and after ion-exchanger containing lipophilic membrane is placed on the channel of the CNTFET. In the inset, transfer curve after membrane is shown [14].

Figure 5.16 shows the gate currents before and after placing the ion exchanger containing lipophilic membrane on the channel of a p-type CNTFET. As seen there is not much improvement in the gate currents. This is because the mobile ions present in the membrane allow ion-exchange between the membrane and solution, hence faradic processes are not stopped.

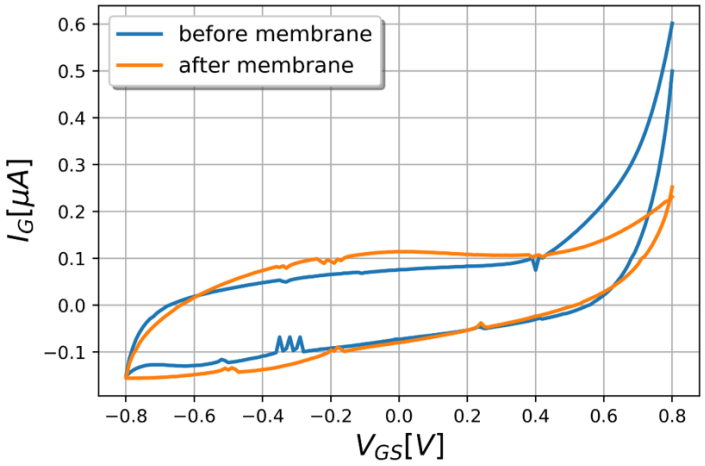

FIGURE 5.16: Gate currents before and after ion-exchanger containing lipophilic membrane is placed on the channel of the CNTFET [14].

5.2.3 n-type CNTFET (Lipophilic membrane + Anion Ion-Exchangers)

In attempt to fabricate n-type CNTFET, experiments have been conducted that involve removal of adsorbed oxygen by annealing [193, 194] but n-type CNTFETs fabricated by such annealing process turn to p-type after oxygen exposure. To solve this problem, the CNTs can be doped with electron donor materials [195] and then a passivation layer can be applied [196]. In such a way air-stable n-type CNTFETs have been achieved, but for electrolyte gated systems, water stability of n-type CNTFETs is a strict requirement. It is observed that use of lipophilic membrane made of ETH500 with only anionic ion-exchanger MDDA-Cl can be used to fabricate water-stable n-type CNTFETs.

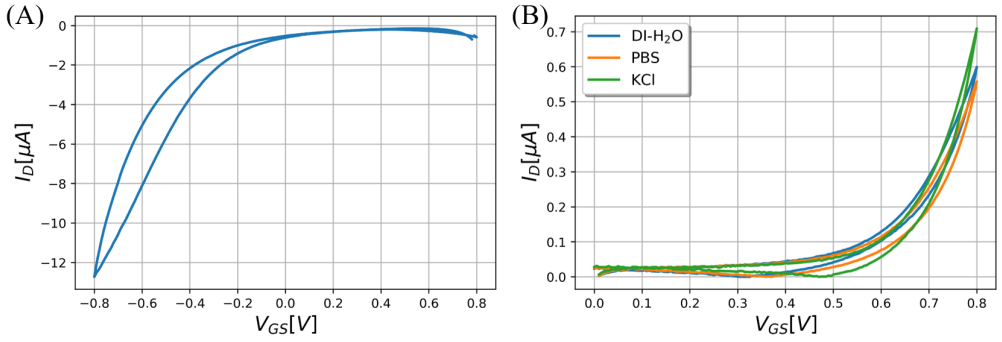

FIGURE 5.17: (A) Transfer curve for p-type CNTFET when V_{GS} is swept from +0.8 V to -0.8 V and V_{DS} is fixed to -0.2V. (B) Transfer curve for n-type CNTFET when V_{GS} is swept from 0 V to +0.8 V and V_{DS} is fixed to -0.2V.

Figure 5.17 (A) shows the transfer curve for the p-type CNTFET and Figure 5.17 (B) shows the transfer curve for the n-type CNTFET prepared after anion ion-exchanger

containing lipophilic membrane is placed on the channel of same p-type CNTFET. Figure 5.17 (B) also contains transfer curve when the n-type CNTFET is measured in DI-H_2O and KCl in addition to PBS. The peak drain current for KCl as gate electrolyte is largest because the mobile chloride (Cl-) ions that are incorporated from MDDA-Cl have easy exchange with Cl- ions of the solution (KCl) at membrane/electrolyte interface.

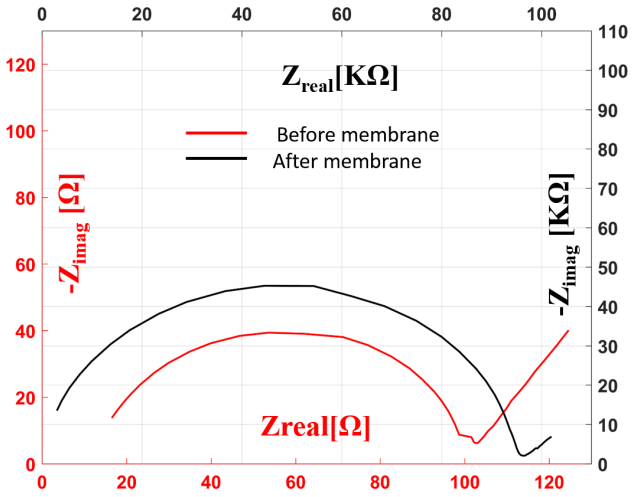

FIGURE 5.18: Electrode impedance spectroscopy results before and after ion-exchanger containing lipophilic membrane is placed on the channel of CNTFET.

Similar to the other variations of lipophilic membranes, there is decrease in drain current after placing the membrane on the channel of the CNTFET. This is because of two main reasons namely increased source-drain resistance and lower gate-to-channel capacitance. There is almost two orders of magnitude increase in source-drain resistance after placing membrane on the channel. The capacitance between gate to channel decreases because of the introduction of additional capacitance of the membrane as shown in equation 5.5 where C_{eff} is the effective gate to channel capacitance, C_{mem} is the capacitance introduced by the membrane and C_{dl} is the double layer capacitance [187].

$$\frac{1}{C_{eff}} = \frac{1}{C_{mem}} + \frac{1}{C_{dl}} \tag{5.5}$$

To investigate the change of impedance in detail, electrode impedance spectroscopy is conducted before and after placing membrane on the CNTFET, and complex plane impedance plots for both conditions are shown in Figure 5.18. These measurements are carried out in a glassy carbon electrode covered with carbon nanotube in 0.1 M KCl solution using signal of amplitude 50 mV at a potential of 0.5 V. The capacitance is computed at the point where the condition ω * R * C = 1. As seen from Figure 5.18 there is three orders of magnitude decrease in the gate to source capacitance after placing the membrane on the channel.

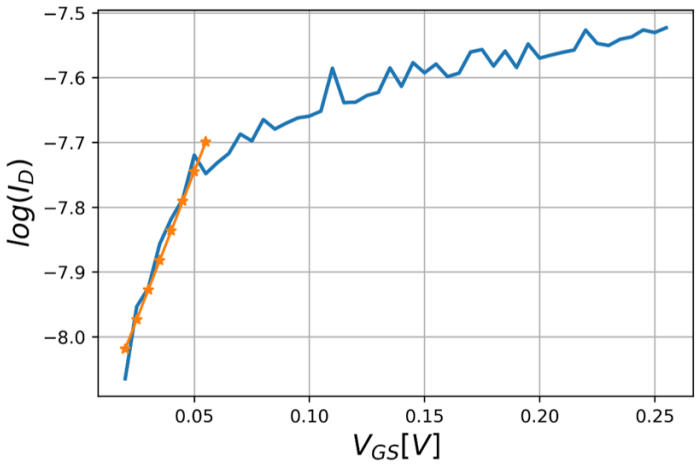

FIGURE 5.19: Logarithmic plot of drain current in the subthreshold region and linear fitting to extract the subthreshold slope (SS). SS = 88 mV/decade.

It is important to realize that the reduced drain current of the n-type CNTFET does not have a negative impact on other transistor characteristics. In reality, there is two fold improvement in the on-off ratio of the CNTFET after it is converted from p-type to n-type. Device characteristics are extracted to evaluate the performance of the n-type CNTFET and the on-off ratio is 200, maximum transconductance ($g_{m,max}$) is 0.1 mS and threshold voltage (V_{th}) is 0.25 V. Figure 5.19 shows the semi log plot of the drain current versus gate to source voltage. The subthreshold slope (SS) extracted from this curve is 88 mV/decade.

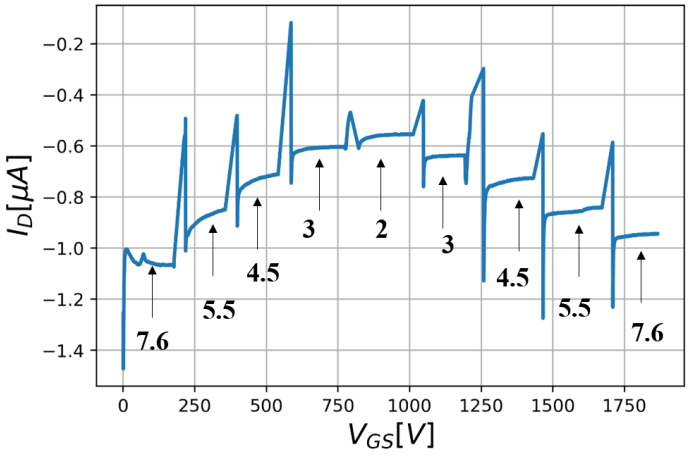

FIGURE 5.20: pH response for a n-type CNTFET[18].

This conversion from p-type to n-type is of relevance only if the intrinsic sensing capabilities of CNTFETs are not lost. To verify the use of n-type CNTFETs as sensors, pH response is measured. For these measurements, solutions of varying pH are prepared from pH = 2 to 7.6 and gate to source voltage V_{GS} and drain to source voltage V_{DS} are

fixed to -0.8V and -0.2V respectively. The results of these measurement is shown in Figure 5.20 where the drain current decreases for decreasing pH. This trend is expected and opposite to that seen for a p-type CNTFET where the current increases with decreasing pH [18]. The sensitivity of the n-type pH sensor is around -0.935 μA/decade for decreasing pH, which is in the same order of magnitude as that for an unmodified p-type CNTFET.

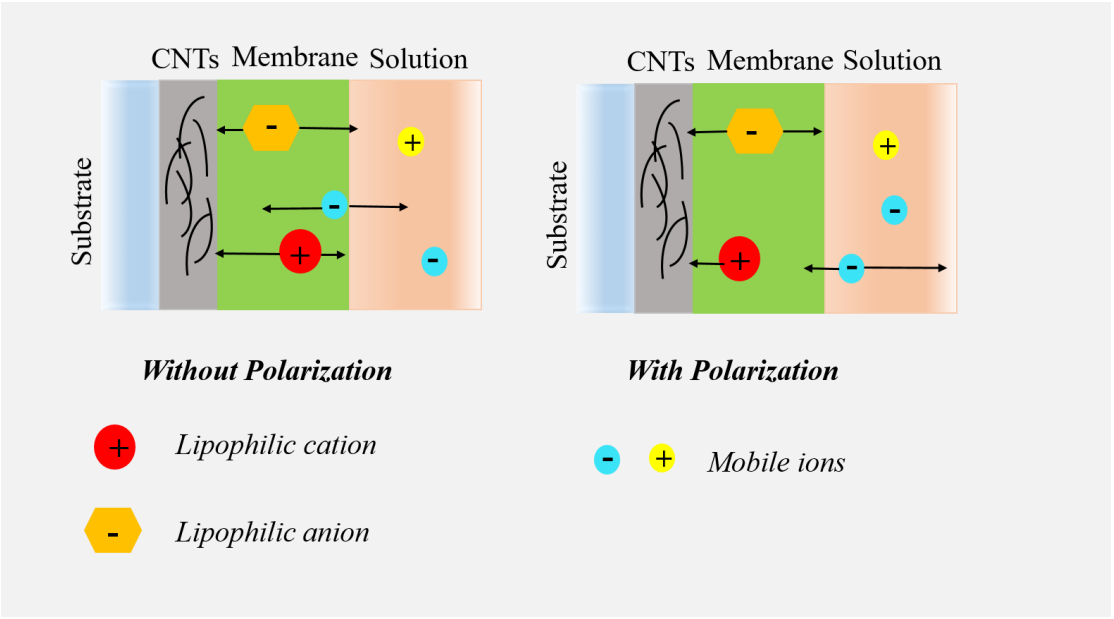

FIGURE 5.21: Schematic representation of the ion movement under bias conditions that lead to a n-type response of the CNTFETs.

A possible reasoning for the conversion of a p-type CNTFET to a n-type CNTFET is explained in this paragraph. The n-type FET turns on for positive gate to source voltage and in this condition, there is negative polarization of the membrane placed on the channel. This membrane contains immobile cation (tridodecylmethylammonium) and anion (tetrakis(4-chlorophenyl)borate) from ETH500, and MDDA-Cl adds extra immobile cation (tridodecylmethylammonium) and mobile chloride ions. Under the condition of negative charge on the membrane, the mobile chloride ions are expelled to the solution which in turn leads to a temporary positive charging of the membrane. This causes negative charges to be developed on the random CNT network underneath and hence the CNTFET behaves as n-type. There is also movement of the lipophilic cation (tridodecylmethylammonium) closer to the CNT network. Figure 5.21 is a schematic drawing of this reasoning.

Experiments to prove this theory are conducted in a system containing a flourescent lipophilic cation. Rhodamine B octadecyl ester perchlorate (RBOE-ClO4) is a lipophilic salt and its cation RBOE has the ability to emit different intensity fluorescence signals depending on its surrounding environment. These experiments performed on a glassy carbon electrode are based on the knowledge that when this cation moves from the membrane-solution interface towards the CNT-membrane interface, the fluorescence

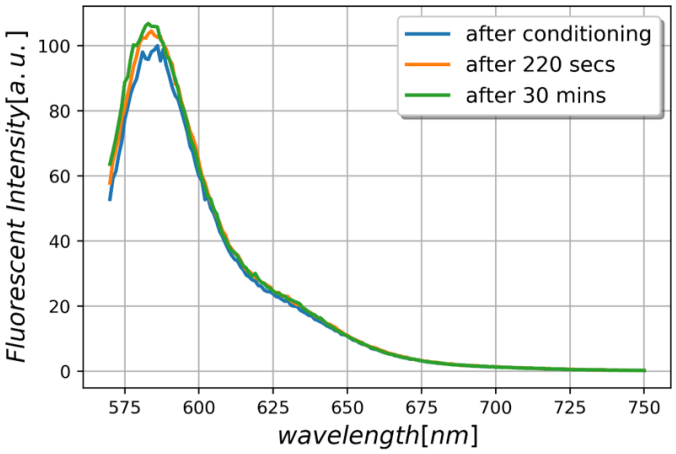

FIGURE 5.22: Emission spectra indicating absence of change in lipophilicity in the membrane.

signal intensity is supposed to increase due to an increase in the lipophilicity of the environment [197]. Figure 5.22 shows the emission spectrum when no polarization is applied on the membrane. The three curves indicate the three different times emission spectra was recorded, immediately after conditioning the electrode in KCl solution, after 220 seconds and after 30 minutes. In Figure 5.22 emission spectra does not change much with time.

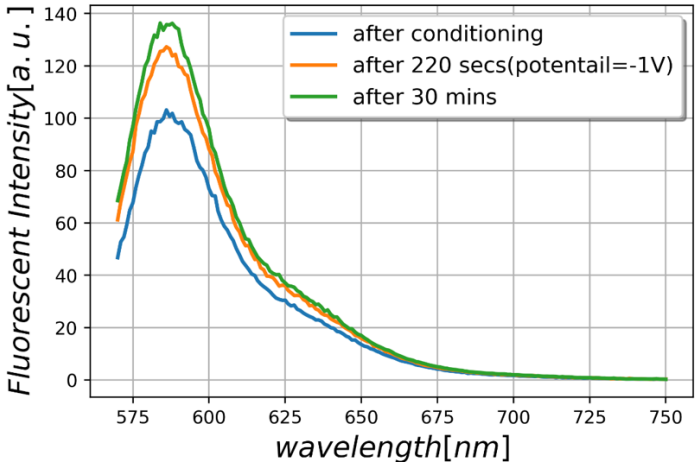

FIGURE 5.23: Emission spectra indicating movement of lipophilic cation in the membrane under negative potential.

But when a negative polarization potential is applied on the membrane there is a clear difference between the three spectra as shown in Figure 5.23. There is a large increase in the fluorescence intensity after the electric potential of -1 V is turned on. This is because under negative polarization the fluorescent cation moves from the membrane/electrolyte

interface towards the more lipophilic bulk. The increase in the lipophilicity of the surroundings give rise to the increase fluorescence.

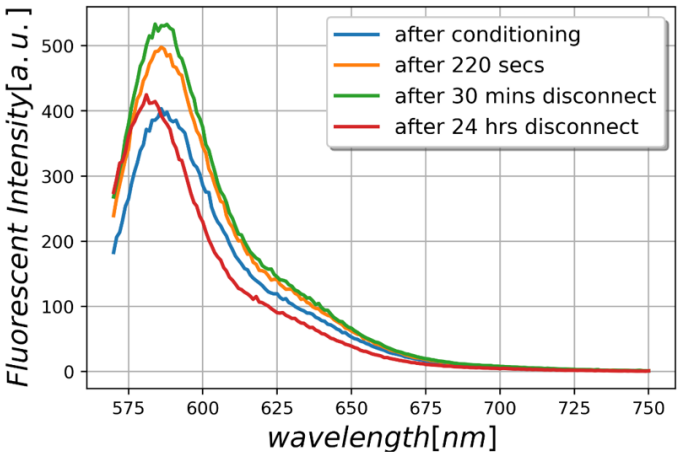

FIGURE 5.24: Emission spectra indicating movement of lipophilic cation in the membrane after negative potential is disconnected.

It is important to note that this effect of ion-movement is reversible, thus when the negative polarization is removed a decrease in the emission is observed as shown in Figure 5.24. However, even after removing the electric signal some increase in emission spectra is observed - as the reorganization of the system requires time. But after twenty four hours a significant restoration of the initial state is achieved [198].

So far we have seen the use of membranes in EGFETs for sensing (ion-selective membranes) and for improving transistor characteristics (lipophilic membrane). Improved transistors have proven to work as good sensors as well. Another way to improve sensing is to use multiple transistors in an amplifying circuit. A simplest configuration of such a circuit with one or two transistors is an inverter. Before demonstrating sensing using inverter, a theoretical overview of logic inverter is presented in below section.

5.3 Inverter : Theory

5.3.1 pMOS-only inverter

The major part of thesis involves CNT as the active semiconductor. As, CNTs are p-type semiconductors in ambient, it becomes necessary to study a pMOS-only inverter. A pMOS only inverter is made using only p-type transistors. The configurations for a pMOS only inverter used in this work is shown in Figure 5.25. P_D and P_L indicate the specific p-type FET working as driver and load respectively [199]. V_I is the input voltage, V_O is the output voltage and V_{DD} is the applied bias.

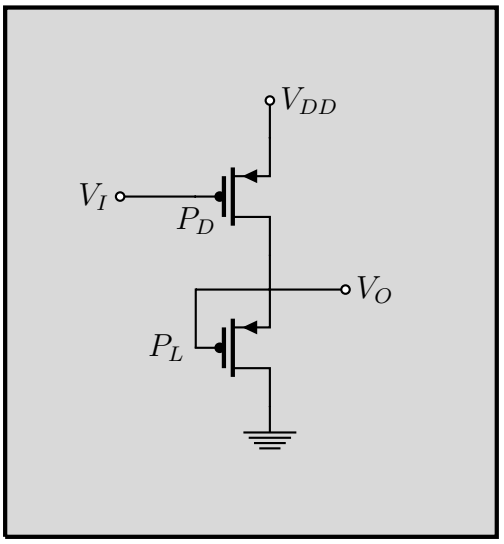

FIGURE 5.25: Inverter configuration with active pMOS load and driver.

In Figure 5.25 the gate of the load transistor is connected to the source, or gate is shorted with the source. To analyze this configuration we consider two cases: (i) input voltage is high and (ii) input voltage is low. For the analysis V_{DD} is assumed to be 0.8V as that is the maximum bias supported in aqueous-electrolyte gated FETs. When the input is low, the gate to source bias for the driver p-type FET (P_D) is -0.8 V and thus the P_D is turned on. In effect this transistors offers very low resistance for current flow from source to drain. This low resistance is called R_{ON}. The expression for V_O can be written by equations 5.6 and 5.7 :

$$V_{DD} - V_O = I_D * R_{ON} \tag{5.6}$$

$$V_O = V_{DD} - (I_D * R_{ON}) \tag{5.7}$$

On the other hand, for the load p-type FET (P_L) the gate to source bias is low and hence it is off. Thus, essentially no current flows through P_L which means it offers a large resistance R_{OFF}. The expression for V_O calculated using P_L can be written by equations 5.8 and 5.9 :

$$V_O = I_D * R_{OFF} \tag{5.8}$$

$$I_D = \frac{V_O}{R_{OFF}} \tag{5.9}$$

Using equations 5.7 and 5.9, V_O can be given by equation 5.10, which simplifies to equation 5.11. As R_{OFF} is large, V_O in case when input is small turns out to be approximately equal to V_{DD}.

$$V_O = V_{DD} - V_O * \frac{R_{ON}}{R_{OFF}} \tag{5.10}$$

$$V_O = V_{DD} * \frac{R_{OFF}}{(R_{OFF} + R_{ON})} \tag{5.11}$$

In case when the input voltage (V_I) is high around 0.8 V the gate to source bias for the driver p-type FET is low around 0 V. This leads to an off state of driver FET and drain current through it is equal to zero. Thus, the driver is in high resistance state of value R_{OFF}. The current-voltage equations for the driver p-type FET in this case can be written as equations 5.12 and 5.13.

$$V_{DD} - V_O = I_D * R_{OFF} \tag{5.12}$$

$$V_O = V_{DD} - I_D * R_{OFF} \tag{5.13}$$

The state of load p-type FET does not change with the change in input voltage and it is still off and offers a large resistance R_{OFF} to current. Hence, equations 5.8 and 5.9 still hold true. So, in case of low input voltage the output voltage can be written as 5.14.

$$V_O = V_{DD} - V_O * \frac{R_{OFF}}{R_{OFF}} \tag{5.14}$$

After simplification, it can be seen that V_O in case of high input voltage is half of V_{DD}.

$$V_O = \frac{V_{DD}}{2} \tag{5.15}$$

5.3.2 nMOS only inverter : Resistor loaded configuration

Similar to a pMOS only logic, there is an nMOS only logic where n-type transistors are used to make logic gates and other digital circuits. Figure 5.26 shows the schematic of a resistive loaded nMOS logic inverter. There is a voltage source V_{DD} which connects to the drain of the nMOS transistor through a resistor R_D. The source of the nMOS is connected to ground and the gate is connected to the input signal V_I.

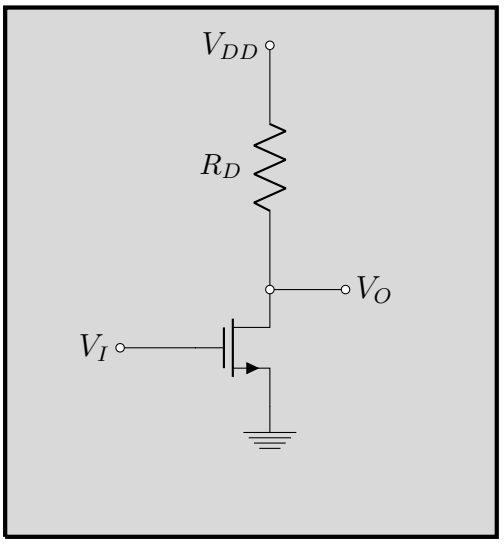

FIGURE 5.26: Circuit Diagram of a nMOS inverter

As the input signal V_I varies, different regions of the nMOS are explored which determine the value of the output signal V_O. The transistor characteristics and load line are shown in Figure 5.27, along with the parametric curve separating the saturation and nonsaturation regions. The voltage transfer characteristics of the inverter are determined by examining the various regions in which the transistor can be biased.

Cut-off Region

When the input voltage V_I is less than or equal to the threshold, i.e. $(V_I \leq V_{th})$, the transistor is cut off and the drain current i.e., $I_D = 0$. The output signal in this region is given by equation 5.16

$$V_O = V_{DD} \tag{5.16}$$

This point in the cut off region of the transistor is marked in Figure 5.27 by red arrow.

Saturation Region

As the input signal is increased slightly above the threshold voltage, the transistor turns on and is biased in the saturation region. The output voltage is given by equation 5.17 where the current (I_D) is given by equation 5.18.

$$V_O = V_{DD} - I_D * R_D \tag{5.17}$$

$$I_D = k_n * (V_{GS} - V_{th})^2 = k_n * (V_I - V_{th})^2 \tag{5.18}$$

Combining equation 5.17 and 5.18 forms the relation between input voltage V_I and output voltage V_O given by equation 5.19. This region is marked by a green color arrow in Figure 5.27.

$$V_O = V_{DD} - k_n * R_D * (V_I - V_{th})^2 \tag{5.19}$$

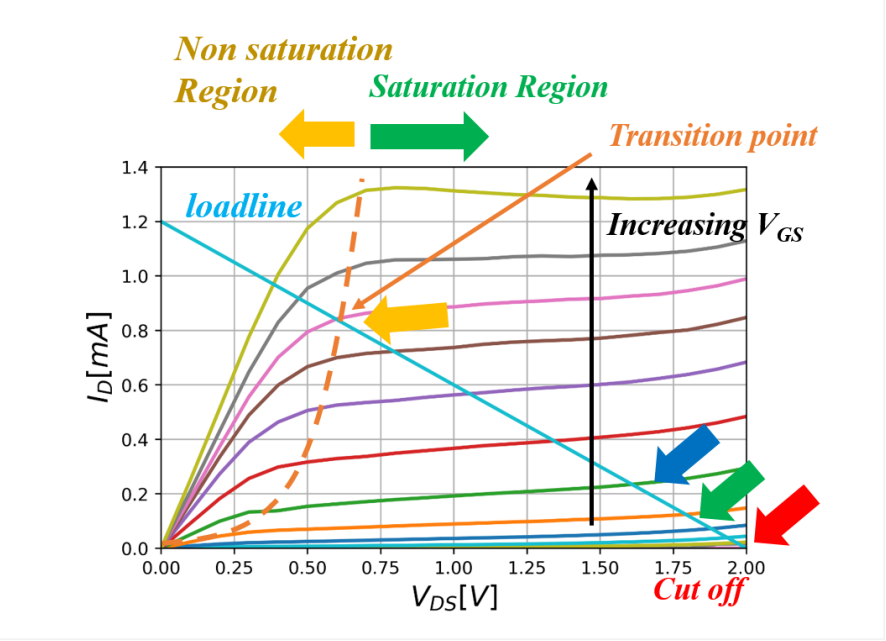

FIGURE 5.27: Transistor characteristics for the nMOS and the load line.

Transition Region

As the input voltage is further increased and the voltage drop across the R_D becomes sufficient to reduce the V_{DS} such that $V_{DS} \leq V_{GS}$ - V_{th}, the Q-point (operating point) of the transistor moves up the load line as marked by blue arrow in Figure 5.27. The drain to source voltage V_{Ot} at the transition point in terms of gate to source voltage V_{It} is given by equation 5.20.

$$V_{Ot} = V_{It} - V_{th} \tag{5.20}$$

Using equation 5.19 and equation 5.20, relation 5.21 is achieved.

$$k_n * R_D * (V_{It} - V_{th})^2 + (V_{It} - V_{th}) - V_{DD} = 0 \tag{5.21}$$

Non-Saturation Region

As the input voltage becomes greater than V_{It}, the transistor becomes biased in the nonsaturation region. The drain current is then given by equation 5.22 (also shown in terms of input and output signal).

$$I_D = k_n * [2 * (V_{GS} - V_{th}) * V_{DS} - V_{DS}^2] = k_n * [2 * (V_I - V_{th}) * V_O - V_O^2] \quad (5.22)$$

Using equation 5.17 and equation 5.22, relation between input and output is established. This region is marked by a yellow color arrow in Figure 5.27.

$$V_O = V_{DD} - k_n * R_D[2 * (V_I - V_{th}) * V_O - V_O^2] \quad (5.23)$$

5.3.3 CMOS inverter

As presented above it is possible to get the inverting behavior by pMOS-only or nMOS-only logic. However, a complementary MOS configuration utilizes the best of both pMOS and nMOS systems. Figure 5.28 shows the circuit diagram for a CMOS inverter. It is made by series combination of a pMOS- and nMOS transistors. The gates of the two transistors are connected together to form the input and the two drains are connected together to form the output.

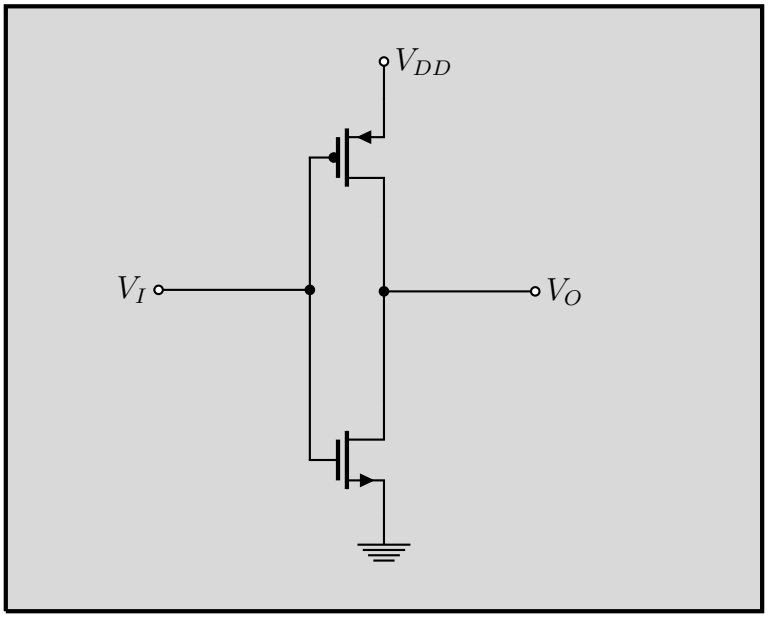

FIGURE 5.28: Circuit Diagram of a CMOS inverter

The operation of such a gate can be understood easily by the help of switch model of MOS transistors. When the input signal V_I is high and equal to V_{DD}, the nMOS transistor is on, while the pMOS is off. The equivalent circuit in this condition is shown in Figure 5.29 (A). There is a direct path between the output V_O and the ground while there is no direct path between V_O and V_{DD}. This causes a value of 0 at V_O. On the other hand, when V_I is low and equal to 0 V, nMOS and pMOS transistors are off and on, respectively. The equivalent circuit of Figure 5.29 (B) shows that a direct path exists

between V_{DD} and V_O but the path between ground and V_O is disconnected. This yields a high output signal. Thus, it clearly works as a logic inverter [19].

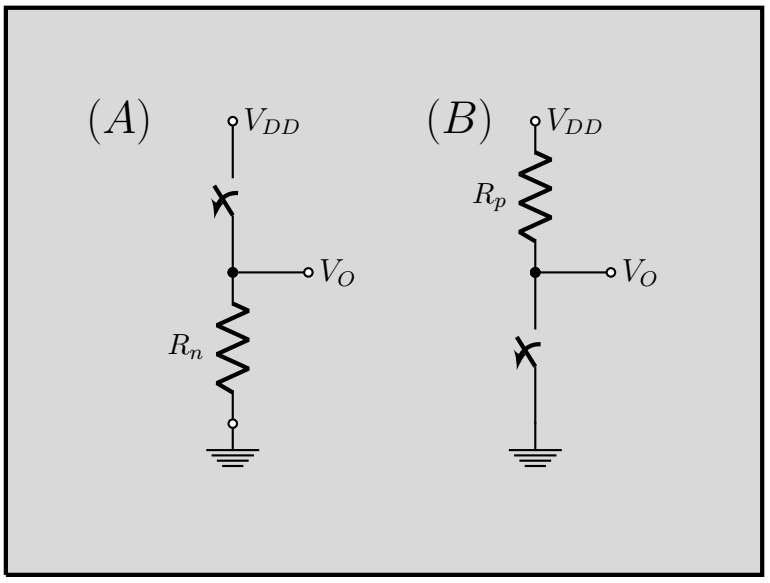

FIGURE 5.29: Switch model for (A) high input and (B) low input.

To extract the voltage transfer characteristics of a CMOS inverter the current characteristics of a pMOS and nMOS transistor are superimposed on each other. Such a curve is traditionally called a load-line plot. It requires that the I-V curves of the nMOS and pMOS devices are transformed onto a common coordinate set. An example plot is shown in Figure 5.30.

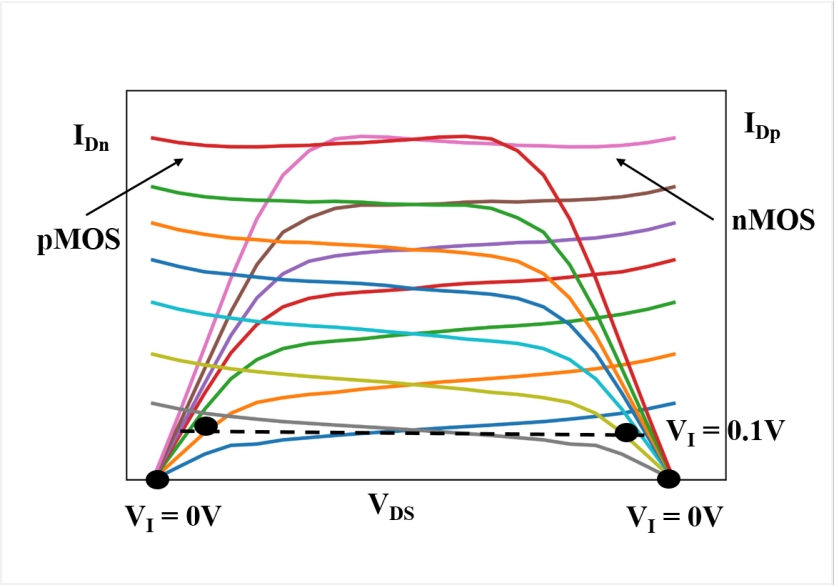

FIGURE 5.30: Loadline curves for nMOS and pMOS transistors of the CMOS inverter, adapted form [19]. The dots indicate operating point (input voltages) for the inverter.

It is important to note here that the dc points are only valid where the currents of both nMOS and pMOS transistors are equal. This translates to physically meaning that

the dc points must be on the intersection of pMOS and nMOS transfer curves. Some of such points are marked on Figure 5.30 and it is very evident that the operating points lie either on the high or low output levels. This imparts a very narrow transition zone to the voltage transfer characteristics and results in high gain when the input signal transitions from a low input to high input. It is important to realize that at this transition point both the nMOS and pMOS are simultaneously on and are in saturation. Thus, in this transition region, a small change in the input voltage results in a large output change. The above explanation leads to the voltage transfer characteristics shown in Figure 5.31[19].

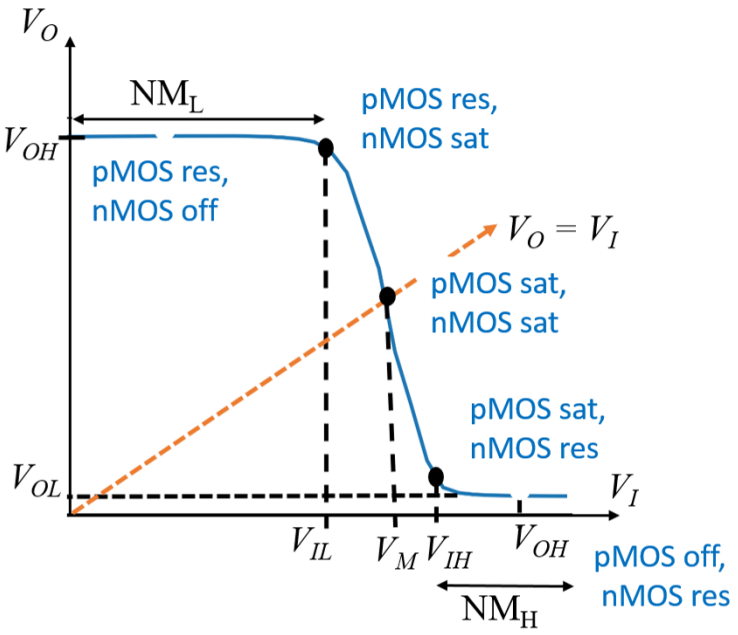

FIGURE 5.31: Voltage transfer characteristics of CMOS inverter. The transistors are either in saturation (sat), resistive (res) or off mode[19].

5.3.4 Concept of noise margin

Once a digital circuit like an inverter is fabricated, it is expected that the circuit performs its designated operation. However, in most cases there are deviations to this expected response. One common reason for this deviation is variations in the manufacturing process. Slight variations in the manufacturing process can cause the variation in dimension and hence the threshold voltage and current of a transistor. Another reason for the deviation from the expected response is the presence of noise. In digital circuits noise is referred to "unwanted" variations of voltages and currents at the logic nodes [200]. There are several ways in which noise can enter a digital circuit and also in many cases noise can be internally generated. Hence, noise is a big concern in digital circuits.

In Figure 5.31 important values like nominal voltages V_{OH} and V_{OL}, and the switching threshold voltage V_M are marked. Signals in digital circuits are not discrete but rather continuous in reality. Such signals are turned into discrete variable by associating a nominal voltage level with each logic state: 1 for V_{OH} and 0 for V_{OL} where V_{OH} and V_{OL} represent the high and the low logic levels, respectively. The difference between these two nominal voltages is called the logic or signal swing V_{sw}. Switching threshold voltage V_M is found at the intersection of the voltage transfer characteristics curve and the line given by $V_O = V_I$ [200].

In reality, even for an ideal input nominal voltage, the output often does not give the nominal voltage. Also, the regions of acceptable high and low voltages are delimited by the V_{IH} and V_{IL} voltage levels respectively. The region that lies between these two voltages is called the undefined region and the gain (dV_O/dV_I) is equal to -1 in this region. To ensure proper circuit operation this region should be avoided [200].

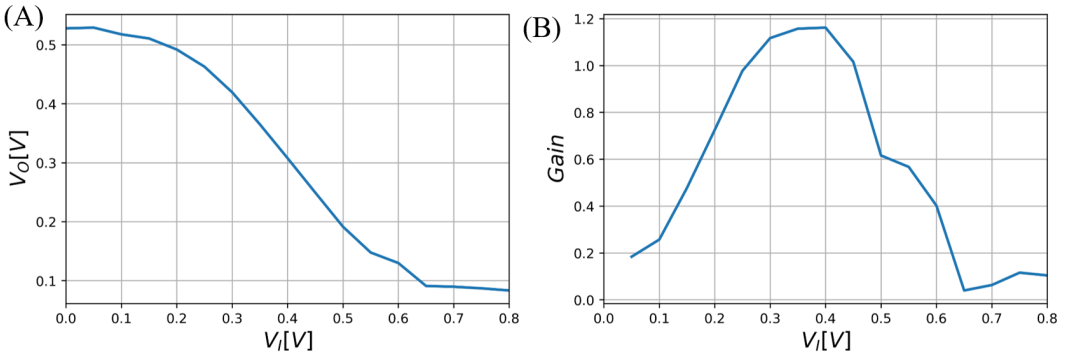

FIGURE 5.32: (A) Voltage Transfer Characteristics for a pMOS inverter. (B) Gain versus input voltage for a pMOS inverter.

To ensure that a digital circuit is robust and insensitive to noise disturbances, the "low" and "high" signal intervals be as large as possible. A measure of the sensitivity of a gate to noise is given by the noise margins NM_H (noise margin high) and NM_L (noise margin low) which sets a fixed maximum threshold on the noise value as given by equation 5.24. Thus, large noise margins are preferred in an inverter circuit.

$$\begin{aligned} NM_L &= V_{IL} - V_{OL} \\ NM_H &= V_{OH} - V_{IH} \end{aligned} \tag{5.24}$$

5.4 A pMOS-only inverter with CNTFETs

Building upon the above understanding, CNTFET based depletion mode inverters are fabricated and used in electrolyte gated configurations. Figure 5.32 (A) shows the voltage

transfer characteristics of a pMOS-only inverter. The supply voltage V_{DD} is 0.8 V and the input voltage V_I is swept from 0 to 0.8 V with a step size of 5 mV.

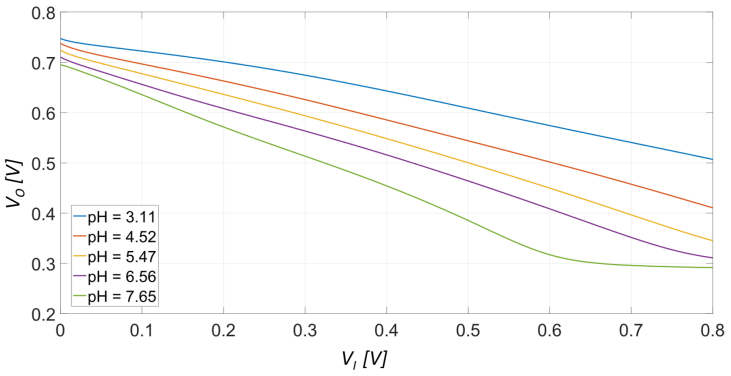

FIGURE 5.33: Voltage Transfer Characteristics (V_O versus V_I) for a pMOS inverter for different pH values.

Gain is calculated from the voltage transfer characteristics as the derivative of output voltage with respect to input voltage. This gain is plotted with respect to the input voltage V_I in Figure 5.32 (B). The maximum value of this gain is around 1.15 V

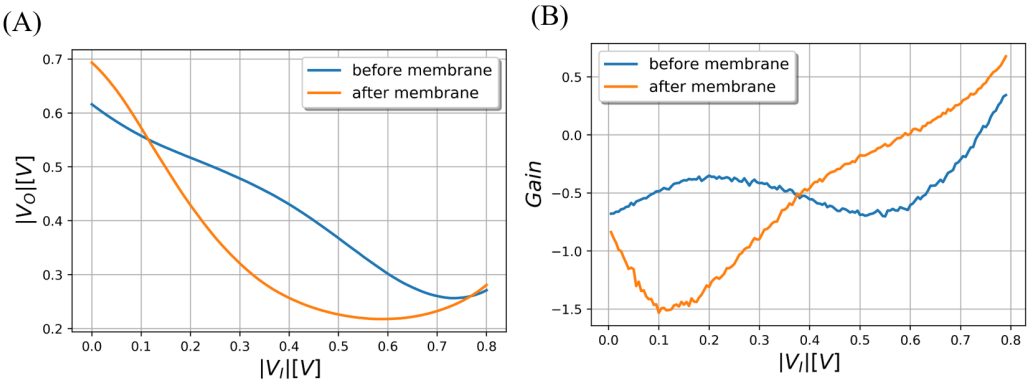

FIGURE 5.34: (A) Voltage Transfer Characteristics (VTC) and (B) Gain versus gate-to-source voltage for the pMOS logic inverter before and after placing a pure lipophilic membrane on channel of CNTFETs. The gain before membrane is -0.7 and after membrane is -1.5 [14].

pH sensing using pMOS inverter

Such inverters can be used for pH sensing by applying ion-selective pH membrane on the driver p-type CNTFET. The load p-type CNTFET is gated with a fixed PBS buffer solution of pH 7.65. The driver on the other hand is gated with solutions of varying pH as 2, 3.1, 4.5, 5.4, 6.5 and 7.6. Figure 5.33 shows the voltage transfer characteristics where the V_{DD} is equal to 0.8 V. The input voltage V_I is swept from 0.1 V to 0.8 V. It can seen that with the decreasing pH value, the voltage transfer characteristics shifts towards lower value of output voltage. Gain for all pH values is below 1. With increasing

pH, the absolute value of the gain of the inverter increases and the point of maximum gain also shifts towards lower input voltages.

5.5 Improved pMOS-only logic inverter

A pure lipophilic membrane improves the performance of a p-type CNTFET significantly. It makes sense to investigate if this improvement can be reflected in a pMOS only logic inverter. Figure 5.34 (A) shows the voltage transfer characteristics for a pMOS inverter first measured with as fabricated CNTFETs. In the next step, the channel of both the CNTFETs is covered with a pure lipophilic membrane and the pMOS inverter is re-measured.

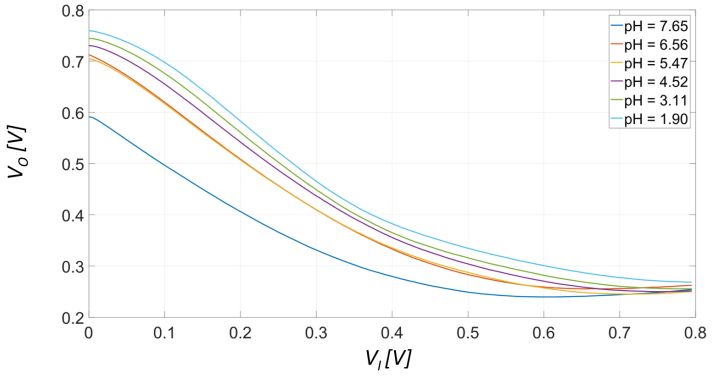

FIGURE 5.35: Voltage transfer characteristics of an inverter for different pH values.

Figure 5.34 (B) is the plot of the gain versus gate to source voltage (V_{GS}) for the pMOS inverter before and after placing a pure lipophilic membrane on both the CNTFET of the pMOS logic inverter. There is clear improvement around (114%) in the gain of the inverter. However, it is important to see that the gain dependence on V_{GS} is not sharp.

pH sensing by the improved pMOS inverters.

The improved pMOS logic inverter is further challenged for pH sensing. Figure 5.35 shows the response of a pMOS logic inverter where pure lipophilic membrane (without any ion-exchangers) covers the channel of both the p-type CNTFETs. With the introduction of the membrane, its selectivity now plays a major role in the pH measurement. It is seen that with decreasing pH the switching point of the inverter moves to more positive input voltages (V_I).

Figure 5.36 shows the gain versus input voltage. There is a clear trend in the gain of the inverter with pH. The absolute value of the gain increases with the decreasing pH value and the point of maximum gain moves towards more positive input voltages.

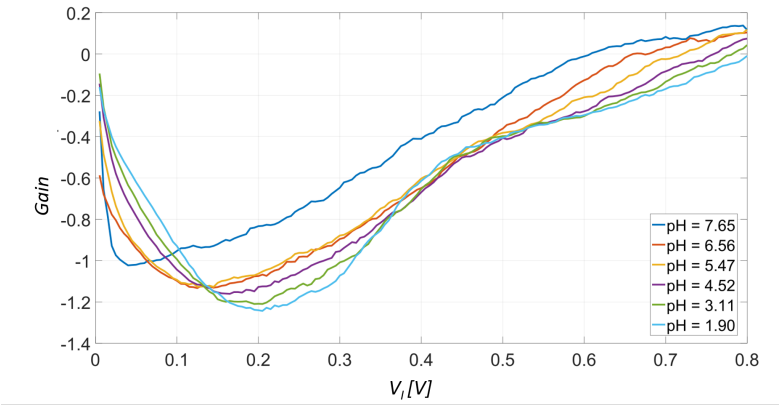

FIGURE 5.36: Gain versus input voltage of a improved inverter for different pH values.

5.6 CMOS inverter using modified CNTFETs

Using the n-type CNTFET and improved p-type CNTFET made from lipophilic membrane, electrolyte gated CMOS inverter is fabricated. The transfer curve for both these transistors is shown in Figure 5.37 measured in 20 mM PBS buffer.

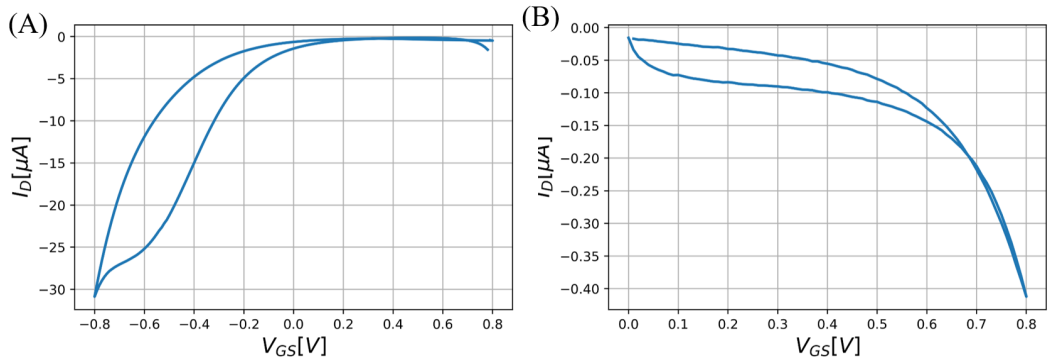

FIGURE 5.37: Transfer curve for (A) p-type CNTFET and (B) n-type CNTFET, used to fabricate a CMOS inverter[18].

Input voltage V_I applied at the gate of both p-type and n-type CNTFETs is swept from 0 V to + 0.8 V. The supply biases are fixed to V_{DD} as + 0.8 V and V_{SS} is fixed to - 0.8 V. Figure 5.38 (A) and (B) shows the voltage transfer characteristics and gain versus input voltage for a CMOS inverter. The maximum gain of this inverter is almost two, higher than pMOS only logic inverter.

To provide the information of reproducibility of such CNTFET CMOS logic inverters, Figure 5.39 shows the gain versus input voltage plot for five different runs of the CMOS inverter.

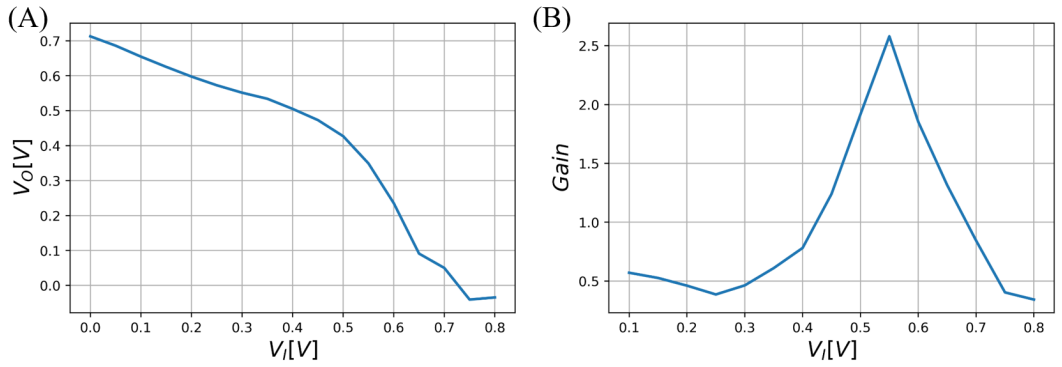

FIGURE 5.38: (A) Voltage transfer characteristics and (B) Gain versus input voltage for a CMOS inverter. [18].

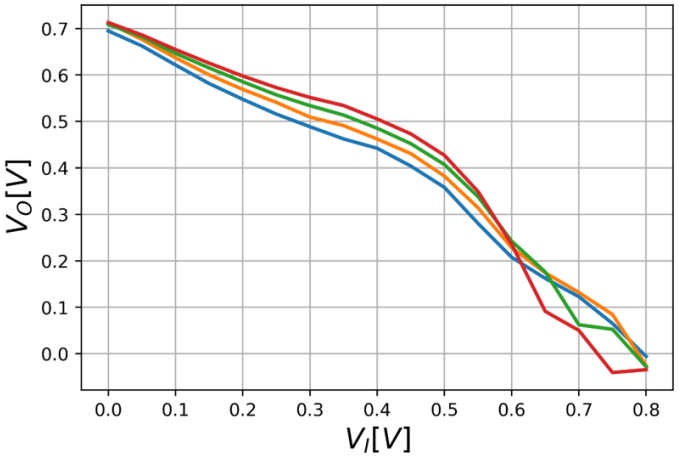

FIGURE 5.39: Voltage transfer characteristics for five different runs of a CMOS inverter.

5.7 Conclusion

In this chapter use of ion-selective and lipophilic membrane on CNTFET is demonstrated. Ion selective membranes can be used on CNTFETs to develop highly sensitive ISFETs. Lipophilic membranes on the other hand have the capability to enhance and alter the nature of CNTFETs, including their conversion to n-type devices. It is possible to make different kinds of electronic logic with these modified CNTFETs, like pMOS and CMOS logic inverters. All these improved or novel devices are water stable, hence are attractive for chemical- and bio- sensing applications. In this work we demonstrate these inverters as pH sensors. Although there is a significant improvement in the device itself, the sensitivity still needs to be improved. Along with sensitivity, these devices suffer from poor noise margins. To improve these characteristics, in the next chapter an alternate n-type material is demonstrated that can be used to achieve a higher gain and better noise margin inverters.

Chapter 6

Indium-Galium-Zinc-Oxide : n-type semiconductor

In the previous chapter lipophilic membrane modified n-type CNTFETs are demonstrated and such FETs are used to make all-CNT CMOS logic inverter circuits. Although such circuits have better performance compared to pMOS only logic, they still do not exhibit very good voltage transfer characteristics. Apart from having moderate gain, they have small noise margins both high and low. This leads one to explore other semiconductors which are high performing and can also be processed in solution.

6.1 Indium Gallium Zinc Oxide

Indium gallium zinc oxide (IGZO) is a semiconductor material first used in thin film transistors (TFTs) by Hideo Hosono's group at Tokyo Institute of Technology and Japan Science and Technology Agency (JST) in 2003 (crystalline IGZO-TFT)[201] and in 2004 (amorphous IGZO-TFT) [20] respectively. It has shown promising electrical performance as an active layer for thin film transistors with high effective mobility ($\sim$3 - 12 cm^2/Vs), low off current (10^{-12} A) and good uniformity compatible with the state-of-the-art substrate size [202]. A comparison between amorphous IGZO with other TFT technologies is present in Table 6.1. It is clear that so far only IGZO TFTs show a balance between high mobility and large area uniformity. This makes them one of the most promising candidates for fabricating transistors in organic light-emitting diode (OLED) displays.

Chemical structure of single crystalline IGZO has alternating layers of indium oxide (InO_2) and gallium oxide (zinc oxide) GaO(ZnO) [203]. Amorphous-IGZO can exists in uniform phase due to the presence of different metal oxides (In_2O_3 & Ga_2O_3) which are introduced to promote the glass phase formation [204] and this amorphous phase is

Technology	Mobility(cm^2/Vs)	Transparency	Large Area Uniformity
a-Si:H	< 1	Poor	Good
Poly-Si	~ 100	Poor	Poor
ZnO	$20 \sim 50$	Good	Poor
a-IGZO	$3 \sim 12$	Good	Good

TABLE 6.1: Comparison of different TFT technologies. [23]

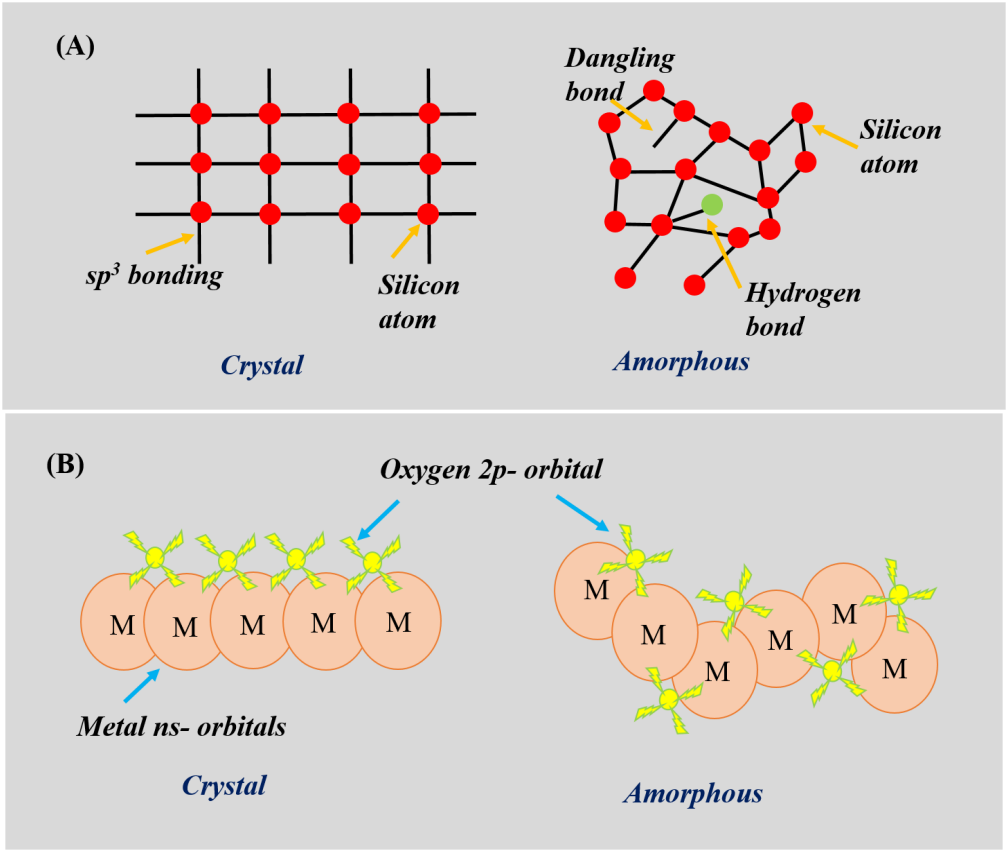

FIGURE 6.1: Schematic drawing of orbital showing electron conduction path in (A) conventional covalent semiconductors (example silicon) and (B) ionic oxide semiconductor. [20]

thermally stable up to $\sim 500°C$ [20]. Despite being an amorphous material amorphous-IGZO has electron mobility ten times higher than crystalline silicon. Additionally it can be sputtered at room temperature and is amenable to solution processing. Hence, in this thesis we focus only on amorphous IGZO.

Amorphous-IGZO is not sensitive to metal-oxide-metal chemical bond angle variance induced by structural randomness due to its unique electronic structure. In conventional semiconductors like silicon the carrier conduction is through a highly directional sp^3 bonding. However, in case of IGZO the carrier conduction is through metal ion's 'ns' orbital. Because of the symmetrical nature of the 'ns' orbital, the conducting path and carrier mobility for these semiconductors is preserved even in the amorphous phase. This is illustrated in Figure 6.1 (A) and (B). To ensure a high mobility in the amorphous

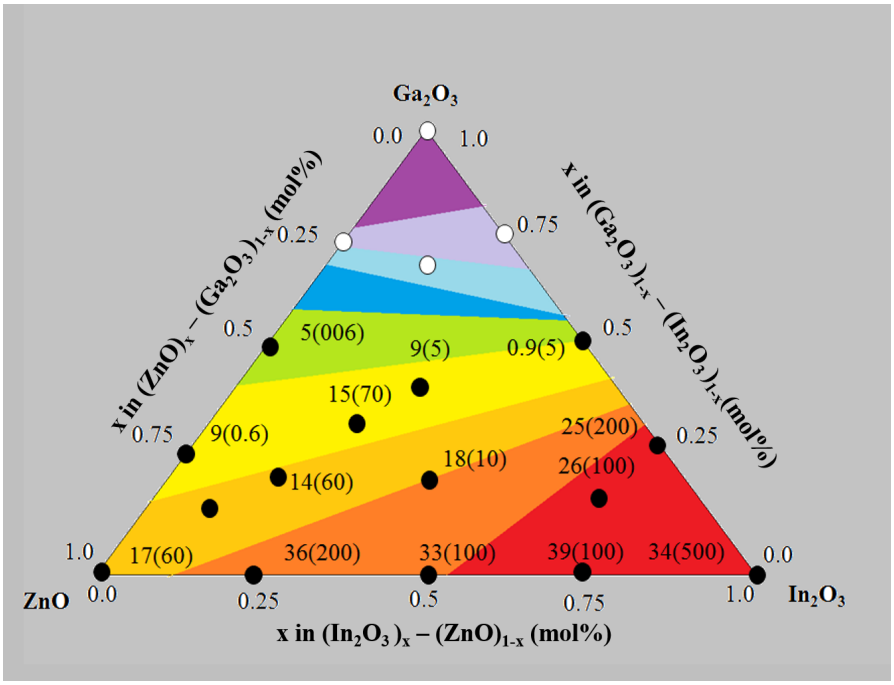

FIGURE 6.2: Hall mobility and composition of a-IGZO. Relation between chemical composition, mobility, and carrier density. The dark circles represent experimental values [21].

phase, sufficient ns orbital overlap between metal ions is necessary, this also leads to the dependence of Hall mobility for amorphous-IGZO on the In_2O_3 content [205] as In^{3+} has the largest ionic radius (n=5) among the metal cations. Figure 6.2 shows the mobilities with composition for an amorphous-IGZO.

For the transistors to exhibit high on-off ratio and low off current, the carrier concentration in the semiconductor should be controlled to a very low level. Metal oxide semiconductors contain oxygen vacancies which can further cause carrier generation. This phenomena has already been reported for zinc oxide films where a very high carrier concentration is seen in as-deposited semiconductor because of generation of excess oxygen vacancies in the thin-film deposited in an unoptimized fashion [206]. In case of IGZO, the presence of Ga^{3+} ions help in suppressing the oxygen vacancies as it has a stronger affinity to oxygen than Zn or In ions [20]. This fact is further proven by a comparative study between amorphous indium zinc oxide and amorphous indium gallium zinc oxide that shows there is five orders of magnitude lower carrier concentration in the thin film oxide with gallium deposited under the same conditions [205].

6.2 IGZO TFTs :Fabrication

The most widely used methods for synthesis of IGZO films are sputtering [207] and pulsed laser deposition (PLD) [208]. In the first process, Ga_2O_3-ZnO (GZO) and In_2O_3

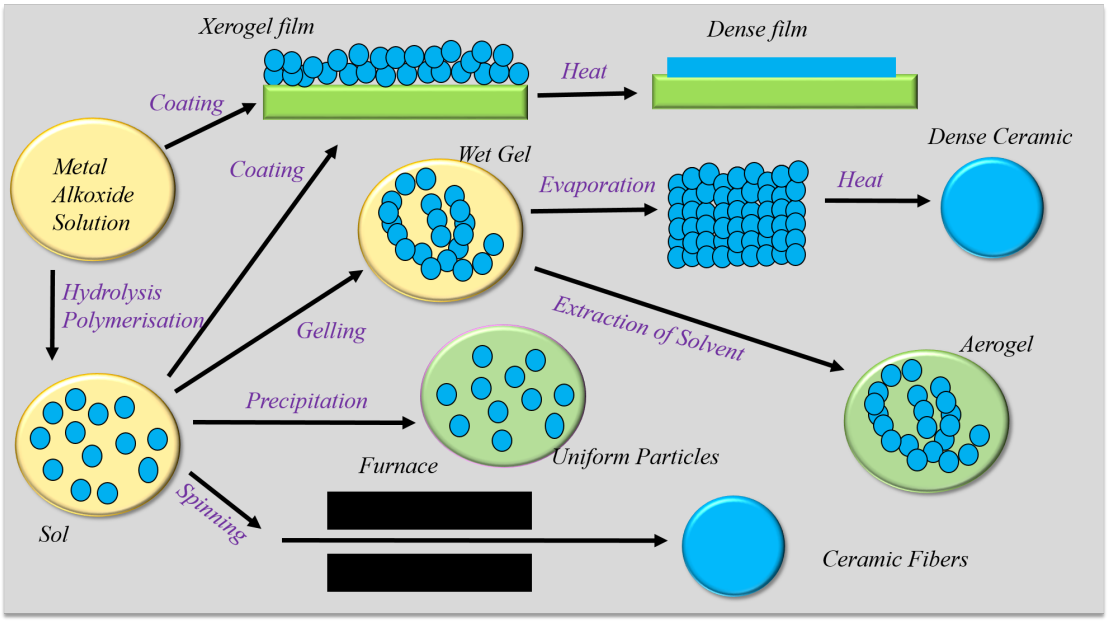

FIGURE 6.3: Schematic representation of the sol–gel technology [22].

are sputtered alternatively on a substrate to obtain IGZO films. In pulsed laser deposition, different frequency laser pulses are focused on nano-sized spots of elemental targets. Although these methods are versatile and useful, there is strict requirement on expensive equipment and time which is not favorable for industrial manufacturing. Solution processable techniques on the other hand are more cost effective alternatives. In an attempt to develop high performing and low cost IGZO devices, an IGZO sol gel is prepared which is spray deposited on a substrate and annealed at high temperature to form a high quality IGZO film.

6.2.1 Sol-gel Synthesis of IGZO films

Sol-gel method has been around since mid 1800s when it was used to make inorganic ceramic and glass materials [209]. In this method, a "sol" (a colloidal suspension of solid particles in liquid) is formed which gradually evolves towards formation of a gel-like system containing both liquid phase and solid phase and finally removal of the solvent as shown in Figure 6.3. This method can be used to form compact films of metal oxide semiconductors [210].

In this work, the precursor solutions are metal nitrates and acetates purchased commercially. These metal precursors, namely $In(NO_3)_3.xH_2O$ (indium nitrate hydrate), $Ga(NO_3)_3.xH_2O$ (gallium nitrate hydrate), $Zn(CH_3COO)_2.2H_2O$ (zinc acetate dehydrate) are dissolved in ethanol solution. The precursors are kept for stirring at 80 °C and this solution is sprayed through a shadow mask on a silicon substrate. The temperature during spray process is kept to 100°C which causes the solvent to evaporate. The substrate is finally annealed to 300°C for one hour in ambient air. The high temperature

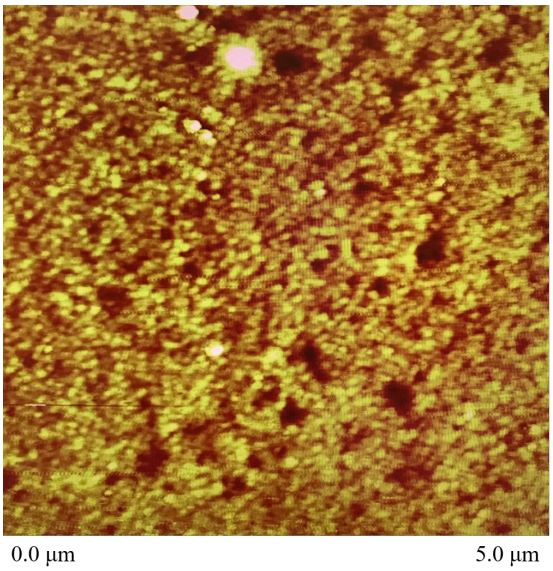

FIGURE 6.4: AFM image of IGZO sprayed on silicon substrate.

step is necessary to eliminate excess precursor materials and further densify the metal oxide film [210]. Figure 6.4 shows the AFM image of the sol-gel IGZO sprayed on silicon substrate. The surface roughness is analyzed for an area of 25 μm^2 and the average roughness (R_a) is 0.338 nm while the root mean square roughness (R_q) is 0.456 nm. This analysis indicates that sol-gel deposited IGZO films have better and smoother surface as compared to IGZO deposited by RF magnetron sputtering [211] and co-sputtering [212].

6.2.2 Contact Fabrication

IGZO TFTs were first attempted in kapton substrate, but the high temperature annealing led to shrinkage of the kapton. Hence we later use silicon as the main substrate for these transistors. For comparison, few FETs are also made in glass substrate. The process flow for contact patterning and metallization is shown in Figure 6.5 (A). Silicon wafers commercially purchased from SiMat with 200 nm thick silicon oxide are cleaned in an ultrasonication bath in acetone and propanol in succession for five minutes each. The cleaned samples are dried with dry nitrogen and ready to use for contact patterning. Using the photolithography steps already described in Section 3.6, contacts are patterned with the aid of negative photolithography followed by liftoff. The contact material is 50 nm thick gold deposited by physical vapor deposition. Figure 6.5 (B) shows the optical microscope image of the final IDES structure of the transistor after liftoff. Figure (C) and (D) are the samples with IGZO TFTs on glass and silicon respectively. On the silicon substrate there is some white residual impression of the solvent which evaporates fast during spray as the substrate is kept at high temperature. The channel length and width of these FETs is 60 μm and 3000 μm respectively.

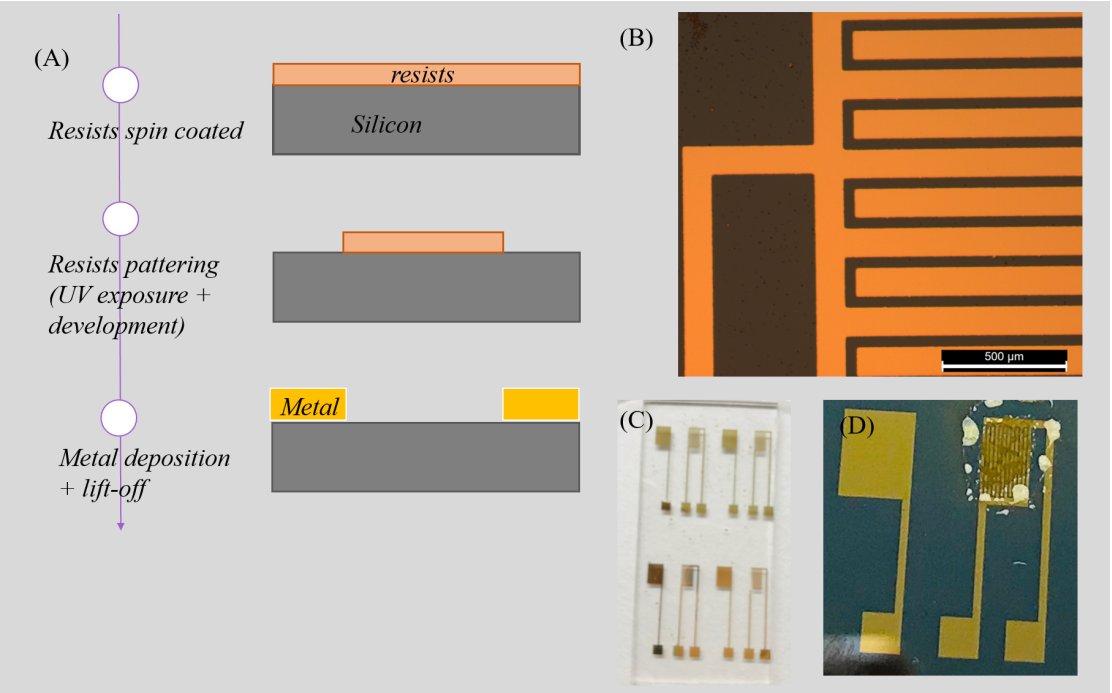

FIGURE 6.5: (A) Schematic representation of various stages of contact patterning in silicon. (B) Optical microscope image showing the final IDES structure after lift-off. (C) Four IGZO FETs fabricated on glass substrate. (D) An IGZO FET fabricated on silicon substrate.

6.3 IGZO FET: Transistor Characterization

The IGZO transistor is measured in an electrolyte gated configuration using ionic liquid, 1-Butyl-3-ethylimidazolium hexafluorophosphate (97.0%) (HPCL) as the gate electrolyte. 20 μl of this viscous solution is dropped on the transistor such that the channel and gate are completely covered with the electrolyte. All the electrical measurements of the IGZO transistors are carried out with a Keithley 2536 source measuring unit (SMU). The measurements are controlled by a Python script which is also used for data analysis. The output characteristics for the ionic liquid gated amorphous IGZO thin film transistor under various gate to source voltages (V_{GS}) ranging from 0.0 V - 1.7 V with a step size of 0.1V are shown in Figure 6.6. During each measurement, the drain to source voltage (V_{DS}) was varied from 0.0 V - 2.0 V. A clear distinction between linear and saturation region is clearly observed.

Figure 6.7 (A) illustrates the transfer characteristics for the ionic liquid gated amorphous IGZO thin film transistor when the V_{DS} is fixed to 1 V and the V_{GS} is varied from 0 V - 3 V. The right y-axis (in green) depicts the drain current and the left y-axis (in blue) depicts the gate current. The plot is a semi - log plot where the currents on the y-axis are in log scale. We extracted the threshold voltage (V_{th}) and transconductance (g_m) as 2.72 V and 5.15 mS respectively. The on-off ratio of the transistor is $> 10^7$ and the maximum drain current is 4.05 mA as shown in Figure 6.7 (B). The maximum gate

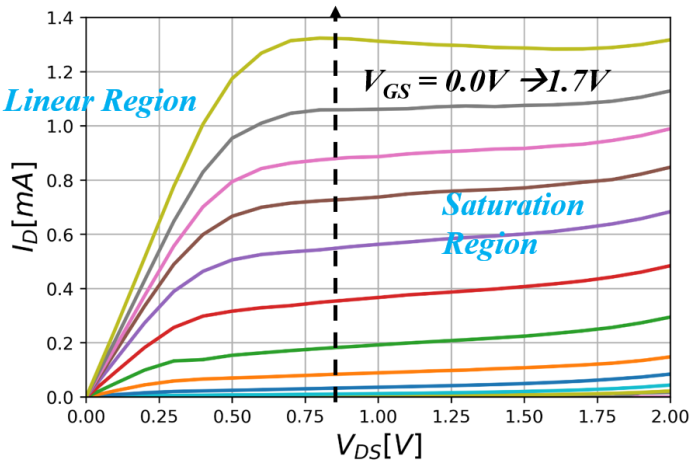

FIGURE 6.6: Output characteristics of an IGZO-EGFET.

current is 3.58 μA and can be seen in the semi log plot of Figure 6.7 (A). Comparing the IGZO TFTs with CNTFETs, IGZO TFTs have much higher on-off ratios (around three orders of magnitude higher) than CNTFETs. Also, in IGZO TFTs the transition from off region to on region (i.e. subthreshold slope) is sharper. There is also clear saturation region seen in the output curve for IGZO TFTs, but it is also important to note that biases applied in characterization of IGZO TFTs are above 1 V as their threshold voltages are normally beyond 1 V.

Table 6.2 provides statistical data for twenty IGZO-transistors. The columns show on-off ratio, threshold voltage and substrate on which the devices were fabricated. Figure 6.8 uses the data from table 6.2 and shows the number of IGZO-transistors that have a specific range of on-off ratio. Out of the twenty transistors, there are eight transistors that have on-off ratio below one hundred and ten transistors have on-off ratio above one thousand. There is indeed device variability due to the spray deposited thin films of IGZO, but post-spray annealing step densifies the film and reduces the variability. Hence, the IGZO TFTs fabricated in the same cycle often show less device variability.

Comparing the sol-gel deposited IGZO TFTs with TFTs made from sputtered IGZO films (work done within our group), the device characteristics look similar The on-off ratio for sputtered IGZO TFT is in the same order of magnitude [213] as reported in this thesis work. One difference is that the sputtered film TFTs are not electrolyte gated but have 50 nm thick alumina (Al_2O_3) as the dielectric, hence the maximum applied biases are high around 10 V. Thus, the so-gel deposited films have additional advantage of being high performing even at low voltages.

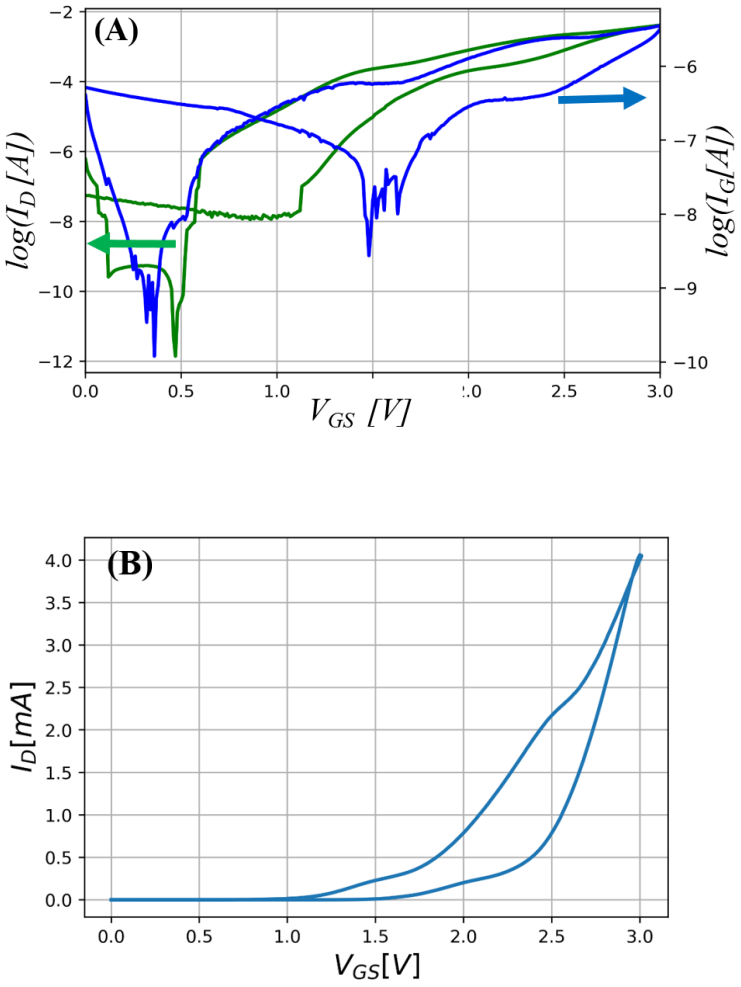

FIGURE 6.7: (A) Logarithmic plot showing drain and gate current on y-axis and gate to source voltage on x-axis. (B) Transfer characteristics of an IGZO-EGFET.

6.4 IGZO FET: Modeling

To extract device parameters and understand the behavior of IGZO TFTs device modeling is performed. Semiconductor device modeling creates models to reflect the behavior of the electrical devices. Physics driven models take into consideration fundamental physics. However, physics driven models are not fast and often empirical models are used for high level tools like SPICE. Such empirical models are called compact models. Compact models describe the major performance of the device with minimum number of model parameters [214].

In this work, we compact model the IGZO FET separately in below and above threshold regions. To model the above threshold region, modified form of Curtice model is used[215]. Curtice model was first developed to model gallium arsenide (GaAs) FETs [216]. The advantage of Curtice model is that it has few input parameters and the

Sr. No.	I_{ON}/I_{OFF}	$V_{th}(V)$	Substrate
1	2030	1.24	Silicon
2	17800	0.969	Silicon
3	59.8	1.43	Silicon
4	83.7	1	Silicon
5	2370	1.1	Silicon
6	487.76	1.3	Silicon
7	80400	1.4	Silicon
8	823	1.6	Silicon
9	3070	1.7	Silicon
10	2690	1.07	Silicon
11	2850	0.9	Silicon
12	31900	0.93	Silicon
13	49400	1.45	Silicon
14	439	0.85	Silicon
15	70.5	1.43	Glass
16	31.1	1.45	Glass
17	48.3	1.53	Glass
18	37.72	1.51	Glass
19	81.2	1.35	Glass
20	47.8	1.28	Glass
21	15000	0.8	Glass

TABLE 6.2: Statistical data for twenty IGZO transistors measured with ionic liquid as the gate electrolyte [23].

above threshold region is described by only one equation. This makes it easy and fast to incorporate. To model the below threshold region well-known subthreshold swing model is used [217].

6.4.1 Above Threshold Region

6.4.1.1 Model Description

In the above threshold region, according to the modified Curtice model [216, 218], the drain current is given as equation 6.1 :

$$I_D = \beta * (V_{GS} - V_{th})^{\gamma} * tanh(\alpha * V_{DS})(1 + \lambda * V_{DS}) \tag{6.1}$$

where parameters have meaning as : α describes the knee region, β is the transconductance parameter, γ is the power-law parameter and λ is the channel length modulation parameter. As per this model, field-effect mobility has power law dependence with the gate voltage and is given as equation 6.2 [218] :

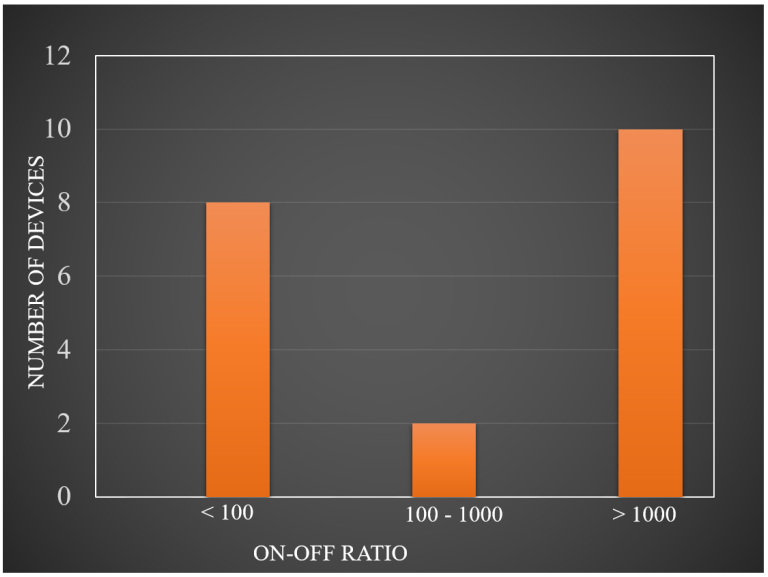

FIGURE 6.8: Summary of the number IGZO-transistors that have a specific range of on-off ratio.

$$\mu_{eff} = \frac{\mu_0 * (V_{GS} - V_{th})^{\gamma}}{V_{AA}} = \mu_{FET0} * (V_{GS} - V_{th})^{\gamma} \tag{6.2}$$

where μ_0 is the field-effect mobility at low electric fields and V_{AA} is an empirical parameter.

Parameter α is calculated as equation 6.3 [218] :

$$\alpha = \frac{g_{ch}}{I_{sat}} \tag{6.3}$$

where g_{ch} is the channel conductance at small V_{DS}. I_{sat} is the saturation current given by equation 6.4 [190] :

$$I_{sat} = \beta * (V_{GS} - V_{th})^{\gamma} \tag{6.4}$$

Parameter β, the transconductance parameter is given by equation 6.5 :

$$\beta = \frac{W}{L} * K_n = \frac{W}{L} * C_i * \mu_{FET0} \tag{6.5}$$

where W and L have their usual meanings as the channel width and channel length of the transistor respectively. K_n is the transconductance and C_i is the gate capacitance.

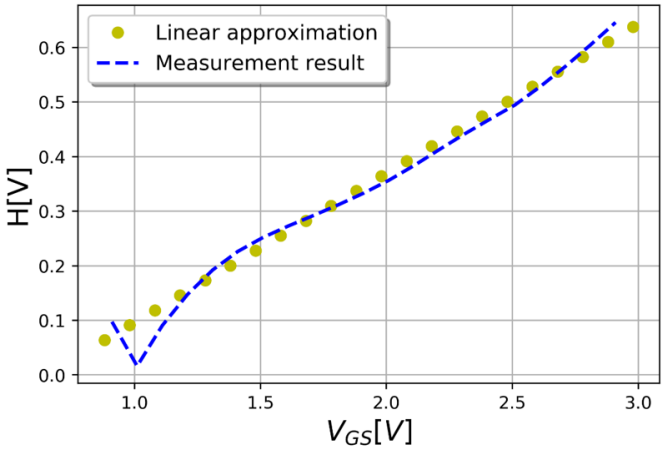

FIGURE 6.9: Integral function H plotted against V_{GS}, for the measurement data and linear approximation given by equation 6.7.

6.4.1.2 Parameter Extraction

To extract the two input parameters that are power-law γ and the threshold voltage V_{th}, an integral function $H(V_{GS})$ is created which is given by equation 6.6 [190] :

$$H(V_{GS}) = \frac{\int_0^{V_{GS}} I_{DS}(x)dx}{I_{DS}(V_{GS})} \tag{6.6}$$

In the linear region of operation, equation 6.6 can be approximated with equation 6.7 [190] :

$$H(V_{GS}) = \frac{V_{GS} - V_{th}}{1+\gamma} \tag{6.7}$$

Figure 6.9 plots the integral function against V_{GS} (equation 6.7). The threshold voltage (V_{th}) is extracted from the interception of this plot with the x-axis and the power law parameter γ is the slope of the curve. These values are listed in table 6.3.

To extract β parameter, the output characteristics in deep saturation region are investigated. V_{DS} is swept from 0.0 V to 1.5 V and V_{GS} is fixed to 1.3 V. The output curve for this bias is shown in Figure 6.10. A linear fitting and extrapolation is done for both the linear region and the saturation region. The point of intersection of the two fitting lines gives the value of I_{sat}. Using this value of I_{sat} and equation 6.8, parameter β can be extracted. The extracted values for I_{sat} and β are added in table 6.3.

$$\beta = \frac{I_{sat}}{(V_{GS} - Vth)^{\gamma} * (1 + \lambda * V_{DS})} \tag{6.8}$$

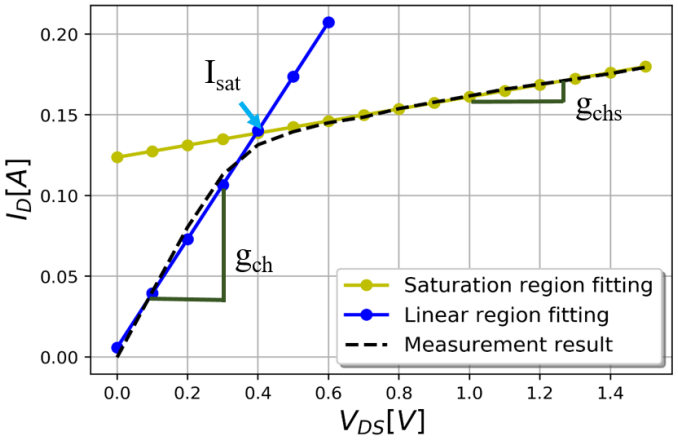

FIGURE 6.10: Current vs voltage curve used to extract channel conductance in linear (g_{ch}) and saturation regime (g_{chs}) as well as the saturation current (I_{sat}).

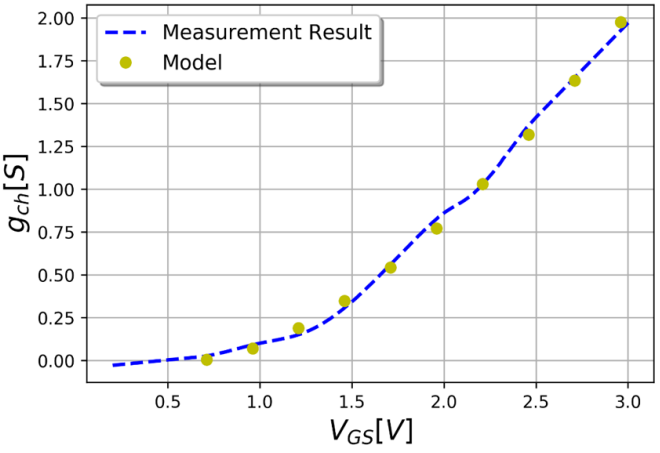

FIGURE 6.11: Measured and modeled values of channel conductance g_{ch} with respect to gate to source voltage(V_{GS}) in the linear region.

In Figure 6.10 the linear and saturation regions are clearly marked. Slope of the linear region gives the channel conductance (g_{ch})and can be easily calculated using the fitting line of the linear region. Calculated value of g_{ch} can be read from the table 6.3. g_{ch} shows a dependence on V_{GS} and in the above-threshold region this dependence can be described by equation 6.9 :

$$g_{ch} = g_{ch0} * (V_{GS} - V_{th})^{(\gamma-1)} \tag{6.9}$$

where g_{ch0} is a empirical parameter extracted from Figure 6.11 and its value is added in table 6.3. Figure 6.11 shows that the model does a very good fitting of the measured channel conductance in above threshold region.

From Figure 6.10, the conductance in the saturation region (g_{chs}) can also be computed as the slope of the linear fitting in the saturation region. Computed value of g_{chs} is mentioned in table 6.3. With the value of g_{chs}, channel length modulation parameter λ can be extracted using equation 6.10 :

$$\lambda = \frac{g_{chs}}{I_{sat}} \tag{6.10}$$

Figure 6.12 is a semi log plot of the transfer curve and it is seen that for $V_{GS} >> V_{th}$, proposed model is a very reasonable match with the experimental results.

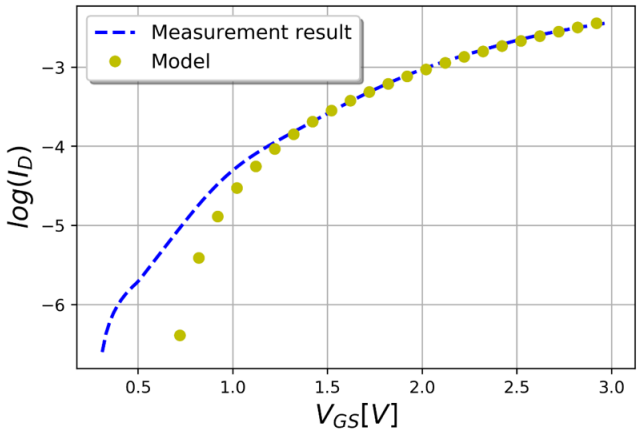

FIGURE 6.12: Comparison of measured versus modeled logarithmic drain–source current in the above-threshold region.

γ	V_{th} (V)	I_{sat} (A)	β	g_{ch} (S)	g_{ch0} (S)	g_{chs} (S)	λ (V^{-1})
2.66	0.64	0.14	0.15	0.336	0.49	0.374	0.267

TABLE 6.3: Values of the model parameters extracted in the above threshold region.

6.4.2 Below Threshold Region

To model the subthreshold regime we use equation 6.11 :

$$I_D = I_S * e^{\frac{(V_{GS}-V_{th})}{n*V_{therm}}} * tanh(\alpha_0 * V_{DS}) * (1 + \lambda * V_{DS}) + I_0 \tag{6.11}$$

where I_S and α_0 are the fitting parameters, n is the ideality factor and V_{therm} is the thermal voltage. In this modified model, the V_{DS} dependence is described by a hyperbolic tangent function instead of the original exponential function. Additionally, a constant leakage current I_0 is added to the below-threshold regime. Figure 6.13 is a semi log plot

of the transfer curve and it can be seen that for below threshold region subthreshold swing model given by equation 6.11 is a reasonably good match with the experimental results.

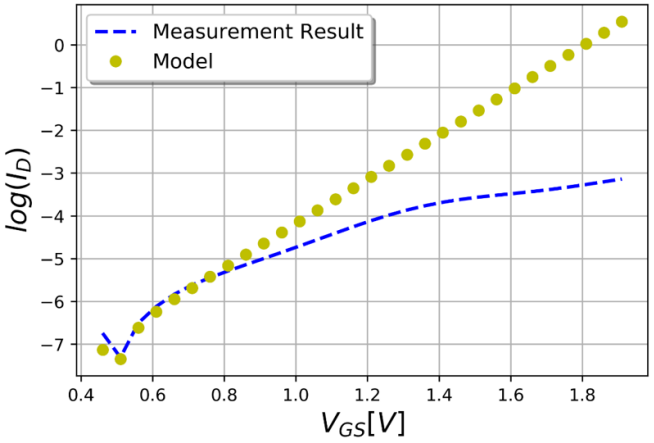

FIGURE 6.13: Comparison of measured versus subthreshold swing (model) logarithmic drain–source current in the below-threshold region.

The ideality factor n of the equation 6.11 can also be extracted from the slope of the linear part of the fitting curve using equation 6.12 :

$$n = \frac{1}{Slope * V_{therm} * ln(10)} \tag{6.12}$$

Extracted values of the fitting parameter I_S and the leakage current I_0 along with the extracted value of ideality factor can be read from the table 6.4.

n	I_S (μA)	I_0 (μA)
3.9	0.985	-0.254

TABLE 6.4: Values of the parameters extracted in the below threshold region.

6.5 IGZO ISFET as a NH_4+ Sensor

Once the IGZO FET is electrically characterized and modeled, its use as a ion-selective (IS)-FET is tested. Ammonium ion selective PVC based polymeric membranes containing nonactin as an ionophore are prepared in THF(tetra hydrofuran) and placed on the channel of the transistor.

Ammonium (NH_4+) ions find their use in environmental monitoring against pollution [219] and in several other industries like food [220] and clinical analysis [221]. Apart from its use in direct ion sensing, ammonium sensors are also used more frequently than

other ion sensors in potentiometric biosensors where enzymes or microbial cells are immobilized on the surface of the sensor [222]. These applications make ammonium ion sensors of high interest.

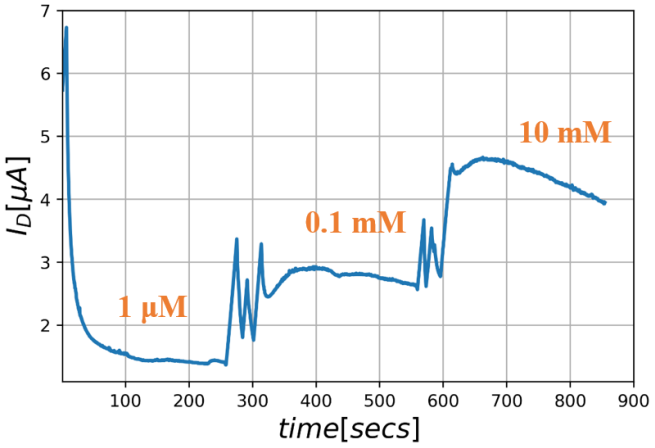

FIGURE 6.14: Response of an ammonium-selective IGZO-FET towards changes in the ammonium ion concentration.

Solutions with balanced conductivity and different concentrations of ammonium ion are placed on the gate and channel of the IGZO-FET and they serve as the gate electrolyte. Real time measurements are done and each solution is measured for about 5-6 minutes with the gate to source voltage (V_{GS}) and drain to source voltage (V_{DS}) held constant to 1.2 V throughout the measurement. Figure 6.14 shows the variation in drain current with varying ammonium ion concentration. In between concentration change the sample is washed thoroughly and hence we see multiple spikes. As seen from the figure, there is continuous increase in the drain current of the IGZO based ISFET for increase in ammonium ion concentration, the response is in accordance with the operation of ion-selective membranes explained in chapter 5. The calculated sensitivity of this ammonium sensor is around -0.6325μA/decade which is higher than the sensitivity of the NH_4+ sensor using CNTFET (refer to section 5.1). Thus, solution processable IGZO-FETs can be used for developing high sensitivity sensors.

6.6 Solution processable inverters

6.6.1 IGZO nMOS-only Inverter

In chapter 5, theory of logic inverters is presented in detail where the operation of pMOS-only, nMOS-only and finally CMOS logic inverters are discussed. In this section, resistive load nMOS-only logic inverters are demonstrated using IGZO-FETs. The influence of the resistor value and scan rate on the device performance is also discussed.

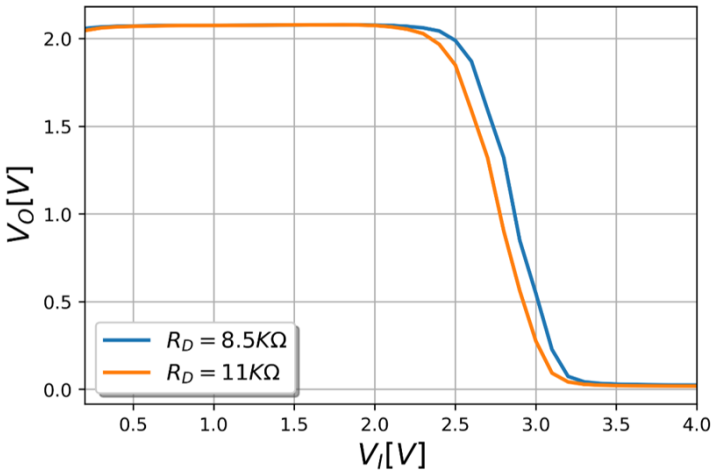

FIGURE 6.15: Voltage transfer characteristics for a resistive load nMOS inverter for two different load resistors.

Figure 6.15 shows the voltage transfer characteristics of resistive load nMOS inverter for two resistor values, where the n-FET is ionic liquid gated IGZO transistor. The inverters have respectable noise margins where the input voltages are limited by the ionic liquid. With the increase in load resistance, there is decrease in the sharpness of the transition region. This can also be related to the decrease in the gain of the inverter with increase in the load resistance. This fact is indicated in Figure 6.16 where the gain of the inverters is plotted against input voltage.

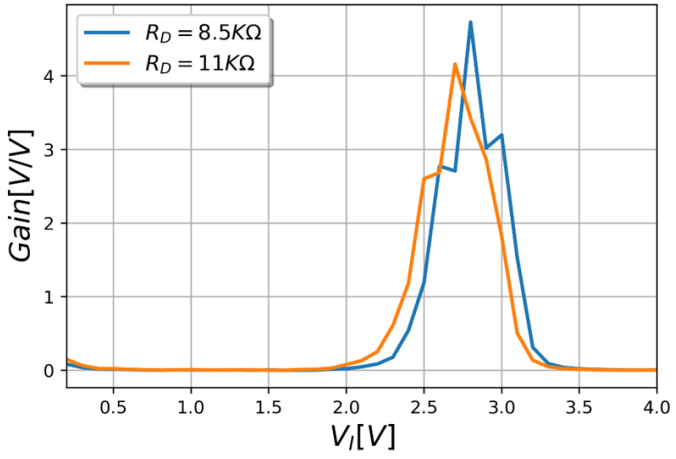

FIGURE 6.16: Gain versus input voltage for a resistive load nMOS inverter for two different load resistors.

Figure 6.17 shows the voltage transfer characteristics for the same resistive load nMOS inverter for three different scan rates of input voltage (V_I). There is a loose dependence of the inverter characteristics on the scan rate. Scan rate (dV/dt) has a direct influence

on the charging current and it increases with increasing scan rate. Figure 6.18 shows the gain with respect to input voltage for varying scan rates. Similar to Figure 6.17 there is loose dependence on the gain of inverter with the scan rate.

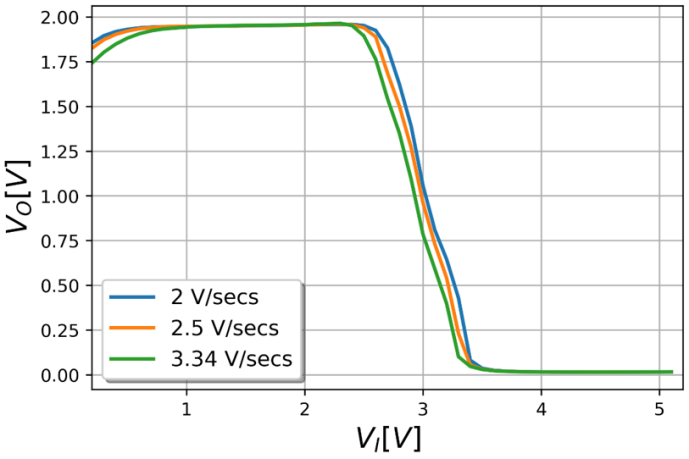

FIGURE 6.17: Voltage transfer characteristics for a resistive load nMOS inverter for three different scan rates.

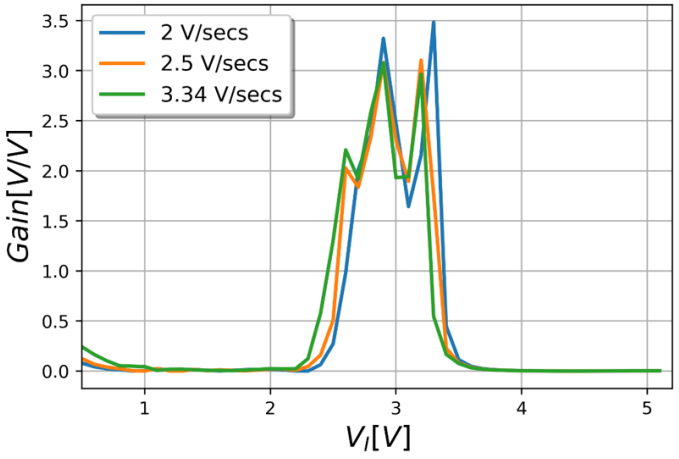

FIGURE 6.18: Gain versus input voltage for a resistive load nMOS inverter for three different scan rates.

6.6.2 CMOS Inverter : IGZO- & CNT- FET

In chapter 5, concept of noise margin and nominal values of input and output was described. The switching threshold V_M is the point in the voltage transfer characteristics where V_I and V_O are equal. At this point V_{GS} and V_{DS} are equal, hence both pMOS and nMOS are in saturation. To obtain an analytical expression for the switching threshold, we equate the currents of both pMOS and nMOS which can be written as equation 6.13 :

$$k_n V_{DSsatn}(V_M - V_{Tn} - \frac{V_{DSsatn}}{2}) + k_p V_{DSsatp}(V_M - V_{DD} - V_{Tp} - \frac{V_{DSsatp}}{2}) = 0 \quad (6.13)$$

Solving equation 6.13 results in equation 6.14 :

$$V_M = \frac{(V_{Tn} + \frac{V_{DSsatn}}{2}) + r(V_{DD} + V_{Tp} + \frac{V_{DSsatp}}{2})}{1 + r} \quad (6.14)$$

where r can be written as equation 6.15 under the assumption of equal oxide thickness for pMOS and nMOS transistors.

$$r = \frac{k_p * V_{DSsatp}}{k_n * V_{DSsatn}} = \frac{v_{satp} * W_p}{v_{satn} * W_n} \quad (6.15)$$

If another assumption can be made on the bias V_{DD} such that it is extremely large compared to threshold voltage and saturation voltage, equation 6.14 can be simplified to equation 6.16

$$V_M \approx \frac{r * V_{DD}}{1 + r} \quad (6.16)$$

Equations 6.15 and 6.16 indicate that the switching threshold is determined by parameter 'r' which in turn depends on the relative drive strength of the pMOS and nMOS transistors. It is also important to realize that a desirable location of the switching threshold V_M is around the middle of the voltage swing as this leads to almost equal values of low and high noise margins. This means a desirable V_M would be at $V_{DD}/2$. This can happen when r = 1, refer equation 6.16. This would result in the relation given by equation 6.17 which is derived from equation 6.15 and establishes a relation between device parameters of pMOS and nMOS.

$$v_{satp} * W_p = v_{satn} * W_n \quad (6.17)$$

It is also worth noting at this point that if one wants to move V_M upwards, a larger value of r is required and hence the pMOS must be made wider. On the other hand, if V_M is desired to be closer to ground, the strength of nMOS must be increased. From equation 6.15 one can also relate mobility of the pMOS and nMOS transistors by equation 6.18, given the transistors have same oxide capacitances and channel length.

$$r = \frac{\mu_n * W_n}{\mu_p * W_p} \quad (6.18)$$

In general case of silicon, the electron mobility is 2-3 times higher than the hole mobility and thus for r = 1 the width of pMOS should be 2-3 times higher than nMOS. However, with different semiconductors this ratio of widths will depend on their relative mobilities.

$$\frac{W_p}{W_n} = \frac{\mu_p}{\mu_n} \approx 2or3 \tag{6.19}$$

With this understanding we fabricate an electrolyte gated CMOS inverter with CNTFET as the "pull up" network and IGZO-FET as the "pull-down" network. Figure 6.19 shows the voltage transfer characteristics of this CMOS inverter.

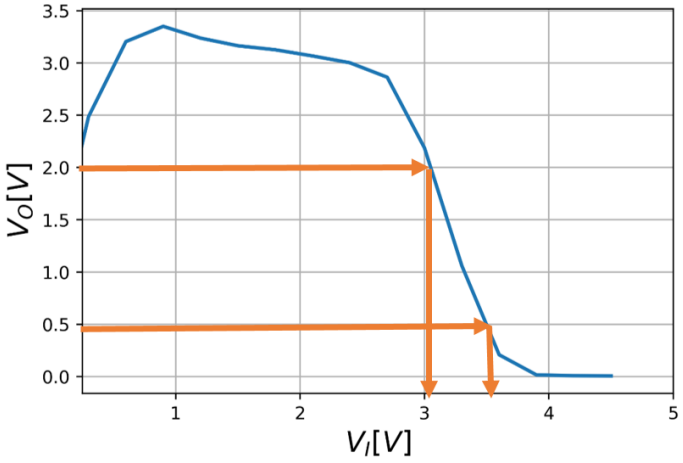

FIGURE 6.19: Voltage transfer characteristics of a CMOS inverter with IGZO-FET and CNTFET.

For this measurement the bias voltage (V_{DD}) is kept at a constant value of 2.2 V. The input voltage that is applied at the gates of the two transistors is swept from 0 V to 4.5 V. The sweep delay is 1 V. The connections and schematic of this system are shown in Figure 6.20 (A).

Figure 6.20 (B) shows one of the CMOS inverters developed in this thesis. CNT- and IGZO- FETs are highlighted in the image. The droplets on the sample are the residues of the ionic liquid used for measurements, being a high viscosity liquid it is not easily removed from the sample by just pipetting. As seen from the figure, the width of the IDES structure for CNTFET is more (1.5 times) than that of an IGZO FET, i.e. the ratio of transistor widths between pMOS CNTFET and nMOS IGZO FET is 1.5. This ratio is verified by SPICE simulations performed for the CMOS inverter with varying transistor width ratios (W_p/W_n = 1, 1.5 , 2 , 4 and 6). LTSpice was used to perform simulations and the transistor parameters used for simulation were extracted from the measurement data. Figure 6.21 shows the experimental and simulated voltage transfer characteristics of a CMOS inverter with the W_p/W_n = 1.5.

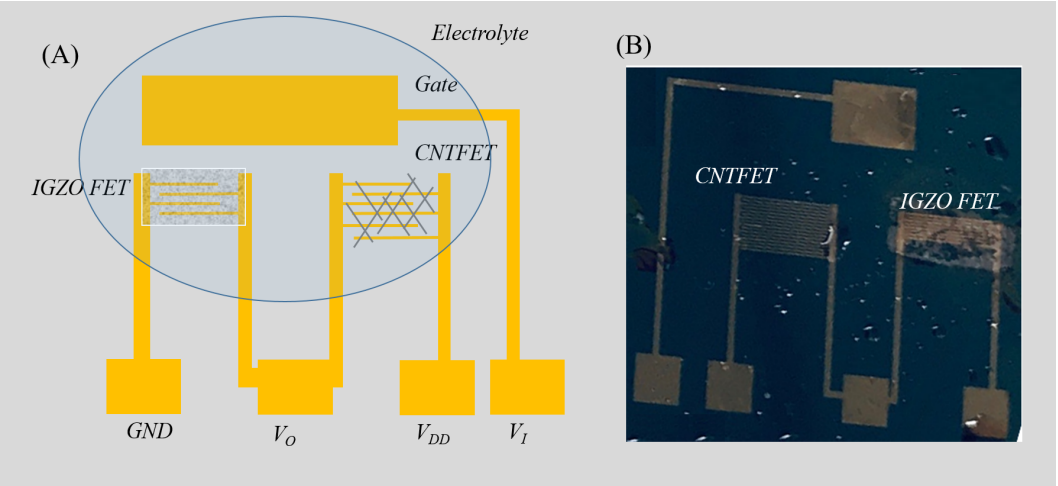

FIGURE 6.20: Schematic representation of the CMOS inverter indicating the voltages used for measurements.

On analyzing figures 6.19 and 6.21, the gain of this electrolyte gated CMOS inverter is extracted and is ~ 4. This is a significant improvement from a CNTFET-only CMOS logic inverter demonstrated in chapter 5. One can also realize that along with high gain, there is significant improvement in the noise margin.

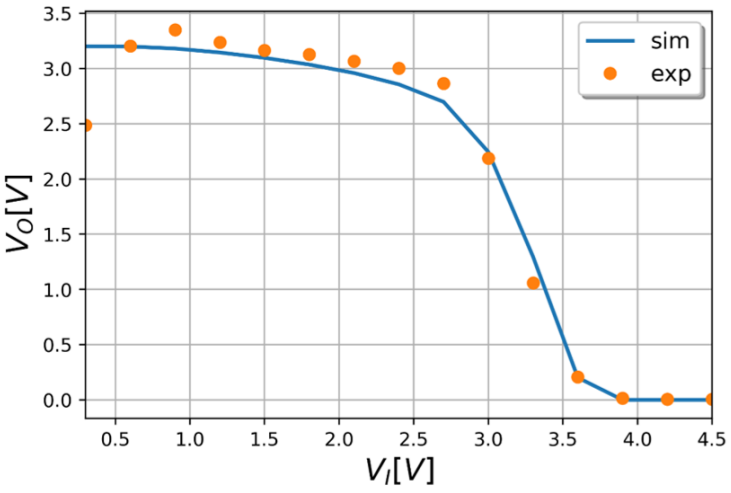

FIGURE 6.21: Experimental (exp) and simulation (sim) results of voltage transfer characteristics for a CMOS inverter with channel width ratio equals 1.5 between pMOS CNTFET and nMOS IGZO-FET.

6.7 Conclusion

In this chapter, sol gel processing of a n-type semiconductor IGZO is explained. Post device fabrication this semiconductor is demonstrated as an active channel material for an ionic liquid gated transistor. This transistor is also used as an ion selective

sensor for measuring different ammonium ion concentrations. Before using this IGZO-FET in a CMOS inverter along with an electrolyte gated CNTFET, it is used in a resistor loaded nMOS inverter configuration. The sol gel deposited IGZO-FET shows higher performance compared to their sputter coated counterparts and the IGZO-ISFET demonstrates high sensitivity comparable/higher to other commonly used semiconductors like CNTs. High performance CMOS logic inverters are demonstrated. This work clearly indicates the potential of IGZO in low voltage electronics. An important aspect in this work is that all the electronic devices, i.e. transistors and inverters are measured in electrolyte gated configuration, hence making them potential candidates for high performance chemical- or bio- sensors.

Chapter 7

Summary and Outlook

7.1 Summary

The field of organic electronics has allowed to develop semiconductors which no longer need to be processed in highly controlled environments. The ability to develop electronic devices by low cost and simple techniques like screen printing, spray deposition has made cheap yet high performance electronics possible. In addition, the possibility of fabricating electronic devices in variety of substrates with features like flexible and bio-compatible has led to an era where sensors are ubiquitous in everyday life.

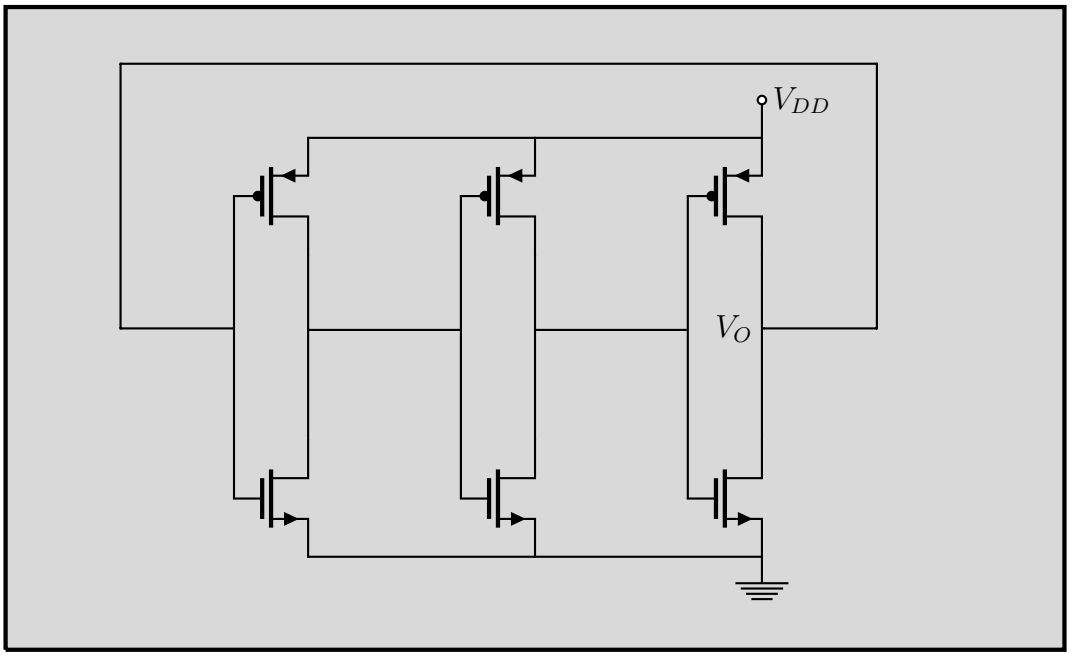

FIGURE 7.1: Circuit diagram for a 3-stage ring oscillator.

This thesis presents extensive research on using novel materials, methods and device architectures to develop low cost biosensors which in future will not be limited to point

of care diagnostics but have the potential to be used in wearables and implants. Towards this goal, field effect transistors using low cost solution processable techniques are developed. These transistors are used in an electrolyte gated configuration, where an electrolyte serves as the gate dielectric. This provides two major advantages: (i) because of the high double layer capacitance, extremely low voltages (even sub 1V) can generate high electric fields in the device hence stimulate charge conduction, (ii) use of electrolyte facilitates in bringing the test solution easily to the transducer surface.

Carbon nanotube (CNT) and indium gallium zinc oxide (IGZO) are used in this work as semiconducting materials which are deposited on low cost polyimide films. Polyimide being a flexible substrate imparts mechanical flexibility to sensors and it is seen that sensors on such substrates have high tolerance to mechanical deformations and bendings. The use of these semiconductors is not only limited to field effect transistors but is further extended in creating amplifying circuits which can be used in sensing or as an amplifier to amplify sensor response post sensing.

7.2 Outlook

Extensive work has been done in this thesis both in aspects of enhancing bio-recognition methods and signal amplification. Nevertheless, follow-up studies can be performed for improvement and developing novel high performance sensing mechanisms. One such scheme uses the inverters developed by the CNT- and IGZO- FETs to design and fabricate ring oscillators such that they can be used for high performance frequency based sensing. Figure 7.1 shows the circuit diagram of a 3-stage ring oscillator.

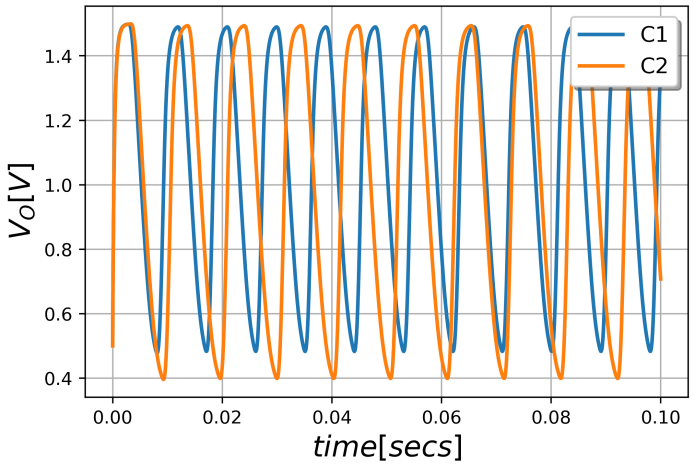

FIGURE 7.2: SPICE simulation for shift in frequency in a 3-stage ring oscillator. C1 and C2 are representatives of two different concentrations, which here are two different threshold voltages of pMOS transistors.

When there is a concentration change in the analyte solution which covers either pMOS, nMOS or all transistors in the ring oscillator, this leads to a change in the threshold voltage of the transistors. Such threshold voltage shift leads to shift in the oscillation frequency of the ring oscillator. Such an idea is illustrated in Figure 7.2, which is SPICE simulation of 3-stage ring oscillator. In this simulation we have manually introduced a threshold voltage shift in the pMOS transistor and one can clearly see a shift in the frequency. We have introduced 100 mV shift in the threshold voltage and this has resulted in a frequency shift of $\sim$ 12 KHz. The advantage of such a sensing principle of measuring frequency shift over the traditional potentiometric method of recording threshold voltage shift is in the simplicity of the measurement system. Measurement of 1 KHz frequency shift can be done readily by a simple microcontroller counter, whereas the measurement of 100 mV voltage shift requires more sophisticated systems. Hence, frequency based sensing is highly sensitive.

List of Publications

Patents

1. Saumya Joshi, Vijay Deep Bhatt, and Paolo Lugli. Sensor arrangement for analyzing substances in a material and method for operating such a sensor arrangement. In *In United States Patent Application Serial No. 16/051,160. TUM180702PUS-5/HK.*

Journal Articles

1. Saumya Joshi, Vijay Deep Bhatt, Ewa Jaworska, Agata Michalska, Krzysztof Maksymiuk, Markus Becherer, Alessio Gagliardi, and Paolo Lugli. Ambient Processed, Water-Stable, Aqueous-Gated sub 1 V n-type Carbon Nanotube Field Effect Transistor. *Nature Scientific Reports*, 8(1):1–8, 2018. ISSN 20452322. doi: 10.1038/s41598-018-29882-w

2. Saumya Joshi, Vijay Deep Bhatt, Ewa Jaworska, Markus Becherer, Krzysztof Maksymiuk, Agata Michalska, and Paolo Lugli. Using Lipophilic Membrane for Enhanced-Performance Aqueous Gated Carbon Nanotube Field Effect Transistors. *Physica Status Solidi (A) Applications and Materials Science*, 215(11):1–7, 2018. ISSN 18626319. doi: 10.1002/pssa.201700993

3. Saumya Joshi, Vijay Deep Bhatt, Andreas Märtl, Markus Becherer, and Paolo Lugli. Regenerative, highly-sensitive, non-enzymatic dopamine sensor and impact of different buffer systems in dopamine sensing. *Biosensors*, 8(1):1–10, 2018. ISSN 20796374. doi: 10.3390/bios8010009

4. S. Joshi, V.D. Bhatt, H. Rani, M. Becherer, and P. Lugli. Understanding the influence of in-plane gate electrode design on electrolyte gated transistor. *Microelectronic Engineering Volume 199, 5 November 2018, Pages 87-91 2018-08*, pages 87–91, Aug 2018. doi: 10.1016/j.mee.2018.07.019

5. Saumya Joshi, Vijay Deep Bhatt, Hao Wu, Markus Becherer, and Paolo Lugli. Flexible Lactate and Glucose Sensors using Electrolyte-Gated Carbon Nanotube Field Effect Transistor for Non-invasive Real-time Monitoring. *IEEE Sensors Journal*, (c):1–1, 2017. ISSN 1530-437X. doi: 10.1109/JSEN.2017.2707521. URL `http://ieeexplore.ieee.org/document/7933216/`

6. Vijay Bhatt, Saumya Joshi, Markus Becherer, and Paolo Lugli. Flexible, Low-Cost Sensor Based on Electrolyte Gated Carbon Nanotube Field Effect Transistor for Organo-Phosphate Detection. *Sensors*, 17(6):1147, 2017. ISSN 1424-8220. doi: 10.3390/s17051147. URL `http://www.mdpi.com/1424-8220/17/5/1147`

7. V.D. Bhatt, S. Joshi, and P. Lugli. Metal-free fully solution-processable flexible electrolyte-gated carbon nanotube field effect transistor. *IEEE Transactions on Electron Devices (Volume: 64, Issue: 3, March 2017) 2017-03*, pages 1375 – 1379, Mar 2017. ISSN 0018-9383. doi: 10.1109/TED.2017.2657882

Conference Proceedings

1. V.D. Bhatt, S. Joshi, K. Melzer, and P. Lugli. Flexible dopamine sensor based on electrolyte gated carbon nanotube field effect transistor. In *2016 IEEE Biomedical Circuits and Systems Conference (BioCAS)*. IEEE Xplore Digital Library, Oct 2016. ISBN Inspec 16620454. doi: 10.1109/BioCAS.2016.7833719. URL `https://ieeexplore.ieee.org/document/7833719/`

Poster Presentations

1. Vijay Deep Bhatt, Saumya Joshi, Andreas Märtl, and Paolo Lugli. Effect of varying pH, Ionic strength and Composition of buffer on an dopamine sensor based on a functionalized Electrolyte Gated CNTFET. *5th International Conference on Bio-Sensing Technology 2017*

2. Saumya Joshi, Vijay Deep Bhatt, and Paolo Lugli. Flexible, low cost histamine sensor for food quality tests using CNTFETs. In *5th International Conference on Bio-Sensing Technology 2017*.

Acknowledgements

This thesis would not have been the same if not for the contributions of many people and I would like to take a moment to thank all of them.

Foremost, I thank Professor Paolo Lugli for giving me such a wonderful opportunity to pursue research in the field of electronic biosensors. Throughout my thesis, he showed great confidence in my work and gave me complete independence to steer the direction of my research. Despite his extremely busy schedule, he always took out time for discussions and in the end for reviewing my thesis in detail.

I cannot thank Professor Markus Becherer enough for being such a big support at the institute. Markus was always available for discussions of any nature, be it regarding research, measurements, manuscript review, lab/equipments or career advice. Thank you so much for being such a wonderful mentor.

I would like to thank Prof. Agata Michalska and Prof. Krzysztof Maksymiuk, University of Warsaw Poland, for their collaboration in the work with membranes. They were extremely helpful and supportive with the work on membranes and electrode measurements. I am so much thankful to them for reviewing with the manuscripts we submitted, in detail and being so accessible whenever I had doubts.

I would also like to express my utmost gratitude towards Professor Alessio Gagliardi for supporting me through DFG project without any issues.

I extend a big thanks to Lucia, Katrin, Susi and Regina for their cooperation and help in all the office paper work. A big thanks to Rosi for keeping the labs running and procuring chemicals almost the next day a request was made to her. I would also like to acknowledge and appreciate the work of master students who worked with me during this period. Hao Wu, Andreas Märtl, Himanshi Rani, Miha Markocic and Rahul Bhalja, I thank all of you for your help with the measurements. I thank Werner Emer for helping me with the German translation of my thesis abstract. I also thank all my colleagues at the institute of nanoelectronics for helping me in one way or other.

A special gratitude and appreciation goes to one person who switched roles from being my life partner to being my guide and colleague everyday when we reached the doors of building N8 at the university, Vijay Deep Bhatt. Vijay's attitude and enthusiasm towards science and learning has been nothing less but inspiring for me. He introduced me to this research field of sensors and since then has been both my support and critic.

There are no words that can express my gratitude towards my father Mr L.P Joshi and my mother Mrs. Sushma Joshi. Their upbringing and values have been a permanent

motivation even when we are living oceans apart. I am thankful everyday for having such supportive and encouraging parents. My siblings Jayshree, Bhagyshree, Kavita, Harshvardhan, Dipesh and Partha along with my nephew Jayesh and niece Kaveri have made every stressful day better by a simple hello on phone.

Bibliography

[1] S. P. Mohanty and E. Kougianos. Biosensors: a tutorial review. *IEEE Potentials*, 25(2):35–40, March 2006. ISSN 0278-6648. doi: 10.1109/MP.2006.1649009.

[2] I. J. Higgins and C. R. Lowe. Introduction to the principles and applications of biosensors. *Philosophical transactions of the Royal Society of London. Series B, Biological sciences*, 316(1176):3–11, 1987. ISSN 09628436. doi: 10.1098/rstb.1987.0013.

[3] Jĭí Janata. *Principles of Chemical Sensors*. 2009. ISBN 9780387699301. doi: 10.1007/b136378.

[4] Mohammad Mahdi Ahmadi and Graham A. Jullien. Current-Mirror-Based Potentiostats for Three- Electrode Amperometric Electrochemical Sensors. *IEEE TRANSACTIONS ON CIRCUITS AND SYSTEMS*, 56(7):1339–1348, 2009.

[5] Renato Seeber, Chiara Zanardi, and György Inzelt. The inherent coupling of charge transfer and mass transport processes: the curious electrochemical reversibility. *ChemTexts*, 2(2):8, 2016. ISSN 2199-3793. doi: 10.1007/s40828-016-0027-3. URL `http://link.springer.com/10.1007/s40828-016-0027-3`.

[6] Pavel Damborsky, Juraj Svitel, and Jaroslav Katrlik. Optical Biosensors. *Essays in Biochemistry*, 60(June):91–100, 2016. ISSN 00092665. doi: 10.1042/EBC201500103.

[7] Spr. `https://nicoyalife.com/technology/surface-plasmon-resonance/localized-surface-plasmon-resonance-theory/`.

[8] M. Lämmerhofer E. Melnik, P. Müllner, R. Hainberger. Photolithographic local surface modification of integrated evanescent wave based biosensors. In *Dresdner Sensor-Symposium 2013*, volume 3, pages 193–197, 2013.

[9] Physiologyweb. `http://www.physiologyweb.com/lecture_notes/resting_membrane_potential/resting_membrane_potential_nernst_equilibrium_potential.html`.

[10] https://www.nanowerk.com/spotlight/spotid=43558_1.php, .

[11] http://www.jcrystal.com/products/wincnt/, .

[12] https://www.sigmaaldrich.com/catalog/substance/nonactin73693683384711?lang=de&region=DE.

[13] Mercketh500. https://www.sigmaaldrich.com/catalog/product/sial/87255?lang=de&region=DE.

[14] Saumya Joshi, Vijay Deep Bhatt, Ewa Jaworska, Markus Becherer, Krzysztof Maksymiuk, Agata Michalska, and Paolo Lugli. Using Lipophilic Membrane for Enhanced-Performance Aqueous Gated Carbon Nanotube Field Effect Transistors. *Physica Status Solidi (A) Applications and Materials Science*, 215(11):1–7, 2018. ISSN 18626319. doi: 10.1002/pssa.201700993.

[15] https://www.sigmaaldrich.com/catalog/substance/potassiumtetrakis4chlorophenylborate496111468077411?lang=de&region=DE.

[16] https://www.sigmaaldrich.com/catalog/substance/tridodecylmethylammoniumchloride57247717354811?lang=de&region=DE.

[17] Gamry instrument. Common Equivalent Circuit Models Part 3. *Gamry Instruments*, 3:1–13, 2017.

[18] Saumya Joshi, Vijay Deep Bhatt, Ewa Jaworska, Agata Michalska, Krzysztof Maksymiuk, Markus Becherer, Alessio Gagliardi, and Paolo Lugli. Ambient Processed, Water-Stable, Aqueous-Gated sub 1 V n-type Carbon Nanotube Field Effect Transistor. *Nature Scientific Reports*, 8(1):1–8, 2018. ISSN 20452322. doi: 10.1038/s41598-018-29882-w.

[19] Anantha Chandrakasan Jan M. Rabaey and Borivoje Nikolic. *"Chapter5 - The CMOS inverter"*. "1999".

[20] Kenji Nomura, Hiromichi Ohta, Akihiro Takagi, and Toshio Kamiya. Room-temperature fabrication of transparent flexible thin-film transistors using amorphous oxide semiconductors. *Nature*, 432(November):3383–3386, 2004. ISSN 00280836. doi: 10.1038/nature03090.

[21] T. Kamiya, K. Nomura, and H. Hosono. Origins of high mobility and low operation voltage of amorphous oxide tfts: Electronic structure, electron transport, defects and doping. *Journal of Display Technology*, 5(7):273–288, July 2009. ISSN 1551-319X. doi: 10.1109/JDT.2009.2021582.

[22] Solgel. https://www.gelest.com/applications/sol-gel-applications/.

[23] Tze-Ching Fung. *Amorphous In-Ga-Zn-O Thin Film Transistor for Future Optoelectronics*. PhD thesis, University of Michigan, 2010.

[24] https://www.nature.com/subjects/biosensors.

[25] Anthony P.F. Turner. Biosensors: Fundamentals and applications – historic book now open access. *Biosensors and Bioelectronics*, 65:A1, 2015. ISSN 0956-5663. doi: https://doi.org/10.1016/j.bios.2014.10.027. URL http://www.sciencedirect.com/science/article/pii/S0956566314008252.

[26] The development and characterisation of conducting polymeric-based sensing devices. *Synthetic Metals*, 154(1):25 – 28, 2005. ISSN 0379-6779. doi: https://doi.org/10.1016/j.synthmet.2005.07.008. URL http://www.sciencedirect.com/science/article/pii/S0379677905004613. Proceedings of the International Conference on Science and Technology of Synthetic Metals.

[27] Yang-Li Yang, Min-Chieh Chuang, Shyh-Liang Lou, and Joseph Wang. Thick-film textile-based amperometric sensors and biosensors. *Analyst*, 135:1230–1234, 2010. doi: 10.1039/B926339J. URL http://dx.doi.org/10.1039/B926339J.

[28] Henning Sirringhaus, Nir Tessler, and Richard H. Friend. Integrated optoelectronic devices based on conjugated polymers. *Science*, 280(5370):1741–1744, 1998. ISSN 0036-8075. doi: 10.1126/science.280.5370.1741. URL http://science.sciencemag.org/content/280/5370/1741.

[29] Zhenan Bao, Ananth Dodabalapur, and Andrew J. Lovinger. Soluble and processable regioregular poly(3-hexylthiophene) for thin film field-effect transistor applications with high mobility. *Applied Physics Letters*, 69(26):4108–4110, 1996. doi: 10.1063/1.117834. URL https://doi.org/10.1063/1.117834.

[30] Sybille Allard, Michael Forster, Benjamin Souharce, Heiko Thiem, and Ullrich Scherf. Organic semiconductors for solution-processable field-effect transistors (ofets). *Angewandte Chemie International Edition*, 47(22):4070–4098, 2008. doi: 10.1002/anie.200701920. URL https://onlinelibrary.wiley.com/doi/abs/10.1002/anie.200701920.

[31] Eric Bakker and Erno Pretsch. Potentiometric sensors for trace-level analysis. *Trends Analyt Chem.*, 24(3):199–207, 2005. ISSN 08966273. doi: 10.1016/j.surg.2006.10.010.Use.

[32] A. Bratov, N. Abramova, and A. Ipatov. Recent trends in potentiometric sensor arrays-A review. *Analytica Chimica Acta*, 678(2):149–159, 2010. ISSN 00032670.

doi: 10.1016/j.aca.2010.08.035. URL http://dx.doi.org/10.1016/j.aca.2010.08.035.

[33] P Bergveld. ISFET , Theory and Practice. Number October, pages 1–26, 2003.

[34] Jiri Homola, Sinclair S. Yee, and Gunter Gauglitz. Surface plasmon resonance sensors review.pdf. *Sensors and Actuators B*, 54:3–15, 1999. doi: 10.1016/S0925-4005(98)00321-9.

[35] Shuwen Zeng, Dominique Baillargeat, Ho Pui Ho, and Ken Tye Yong. Nanomaterials enhanced surface plasmon resonance for biological and chemical sensing applications. *Chemical Society Reviews*, 43(10):3426–3452, 2014. ISSN 14604744. doi: 10.1039/c3cs60479a.

[36] Juan B. González-Díaz, Antonio García-Martín, José M. García-Martín, Alfonso Cebollada, Gaspar Armelies, Borja Sepúlveda, Yury Alaverdyan, and Mikael Käll. Plasmonic Au/Co/Au nanosandwiches with enhanced magneto-optical activity. *Small*, 4(2):202–205, 2008. ISSN 16136810. doi: 10.1002/smll.200700594.

[37] Alexander M. Smith, Alpha A. Lee, and Susan Perkin. The Electrostatic Screening Length in Concentrated Electrolytes Increases with Concentration. *Journal of Physical Chemistry Letters*, 7(12):2157–2163, 2016. ISSN 19487185. doi: 10.1021/acs.jpclett.6b00867.

[38] Yan Levin. Reports on Progress in Physics Related content Electrostatic correlations : from plasma to biology Electrostatic correlations : from plasma to biology. *Reports on Progress in Physics*, 65(11):1577–1632, 2002.

[39] Yufei Jing, Vikram Jadhao, Jos W. Zwanikken, and Monica Olvera De La Cruz. Ionic structure in liquids confined by dielectric interfaces. *Journal of Chemical Physics*, 143(19), 2015. ISSN 00219606. doi: 10.1063/1.4935704.

[40] Estimating the Debye length The Debye length is the distance over which a charge.

[41] https://www.ceb.cam.ac.uk/research/groups/rg-eme/teaching-notes/the-electrical-double-layer, .

[42] https://web.nmsu.edu/~snsm/classes/chem435/Lab14/double_layer.html, .

[43] https://www.chem.uci.edu/~ardo/echem/UCI-CHEM248-2017W_lecture14.pdf.

[44] Paul Travers Mark Walport Charles A Janeway, Jr and Mark J Shlomchik. New York: Garland Science, 5 edition. ISBN 0-8153-3642-X.

[45] S. Tombelli, M. Minunni, and M. Mascini. Analytical applications of aptamers. *Biosensors and Bioelectronics*, 20(12):2424 – 2434, 2005. ISSN 0956-5663. doi: https://doi.org/10.1016/j.bios.2004.11.006. URL http://www.sciencedirect.com/science/article/pii/S0956566304005524. 20th Anniversary of Biosensors and Bioelectronics.

[46] C Tuerk and L Gold. Systematic evolution of ligands by exponential enrichment: Rna ligands to bacteriophage t4 dna polymerase. *Science*, 249(4968):505–510, 1990. ISSN 0036-8075. doi: 10.1126/science.2200121. URL http://science.sciencemag.org/content/249/4968/505.

[47] Marta Elena Díaz-García and Rosana Badía Laínño. Molecular imprinting in sol-gel materials: Recent developments and applications. *Microchimica Acta*, 149 (1):19–36, Feb 2005. ISSN 1436-5073. doi: 10.1007/s00604-004-0274-7. URL https://doi.org/10.1007/s00604-004-0274-7.

[48] Randy L. Haupt and Sue Ellen Haupt. John Wiley and Sons, Inc., 2 edition. ISBN 9780471455653.

[49] Amir Syahir, Kenji Usui, Kin-ya Tomizaki, Kotaro Kajikawa, and Hisakazu Mihara. Label and Label-Free Detection Techniques for Protein Microarrays. *Microarrays*, 4(2):228–244, 2015. ISSN 2076-3905. doi: 10.3390/microarrays4020228. URL http://www.mdpi.com/2076-3905/4/2/228/.

[50] Eva Maria Schmitteckert and Hans-Jürgen Schlicht. Detection of the human hepatitis b virus x-protein in transgenic mice after radioactive labelling at a newly introduced phosphorylation site. *Journal of General Virology*, 80(9):2501–2509, 1999. URL http://jgv.microbiologyresearch.org/content/journal/jgv/10.1099/0022-1317-80-9-2501.

[51] Nuo DUAN, Shi-Jia WU, and Zhou-Ping WANG. An aptamer-based fluorescence assay for ochratoxin a. *Chinese Journal of Analytical Chemistry*, 39(3):300 – 304, 2011. ISSN 1872-2040. doi: https://doi.org/10.1016/S1872-2040(10)60423-9. URL http://www.sciencedirect.com/science/article/pii/S1872204010604239.

[52] Cheng Yang, Yong Wang, Jean-Louis Marty, and Xiurong Yang. Aptamer-based colorimetric biosensing of ochratoxin a using unmodified gold nanoparticles indicator. *Biosensors and Bioelectronics*, 26(5):2724 – 2727, 2011. ISSN 0956-5663. doi: https://doi.org/10.1016/j.bios.2010.09.032. URL http://www.sciencedirect.com/science/article/pii/S0956566310006469.

[53] Amina Rhouati, Gaelle Catanante, Gilvanda Nunes, Akhtar Hayat, and Jean-Louis Marty. Label-free aptasensors for the detection of mycotoxins. *Sensors*, 16

(12), 2016. ISSN 1424-8220. doi: 10.3390/s16122178. URL http://www.mdpi.com/1424-8220/16/12/2178.

[54] Jonathan Daniels and Nader Pourmand. Label-Free Impedance Biosensors: Opportunities and Challenges. *Electroanalysis.*, 19(12):1239–1257, 2007. ISSN 15378276. doi: 10.1016/j.immuni.2010.12.017.Two-stage.

[55] Xiliang Luo and Jason J. Davis. Electrical biosensors and the label free detection of protein disease biomarkers. *Chem. Soc. Rev.*, 42:5944–5962, 2013. doi: 10.1039/C3CS60077G. URL http://dx.doi.org/10.1039/C3CS60077G.

[56] Sumio Iijima. Helical microtubes of graphitic carbon. *Nature*, 354:56–58, 1991. ISSN 0028-0836. doi: 10.1038/354056a0.

[57] Sumio Iijima and Toshinari Ichihashi. Single-shell carbon nanotubes of 1-nm diameter. *Nature*, 363(6430):603–605, 1993. ISSN 0028-0836. doi: 10.1038/363603a0. URL http://www.nature.com/articles/363603a0.

[58] D. S. Bethune, C. H. Kiang, M. S. de Vries, G. Gorman, R. Savoy, J. Vazquez, and R. Beyers. Cobalt-catalysed growth of carbon nanotubes with single-atomic-layer walls. *Nature*, 363(6430):605–607, 1993. ISSN 0028-0836. doi: 10.1038/363605a0. URL http://www.nature.com/articles/363605a0.

[59] Marc Monthioux and Vladimir L. Kuznetsov. Who should be given the credit for the discovery of carbon nanotubes? *Carbon*, 44(9):1621–1623, 2006. ISSN 00086223. doi: 10.1016/j.carbon.2006.03.019.

[60] Charles Roland Chambers and Theophilus Waughan Hughes. Manufacture of Carbon Filaments., 1889.

[61] V.M. Radushkevich, L.V. and Lukyanovich. The Structure of Carbon Forming in Thermal Decomposition of Carbon Monoxide on an Iron Catalyst. *Russian Journal of Physical Chemistry (In Russian)*, 26:88–95, 1952.

[62] Jan Prasek, Jana Drbohlavova, Jana Chomoucka, Jaromir Hubalek, Ondrej Jasek, Vojtech Adam, and Rene Kizek. Methods for carbon nanotubes synthesis - Review. *Journal of Materials Chemistry*, 21(40):15872–15884, 2011. ISSN 09599428. doi: 10.1039/c1jm12254a.

[63] Rajesh Purohit, Kuldeep Purohit, Saraswati Rana, R.S. Rana, and Vivek Patel. Carbon Nanotubes and Their Growth Methods. *Procedia Materials Science*, 6 (Icmpc):716–728, 2014. ISSN 22118128. doi: 10.1016/j.mspro.2014.07.088. URL http://linkinghub.elsevier.com/retrieve/pii/S2211812814004532.

[64] T. W. Ebbesen and P. M. Ajayan. Large-scale synthesis of carbon nanotubes. *Nature*, 358(6383):220–222, 1992. ISSN 00280836. doi: 10.1038/358220a0.

[65] T. Guo, P. Nikolaev, A. Thess, D. T. Colbert, and R. E. Smalley. Catalytic growth of single-walled manotubes by laser vaporization. *Chemical Physics Letters*, 243 (1-2):49–54, 1995. ISSN 00092614. doi: 10.1016/0009-2614(95)00825-O.

[66] Tomoaki Ikegami, Futoshi Nakanishi, Makoto Uchiyama, and Kenji Ebihara. Optical measurement in carbon nanotubes formation by pulsed laser ablation. *Thin Solid Films*, 457(1):7–11, 2004. ISSN 00406090. doi: 10.1016/j.tsf.2003.12.033.

[67] Mukul Kumar and Yoshinori Ando. Chemical Vapor Deposition of Carbon Nanotubes: A Review on Growth Mechanism and Mass Production. *Journal of Nanoscience and Nanotechnology*, 10(6):3739–3758, 2010. ISSN 15334880. doi: 10.1166/jnn.2010.2939. URL `http://openurl.ingenta.com/content/xref?genre=article{&}issn=1533-4880{&}volume=10{&}issue=6{&}spage=3739`.

[68] von Sturm Ferdinand. Graphite fibers and filaments. springer series in materials science, vol. 5. by m. s. dresselhaus, g. dresselhaus, k. sugihara, i. l. spain and h. a. goldberg. springer, berlin/heidelberg 1988. x, 382 pp., hard cover, dm 122.00.—isbn 3-540-18938-6. *Advanced Materials*, 1(4):130–131. doi: 10.1002/adma.19890010411. URL `https://onlinelibrary.wiley.com/doi/abs/10.1002/adma.19890010411`.

[69] M.S. Dresselhaus, G. Dresselhaus, and P.C. Eklund. Chapter 3 - structure of fullerenes. In M.S. Dresselhaus, G. Dresselhaus, and P.C. Eklund, editors, *Science of Fullerenes and Carbon Nanotubes*, pages 60 – 79. Academic Press, San Diego, 1996. ISBN 978-0-12-221820-0. doi: https://doi.org/10.1016/B978-012221820-0/50003-4. URL `http://www.sciencedirect.com/science/article/pii/B9780122218200500034`.

[70] Phaedon Avouris. Molecular electronics with carbon nanotubes. *Accounts of Chemical Research*, 35(12):1026–1034, 2002. ISSN 00014842. doi: 10.1021/ar010152e.

[71] Prabhakar R Bandaru. Electrical Properties and Applications of Carbon Nanotube Structures. *Journal of Nanoscience and Nanotechnology*, 7 (4):1239–1267, 2007. ISSN 15334880. doi: 10.1166/jnn.2007.307. URL `http://openurl.ingenta.com/content/xref?genre=article{&}issn=1533-4880{&}volume=7{&}issue=4{&}spage=1239`.

[72] W. S. Su, T. C. Leung, and C. T. Chan. Work function of single-walled and multiwalled carbon nanotubes: First-principles study. *Physical Review B - Condensed Matter and Materials Physics*, 76(23):2–9, 2007. ISSN 10980121. doi: 10.1103/PhysRevB.76.235413.

[73] AK Geim and KS Novoselov. The rise of graphene. *Nature materials*, pages 183–191, 2007. URL `http://www.nature.com/articles/doi:10.1038{%}2Fnmat1849`.

[74] Sami Rosenblatt, Hao Lin, Vera Sazonova, Sandip Tiwari, and Paul L. McEuen. Mixing at 50 GHz using a single-walled carbon nanotube transistor. *Applied Physics Letters*, 87(15):1–3, 2005. ISSN 00036951. doi: 10.1063/1.2103391.

[75] D A Stewart. Photocurrents in nanotube junctions. (1):1–5.

[76] Ji Ung Lee. Band-gap renormalization in carbon nanotubes: Origin of the ideal diode behavior in carbon nanotube p-n structures. *Physical Review B - Condensed Matter and Materials Physics*, 75(7):1–5, 2007. ISSN 10980121. doi: 10.1103/PhysRevB.75.075409.

[77] M. Krüger, M. R. Buitelaar, T. Nussbaumer, C. Schönenberger, and L. Forró. Electrochemical carbon nanotube field-effect transistor. *Applied Physics Letters*, 78(9):1291–1293, 2001. ISSN 00036951. doi: 10.1063/1.1350427.

[78] Koen Besteman, Jeong O. Lee, Frank G.M. Wiertz, Hendrik A. Heering, and Cees Dekker. Enzyme-coated carbon nanotubes as single-molecule biosensors. *Nano Letters*, 3(6):727–730, 2003. ISSN 15306984. doi: 10.1021/nl034139u.

[79] Keith Bradley, Alona Davis, Jean Christophe P. Gabriel, and G. Grüner. Integration of cell membranes and nanotube transistors. *Nano Letters*, 5(5):841–845, 2005. ISSN 15306984. doi: 10.1021/nl050157v.

[80] Iddo Heller, Jing Kong, Keith A. Williams, Cees Dekker, and Serge G. Lemay. Electrochemistry at single-walled carbon nanotubes: The role of band structure and quantum capacitance. *Journal of the American Chemical Society*, 128(22):7353–7359, 2006. ISSN 00027863. doi: 10.1021/ja061212k.

[81] Zhuang Liu, Weibo Cai, Lina He, Nozomi Nakayama, Kai Chen, Xiaoming Sun, Xiaoyuan Chen, and Hongjie Dai. In vivo biodistribution and highly efficient tumour targeting of carbon nanotubes in mice. *Nature Nanotechnology*, 2(1):47–52, 2007. ISSN 17483395. doi: 10.1038/nnano.2006.170.

[82] J.-P. Salvetat, J.-M. Bonard, and N.H. Thomson. Mechanical properties of carbon nanotubes. *Applied Physics A*, 69(3):255–260, 1999.

ISSN 0947-8396. doi: 10.1007/s003390050999. URL http://link.springer.com/10.1007/s003390050999$\delimiter"026E30F$nhttp://link.springer.com/article/10.1007/s003390050999.

[83] M. M. J. Treacy, T. W. Ebbesen, and J. M. Gibson. Exceptionally high Young's modulus observed for individual carbon nanotubes. 381(6584):678–680, 1996. ISSN 0028-0836. doi: 10.1038/381678a0. URL http://www.nature.com/doifinder/10.1038/381678a0.

[84] B. I. Yakobson. Mechanical relaxation and "intramolecular plasticity" in carbon nanotubes. *Applied Physics Letters*, 72(8):918–920, 1998. ISSN 00036951. doi: 10.1063/1.120873.

[85] Min-Feng Yu, Bradley S. Files, Sivaram Arepalli, and Rodney S. Ruoff. Tensile Loading of Ropes of Single Wall Carbon Nanotubes and their Mechanical Properties. *Physical Review Letters*, 84(24):5552–5555, 2000. ISSN 0031-9007. doi: 10.1103/PhysRevLett.84.5552. URL http://www.ncbi.nlm.nih.gov/pubmed/10990992{%}5Cnhttp://link.aps.org/doi/10.1103/PhysRevLett.84.5552.

[86] B C Edwards. The space elevator: an ideal application for the free electron laser. *Laser and Beam Control Technologies*, 4632:134–140, 2002. ISSN 0277786X. doi: 10.1117/12.469764.

[87] Akira Toriumi, Masao Iwase, and Hiroyuki Tango. On the Universality of Inversion Layer Mobility in Si MOSFET's: Part I—Effects of Substrate Impurity Concentration. *IEEE Transactions on Electron Devices*, 41(12):2357–2362, 1994. ISSN 15579646. doi: 10.1109/16.337449.

[88] Marko Burghard, Hagen Klauk, and Klaus Kern. Carbon-based field-effect transistors for nanoelectronics. *Advanced Materials*, 21(25-26):2586–2600, 2009. ISSN 09359648. doi: 10.1002/adma.200803582.

[89] S. H. Lo, D. A. Buchanan, Y. Taur, and W. Wang. Quantum-mechanical modeling of electron tunneling current from the inversion layer of ultra-thin-oxide nMOSFET's. *IEEE Electron Device Letters*, 18(5):209–211, 1997. ISSN 07413106. doi: 10.1109/55.568766.

[90] Seung Chul Song, Zhibo Zhang, Craig Huffman, Jang H. Sim, Sang Ho Bae, Paul D. Kirsch, Prashant Majhi, Rino Choi, Naim Moumen, and Byoung Hun Lee. Highly manufacturable advanced gate-stack technology for sub-45-nm self-aligned gate-first CMOSFETs. *IEEE Transactions on Electron Devices*, 53(5):979–989, 2006. ISSN 00189383. doi: 10.1109/TED.2006.872700.

[91] Sj Tans, Arm Verschueren, and Cees Dekker. Room-temperature transistor based on a single carbon nanotube. *Nature*, 672(1989):669–672, 1998. ISSN 0028-0836. doi: 10.1038/29954. URL `http://www.nature.com/nature/journal/v393/n6680/abs/393049a0.html`.

[92] R. Martel, T. Schmidt, H. R. Shea, T. Hertel, and Ph Avouris. Single- and multi-wall carbon nanotube field-effect transistors. *Applied Physics Letters*, 73 (17):2447–2449, 1998. ISSN 00036951. doi: 10.1063/1.122477.

[93] S. Ilani, L. A. K. Donev, M. Kindermann, and P. L. McEuen. Measurement of the quantum capacitance of interacting electrons in carbon nanotubes. *Nature Physics*, 2(10):687–691, 2006. ISSN 1745-2473. doi: 10.1038/nphys412. URL `http://www.nature.com/doifinder/10.1038/nphys412`.

[94] J. Appenzeller, M. Radosavljević, J. Knoch, and Ph Avouris. Tunneling Versus Thermionic Emission in One-Dimensional Semiconductors. *Physical Review Letters*, 92(4):4, 2004. ISSN 10797114. doi: 10.1103/PhysRevLett.92.048301.

[95] M. H. Yang, K. B K Teo, Laurent Gangloff, W. I. Milne, D. G. Hasko, Y. Robert, and P. Legagneux. Advantages of top-gate, high-k dielectric carbon nanotube field-effect transistors. *Applied Physics Letters*, 88(11):23–25, 2006. ISSN 00036951. doi: 10.1063/1.2186100.

[96] Yuerui Lu, Sarunya Bangsaruntip, Xinran Wang, Li Zhang, Yoshio Nishi, and Hongjie Dai. DNA functionalization of carbon nanotubes for ultrathin atomic layer deposition of high κ dielectrics for nanotube transistors with 60 mV/decade switching. *Journal of the American Chemical Society*, 128(11):3518–3519, 2006. ISSN 00027863. doi: 10.1021/ja058836v.

[97] S. J. Wind, J. Appenzeller, R. Martel, V. Derycke, and Ph Avouris. Vertical scaling of carbon nanotube field-effect transistors using top gate electrodes. *Applied Physics Letters*, 80(20):3817–3819, 2002. ISSN 00036951. doi: 10.1063/1.1480877.

[98] S Heinze, J Tersoff, R Martel, V Derycke, J Appenzeller, and Ph Avouris. Carbon nanotubes as schottky barrier transistors. *Physical review letters*, 89(10):106801, 2002. ISSN 0031-9007. doi: 10.1103/PhysRevLett.89.106801.

[99] Ali Javey, Jing Guo, Qian Wang, Mark Lundstrom, and Hongjie Dai. Ballistic carbon nanotube field-effect transistors. *Nature*, 424(6949):654–657, 2003. ISSN 00280836. doi: 10.1038/nature01797.

[100] Mark C. Hersam. Progress towards monodisperse single-walled carbon nanotubes. *Nature Nanotechnology*, 3(7):387–394, 2008. ISSN 17483395. doi: 10.1038/nnano.2008.135.

[101] Li Zhang, Sasa Zaric, Xiaomin Tu, Xinran Wang, Wei Zhao, and Hongjie Dai. Assessment of chemically separated carbon nanotubes for nanoelectronics. *Journal of the American Chemical Society*, 130(8):2686–2691, 2008. ISSN 00027863. doi: 10.1021/ja7106492.

[102] N. Izard, S. Kazaoui, K. Hata, T. Okazaki, T. Saito, S. Iijima, and N. Minami. Semiconductor-enriched single wall carbon nanotube networks applied to field effect transistors. *Applied Physics Letters*, 92(24), 2008. ISSN 00036951. doi: 10.1063/1.2939560.

[103] Melburne C. LeMieux, Mark Roberts, Soumendra Barman, Wan Jin Yong, Min Kim Jong, and Zhenan Bao. Self-sorted, aligned nanotube networks for thin-film transistors. *Science*, 321(5885):101–104, 2008. ISSN 00368075. doi: 10.1126/science.1156588.

[104] Stéphane Auvray, Vincent Derycke, Marcelo Goffman, Arianna Filoramo, Oliver Jost, and Jean Philippe Bourgoin. Chemical optimization of self-assembled carbon nanotube transistors. *Nano Letters*, 5(3):451–455, 2005. ISSN 15306984. doi: 10.1021/nl048032y.

[105] Richard E. Smalley Michael S. Strano, Christopher A. Dyke, Monica L. Usrey, Paul W. Barone, Mathew J. Allen, Hongwei Shan, Carter Kittrell, Robert H. Hauge, James M. Tour. Electronic Structure Control of Single-Walled Carbon Nanotube Functionalization. *Science*, 301(5639):1519–1522, 2003. ISSN 0036-8075. doi: 10.1126/science.1087691. URL `http://www.sciencemag.org/cgi/doi/10.1126/science.1087691`.

[106] Shouhei Toyoda, Yoshifumi Yamaguchi, Masataka Hiwatashi, Yasuhiko Tomonari, Hiroto Murakami, and Naotoshi Nakashima. Separation of semiconducting single-walled carbon nanotubes by using a long-alkyl-chain benzenediazonium compound. *Chemistry - An Asian Journal*, 2(1):145–149, 2007. ISSN 18614728. doi: 10.1002/asia.200600279.

[107] Houjin Huang, Ryuichiro Maruyama, Kazuhiro Noda, Hisashi Kajiura, and Koji Kadono. Preferential destruction of metallic single-walled carbon nanotubes by laser irradiation. *Journal of Physical Chemistry B*, 110(14):7316–7320, 2006. ISSN 15206106. doi: 10.1021/jp056684k.

[108] Seong Jun Kang, Coskun Kocabas, Taner Ozel, Moonsub Shim, Ninad Pimparkar, Muhammad a Alam, Slava V Rotkin, and John a Rogers. High-performance electronics using dense, perfectly aligned arrays of single-walled carbon nanotubes. *Nature nanotechnology*, 2(4):230–236, 2007. ISSN 1748-3387. doi: 10.1038/nnano.2007.77.

[109] Qing Cao and John A. Rogers. Random networks and aligned arrays of single-walled carbon nanotubes for electronic device applications. *Nano Research*, 1(4): 259–272, 2008. ISSN 1998-0124. doi: 10.1007/s12274-008-8033-4. URL http://link.springer.com/10.1007/s12274-008-8033-4.

[110] Lithography. http://www.lithoguru.com/scientist/lithobasics.html.

[111] Chris Mack. In Chris Mack, editor, *Fundamental Principles of Optical Lithography*. Wiley, 2007. ISBN 978-0-470-01893-4.

[112] hmds. www.microchemicals.com/downloads/application_notes.html.

[113] Matteo Altissimo. E-beam lithography for micro-/nanofabrication. *Biomicrofluidics*, 4(2):2–7, 2010. ISSN 19321058. doi: 10.1063/1.3437589.

[114] Juan R. Maldonado and Martin Peckerar. X-ray lithography: Some history, current status and future prospects. *Microelectronic Engineering*, 161:87–93, 2016. ISSN 01679317. doi: 10.1016/j.mee.2016.03.052. URL http://dx.doi.org/10.1016/j.mee.2016.03.052.

[115] C Rensch, S Hell, M V Schickfus, and S Hunklinger. Laser scanner for direct writing lithography. *Applied optics*, 28(17):3754–8, 1989. ISSN 0003-6935. doi: 10.1364/AO.28.003754. URL http://www.ncbi.nlm.nih.gov/pubmed/20555769.

[116] Steven Barcelo and Zhiyong Li. Nanoimprint lithography for nanodevice fabrication. *Nano Convergence*, 3(1):21, 2016. ISSN 2196-5404. doi: 10.1186/s40580-016-0081-y. URL http://nanoconvergencejournal.springeropen.com/articles/10.1186/s40580-016-0081-y.

[117] https://www.che.iitb.ac.in/faculty/prasad/CL240/Metallization_lecture.pdf.

[118] Hugh O. Pierson. *Handbook of Chemical Vapor Deposition (CVD)*. NOYES PUBLICATIONS, New Jersey, U.S.A. WILLIAM, 2nd edition, 1999. ISBN 0-8155-1432-8. doi: 10.1016/B978-081551432-9.50006-1.

[119] http://www.fhi-berlin.mpg.de/acnew/department/pages/teaching/pages/teaching__wintersemester__2012_2013/julian_tornow__chemical-vapor-deposition__130118.pdf.

[120] Richard W. Johnson, Adam Hultqvist, and Stacey F. Bent. A brief review of atomic layer deposition: from fundamentals to applications. *Materials Today*, 17(5):236 – 246, 2014. ISSN 1369-7021. doi: https://doi.org/10.1016/j.mattod.2014.04.026. URL http://www.sciencedirect.com/science/article/pii/S1369702114001436.

[121] Cesar Augusto Duarte Rodriguez and Germano Tremiliosi-Filho. *Electrochemical Deposition*, pages 918–922. Springer US, Boston, MA, 2013. ISBN 978-0-387-92897-5. doi: 10.1007/978-0-387-92897-5_700. URL https://doi.org/10.1007/978-0-387-92897-5_700.

[122] https://nptel.ac.in/courses/103106075/12.

[123] K. Alavi. Molecular beam epitaxy. In K.H. Jürgen Buschow, Robert W. Cahn, Merton C. Flemings, Bernhard Ilschner, Edward J. Kramer, Subhash Mahajan, and Patrick Veyssière, editors, *Encyclopedia of Materials: Science and Technology*, pages 5765 – 5780. Elsevier, Oxford, 2001. ISBN 978-0-08-043152-9. doi: https://doi.org/10.1016/B0-08-043152-6/01002-0. URL http://www.sciencedirect.com/science/article/pii/B0080431526010020.

[124] A.Y. Cho and I. Hayashi. Surface structures and photoluminescence of molecular beam epitaxial films of gaas. *Solid-State Electronics*, 14(2):125 – 132, 1971. ISSN 0038-1101. doi: https://doi.org/10.1016/0038-1101(71)90087-6. URL http://www.sciencedirect.com/science/article/pii/0038110171900876.

[125] D. Depla, S. Mahieu, and J.E. Greene. Chapter 5 - sputter deposition processes. In Peter M. Martin, editor, *Handbook of Deposition Technologies for Films and Coatings (Third Edition)*, pages 253 – 296. William Andrew Publishing, Boston, third edition edition, 2010. ISBN 978-0-8155-2031-3. doi: https://doi.org/10.1016/B978-0-8155-2031-3.00005-3. URL http://www.sciencedirect.com/science/article/pii/B9780815520313000053.

[126] Gavin A. Bernardin, Nathan A. Davies, and Chris E. Finlayson. Spray-coating deposition techniques for polymeric semiconductor blends. *Materials Science in Semiconductor Processing*, 71:174 – 180, 2017. ISSN 1369-8001. doi: https://doi.org/10.1016/j.mssp.2017.07.026. URL http://www.sciencedirect.com/science/article/pii/S1369800117312489.

[127] Ludwig Julius Gauckler. Thin Film Deposition Using Spray Pyrolysis. (March 2005):103–104, 2015. doi: 10.1007/s10832-005-0870-x.

[128] Mariya Petrova Aleksandrova, Nikola Petrov Nikolov, and Svetozar Krastev Andreev. Investigation of Spray Coating as a Deposition Technique for Fabrication of Multilayer Organic Structures. pages 215–218, 2009.

[129] Mang Mang Ling and Zhenan Bao. Thin film deposition, patterning, and printing in organic thin film transistors. *Chemistry of Materials*, 16(23):4824–4840, 2004. doi: 10.1021/cm0496117. URL https://doi.org/10.1021/cm0496117.

[130] Zhenan Bao, Yi Feng, Ananth Dodabalapur, V. R. Raju, and Andrew J. Lovinger. High-performance plastic transistors fabricated by printing techniques. *Chemistry of Materials*, 9(6):1299–1301, 1997. doi: 10.1021/cm9701163. URL https://doi.org/10.1021/cm9701163.

[131] T. Kawase, H. Sirringhaus, R. H. Friend, and T. Shimoda. Inkjet printed via-hole interconnections and resistors for all-polymer transistor circuits. *Advanced Materials*, 13(21):1601–1605. doi: 10.1002/1521-4095(200111)13:21⟨1601::AID-ADMA1601⟩3.0.CO;2-X.

[132] http://home.deib.polimi.it/sampietr/ESO/Grimoldi.pdf.

[133] Saumya Joshi, Vijay Deep Bhatt, Andreas Märtl, Markus Becherer, and Paolo Lugli. Regenerative, highly-sensitive, non-enzymatic dopamine sensor and impact of different buffer systems in dopamine sensing. *Biosensors*, 8(1):1–10, 2018. ISSN 20796374. doi: 10.3390/bios8010009.

[134] Liviu M. Dumitru, Kyriaki Manoli, Maria Magliulo, Luigia Sabbatini, Gerardo Palazzo, and Luisa Torsi. Plain poly(acrylic acid) gated organic field-effect transistors on a flexible substrate. *ACS Applied Materials & Interfaces*, 5(21):10819–10823, 2013. doi: 10.1021/am403008b. URL https://doi.org/10.1021/am403008b. PMID: 24144062.

[135] Kosuke Izutsu. *Electrodeposition from Ionic Liquids Nanostructured Materials in Electrochemistry Electrochemistry*. 2009. ISBN 9783527315659. URL http://onlinelibrary.wiley.com/book/10.1002/9783527629152.

[136] Felix Buth, Andreas Donner, Matthias Sachsenhauser, Martin Stutzmann, and Jose A. Garrido. Biofunctional electrolyte-gated organic field-effect transistors. *Advanced Materials*, 24(33):4511–4517. doi: 10.1002/adma.201201841. URL https://onlinelibrary.wiley.com/doi/abs/10.1002/adma.201201841.

[137] Hong Xue, Rajendar Verma, and Jean'ne M. Shreeve. Review of ionic liquids with fluorine-containing anions. *Journal of Fluorine Chemistry*, 127(2):159 – 176, 2006. ISSN 0022-1139. doi: https://doi.org/10.1016/j.jfluchem.2005.11.007. URL http://www.sciencedirect.com/science/article/pii/S0022113905003350.

[138] T. Uemura, M. Yamagishi, S. Ono, and J. Takeya. Low-voltage operation of n-type organic field-effect transistors with ionic liquid. *Applied Physics Letters*, 95 (10):103301, 2009. doi: 10.1063/1.3225153. URL https://doi.org/10.1063/1.3225153.

[139] Elias Said, Xavier Crispin, Lars Herlogsson, Sami Elhag, Nathaniel D. Robinson, and Magnus Berggren. Polymer field-effect transistor gated via a

poly(styrenesulfonic acid) thin film. *Applied Physics Letters*, 89(14):143507, 2006. doi: 10.1063/1.2358315. URL `https://doi.org/10.1063/1.2358315`.

[140] Loig Kergoat, Lars Herlogsson, Daniele Braga, Benoit Piro, Minh Chau Pham, Xavier Crispin, Magnus Berggren, and Gilles Horowitz. A water-gate organic field-effect transistor. *Advanced Materials*, 22(23):2565–2569, 2010. ISSN 09359648. doi: 10.1002/adma.200904163.

[141] Denjung Wang, Vincent Noël, and Benoît Piro. Electrolytic gated organic field-effect transistors for application in biosensors—a review. *Electronics*, 5(1), 2016. ISSN 2079-9292. doi: 10.3390/electronics5010009. URL `http://www.mdpi.com/2079-9292/5/1/9`.

[142] Zhigang Zhu, Luis Garcia-Gancedo, Andrew J Flewitt, Huaqing Xie, Francis Moussy, and William I Milne. A critical review of glucose biosensors based on carbon nanomaterials: carbon nanotubes and graphene. *Sensors (Basel, Switzerland)*, 12(5):5996–6022, 2012. ISSN 1424-8220. doi: 10.3390/s120505996. URL `http://www.mdpi.com/1424-8220/12/5/5996/htm`.

[143] Hideaki Ishii and Yusuke Nishida. Effect of lactate accumulation during exercise-induced muscle fatigue on the sensorimotor cortex. *Journal of Physical Therapy Science*, 25(12):1637–1642, 2013. doi: 10.1589/jpts.25.1637.

[144] Cristina Boero, Sandro Carrara, Giovanna Del Vecchio, Laura Calzà, and Giovanni De Micheli. Highly sensitive carbon nanotube-based sensing for lactate and glucose monitoring in cell culture. *IEEE Transactions on Nanobioscience*, 10(1):59–67, 2011. ISSN 15361241. doi: 10.1109/TNB.2011.2138157.

[145] Hyeonseok Yoon, Sungrok Ko, and Jyongsik Jang. Field-effect-transistor sensor based on enzyme-functionalized polypyrrole nanotubes for glucose detection. *Journal of Physical Chemistry B*, 112(32):9992–9997, 2008. ISSN 15206106. doi: 10.1021/jp800567h.

[146] Qin Yan, Hong-ning Zheng, Chuan Jiang, Kun Li, and Shou-jun Xiao. EDC/NHS activation mechanism of polymethacrylic acid: anhydride versus NHS-ester. pages 69939–69947, 2015. doi: 10.1039/c5ra13844b.

[147] Junjie Shan, Jinhua Li, Xueying Chu, Mingze Xu, Fangjun Jin, and Xiaojun Wang. concentrations using a MoS2-based field-effect. pages 7942–7948, 2018. doi: 10.1039/c7ra13614e.

[148] Meng Zhang, Caizhi Liao, Chun Hin Mak, Peng You, Chee Leung Mak, and Feng Yan. Highly sensitive glucose sensors based on enzyme-modified whole-graphene solution-gated transistors. pages 1–6, 2015. doi: 10.1038/srep08311.

[149] Wenzhao Jia, Amay J Bandodkar, Gabriela Valde-Ramírez, Joshua R Windmiller, Zhanjun Yang, Julian Ramírez, Garrett Chan, and Joseph Wang. Electrochemical Tattoo Biosensors for Real-Time Noninvasive Lactate Monitoring in Human Perspiration. 2013. doi: 10.1021/ac401573r.

[150] Ming Xing Chu, Kumiko Miyajima, Daishi Takahashi, Takahiro Arakawa, Kenji Sano, Shin ichi Sawada, Hiroyuki Kudo, Yasuhiko Iwasaki, Kazunari Akiyoshi, Manabu Mochizuki, and Kohji Mitsubayashi. Soft contact lens biosensor for in situ monitoring of tear glucose as non-invasive blood sugar assessment. *Talanta*, 83(3):960 – 965, 2011. ISSN 0039-9140. doi: https://doi.org/10.1016/j.talanta.2010.10.055. URL `http://www.sciencedirect.com/science/article/pii/S0039914010008519`.

[151] Seon Joo Park, Heehong Yang, Seung Hwan Lee, Hyun Seok Song, Chul Soon Park, Joonwon Bae, Oh Seok Kwon, Tai Hyun Park, and Jyongsik Jang. Dopamine Receptor D1 Agonism and Antagonism Using a Field-Effect Transistor Assay. *ACS Nano*, page acsnano.7b01722, 2017. ISSN 1936-0851. doi: 10.1021/acsnano.7b01722. URL `http://pubs.acs.org/doi/abs/10.1021/acsnano.7b01722`.

[152] D Clark and F J White. D1 dopamine receptor - the search for a function: a critical evaluation of the D1/D2 dopamine classification and its functional implications. *Synapse*, 1:347–388, 1997.

[153] John D. Elsworth and Robert H. Roth. Dopamine Synthesis, Uptake, Metabolism, and Receptors: Relevance to Gene Therapy of Parkinson's Disease. *Experimental Neurology*, 144(1):4–9, 1997. ISSN 00144886. doi: 10.1006/exnr.1996.6379. URL `http://linkinghub.elsevier.com/retrieve/pii/S0014488696963797`.

[154] Jong-Hoon Kim, Jonathan M. Auerbach, José A. Rodríguez-Gómez, Iván Velasco, Denise Gavin, Nadya Lumelsky, Sang-Hun Lee, John Nguyen, Rosario Sánchez-Pernaute, Krys Bankiewicz, and Ron McKay. Dopamine neurons derived from embryonic stem cells function in an animal model of Parkinson's disease. *Nature*, 418(6893):50–56, 2002. ISSN 0028-0836. doi: 10.1038/nature00900. URL `http://www.nature.com/doifinder/10.1038/nature00900`.

[155] Victoria Carrera, Esther Sabater, Eugenio Vilanova, and Miguel A. Sogorb. A simple and rapid HPLC-MS method for the simultaneous determination of epinephrine, norepinephrine, dopamine and 5-hydroxytryptamine: Application to the secretion of bovine chromaffin cell cultures. *Journal of Chromatography B: Analytical Technologies in the Biomedical and Life Sciences*, 847(2):88–94, 2007. ISSN 15700232. doi: 10.1016/j.jchromb.2006.09.032.

[156] Mariusz Mamiński, Małgorzata Olejniczak, Michał Chudy, Artur Dybko, and Zbigniew Brzózka. Spectrophotometric determination of dopamine in microliter scale using microfluidic system based on polymeric technology. *Analytica Chimica Acta*, 540(1):153–157, 2005. ISSN 00032670. doi: 10.1016/j.aca.2004.09.011.

[157] Nengqin Jia, Zhiyong Wang, Guofeng Yang, Hebai Shen, and Longzhang Zhu. Electrochemical properties of ordered mesoporous carbon and its electroanalytical application for selective determination of dopamine. *Electrochemistry Communications*, 9(2):233–238, 2007. ISSN 13882481. doi: 10.1016/j.elecom.2006.08.050.

[158] Shah R Ali, Yufeng Ma, Rishi R Parajuli, Yetunde Balogun, Warren Y Lai, Huixin He, Bell Labs, and Murray Hill. A Nonoxidative Sensor Based on a Self-Doped Polyaniline / Carbon Nanotube Composite for Sensitive and Selective Detection of the Neurotransmitter Dopamine. *Analytical Chemistry*, 79(6):2583–2587, 2007. ISSN 0003-2700. doi: Doi10.3390/S8128423.

[159] Hao Tang, Peng Lin, Helen L W Chan, and Feng Yan. Highly sensitive dopamine biosensors based on organic electrochemical transistors. *Biosensors and Bioelectronics*, 26(11):4559–4563, 2011. ISSN 09565663. doi: 10.1016/j.bios.2011.05.025. URL `http://dx.doi.org/10.1016/j.bios.2011.05.025`.

[160] Analysis of dopamine and tyrosinase activity on Ion-Sensitive Field-Effect Transistor (ISFET) devices. *Chemistry - A European Journal*, 13(26):7288–7293, 2007. ISSN 09476539. doi: 10.1002/chem.200700734.

[161] Takao Someya, Ananth Dodabalapur, Jia Huang, Kevin C. See, and Howard E. Katz. Chemical and physical sensing by organic field-effect transistors and related devices. *Advanced Materials*, 22(34):3799–3811, 2010. ISSN 09359648. doi: 10.1002/adma.200902760.

[162] Daniel A. Bernards, Daniel J. Macaya, Maria Nikolou, John A. DeFranco, Seiichi Takamatsu, and George G. Malliaras. Enzymatic sensing with organic electrochemical transistors. *J. Mater. Chem.*, 18(1):116–120, 2008. ISSN 0959-9428. doi: 10.1039/B713122D. URL `http://xlink.rsc.org/?DOI=B713122D`.

[163] Dong C. Li, Po Hung Yang, and M. S C Lu. CMOS open-gate ion-sensitive field-effect transistors for ultrasensitive dopamine detection. *IEEE Transactions on Electron Devices*, 57(10):2761–2767, 2010. ISSN 00189383. doi: 10.1109/TED.2010.2063330.

[164] Bor Ran Li, Chien Wei Chen, Wan Ling Yang, Ti Yu Lin, Chien Yuan Pan, and Yit Tsong Chen. Biomolecular recognition with a sensitivity-enhanced nanowire transistor biosensor. *Biosensors and Bioelectronics*, 45(1):252–259, 2013. ISSN

09565663. doi: 10.1016/j.bios.2013.02.009. URL http://dx.doi.org/10.1016/j.bios.2013.02.009.

[165] Omid Ghaffari Nik, Xiao Yuan Chen, and Serge Kaliaguine. Amine-functionalized zeolite FAU/EMT-polyimide mixed matrix membranes for CO2/CH4 separation. *Journal of Membrane Science*, 379(1-2):468–478, 2011. ISSN 03767388. doi: 10.1016/j.memsci.2011.06.019. URL http://dx.doi.org/10.1016/j.memsci.2011.06.019.

[166] J. A. Faniran and H F Shurvell. Infrared spectra of phenylboronic acid (normal and deuterated) and diphenyl phenylboronate. *Canadian Journal of Chemistry*, 46(12):2089–2095, 1968. ISSN 0008-4042. doi: 10.1139/v68-341. URL http://www.nrcresearchpress.com/doi/abs/10.1139/v68-341.

[167] Jun Seop Lee, Jungkyun Oh, Sung Gun Kim, and Jyongsik Jang. Highly sensitive and selective field-effect-transistor nonenzyme dopamine sensors based on pt/conducting polymer hybrid nanoparticles. *Small*, 11(20):2399–2406, 2015. doi: 10.1002/smll.201403263. URL https://onlinelibrary.wiley.com/doi/abs/10.1002/smll.201403263.

[168] J. A. Goode, J. V.H. Rushworth, and P. A. Millner. Biosensor Regeneration: A Review of Common Techniques and Outcomes. *Langmuir*, 31(23):6267–6276, 2015. ISSN 15205827. doi: 10.1021/la503533g.

[169] Lin Liu, Ning Xia, Yun Xing, and Dehua Deng. Boronic acid-based electrochemical sensors for detection of biomolecules. *International Journal of Electrochemical Science*, 8(9):11161–11174, 2013. ISSN 14523981.

[170] Bharat B. Aggarwal. Tumor necrosis factors: Developments during the last decade. *European Cytokine Network*, 7(2):93–124, 1996. ISSN 1148-5493.

[171] Dan Aderka. The potential biological and clinical significance of the soluble tumor necrosis factor receptors. *Cytokine & Growth Factor Reviews*, 7(3):231 – 240, 1996. ISSN 1359-6101. doi: https://doi.org/10.1016/S1359-6101(96)00026-3. URL http://www.sciencedirect.com/science/article/pii/S1359610196000263.

[172] W. Joshua Frazier and Mark W. Hall. Immunoparalysis and adverse outcomes from critical illness. *Pediatric Clinics of North America*, 55(3):647 – 668, 2008. ISSN 0031-3955. doi: https://doi.org/10.1016/j.pcl.2008.02.009. URL http://www.sciencedirect.com/science/article/pii/S0031395508000825. Pediatric Critical Care.

[173] Ana de Moraes and Lauro Kubota. Recent Trends in Field-Effect Transistors-Based Immunosensors. *Chemosensors*, 4(4):20, 2016. ISSN 2227-9040. doi: 10.3390/chemosensors4040020. URL `http://www.mdpi.com/2227-9040/4/4/20`.

[174] A.T. Charlie Johnson Mitchell Lerner, Brett Goldsmith, Ronald McMillon, Jennifer Dailey, Shreekumar Pillai, Shree R. Singh. A Carbon Nanotube Immunosensor for Salmonella. URL `arxiv.org`.

[175] K Maehashi and K Matsumoto. Aptamer-Based Label-Free Immunosensors Using Carbon Nanotube Field-Effect Transistors. pages 1868–1871, 2009.

[176] Maria Magliulo, Donato De Tullio, Inger Vikholm-Lundin, Willem M. Albers, Tony Munter, Kyriaki Manoli, Gerardo Palazzo, and Luisa Torsi. Label-free C-reactive protein electronic detection with an electrolyte-gated organic field-effect transistor-based immunosensor. *Analytical and Bioanalytical Chemistry*, 408(15): 3943–3952, 2016. ISSN 16182650. doi: 10.1007/s00216-016-9502-3. URL `http://dx.doi.org/10.1007/s00216-016-9502-3`.

[177] Qiaoming Zhang, Francesca Leonardi, Stefano Casalini, Inés Temiño, and Marta Mas-Torrent. High performing solution-coated electrolyte-gated organic field-effect transistors for aqueous media operation. *Scientific Reports*, 6(October):1–10, 2016. ISSN 20452322. doi: 10.1038/srep39623. URL `http://dx.doi.org/10.1038/srep39623`.

[178] David Vehlow, Romy Schmidt, Annett Gebert, Maximilian Siebert, Katrin Susanne Lips, and Martin Müller. Polyelectrolyte complex based interfacial drug delivery system with controlled loading and improved release performance for bone therapeutics. *Nanomaterials*, 6(3), 2016. ISSN 2079-4991. doi: 10.3390/nano6030053. URL `http://www.mdpi.com/2079-4991/6/3/53`.

[179] P Bergveld. Development of an Ion-Sensitive Solid-State Device for Neurophysiological Measurements. *IEEE TRANSACTIONS ON BIO-MEDICAL ENGINEERING*, (January):70–71, 1970.

[180] TADAYUKI MATSUO and KENSALL D. WISE. An Integrated Field-Effect Electrode for Biopotential Recording. *IEEE TRANSACTIONS ON BIOMEDICAL ENGINEERING,*, pages 485–487, 1974.

[181] Eric Bakker, Philippe Bühlmann, and Ernö Pretsch. Polymer Membrane Ion - Selective Electrodes – What are the Limits ? *Electroanalysis*, 11(13):915–933, 1999. doi: 10.1002/(SICI)1521-4109(199909)11.

[182] Eric Bakker, Philippe Bühlmann, and Ernö Pretsch. Carrier-based ion-selective electrodes and bulk optodes. 1. general characteristics. *Chemical Reviews*, 97

(8):3083–3132, 1997. doi: 10.1021/cr940394a. URL https://doi.org/10.1021/cr940394a. PMID: 11851486.

[183] A. M. Münzer, M. Heimgreiter, K. Melzer, A. Weise, B. Fabel, A. Abdellah, P. Lugli, and G. Scarpa. Back-gated spray-deposited carbon nanotube thin film transistors operated in electrolytic solutions: an assessment towards future biosensing applications. *J. Mater. Chem. B*, 1:3797–3802, 2013. doi: 10.1039/C3TB20170H. URL http://dx.doi.org/10.1039/C3TB20170H.

[184] P. Bergveld. Thirty years of ISFETOLOGY: What happened in the past 30 years and what may happen in the next 30 years. *Sensors and Actuators, B: Chemical*, 88(1):1–20, 2003. ISSN 09254005. doi: 10.1016/S0925-4005(02)00301-5.

[185] Chang-Hwei Chen. Activation and Detoxification Enzymes. pages 7–17, 2012. ISSN 10282092. doi: 10.1007/978-1-4614-1049-2. URL http://link.springer.com/10.1007/978-1-4614-1049-2.

[186] Yi Yang, Zhongwu Wang, Zeyang Xu, Kunjie Wu, Xiaoqin Yu, Xiaosong Chen, Yancheng Meng, Hongwei Li, Song Qiu, Hehua Jin, Liqiang Li, and Qingwen Li. Low Hysteresis Carbon Nanotube Transistors Constructed via a General Dry-Laminating Encapsulation Method on Diverse Surfaces. *ACS Applied Materials and Interfaces*, 9(16):14292–14300, 2017. ISSN 19448252. doi: 10.1021/acsami.7b02684.

[187] Se Hyun Kim, Kihyon Hong, Wei Xie, Keun Hyung Lee, Sipei Zhang, Timothy P. Lodge, and C. Daniel Frisbie. Electrolyte-gated transistors for organic and printed electronics. *Advanced Materials*, 25(13):1822–1846, 2013. ISSN 09359648. doi: 10.1002/adma.201202790.

[188] Rebecca Sejung Park, Max Marcel Shulaker, Gage Hills, Luckshitha Suriyasena Liyanage, Seunghyun Lee, Alvin Tang, Subhasish Mitra, and H. S Philip Wong. Hysteresis in Carbon Nanotube Transistors: Measurement and Analysis of Trap Density, Energy Level, and Spatial Distribution. *ACS Nano*, 10(4):4599–4608, 2016. ISSN 1936086X. doi: 10.1021/acsnano.6b00792.

[189] Albert Lin, Nishant Patil, Koungmin Ryu, Alexander Badmaev, Lewis Gomez De Arco, Chongwu Zhou, Subhasish Mitra, and H. S. Philip Wong. Threshold voltage and on-off ratio tuning for multiple-tube carbon nanotube FETs. *IEEE Transactions on Nanotechnology*, 8(1):4–9, 2009. ISSN 1536125X. doi: 10.1109/TNANO.2008.2004706.

[190] Adelmo Ortiz-Conde, Antonio Cerdeira, Magali Estrada, Francisco J. García Sánchez, and Rodolfo Quintero. A simple procedure to extract the threshold

voltage of amorphous thin film MOSFETs in the saturation region. *Solid-State Electronics*, 45(5):663–667, 2001. ISSN 00381101. doi: 10.1016/S0038-1101(01)00123-X.

[191] Vijay Bhatt, Saumya Joshi, Markus Becherer, and Paolo Lugli. Flexible, Low-Cost Sensor Based on Electrolyte Gated Carbon Nanotube Field Effect Transistor for Organo-Phosphate Detection. *Sensors*, 17(6):1147, 2017. ISSN 1424-8220. doi: 10.3390/s17051147. URL `http://www.mdpi.com/1424-8220/17/5/1147`.

[192] Setsuko Yajima, Koji Tohda, Philippe Bühlmann, and Yoshio Umezawa. Donnan Exclusion Failure of Neutral Ionophore-Based Ion-Selective Electrodes Studied by Optical Second-Harmonic Generation. *Analytical Chemistry*, 69(10):1919–1924, 1997. ISSN 00032700. doi: 10.1021/ac961315t.

[193] V. Derycke, R. Martel, J. Appenzeller, and Ph Avouris. Controlling doping and carrier injection in carbon nanotube transistors. *Applied Physics Letters*, 80(15):2773–2775, 2002. ISSN 00036951. doi: 10.1063/1.1467702.

[194] V. Derycke, R. Martel, J. Appenzeller, and Ph. Avouris. Carbon Nanotube Inter- and Intramolecular Logic Gates. *Nano Lett.*, 1(9):453–456, 2001. ISSN 1530-6984. doi: 10.1021/nl015606f. URL `http://pubs.acs.org/doi/abs/10.1021/nl015606f`.

[195] Ali Javey, Ryan Tu, Damon B Farmer, Jing Guo, Roy G Gordon, and Hongjie Dai. Transistors with Chemically Doped Contacts High Performance n-Type Carbon Nanotube Field-Effect Transistors with Chemically Doped Contacts. *Nano*, 2, 2005. ISSN 1530-6984. doi: 10.1021/nl047931j.

[196] Daisuke Kaminishi, Hirokazu Ozaki, Yasuhide Ohno, Kenzo Maehashi, Koichi Inoue, Kazuhiko Matsumoto, Yasuhiro Seri, Atsushi Masuda, and Hideki Matsumura. Air-stable n-type carbon nanotube field-effect transistors with Si 3N4 passivation films fabricated by catalytic chemical vapor deposition. *Applied Physics Letters*, 86(11):1–3, 2005. ISSN 00036951. doi: 10.1063/1.1886898.

[197] Gerhard J. Mohr and Otto S. Wolfbeis. Optical sensing of anions via polarity-sensitive dyes: A bulk sensor membrane for nitrate. *Analytica Chimica Acta*, 316(2):239–246, 1995. ISSN 00032670. doi: 10.1016/0003-2670(95)00370-F.

[198] Smita Jadhav, Amnon J. Meir, and Eric Bakker. Normal pulse voltammetry as improved quantitative detection mode for amperometric solvent polymeric membrane ion sensors. *Electroanalysis*, 12(16):1251–1257, 2000. ISSN 10400397. doi: 10.1002/1521-4109(200011)12:16⟨1251::AID-ELAN1251⟩3.0.CO;2-P.

[199] Prof Manuel Jiménez. MOS Inverters.

[200] Anantha Chandrakasan Jan M. Rabaey and Borivoje Nikolic. *Chapter1 - Introduction*. 1999.

[201] Kenji Nomura, Hiromichi Ohta, Kazushige Ueda, Toshio Kamiya, Masahiro Hirano, and Hideo Hosono. Thin-film transistor fabricated in single-crystalline transparent oxide semiconductor. *Science*, 300(5623):1269–1272, 2003. ISSN 0036-8075. doi: 10.1126/science.1083212. URL `http://science.sciencemag.org/content/300/5623/1269`.

[202] Je-hun Lee, Do-hyun Kim, Dong-ju Yang, Sun-young Hong, Kap-soo Yoon, Pil-soon Hong, Chang-oh Jeong, Hong-sik Park, Shi Yul Kim, Soon Kwon Lim, Sang Soo Kim, Kyoung-seok Son, Tae-sang Kim, Jang-yeon Kwon, and Sang-yoon Lee. World's Largest (15-inch) XGA AMLCD Panel Using IGZO Oxide TFT. *SID Symposium Digest of Technical Papers*, 39(1):625, 2008. ISSN 0097-966X. doi: 10.1889/1.3069740. URL `http://doi.wiley.com/10.1889/1.3069740`.

[203] Kenji Nomura, Toshio Kamiya, Hiromichi Ohta, Tomoya Uruga, Masahiro Hirano, and Hideo Hosono. Local coordination structure and electronic structure of the large electron mobility amorphous oxide semiconductor In-Ga-Zn-O: Experiment and ab initio calculations. *Physical Review B - Condensed Matter and Materials Physics*, 75(3):2–6, 2007. ISSN 10980121. doi: 10.1103/PhysRevB.75.035212.

[204] M. Orita, H. Ohta, M. Hirano, S. Narushima, and H. Hosono. Amorphous transparent conductive oxide ingao3(zno)m (m 4): a zn4s conductor. *Philosophical Magazine B*, 81(5):501–515, 2001. doi: 10.1080/13642810110045923. URL `https://doi.org/10.1080/13642810110045923`.

[205] Hideo Hosono. Ionic amorphous oxide semiconductors: Material design, carrier transport, and device application. *Journal of Non-Crystalline Solids*, 352(9): 851 – 858, 2006. ISSN 0022-3093. doi: https://doi.org/10.1016/j.jnoncrysol.2006.01.073. URL `http://www.sciencedirect.com/science/article/pii/S0022309306002936`. Amorphous and Nanocrystalline Semiconductors - Science and Technology.

[206] P. F. Carcia, R. S. McLean, M. H. Reilly, and G. Nunes. Transparent ZnO thin-film transistor fabricated by rf magnetron sputtering. *Applied Physics Letters*, 82 (7):1117–1119, 2003. ISSN 00036951. doi: 10.1063/1.1553997.

[207] Chao-ming Hsu, Wen-cheng Tzou, Cheng-fu Yang, and Yu-jhen Liou. Investigation of the High Mobility IGZO Thin Films by Using Co-Sputtering Method. pages 2769–2781, 2015. doi: 10.3390/ma8052769.

[208] B. J. Jin, S. Im, and S. Y. Lee. Violet and UV luminescence emitted from ZnO thin films grown on sapphire by pulsed laser deposition. *Thin Solid Films*, 366 (1-2):107–110, 2000. ISSN 00406090. doi: 10.1016/S0040-6090(00)00746-X.

[209] Larry L. Hench and Jon K. West. The sol-gel process. *Chemical Reviews*, 90(1): 33–72, 1990. ISSN 00278874. doi: 10.1093/jnci/84.12.925. URL `http://pubs.acs.org/doi/abs/10.1021/cr00099a003`.

[210] Robert A. Street, Tse Nga Ng, Ren A. Lujan, Inyoung Son, Matthew Smith, Sangbok Kim, Taegweon Lee, Yongsik Moon, and Sungseo Cho. Sol-gel solution-deposited InGaZnO thin film transistors. *ACS Applied Materials and Interfaces*, 6(6):4428–4437, 2014. ISSN 19448252. doi: 10.1021/am500126b.

[211] K C Sanal, M Majeesh, and M K Jayaraj. Growth of IGZO Thin Films and Fabrication of Transparent Thin Film Transistor by RF Magnetron Sputtering. 8818:1–7, 2013. doi: 10.1117/12.2023865.

[212] Nidhi Tiwari, Narayan Chauhan, Po-tsun Liu, and Han-ping D Shieh. RSC Advances Electrical characteristics of InGaZnO thin film transistor prepared by co-sputtering dual InGaZnO and ZnO targets. pages 51983–51989, 2015. doi: 10.1039/c5ra08793g.

[213] L. Petti, F. Loghin, G. Cantarella, C. Vogt, N. Münzenrieder, A. Abdellah, M. Becherer, T. Haeberle, A. Daus, G. Salvatore, G. Tröster, and P. Lugli. Gain-tunable complementary common-source amplifier based on a flexible hybrid thin-film transistor technology. *IEEE Electron Device Letters*, 38(11):1536–1539, Nov 2017. ISSN 0741-3106. doi: 10.1109/LED.2017.2748596.

[214] Chenming Hu. Compact modeling for the changing transistor. *International Conference on Simulation of Semiconductor Processes and Devices, SISPAD*, pages 49–52, 2013. doi: 10.1109/CCTA.2017.8062457.

[215] Gabriel Cadilha Marques, Suresh Kumar Garlapati, Debaditya Chatterjee, Simone Dehm, Subho Dasgupta, Jasmin Aghassi, and Mehdi B. Tahoori. Electrolyte-Gated FETs Based on Oxide Semiconductors: Fabrication and Modeling. *IEEE Transactions on Electron Devices*, 64(1):279–285, 2016. ISSN 00189383. doi: 10.1109/TED.2016.2621777.

[216] W.R. Curtice. A MESFET Model for Use in the Design of GaAs Integrated Circuits. *IEEE Transactions on Microwave Theory and Techniques*, 28(5):448–456, 1980. ISSN 0018-9480. doi: 10.1109/TMTT.1980.1130099.

[217] file = :C\:/Users/ga45fas/AppData/Local/Mendeley Ltd./Mendeley Desktop/-Downloaded/Unknown - Unknown - No Title.pdf:pdf isbn = 0471143235

mendeley-groups = Study material publisher = A JOHN WILEY & SONS, JNC., PUBLICATION title = Physics of Semiconductor Devices year = 2006 Sze, S. M.; Ng, K. K., edition = 3rd ed. Hoboken, NJ.

[218] Kwyro Lee, Michael Shur, Tor A. Fjeldly, and Trond Ytterdal. *Semiconductor Device Modeling for VLSI*. Prentice-Hall, Inc., Upper Saddle River, NJ, USA, 1993. ISBN 0-13-805656-0.

[219] Peter W. Alexander, Telis Dimitrakopoulos, and D. Brynn Hibbert. Photo-Cured Ammonium and Hydrogen Ion Selective Coated-Wire Electrodes Used Simultaneously in a Portable Battery-Powered Flow Injection Analyzer. *Electroanalysis*, 9 (17):1331–1336, 1997. ISSN 10400397. doi: 10.1002/elan.1140091706.

[220] José F.C.C. Lima, Cristina Delerue-Matos, and M. Carmo Vaz. Flow-injection analysis of Kjeldahl nitrogen in milk and dairy products by potentiometric detection. *Analytica Chimica Acta*, 385(1-3):437–441, 1999. ISSN 00032670. doi: 10.1016/S0003-2670(98)00687-4.

[221] Júlia M.C.S. Magalhães and Adélio A.S.C. Machado. Array of potentiometric sensors for the analysis of creatinine in urine samples. *Analyst*, 127(8):1069–1075, 2002. ISSN 00032654. doi: 10.1039/b201173e.

[222] Manami Ikeda, Hiromitsu Hachiya, Satoshi Ito, Yasukazu Asano, and Toshihiko Imato. Development of long-term stable ammonium ion sensor in conjunction with a microbial membrane. *Biosensors and Bioelectronics*, 13(5):531–537, 1998. ISSN 09565663. doi: 10.1016/S0956-5663(97)00120-6.

[223] Saumya Joshi, Vijay Deep Bhatt, and Paolo Lugli. Sensor arrangement for analyzing substances in a material and method for operating such a sensor arrangement. In *In United States Patent Application Serial No. 16/051,160. TUM180702PUS-5/HK.* .

[224] S. Joshi, V.D. Bhatt, H. Rani, M. Becherer, and P. Lugli. Understanding the influence of in-plane gate electrode design on electrolyte gated transistor. *Microelectronic Engineering Volume 199, 5 November 2018, Pages 87-91 2018-08*, pages 87–91, Aug 2018. doi: 10.1016/j.mee.2018.07.019.

[225] Saumya Joshi, Vijay Deep Bhatt, Hao Wu, Markus Becherer, and Paolo Lugli. Flexible Lactate and Glucose Sensors using Electrolyte-Gated Carbon Nanotube Field Effect Transistor for Non-invasive Real-time Monitoring. *IEEE Sensors Journal*, (c):1–1, 2017. ISSN 1530-437X. doi: 10.1109/JSEN.2017.2707521. URL `http://ieeexplore.ieee.org/document/7933216/`.

[226] V.D. Bhatt, S. Joshi, and P. Lugli. Metal-free fully solution-processable flexible electrolyte-gated carbon nanotube field effect transistor. *IEEE Transactions on Electron Devices (Volume: 64, Issue: 3, March 2017) 2017-03*, pages 1375 – 1379, Mar 2017. ISSN 0018-9383. doi: 10.1109/TED.2017.2657882.

[227] V.D. Bhatt, S. Joshi, K. Melzer, and P. Lugli. Flexible dopamine sensor based on electrolyte gated carbon nanotube field effect transistor. In *2016 IEEE Biomedical Circuits and Systems Conference (BioCAS)*. IEEE Xplore Digital Library, Oct 2016. ISBN Inspec 16620454. doi: 10.1109/BioCAS.2016.7833719. URL `https://ieeexplore.ieee.org/document/7833719/`.

[228] Vijay Deep Bhatt, Saumya Joshi, Andreas Märtl, and Paolo Lugli. Effect of varying pH, Ionic strength and Composition of buffer on an dopamine sensor based on a functionalized Electrolyte Gated CNTFET. *5th International Conference on Bio-Sensing Technology 2017*.

[229] Saumya Joshi, Vijay Deep Bhatt, and Paolo Lugli. Flexible, low cost histamine sensor for food quality tests using CNTFETs. In *5th International Conference on Bio-Sensing Technology 2017*. .